



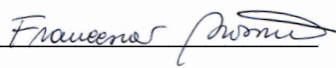
DOTTORATO DI RICERCA IN INGEGNERIA CIVILE

XXX CICLO DEL CORSO DI DOTTORATO

"Strengthening of masonry vaults with Steel Reinforced Grout"


Francesca Roscini

Dottoranda


firma

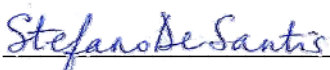
Prof. Gianmarco de Felice

Tutor


firma

Dr. Stefano De Santis

Co-Tutor


firma

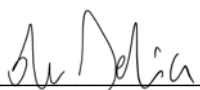
Dr. Maurizio Guadagnini

Co-Tutor


firma

Prof. Gianmarco de Felice

Coordinatore


firma

Collana delle tesi di Dottorato di Ricerca
In Scienze dell'Ingegneria Civile
Università degli Studi Roma Tre
Tesi n° 73

Dedicated to Alessandro

Abstract

In a period characterized by the urgent need of ensuring an adequate safety level to the building stock, including architectural heritage, Steel Reinforced Grout (SRG), comprising Ultra High Tensile Strength Steel cords embedded in a mortar matrix, is emerging as a particularly advantageous solution for the externally bonded strengthening of existing structures. Nevertheless, its development is still at a relatively earlier stage with respect to the already well-established Fibre Reinforced Polymers (which make use of organic matrices) as well as to other mortar-based composite materials, such as Textile Reinforced Mortars or Fabric Reinforced Cementitious Matrix (which comprise carbon, glass, basalt or PBO meshes). Therefore, a deep knowledge needs to be gained on mechanical properties, acceptance criteria and behaviour of reinforced structural members in order to develop suitable design relationships and assessment criteria, which would allow for a more confident use of SRG in structural rehabilitation practice.

This work provides a wide experimental evidence of SRG composites with lime-based mortars for the reinforcement of masonry vaulted structures. First, direct tensile tests on bare textile specimens and SRG coupons as well as single-lap shear bond tests were performed to investigate the main mechanical properties (tensile strength and stiffness, crack pattern, cord-to-matrix and SRG-to-substrate load transfer capacity, failure modes) and derive fundamental acceptance and design parameters. Then, bond tests were performed on curved substrates to investigate the influence of convex and concave curvatures on the SRG-to-masonry bond behaviour. Both double-lap double-prism test and three point bending tests were performed to study intermediate debonding mechanisms and analyse the effect of testing setups. Simplified relationships were also derived that account for substrate curvature, which may be useful for a preliminary estimate of SRG bond strength. Finally, full-scale tests on masonry vaults reinforced either at the extrados or at the intrados with different SRG systems were carried out. Specimens were provided with buttresses and backfill. Reinforcements included connectors at the abutments or along the barrel vault. The use of unconventional measurement techniques, such as the digital image correlation, provided information on crack occurrence and arch-fill

interaction. Test outcomes revealed the effectiveness of SRG in improving the load-carrying and the deflection capacity of masonry arched members.

Index

FIGURE CAPTIONS	X
TABLE CAPTIONS	XV
1. INTRODUCTION	1
AIM OF THIS RESEARCH	2
1.1 <i>Research Objectives</i>	3
1.2 <i>Structure of the dissertation</i>	3
1.2.1 Chapter 1 “Introduction”	3
1.2.2 Chapter 2 “Steel Reinforced Grout State of the Art”	4
1.2.3 Chapter 3 “Methodology chapter”	4
1.2.4 Chapter 4 “SRG system properties and experimental tests for accreditation”	5
1.2.5 Chapter 5 “SRG bond on curved masonry substrate”	5
1.2.6 Chapter 6 “Full-scale tests on timber masonry vaults strengthened with Steel Reinforced Grout”	5
1.2.7 Chapter 7 “Conclusions”	5
2. STEEL REINFORCED GROUT STATE OF THE ART	6
ABSTRACT	6
2.1 <i>INTRODUCTION</i>	6
2.2 <i>Mechanical properties of steel textile, mortar and Steel Reinforced Grout composite (Materials)</i>	10
2.2.1 Tensile behaviour of steel textiles for SRG applications	10
2.2.2 Tensile behaviour of steel textiles and SRG composites RRT	10
2.3 <i>SRG-to-substrate bond behaviour</i>	11
2.3.1 Bond behaviour of composites material overview	11
2.3.2 SRG-to-concrete bond behaviour	11
2.3.3 SRG-to-masonry bond behaviour	17
2.3.4 SRG-to-tuff bond behaviour	18
2.4 <i>Analytical prediction of the bond strength</i>	20
2.5 <i>A qualification method for externally bonded FRCM</i>	21
2.6 <i>Strengthening of reinforced concrete structures</i>	21
2.6.1 Strengthening of beams in bending	21
2.6.2 Confinement of RC prismatic specimens and RC cylinders	25
2.6.3 SRG jacketing of columns	28
2.6.4 Slab reinforced with SRG	29
2.7 <i>Strengthening of reinforced masonry structures</i>	30
2.7.1 SRG strengthening system applied on arches and vaults of beams	30
2.7.2 SRG reinforcement for confinement	30
2.7.3 Out-of-plane reinforcement for walls	31
2.7.4 In-plane reinforcement wall	32
2.7.5 Reinforcement of masonry ring-beams	33
2.7.6 Reinforcement of curved structural elements	35
2.7 <i>CONCLUDING REMARKS</i>	35

3. METHODOLOGY CHAPTER	36
3.1 Research Methodology	36
3.2 Experimental Program	36
3.3 Materials	39
3.4 Material properties, qualification procedures of SRG (Phases 1 and 2)	41
3.5 Evaluation of bond behavior of SRG applied to curved masonry substrate via double-lap shear bond and bending tests (Phase 3).....	42
3.6 Experimental tests on masonry arches strengthened with SRG (Phase 6)	42
3.7 Simplified design equations (Phases 3, 5 and 7)	43
4. SRG SYSTEM PROPERTIES AND EXPERIMENTAL TESTS FOR ACCREDITATION	44
ABSTRACT	44
4.1 INTRODUCTION	45
4.2 EXPERIMENTAL INVESTIGATIONS.....	46
4.2.1 Experimental plan	46
4.2.2 Materials	48
4.2.2.1 Steel textiles.....	48
4.2.2.2 Mortar matrices.....	48
4.2.2.3 Strengthening systems.....	48
4.2.3 Manufacturing of specimens	50
4.2.4 Experimental setups	54
4.3 STEEL REINFORCED GROUT EXPERIMENTAL RESULTS	57
4.3.1 GS-G system (galvanized steel and lime with geopolymer binders mortar).....	60
4.3.1.1 GS Steel textile	60
4.3.1.1.1 Durability of GS steel textile.....	60
4.3.1.2 GS-G composite under tensile loading.....	62
4.3.1.3 GS-G-BMAS shear bond performance	62
4.3.2 GS-M system (galvanized steel and mineral mortar)	67
4.3.2.1 GS Steel textile	67
4.3.2.2 GS-M composite under tensile loading.....	67
4.3.2.3 GS-M-BMAS shear bond performance.....	67
4.3.3 SS-L system (stainless steel and lime mortar)	71
4.3.3.1 SS Steel textile	71
4.3.3.2 SS-L composite under tensile loading.....	71
4.3.3.3 SS-L-BMAS shear bond performance	71
4.4 FAILURE BOND ANALYTICAL PROCEDURE FOR SRG STRENGTHENING SYSTEM-TO-MASONRY SUBSTRATE	75
4.5 COMPARISON BETWEEN SRG AND FRCC SYSTEMS.....	82
4.5.1 B-L system (basalt and lime mortar).....	85
4.5.2 C20-C system (carbon and cementitious mortar)	86
4.5.3 C10-CC system (carbon and cementitious mortar).....	87
4.5.4 W-L system (glass and lime mortar)	88
4.5.5 AG-G system (aramid glass and lime with geopolymer binders mortar).....	89
4.5.6 P-CM system (PBO and cementitious mortar)	90
4.5.7 Round Robin Test results	91
4.5.7.1 Textile tensile test	91
4.5.7.2 Composite material specimen tensile test	93

4.5.7.3 Shear bond test.....	95
4.5.8 Qualification procedures	98
4.5.9 Digital Image Correlation method in FRCM mechanical characterization.....	99
4.6 CONCLUDING REMARKS.....	101
5. SRG BOND ON CURVED MASONRY SUBSTRATE	104
ABSTRACT	104
5.1 INTRODUCTION.....	105
5.2 EXPERIMENTAL PROGRAM	108
5.2.1 Manufacturing.....	110
5.2.1.1 Double-lap double-prism push-pull manufacturing	112
5.2.1.2 Four-point bending test manufacturing	116
5.3 TESTING SETUP	120
5.3.1 Double-lap double-prism push-pull tests setup	120
5.3.2 Four-point bending test setup	122
5.4 EXPERIMENTAL RESULTS	125
5.4.1 Double-lap double-prism push-pull tests results	125
5.4.1.1 Reinforcement application on intradosal side	125
5.4.1.2 Reinforcement application on extradosal side.....	128
5.4.2 Four-point bending test results	132
5.5 BOND FAILURE FORCE TO CURVATURE RELATIONSHIP	142
5.6 CONCLUDING REMARKS.....	144
6. FULL-SCALE TESTS ON TIMBREL MASONRY VAULTS STRENGTHENED WITH STEEL REINFORCED GROUT	147
ABSTRACT	147
6.1 INTRODUCTION.....	148
6.2 EXPERIMENTAL SETUP	151
6.2.1 Construction of the vault specimens.....	151
6.3 STRENGTHENING SYSTEM AND INSTALLATION.....	154
6.3.1 Materials	154
6.3.2 Extrados strengthening.....	155
6.3.3 Intrados strengthening.....	156
6.4 INSTRUMENTATION	158
6.5 TEST RESULTS.....	159
6.5.1 Unreinforced vault	164
6.5.2 Vaults reinforced at the extrados	165
6.5.3 Vault reinforced at the intrados	169
6.6 ANALYTICAL ESTIMATE OF THE LOAD CARRYING CAPACITY	177
6.7 CONCLUDING REMARKS.....	181
7. CONCLUSIONS.....	183
FUTURE DEVELOPMENTS.....	185
REFERENCES.....	186
RINGRAZIAMENTI.....	203

Figure captions

Figure 2.1. Type of failure [Cancelli et al., 2007].....	13
Figure 2.2. Single-lap direct-shear test set-up (a) front view, (b) side view, and (c) top view (dimensions in mm) [Sneed et al., 2016].....	15
Figure 2.3. Pictures of single-lap direct-shear test (a) specimen with external matrix layer (specimen DS_K_330_50_3 shown) and (b) specimen with the external matrix layer ..	16
omitted (specimen DS_K_330_50_L_2 shown). Note the fibers extending beyond the bonded area at the free end (circled in the photographs) [Sneed et al., 2016].....	16
Figure 2.4. Pictures of single-lap shear test specimens: (a) crack along interface of cords and matrix, (b) surface of internal matrix layer after failure (specimen DS_K_330_50_1 shown), and (c) cracking observed on surface of external matrix layer [Sneed et al., 2016]	16
Figure 2.5. Applied load P – global slip g response and applied stress σ – global slip g 17 response of single-lap direct-shear specimens [Sneed et al., 2016]	17
Figure 2.6. a) Experimental set-up for push-pull bond test; b) example of specimen positioned in the testing apparatus; c) painted surface of the matrix for DIC; d) position of strain gauges and LVDTs for specimens made of single tuff stone e prisms	18
[Bilotta et al., 2017]	18
Figure 2.7. Failure modes: a) tensile failure of the glass fibers; b) debonding at the tuff-matrix interface; c) slippage of the fibers from the matrix [Bilotta et al., 2017].....	19
Figure 2.8. Steel reinforcement: (a) steel tape, (b) 3X2 cord and (c) 3SX cord [Barton et al., 2005]	21
Figure 2.9. Schematic representation of RC beam test setup [Barton et al., 2005].....	22
Figure 2.10. Load–midspan deflection of reinforced concrete beams with and without SRG strengthening elements [Huang et al., 2005]	23
Figure 2.11. Failure of SRG strengthened reinforced concrete beams. SRP (a), SRG (b) [Huang et al., 2005]	23
¹ [Bencardino and Condello, 2014]; ² [Barton et al., 2005]; ³ [Pecce et al., 2006].....	24
Figure 2.12a. Strengthening of prismatic specimens by steel cords [Thermou et al., 2013]	26
Figure 2.12b. Strengthening of cylinder by steel cords [Thermou et al., 2015].....	26
Figure 2.13. Cords (a-b) and textile steel mesh, high density (c), medium density(d) and low density (e) [Thermou et al., 2015].....	26
Figure 2.14. Specimen geometry and cross section shapes (dimensions in mm).....	27
[Thermou et al., 2016]	27
Figure 2.15. Preparation of the steel-reinforced fabrics and fabrication of the SRG jackets to circular and square cross section specimens [Thermou et al., 2016]	28
Figure 2.16. Test set up [Thermou et al., 2007].....	28
Figure 2.17. Test assembly: geometry and reinforcement details (dimensions in mm) [Thermou et al., 2007]	29
Figure 2.18. Hooping with stainless steel cords: application [Borri et al., 2013]	30

Figure 2.19. Failure mode for clay brick masonry columns: (a) unconfined; (b) confined with BFRCM wraps; (c) reinforced by steel wire collaring. (d) Tensile fracture of the basalt fiber mesh. [Fossetti et al., 2016].....	31
Figure 2.20. Geometrical configuration and boundary conditions for masonry panels tested in diagonal compression [Borri et al., 2011].....	32
Figure 2.21. Ring – beams built by perforated bricks and SRG laminates [Borri et al., 2010]	34
Figure 2.22. Test setup scheme: horizontal action [Borri et al., 2010]	34
Figure 2.23. Test setup scheme: vertical action [Borri et al., 2010].....	34
Figure 3.1. Experimental program flowchart	38
Figure 3.2. Steel mesh having 0.108mm ² cross section area (a), steel mesh having 0.2016 mm ² cross section area (b) and architecture of an individual strand(c)	40
Figure 4.1. Experimental setups for tensile tests on dry textile.....	47
steel (a), SRG coupons (b), and for shear bond tests (c)	47
Figure 4.2. FRCM specimen geometry (the measures are only advised).....	50
Figure 4.3. FRCM reinforcement applied on brickwork masonry geometry	51
Fig. 4.4.1. Plexiglass moulds	52
Fig. 4.4.2. FRCM coupons casting.....	52
Fig. 4.4.3. Keeping in water	52
Fig. 4.4.4. Storing on a plane surface «lying sideways on»	52
Fig. 4.4.5. Drying for 15 days on supports for uniform drying.....	52
Fig. 4.4.6. Specimen before testing.....	52
Figure 4.4. Composite material specimens manufacturing procedure	52
Fig. 4.5.1. Masonry prisms manufacturing	53
Fig. 4.5.2. Prisms curing in laboratory conditions	53
Fig. 4.5.3. Prisms before reinforcement applying	53
Fig. 4.5.4. Aluminium moulds	53
Fig. 4.5.5. FRCM first layer.....	53
Fig. 4.5.6. Textile inside mortar.....	53
Fig. 4.5.7. FRCM second layer	53
Fig. 4.5.8. Reinforcement applied.....	53
Fig. 4.5.9. Keeping wet for 26 days	53
Fig. 4.5.10. Prisms FRCM reinforced	53
Figure 4.5. Shear bond test specimens manufacturing procedure	53
Fig. 4.6.1. Extensometer on textile	55
Fig. 4.6.2. Extensometer (red), potentiometers (yellow) and DIC speckle pattern on coupon surface	55
Fig. 4.6.3. Extensometer (red), LVDTs (yellow), DIC on markers and DIC speckle pattern on reinforcement surface and on marker (light blue)	55
Figure 4.6. Traditional instrumentation setup	55

Fig. 4.7.1. Grey-scale matrix.....	55
Fig. 4.7.2. Speckle pattern on reinforcement	55
Fig. 4.7.3. Theory of high resolution camera position for DIC.....	56
Fig. 4.7.4. High resolution camera for DIC detection	56
Figure 4.7. Contact-less method DIC setup	56
Figure 4.8.1. Ascione et al. [2015] proposed procedure for accreditation of strengthening system	57
Figure 4.8.2. Comparison between procedure proposed by Ascione et al. [2015] and procedure developed in 2017	57
Figure 4.9. Tensile failure modes (RILEM procedure).....	59
Figure 4.10. Shear bond test failure modes [de Felice et al., 2014 -Ascione et al. 2015]	59
Figure 4.11. Microscope analysis. (a) none ageing (optical microscope), (b) 2000h(SEM), (c) 3000h(SEM)	61
Figure 4.12. Qualification procedures GS-G	65
Figure 4.13. Qualification procedures GS-M.....	70
Figure 4.14. Qualification procedures SS-L.....	74
Figure 4.15. Qualification procedures B-L	85
Figure 4.16. Qualification procedures C20-C	86
Figure 4.17. Qualification procedures C10-CC	87
Figure 4.18. Qualification procedures W-L	88
Figure 4.19. Qualification procedures AG-G.....	89
Figure 4.20. Qualification procedures P-CM.....	90
Figure 4.21. Stress-Strain graphs for textile tensile tests (average values)	92
Figure 4.22. Stress-Strain graph for direct tensile test on composite material specimens (average values)	94
Figure 4.23. Stress-Slip graph for shear bond tests results (average values)	96
Figure 4.24. Focus on interlocking in GS-G system	97
Figure 4.25. Textile sliding in SS-L system.....	97
Figure 4.26. Focus on cross nodes in B-L system.....	97
Figure 4.27. Displacements and strains development plot for coupons tensile test	99
Figure 4.29. Stress-transfer mechanism stages (b), idealized P - g global slip response for FRP(a)	101
Figure 4.30. Detachment at the interface mortar-masonry substrate.....	103
Figure 5.1. Hinges kinematic collapse, in asymmetric load condition.....	106
Figure 5.3. Reinforcement applied at the “intrados” side	107
Figure 5.2. Intradosal hinge	107
Figure 5.4. Reinforcement applied at the “extrados” side.....	107
Figure 5.5. Extradosal hinge	107
Figure 5.6. Curved specimens obtained as portion of most common curved structural elements	108

Figure 5.7. Arch or vault with curvature radius similar to specimens with 1800mm of radius.....	109
Figure 5.8. Arch or vault with curvature radius similar to specimens with 2650mm of radius.....	109
Figure 5.9. Arch or vault with curvature radius similar to specimens with 5000mm of radius.....	110
Figure 5.10. Drilling of bricks	111
Figure 5.11. Papers shaped of curved elements design	111
Figure 5.12. Milling machine.....	111
Figure 5.13. Procedure to insert steel bars	113
Figure 5.14. Strain gauge on the UHTSS cords (a), steel textile placed on the first layer of mortar (b), second layer of mortar applied between tracks(c).	114
Figure 5.15. Lateral view (a-g) and bottom and side view (h) of the specimens under investigation with concave (a-c), convex (d-f) and plane (g) surface for double-lap double-prism push-pull.	115
Figure 5.16. Steel bars inside the specimen, the scheme (a) and the “virtual” 3D render	116
Figure 5.17. Drilled brickwork from the top.....	116
Figure 5.18. Bar inserted.....	116
Figure 5.19. Brickwork realizing	117
Figure 5.20. Masonry surface before reinforcing (a), first layer of mortar application (b), steel textile placed on the first layer of mortar (c), second layer of mortar applied between tracks (d).	117
Figure 5.21. Strain gauges on the UHTSS cords.....	118
Figure 5.22. Specimens before testing	118
Figure 5.23. Lateral view (a-g) and bottom and side view (h) of the specimens under investigation with concave (a-c), convex (d-f) and plane (g) surface for four-point bending test.	119
Figure 5.24. Concave specimen set up.....	121
Figure 5.25. Convex specimen set up	121
Figure 5.26. Set up design.....	121
Figure 5.27. Strain gauge position with respect to the specimen	121
Figure 5.28. Potentiometers and LVDT	121
Figure 5.29. Potentiometers	121
Figure 5.30. Double DIC camera	122
Figure 5.31. Upper and bottom reinforcement slip measurement.....	122
Figure 5.32. Experimental setup, front design(a), axonometric design(b), real image(c)	123
Figure 5.33. DIC setup in four-point bending test	124
Figure 5.34. Concave test results	126

Figure 5.35. Concave test: vertical displacement just before failure, left side(a) and right side(b) and vertical strains just before failure, left side(a) and right side(b).....	127
Figure 5.36. Failure mode image and C failure mode [Ascione et al. 2015]	128
Figure 5.37. Convex test results.....	129
Figure 5.38. Concave test: vertical displacement just before failure, left side (a) and right side(b)and vertical strains just before failure, left side(a) and right side(b).....	130
Figure 5.39. Double lap shear bond test failure load vs. curvature	131
Figure 5.40. Horizontal displacement plot for front D.I.C.....	132
Figure 5.41. Points of vertical lines	133
Figure 5.42. Indeformed vertical lines before bending test.....	133
Figure 5.43. Image with deformations	133
Figure 5.44. Neutral axis distance (y) from compressed surface	133
Figure 5.45. Neutral axis using for flexural moment calculation.....	133
Figure 5.46. Intradosal surface procedure.....	134
Figure 5.47. Rectilinear surface procedure	134
Figure 5.48. Extradossal surface procedure.....	135
Figure 5.49. Failure load vs. curvature	138
Figure 5.50. Test results provided by DIC: displacement (a,b) and strain (c,d) fields on lateral (a,c) and lower (b,d) surfaces at failure for intradosal specimen I-5000-01	140
Figure 5.51. Test results provided by DIC: displacement (a,b) and strain (c,d) fields on lateral (a,c) and lower (b,d) surfaces at failure for extradossal specimen E-1800-01	141
Figure 5.52. Trend line of double-lap double-prism push-pull tests	142
Figure 5.53. Trend line of four-point bending tests	143
Figure 5.54. Average Load-Slip curve about SRG reinforcement comparing, characterized by different curvature radii.	145
Figure 6.1. Side and top view of the experimental setup.	152
Figure 6.2. Construction of masonry vault specimens.	153
Figure 6.3. Ultra High Tensile Strength Steel (UHTSS) cord (a) and textiles with 8 cord/in density (b) and 4 cord/in density (c).	155
Figure 6.4. Installation of the SRG reinforcement at the extradoss of the vault.....	157
Figure 6.5. Installation of the SRG reinforcement at the intrados of the vault.....	157
Figure 6.6. Vertical displacements of bricks 10 and 17 (a), horizontal displacements of the abutments (b), out-of-plane displacements of the wood and Plexiglas panels (c), and vertical displacements of brick 17 and of the IPE240 beam (d) vs. time.	161
Figure 6.7. Load-displacement response curves.	162
Figure 6.8. Failure mode of UNR specimen.	165
Figure 6.9. Crack pattern, failure mode and strains in the textile of EX8 specimen.	168
Figure 6.10. Crack pattern, failure mode and strains in the textile for EX4 specimen..	169
Figure 6.11. Crack pattern, failure mode and strains in the textile for IN4 specimen...	172

Figure 6.12. Damage pattern surveyed after the test on EX8 (a-c), EX4 (d-f) and IN4 (g-i) vault specimens.	173
Figure 6.13. Deformed configurations of EX8 (a,b), EX4 (c,d) and IN4 (e,f) specimens compared to those of UNR at peak load (a,c,e) and at collapse (b,d,f).	174
Figure 6.14. Field of vertical displacements and arrows of total displacements at peak load in UNR (a), EX8 (b), EX4 (c) and IN4 (d) specimens. Arrows scaled by 2.	175
Figure 6.15. Field of vertical displacements and arrows of total displacements at collapse in UNR (a), EX8 (b), EX4 (c) and IN4 (d) specimens. Arrows scaled by 0.8.	176
Figure 6.16. Collapse mechanisms of EX8 (a) and IN4 (b) specimens used for the analytical estimate of their load carrying capacity with limit analysis based approaches.	179
Figure 6.17. Axial load – bending moment strength domains of the cross section of the arch reinforced at the extrados (a) and at the intrados (b).	180

Table captions

Table 2.1. Material properties of SRP and SRG	12
Table 2.2. SRG test results (1 – 12 cords/in density)	12
Table 2.3. Test results.	13
Table 2.4. Shear test matrix	14
Table 2.5. Shear tests: result summary.....	14
Table 2.6. Steel-FRCM single-lap direct-shear test specimens.....	15
Table 2.7. SRG bond results with different anchorage length	17
Table 2.8. Results of bond tests on FRCM and SRG	19
Table 2.9. Efficiency coefficients for SRG system.....	24
Table 2.11. Test results	35
Table 3.1. Physical properties of steel textile (Datasheet)	40
Table 3.2. Properties of mortar (Tests conducted in the laboratory).....	
[De Santis et al., 2017a]	40
Table 3.3. Properties of substrate (Datasheet).....	41
Table 3.4 Mortar joints (Datasheet)	41
Table 4.1. Textiles description.....	49
Table 4.2. Mortar matrices description	49
Table 4.3. Strengthening systems description	49
Table 4.4. Textiles properties (Data sheet)	50
Table 4.5. Mortars properties (Data sheet).....	50
Table 4.6. Results of tensile tests on textile specimens (CV in round brackets).....	62
Table 4.7. GS series	63
Table 4.8. GS-G series	63
Table 4.9. GS-G failure modes	64
Table 4.10. GS-G-BMAS series	64

Table 4.11. GS-G-BMAS failure modes.....	65
Table 4.12. GS series	68
Table 4.13. GS-M series	68
Table 4.14. GS-M failure modes.....	69
Table 4.15. GS-M-BMAS series.....	69
Table 4.16. GS-M-BMAS failure modes	70
Table 4.17. SS series.....	72
Table 4.18. SS-L series	72
Table 4.19. SS-L failure modes	72
Table 4.20. SS-L-BMAS series.....	73
Table 4.21. SS-L-BMAS failure modes.....	73
Table 4.22. Experimental data for mortar properties characterization	
[De Santis et al., 2017a].....	77
Table 4.23. GS-G series.....	78
Table 4.24. GS-M – SS-L series	79
Table 4.25. R-F series	80
Table 4.27. Textiles properties (Data sheets).....	82
Table 4.28. Mortars properties (Data sheets)	82
Table 4.29. Textiles description.....	83
Table 4.30. Mortar matrices description	84
Table 4.31. Strengthening systems description.....	84
Table 4.32. Textile tensile tests results (average values)	91
Table 4.33. FRCM tensile tests results (average values)	93
Table 4.34. Shear bond tests results (average values).....	95
Table 5.1: Tests results “Double-lap double-prism push-pull”	131
Table 5.2. Tests results “Four-point bending test”	139
Table 5.3. Failure bond prediction formula depending on curvature	143
Table 6.1. Test results	163

1. Introduction

Recent earthquakes in Italy have highlighted the need to ensure the safety of existing buildings and increase their resilience. This is particularly true for cultural heritage, which, in addition to external actions, has been subjected to environmental degradation, several changes of use and sequences of hazard events. With this in mind, different solutions for the strengthening and rehabilitation of heritage structures have been adopted throughout history, ranging from techniques using more traditional materials and systems (not always appropriate), such as chains, connectors, anchors, steel pins, concrete edge beams (concrete curbs), reinforced injections, as well as more innovative materials, such as externally bonded advanced composites reinforcement (EBRs). In the past decades, the use of advanced composites in strengthening solutions, has been receiving a great deal of attention [[Valluzzi et al., 2014a](#)] because of their ability to increase load-bearing capacity without altering original geometry, mass and stiffness. The rapid uptake of advanced composites in strengthening applications has been facilitated by their versatility and adaptability, thus making them suitable for installation on any structural element of existing building and to comply with the preservation criteria for cultural heritage. In literature are available codes about Externally Bonded Reinforced (EBR). In particular, American Concrete Institute guidelines are made for FRP, like

- i. ACI 440.2R-08: “Guide for the Design and Construction of Externally Bonded FRP Systems for Strengthening Concrete Structures”
- ii. ACI 440.7R-10: “Guide for the Design and Construction of Externally Bonded Fiber-Reinforced Polymer Systems for Strengthening Unreinforced Masonry Structures”

At the same time, l’Association Française de Génie Civil published:

- iii. AFGC: “Réparation et renforcement des structures en béton au moyen des matériaux composites”

Regarding FIB bulletin, it can consider:

- iv. FIB bulletin 40: “FRP reinforcement in RC structures” and

in particular, “Externally applied FRP reinforcement for concrete structures: technical report prepared by a working party of the T5.1 FRP reinforcement for concrete structures” (in process to be promulgate)

- v. FIB bulletin 40: “Model Code 2010”
About italian normative, is available this document from CNR “CNR – Commissione di Studio per la Predisposizione e l’Analisi di Norme Tecniche relative alle costruzioni”:
- vi. CNR-DT 200 R1/2013 – “Istruzioni per la Progettazione, l’Esecuzione ed il Controllo di Interventi di Consolidamento Statico mediante l’utilizzo di Compositi Fibrorinforzati -Materiali, strutture di c.a. e di c.a.p., strutture murarie”

Nevertheless, normative design for documents Fabric-Reinforced Cementitious Matrix (FRCM) have not yet been made available, with the exception of the American guidelines «ACI 549, 4R-13». Italian guidelines about FRCM are about to be published. Therefore, the aim of this thesis is to develop the required understanding of the fundamental behavior of masonry elements strengthened with EBR composites and contribute to the development of the forthcoming guidelines [Ascione et al., 2015]. This work will investigate primarily the behavior of novel reinforcement systems using Ultra High Tensile Strength Steel cords embedded in a mortar matrix (Steel Reinforced Grout - SRG) [De Santis and de Felice, 2015b - De Santis et al., 2017a], for masonry vaults [Valluzzi et al., 2001 - Girardello et al., 2013 - De Santis et al., 2017b].

AIM OF THIS RESEARCH

The aim of this research is to examine the strengthening of masonry vaults with Steel Reinforced Grout via full-test experimental investigations. For that purpose, this document deals with SRG composite material analysis by means of their mechanical characterization and development an in depth understanding about reinforcement to substrate bond behavior applied to masonry substrates, either rectilinear and curved ones.

1.1 Research Objectives

In order to achieve the main aim of this research the following specific objectives are identified:

- ✓ to review the existing literature on SRG
- ✓ to propose guidelines about SRG
- ✓ to show and as a result, to justify effectiveness using SRG in rehabilitation
- ✓ pointing out advantages and drawbacks of Steel Reinforced Grout
- ✓ to determine the SRG reinforcement-to-substrate bond performance in terms of strength and failure mode
- ✓ to contribute identifying standardized procedures for product qualification and material assurance purposes and to demonstrate the benefits of SRG over others FRCM strengthening systems
- ✓ to investigate bond behaviour of Steel Reinforced Grout applied to curved masonry substrates
- ✓ to show that SRG, applied on full-scale timber vault specimens, prevents the development of the four-hinge mechanism and avoided damage concentrations
- ✓ to develop standardized guidelines for shear bond tests, which are needed to improve the reliability of the mechanical parameters of the SRG systems and the safety level of reinforced structures
- ✓ to estimate load carrying capacity of the reinforced arch with a simplified analytical procedure based on limit analysis (static and kinematic approaches)

1.2 Structure of the dissertation

This thesis consists of seven chapters.

1.2.1 Chapter 1 “Introduction”

Provides background; identifies the problem, purpose and research significance; in addition, the overall methodology and layout of the thesis are briefly summarized.

1.2.2 Chapter 2 “Steel Reinforced Grout State of the Art”

In this chapter, a detailed literature review of “SRG State of The Art” is presented and the following key issues are discussed:

- ✓ Overview about composite materials
- ✓ Properties of FRP reinforcement
- ✓ Improving of properties in FRCM respect with FRP: PROs and CONs
- ✓ Steel cords introducing like reinforcement textile
- ✓ Benefits of grout matrix respect to epoxy resin
- ✓ SRP vs SRG
- ✓ Advantages and drawback of SRG
- ✓ SRG phenomena analysis: interlocking, durability, reversibility and de-cohesion
- ✓ Mechanical characterization of SRG composite materials
- ✓ Durability of materials
- ✓ Investigation tests of SRG-to-substrate (concrete, masonry and tuff) bond behavior
- ✓ Analytical prediction of the bond strength: literature reviewed
- ✓ SRG applications on concrete middle-scale and full-scale specimens
- ✓ SRG applications on masonry middle-scale and full-scale tests
- ✓ Conclusions: explanation of the effectiveness of the SRG system
- ✓ Contribution of this paper to existing knowledge for scientific community and suggestions on further future researches.

1.2.3 Chapter 3 “Methodology chapter”

This chapter describes the methodology adopted to investigate performance of SRG application in masonry substrate; multi-scale experimental test for detecting bond behaviour and full-scale experimental program carried on vaults reinforced with Steel Reinforced Grout. The purpose is develop an analytical approach for bond behaviour to propose predictive recommendation, in accordance with CNR DT 200 R1/2013 method.

1.2.4 Chapter 4 “SRG system properties and experimental tests for accreditation”

In this chapter, SRG system properties and experimental tests for accreditation are illustrated aiming at deriving engineering design parameters and to provide a theoretical prediction in terms of debonding value [[Roscini et al., 2016](#) - [De Santis et al., 2017a](#)].

1.2.5 Chapter 5 “SRG bond on curved masonry substrate”

This chapter explains SRG application on curved masonry substrate: middle-scale test results contribute to the knowledge on the SRG-to-masonry bond behaviour via double-lap double-prism push-pull and four-point bending and could help developing design relationships for the reinforcement of masonry curved members [[De Santis, 2017](#) - [Roscini et al., 2017](#)].

1.2.6 Chapter 6 “Full-scale tests on timber masonry vaults strengthened with Steel Reinforced Grout”

The Chapter 6, the last concerning to laboratory test, describes an experimental investigation on four full-scale timber vault specimens. One of them is tested unreinforced, while the other ones were strengthened with Steel Reinforced Grout (SRG) [[De Santis, Roscini, de Felice, 2018](#)].

1.2.7 Chapter 7 “Conclusions”

This chapter includes a summary of results, followed by recommendations for further studies and open issues.

2. Steel Reinforced Grout State of the Art

ABSTRACT

Steel Reinforced Grout (SRG) has been recently introduced as an advanced composite system for the retrofitting of existing structures. This system comprises unidirectional textile of High Tensile Strength Steel embedded in a mortar matrix. The first investigation on SRG was carried out in 2004 [Wobbe et al.] and several studies ranging from basic mechanical characterization to practical structural applications have been carried out since. Despite the relatively large amount of available literature, however, specific design guidelines or standardised testing methods for SRG have not yet been developed. An in-depth review of the state-of-the-art on SRG is presented here to provide a critical assessment of currently open issues, including experimental methodologies, analytical and numerical modelling, and structural performance in typical applications so as to assess the potential of SRG as a strengthening system.

The performance of SRG systems is compared to that of alternative advanced strengthening solutions, such as FRP (Fabric Reinforced Polymer), SRP (Steel Reinforced Polymer) and FRCM (Fabric Reinforced Cementitious Mortar), as well as traditional retrofitting techniques.

2.1 INTRODUCTION

The use of composite materials has increased rapidly in the last decades as an innovative alternative technique to the more traditional steel chains, post-tensioned steel cables and reinforced concrete edge beams, especially in strengthening applications of existing buildings as a response to recent earthquakes. The first paper on the application of FRP for structural use was published in 1992 by Triantafillou [Triantafillou, T.C. Plevris, N., 1992] and these materials quickly became popular in civil engineering

applications thanks to their high strength, corrosion resistance, and electromagnetic neutrality. Advanced composites reinforced with textile reinforcement are widely used thanks to their flexibility, mouldability to any surface and wide range of mechanical properties provided by the reinforcing material. The most commonly used reinforcing materials are aramid, basalt, carbon, glass and PBO (polyparaphenylene benzobisoxazole). The mechanical properties of these types of fibers (e.g. strength and elastic modulus) are comparable, or often superior, to those of conventional steel reinforcement. When firstly introduced in civil engineering applications, these textiles were combined with epoxy resins (polymeric matrix) to obtain FRP strengthening systems. FRPs are characterised by a high strength to weight ratio, good fatigue resistance, and can be used in a variety of different applications [Ghiassi et al., 2014 - Bencardino et al. 2015a]. FRPs are virtually corrosion-free thanks to the protection offered by the organic resin matrix to severe environments and exposure conditions [Borri et al., 2015]. On the other hand, as reported by various researchers [Papanicolaou et al. 2007 - Papanicolaou et al. 2008 - Grande et al., 2013 – Razavizadeh et al., 2014 - Tetta et al. 2015 - Borri et al, 2015 - Fossetti et al., 2016 - Thermou et al., 2016], FRPs have several limitations, including: (a) poor performance of polymer matrix at temperatures above their glass transition point; (b) high cost, in particular epoxy-based FRPs; (c) resins can be harmful and need to be handled with care; (d) degradation of epoxy matrix due to hydrolysis, plasticization, and swelling in alkaline solution; (e) difficulties in applying FRPs on wet surface or at low temperatures; (f) lack of vapour permeability; (g) polymeric matrix is not suitable for applications on substrate materials like clay or masonry (bond is affected by porosity, surface unevenness and/or roughness properties of brick) and applications on cultural heritage buildings where reversibility is an important requirement; (h) difficulty in detecting possible damages after loading events (e.g. earthquake) on areas covered with FRP.

Given the limitations discussed above, the use of alternative matrices, such as mortar, has been examined by several researchers [Thermou et al., 2007 - Papanicolaou et al., 2007 - Papanicolaou et al., 2008 - Razavizadeh et al., 2014 - Fossetti et al., 2016] and FRCM (Fabric Reinforced Cementitious Matrix) composites are currently receiving a great deal of attention, especially for the strengthening of reinforced concrete and masonry structures, as they allow to improve the structural capacity without altering significantly the original geometry, mass and stiffness.

Although the application of FRCM increased significantly after recent earthquakes (e.g. L'Aquila 2009, Emilia 2012, Amatrice 2016) normative documents have not yet been developed, and only two sets of recommendations are currently available: the american bylaws «ACI 549,4R-13»; and the Italian «Linee guida per la qualificazione e il controllo di accettazione di compositi fibrorinforzati a matrice inorganica da utilizzarsi per il consolidamento strutturale di costruzioni esistenti» (draft in progress, to be published).

As summarized in [Borri et al., 2011a - Razavizadeh et al., 2014], FRCM are an excellent solution for the strengthening of heritage structures and their most important advantages are: (a) resistance to high temperatures and ultraviolet radiations; (b) good long term performance; (c) compatibility with the substrates due to vapor permeability, durability to external agents and reversibility of the intervention; and (d) increased sustainability thanks to the use of lime, which requires less energy and emits less carbon-dioxide. Given the physical and mechanical characteristics of the mortar matrix, some of the fibres used in FRCM (e.g. glass and basalt) require a protecting coating to ensure a good long term performance and suitable bond between the fibers and the mortar, which can be one of the critical design parameters.

Along with the more conventional types of fibres typically used in the manufacturing of FRP, the use of steel mesh reinforcement has recently been introduced. The use of steel cords, typically high strength twisted steel wires, allows the development of ductile systems [Casadei et al., 2005 - Grande et al., 2013 - Razavizadeh et al., 2014], a reduction in the cost of materials as well as their installation [Borri et al., 2010] and, at the same time, easier solutions for connection and anchorage systems [Borri et al., 2011b]. The first examples of steel textile reinforced composites used a polymeric matrix and were referred to as Steel Reinforced Polymers (SRP) [Huang et al., 2005]. SRP have been examined by several researchers and their possible application in both existing buildings and new constructions has been investigated [De Santis et al., 2016 - Napoli et al., 2016]. Continuous steel fibers (typically Ultra High Tensile Strength Steel, UHTSS) embedded in inorganic matrices are referred to as Steel Reinforced Grout (SRG) [Ghiassi et al., 2014 - Borri et al., 2015]. The first studies on SRG were published in 2004 by [Wobbe et al., 2004] and 2005 by [Matana et al., 2005]. Wobbe et al. argued that, in general, the success of composite materials for building retrofitting application depends on cost and performance and SRG can be very competitive. An additional

advantage of SRG is the inherent fire resistance of the inorganic mortar matrix. Typical steel fabrics are brass or zinc coated and offer excellent durability in different conditions of environmental exposure, also as a result of the protection offered by the matrix (mortar or resin).

The bond behaviour of both SRP and SRG can differ significantly from that of FRP and this was studied by several researchers [Ascione et al., 2015 - Valluzzi et al., 2012 - Papanicolaou G.C. et al., 2007 - Papanicolaou G.C. et al., 2008 - Grande et al., 2015 – Bencardino et al., 2015b - De Santis et al., 2017]. In fact, while damage in FRP systems occurs primarily in the substrate (concrete or masonry), debonding of SRP from concrete mainly occurs at the interface between the steel fibres and the epoxy resin and debonding of SRP from masonry primarily occurs within the brickwork substrate, which is generally weaker than the organic matrix. When SRGs are used, debonding depends, first at all, on mortar typology (lime or cementitious based, the latter with properties similar to epoxy resins) and additional mechanisms such as interlocking between steel wires and matrix, density of the fabric, and slippage of the adhesive layer from the support. In order to fill gaps in literature this document contributes to analyse all researches about SRG.

First of all, tensile tests on textile and composite material coupons are carried out to detect mechanical properties like stress, strain and Young's moduli. Then, shear bond behaviour is investigated by means of SRG reinforcement on concrete and masonry substrates to study stress transfer and failure modes.

At the same time, experimental programs of SRG applications on full-scale structural elements, both concrete and masonry substrates, are reported showing load bearing capacity increasing thanks to this reinforcement.

Regarding SRG reinforcement of concrete structures, research has focused on beams due to bending behaviour and on cylinder confinement. Some authors have studied beam-column joints behaviour reinforced by SRG, others have realized SRG reinforcements on slabs.

On the other hand, about masonry substrates, experimental tests are carried out, like in plane and out of plane ones, to avoid structural damages. For this reason, full-scale samples such as walls, shaped of C walls and curved structural elements, like arches and timber vaults, are reinforced by SRG strengthening systems. This typology of reinforcement is also applied for columns confinement by different procedures [Borri et al., 2013], above all against seismic hazards.

Finally, this document has demonstrated so far that SRG represents an effective strengthening system for existing building, first at all for cultural heritage thanks to taking advantages of high compatibility of mortar matrix using on historical substrate and thanks to steel wire contribution in terms of ductility and durability. Absolutely, open issues will be deepened in the future research works, above all about durability: this is the reason why, it necessary to study long-term performances.

2.2 Mechanical properties of steel textile, mortar and Steel Reinforced Grout composite (Materials)

The mechanical characterization of SRG components is discussed in the following in terms of geometrical properties and tensile properties.

2.2.1 Tensile behaviour of steel textiles for SRG applications

A recent research work by De Santis et al. [De Santis et al., 2016] discussed the characteristics of five typologies of steel meshes, which were previously used in SRP applications.

2.2.2 Tensile behaviour of steel textiles and SRG composites RRT

In order to qualify the tensile properties of FRCM and SRG strengthening systems, tensile tests on coupons are required. A large Round Robin Test (RRT) exercise was organized by RILEM TC-250-CSM Committee and carried out at several research laboratories across Europe [de Felice et al., 2016].

The SRG systems examined in the RRT included:

1. galvanized steel cords and lime mortar
2. galvanized steel cords and geopolymer mortar
3. stainless steel cords and lime and pozzolan mortar
4. stainless steel ropes and cement mortar

The results on the SRG systems were summarised in [De Santis et al., 2017] in terms of Young's modulus and complete stress-strain response, which is characterised by the development of three stages [Roscini et al., 2016]: (i) un-cracked stage (in which the mortar matrix contributes to both load bearing capacity and stiffness), (ii) crack development stage (during which crack pattern develops progressively), and (iii) cracked stage (in which crack pattern is completely developed). For each test, crack spacing after crack stabilisation and failure modes were also reported.

2.3 SRG-to-substrate bond behaviour

Several experimental studies are currently ongoing, or have been recently completed, to study the bond behaviour of SRG strengthening systems applied to different typologies of substrates.

2.3.1 Bond behaviour of composites material overview

The bond behaviour of FRPs-to-concrete was examined in detail by Mazzotti et al. in [Bond between EBR FRP and concrete, 2012]. RILEM Technical Committee 223-MSC coordinated a RRT to study the bond of composites to masonry, specifically clay brick, and the relevant results were summarised in [Valluzzi et al. \[2012\]](#). Several other authors have since investigated the bond behaviour of FRP to masonry, for example [Ceroni et al. \[2014\]](#), who reported the results of more than 250 bond tests available in the literature. Thanks to these investigations, equations to predict the debonding strength were proposed, including those recommended in the Italian guidelines CNR-DT 200 R1/2013. Such models have been developed from tests on a variety of different FRP types, namely comprising carbon, glass and aramid textiles, and are suitable for different substrates (concrete and masonry) through the use of adjusting parameters. Nevertheless, it should be noted that existing models cannot account for the use of steel textiles as main reinforcement (SRP). The results of all experimental tests on SRP are summarised in [\[De Santis et al., 2016\]](#), who investigated the shear bond behaviour of SRP strengthening systems to both concrete and masonry. The results of such tests enabled the development of predictive bond models for SRP that were in line with the recommendations of CNR-DT 200 R1/2013.

Recent work on bond has focused on the behaviour of mortar based strengthening systems and studies on both FRCM and SRG bonded to concrete, masonry and tuff substrate, via single-lap tests are already available in the literature. However, bond design models for FRCM and SRG are still not available and more work is needed in this field.

2.3.2 SRG-to-concrete bond behaviour

The first study bond of SRG-to-concrete was carried out in 2005 [\[Matana, Galecki, Maerz, Nanni, 2005\]](#) and the stress transfer behaviour was examined through a series of pull-off and shear bond tests.

Matana et al. in 2005 [\[Matana, Nanni, Dharani, Silva and Tunis, 2005\]](#) studied the bond behaviour of SRG (Table 2.1) to concrete substrate and examined the effect of surface roughness and bonded length of the

reinforcement. One of the main conclusions was that ultimate load was found to increase with the increase of bond length (Table 2.2) and there was no evidence of the existence of a notional effective length, which generally limits the bond performance of FRP.

Table 2.1. Material properties of SRP and SRG

Material property / Lamina type	SRG
Cord type	3SX
Cord area (in ²)	1.26×10 ⁻³
Sheet density (cords/in)	12
Average sheet thickness for 1 ply (in)	0.152
Tensile strength, f_{tu} (ksi)	247
Modulus of elasticity, E_r (ksi)	21000
Strain at failure, ϵ_{fu} (%)	1.68

Note: 1 in = 25.4 mm, 1 ksi = 6.89 MPa

Table 2.2. SRG test results (1 – 12 cords/in density)

Specimen (1)	Ultimate load (lb) (2)	Ultimate strength (ksi) (3)	Ultimate strain - calculated (in/in) (4)
G - 4 - 1	4.2	69	0.0033
G - 4 - 2	3.2	52	0.0025
G - 4 - 3	3.5	58	0.0028
G - 4 - 4	3.7	61	0.0029
G - 8 - 1	7.5	124	0.0059
G - 8 - 2	7.1	118	0.0056
G - 8 - 3	4.7	78	0.0037
G - 8 - 4	4.4	74	0.0035
G - 12 - 1	6.4	106	0.0051
G - 12 - 2	5.7	94	0.0045
G - 12 - 3	4.9	81	0.0039

Note: N/A = Not available; 1 in = 25.4 mm, 1 kip = 4.45 kN, 1 ksi = 6.89 MPa

Subsequent research studies on the use of SRG on concrete elements have focused on aspects such as cost and durability performance. [Cancelli et al., 2007] studied the bond behaviour of SRP/SRG reinforcements to concrete and examined the effect of the matrix and density of the reinforcement through a series of direct shear tests. Different types of failure modes were observed as a function on the type of matrix, polymer or grout, and on the density of the reinforcement, low and high. SRG with a low density mesh

reinforcement (SRGL) failed due to micro-debonding in the layer of grout, while a high density mesh (SRGH) caused failure at the interface between clay brick and mortar with a macro-debonding (Figure 2.1). This difference in failure behaviour demonstrates that low density allows a good stress transfer between mortar layers (Table 2.3); nevertheless the bond strength of SRGL was found to be lower than that of SRGH (failure bond values are collected in the Table 2.3). In SRP, like in FRP, failure occurs always at the interface between matrix and surface as a result of the high strength of polymers. [Stievanin et al., 2013] carried out pull-off tests and shear bond tests on two typologies of steel bonded with both polymer and grout matrices to concrete prisms taken from a decommissioned bridge.

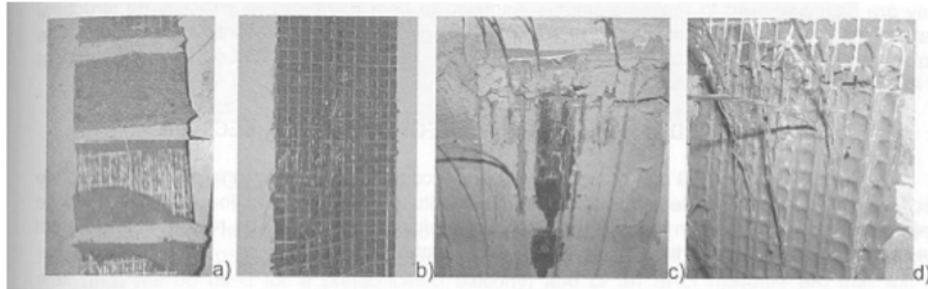


Figure 2.1. Type of failure [Cancelli et al., 2007]

Table 2.3. Test results.

Specimens	Fu (kN)	Average	Failure type	
SRGL_1	8.93	10.61	Micro-debonding*	1b
SRGL_2	12.3		Micro-debonding*	1b
SRGH_1	15.5	16.84	Macro-debonding(g)	1a
SRGH_2	18.19		Macro-debonding(g)	1a

*=debonding in the layer of grout

From shear bond tests on SRG-to-concrete it was found that the steel mesh density plays a critical role on bond behaviour: in “FID” (1.57 cords/cm) failure loads values are greater than in “DB” (3.15 cords/cm) (Table 2.4). This phenomenon can be attributed to the fact that the low density of cords enables a better stress transfer among mortar layers, allowing interlocking action between cords surface and mortar. As a result, failure mode in “FID” occurs within the mortar because its shear strength is lower than the cord-mortar bond shear strength. The textile reinforcement with a high cord density forms a brittle plane, along which failure occurs before the cords can develop their maximum strength. On the other hand, in “DB” slipping

of the fibres within the mortar matrix occurs before the maximum failure bond strength can be achieved. Table 2.5 reports all data from the tests, as well as the respective failure mode.

Table 2.4. Shear test matrix

ID	Steel	fibres	Matrix
TCA_FID_01	FID	(Fidsteel)	cem.mortar
TCA_FID_02			
TCA_DB_01	DB	(Dalla Betta)	cem. mortar
TCA_DB_02			

Table 2.5. Shear tests: result summary

ID	Pmax (kN)	δ_{max} (mm)	Failure mode
TCA_FID_01	12.7	1.3	Interface failure
TCA_FID_02	11.96	2.35	
average	12.33	1.83	
TCA_DB_01	4.16	0.97	Fiber slip
TCA_DB_02	4.48	0.7	
average	4.32	0.84	

[Sneed et al., 2016] performed direct shear bond tests on steel-FRCM bonded to concrete along with flexural tests on beams reinforced with the same strengthening system. From direct shear bond tests (set-up design presented in Figure 2.2 and the corresponding pictures in Figure 2.3), the main failure modes observed were fiber slippage and debonding cracking at the interface between internal matrix layer and fiber (Figure 2.4b). Response curves of single-lap direct-shear specimens are collected in the graph in Table 2.5. Geometrical properties, maximum load and ultimate stress, are shown in Table 2.6.

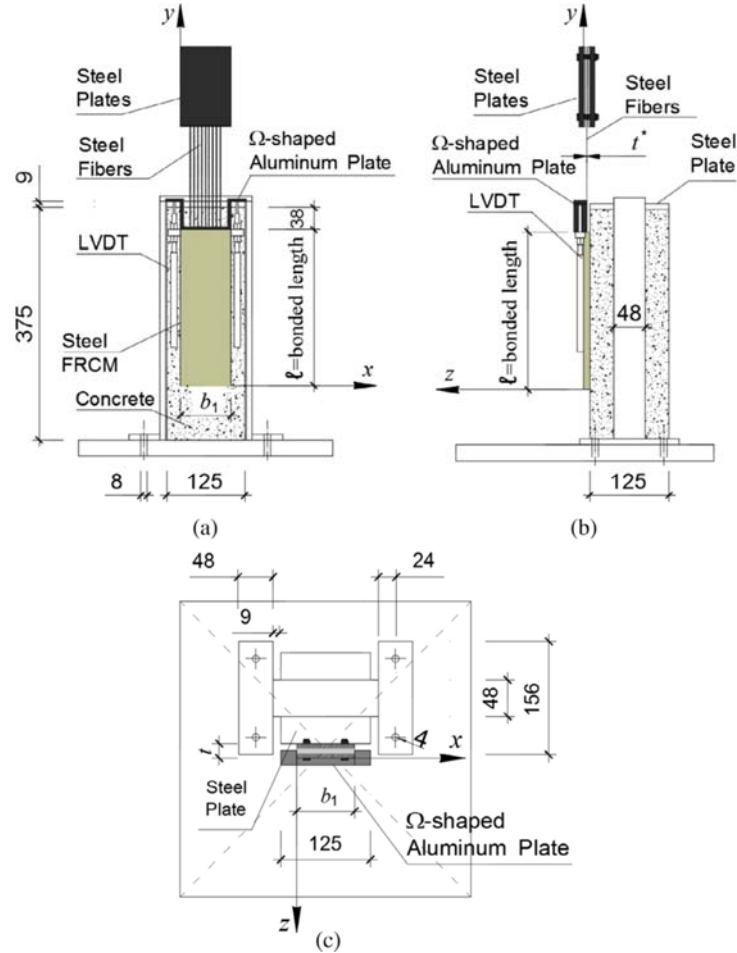


Figure 2.2. Single-lap direct-shear test set-up (a) front view, (b) side view, and (c) top view (dimensions in mm) [Sneed et al., 2016]

Table 2.6. Steel-FRCM single-lap direct-shear test specimens

Note: Specimen DS_K_330_50_2 is not included because of problems during testing

Specimen	Composite width (mm)	Composite length l (mm)	Number of fiber cords n	Maximum load P* (kN)	Ultimate stress σ^* (N/mm ²)
DS_K_330_50_1	50	330	24	9.48	734
DS_K_330_50_3	50	330	24	8.57	664
DS_K_330_50_4	50	330	24	8.8	682
DS_K_330_50_L_1	50	330	24	8.07	625
DS_K_330_50_L_2	50	330	24	9.64	747
DS_K_330_50_L_3	50	330	24	9.92	768
DS_K_330_50_L_4	50	330	24	9.45	732

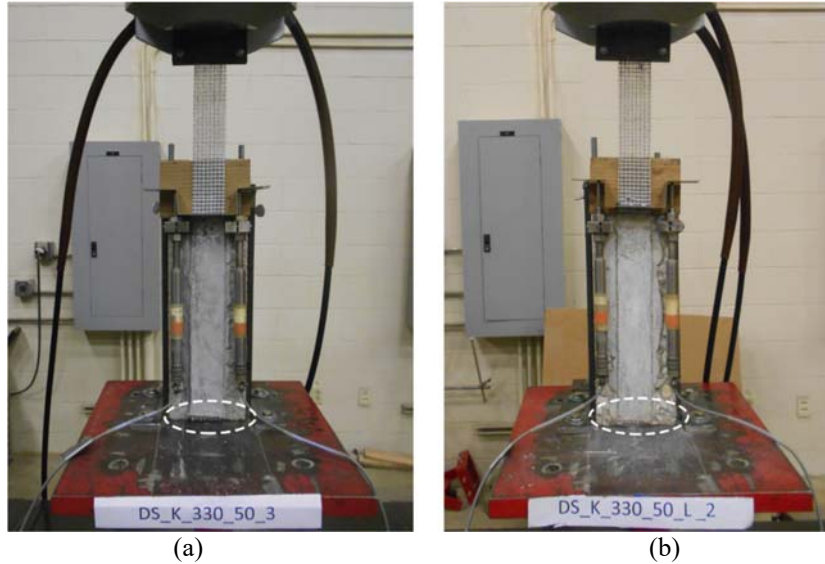


Figure 2.3. Pictures of single-lap direct-shear test (a) specimen with external matrix layer (specimen DS_K_330_50_3 shown) and (b) specimen with the external matrix layer omitted (specimen DS_K_330_50_L_2 shown). Note the fibers extending beyond the bonded area at the free end (circled in the photographs) [Sneed et al., 2016]

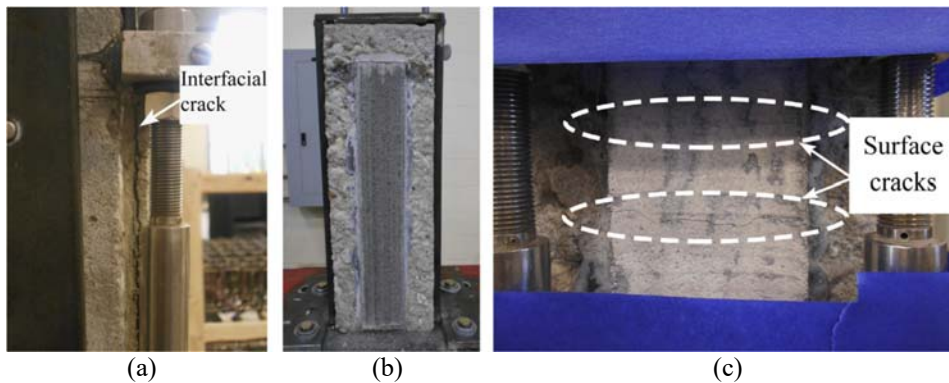


Figure 2.4. Pictures of single-lap shear test specimens: (a) crack along interface of cords and matrix, (b) surface of internal matrix layer after failure (specimen DS_K_330_50_1 shown), and (c) cracking observed on surface of external matrix layer [Sneed et al., 2016]

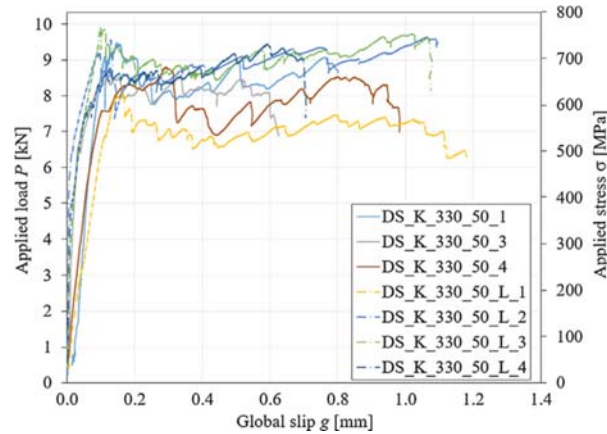


Figure 2.5. Applied load P – global slip g response and applied stress σ – global slip g response of single-lap direct-shear specimens [Sneed et al., 2016]

2.3.3 SRG-to-masonry bond behaviour

The bond behaviour of SRG to masonry (either clay brick or brickwork), was examined by [Carbone and de Felice, 2008] using double lap tests. From the experimental results, it was observed that, for the same anchorage length, SRG reinforcement provides higher debonding strength than carbon FRP sheets.

Table 2.7 shows the results of tests on SRG systems with different anchorage lengths, in terms of debonding load, slip at failure and failure mode.

Table 2.7. SRG bond results with different anchorage length

Specimen	Collapse force (N)	Type of collapse	Slip at collapse (mm)
A-SRG1	3995	a	–
A-SRG2	3883	a	–
A-SRG3	3455	a	–
B-SRG1	6368	b	–
B-SRG2	6190	b	0.36
B-SRG3	6358	b	0.27
B-SRG4	7516	b	–
B-SRG5	6754	b	–
B-SRG6	6462	b	0.23
C-SRG1	6166	b	0.72
C-SRG2	5977	b	–
C-SRG3	5589	b	0.82
C-SRG4	5438	b	0.42
C-SRG5	5309	b	0.69
C-SRG6	5599	b	0.57

[Razavizadeh et al. 2014] examined the effect of curing time on bond strength, after a minimum surface treatment of one month (1.48kN) and five months (2.11kN) with a clear increase of 43%. Sandblasting the surface of the substrate resulted in an average debonding force of 2.96kN after one months of curing, 4.09kN after three and 4.46kN after five months of curing; in this case the increase was 51% from month 1 to month 5. These data demonstrate that substrate surface preparation is of greater importance than curing time and sandblasting seems to be an effective surface preparation technique.

2.3.4 SRG-to-tuff bond behaviour

[Bilotta et al., 2017] carried out an experimental study on bond behaviour of two types of SRG strengthening systems made with unidirectional steel cords of different densities. The SRG were bonded to Neapolitan yellow tuff and tested through single push-pull tests (Figure 2.6).

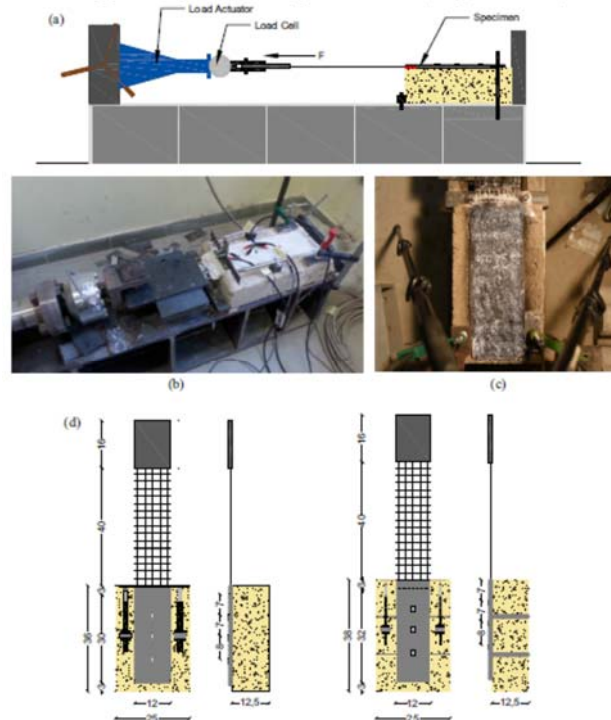


Figure 2.6. a) Experimental set-up for push-pull bond test; b) example of specimen positioned in the testing apparatus; c) painted surface of the matrix for DIC; d) position of strain gauges and LVDTs for specimens made of single tuff stone e prisms [Bilotta et al., 2017]

The results are summarised in Table 2.8 and an average value of 6.8kN was found for the S100 steel textile with a cord diameter of 1.38mm and a textile area of 16.44mm². The S200 textile reinforcement (area of 14.49mm²), which failed at a maximum average load of 16.5kN, also exhibited failure (Figure 2.7) through debonding at the tuff-matrix interface at a lower average load of 6.5kN.

Table 2.8. Results of bond tests on FRCM and SRG

Specimen	Support	FRCM/SRG	Failure	F _{max}	F _{max,av}	η _{dry}	η _{comp}	ε _{max,1}	ε _{max,2}
				[kN]	[kN]	[-]	[-]	[%]	[%]
TB_BN_S100_MX2_1	Single block tuff BN	Steel grid S100	D	3	3 (-)	0.12	-	0.027	0.09
TB_BN_S100_MX2_2	Single block tuff BN	Steel grid S100	S	7.2	6.8 (9%)	0.28	-	0.064	0.22
TB_BN_S100_MX2_3	Single block tuff BN	Steel grid S100	S	6.3	6.8 (9%)	0.24	-	0.056	0.19
TB_BN_S200_MX2_1	Single block tuff BN	Steel grid S200	T	16.2	16.5(3%)	0.71	1.1	0.202	0.56
TB_BN_S200_MX2_2	Single block tuff BN	Steel grid S200	T	16.8		0.74	1.14	0.21	0.58
TB_BN_S200_MX2_3	Single block tuff BN	Steel grid S200	D	6.9	6.5(9%)	0.3	0.47	0.086	0.24
TB_BN_S200_MX2_4	Single block tuff BN	Steel grid S200	D	6.1		0.27	0.41	0.076	0.21

S = Slippage of grid from matrix, T = Tensile failure of fibers, D = Debonding at tuff-matrix interface



Figure 2.7. Failure modes: a) tensile failure of the glass fibers; b) debonding at the tuff-matrix interface; c) slippage of the fibers from the matrix [Bilotta et al., 2017]

Different failure modes were observed as a result of different resisting mechanisms:

- 1) Slippage in S100 (Figure 2.7c): slip occurs between matrix and steel cords with a relatively large diameter. Although the larger spacing of the cords allows a better interlocking within the mortar and does not lead to a strong interaction between the stress field transferred between the cords and the surrounding mortar, the relatively larger diameter results in the development of bond shear stresses greater than the bond shear strength at grout-cord interface.
- 2) Tensile failure of fibers in S200 (Figure 2.7a): the relatively smaller diameter of the cords, 0.93mm, enabled the development of stresses within the steel cords equivalent to their rupture strength before critical shear bond stresses could be developed.
- 3) Debonding at tuff-matrix interface in S200 (Figure 2.7b): this typology of failure occurs when the high textile density prevents adequate interlocking between the mortar layers and the mortar strength is higher than the bond strength of the mortar-tuff interface.

According to the authors, the observed failure modes were also a function of: curing phase of the mortar due to the non-regular surface of tuff and handling problem during the manufacturing phase, in particular the difficulty in the alignment of the cords.

2.4 Analytical prediction of the bond strength

[Ceroni et al., 2014] analysed a large database of results and developed analytical and numerical models, using both 2D and 3D FEA. [Carloni et al., 2014] investigated further the interface behaviour and the differences observed in bonded FRP, which generally debonds at the interface between the concrete and the FRP, and FRCM, which generally fail within the mortar [Ascione et al., 2015]. [Carozzi et al., 2016] examined FRCM debonding by means of an analytical approach, considering a zero thickness layer for the bond interface and locating the failure surface within the mortar matrix-to-fiber interface. The τ -slip constitutive law at the interface for FRCM was calibrated through experimental tests. [Focacci et al., 2017] have introduced an indirect method to calibrate the cohesive material law of FRCM-concrete joints, without any requirement of strain measurements.

[D'Antino et al., 2014] proposed an experimentally calibrated bond constitutive law for PBO-FRCM, while [Ombres, in 2015] proposed an interface law for the concrete substrate.

Numerical investigations on the bond of FRCM systems were carried out by several researchers. [Grande et al., 2013] suggested bond stress slip laws for the interface between reinforcement-to-substrate from experimental tests carried out on SRP and on SRG. [Razavizadeh et al. 2014] validated a numerical model for SRG reinforcement bonded to masonry and identified the parameters for their proposed bond-slip law. [Malena and de Felice, 2014] examined the behaviour of SRG bonded to curved masonry substrates and developed a detailed analytical approach.

2.5 A qualification method for externally bonded FRCM

[Ascione et al., 2015] proposed a procedure for the qualification of mortar matrix based strengthening system, including both FRCM and SRG, on the basis of both tensile tests on the composite itself and shear bond tests on the relevant substrate.

2.6 Strengthening of reinforced concrete structures

2.6.1 Strengthening of beams in bending

[Barton et al., 2005] carried out an experimental study on RC beams retrofitted with SRP/SRG (Figure 2.8). The test results were compared with analytical models correlating well midspan deflection data for RC beam reinforced with SRG (Figure 2.9).

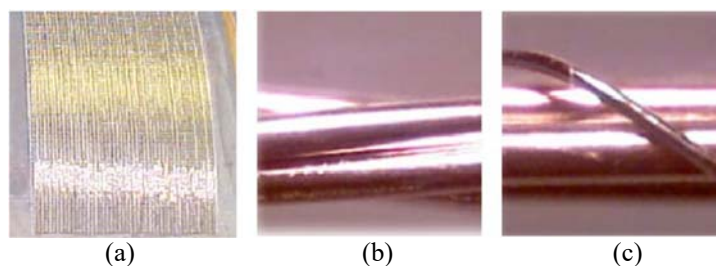


Figure 2.8. Steel reinforcement: (a) steel tape, (b) 3X2 cord and (c) 3SX cord [Barton et al., 2005]

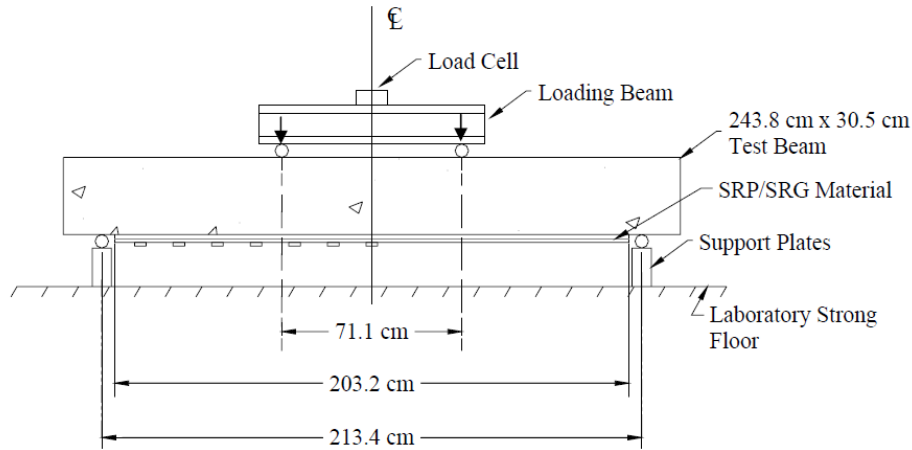


Figure 2.9. Schematic representation of RC beam test setup [Barton et al., 2005]

[Wobbe et al., 2004] carried out tests on RC beams reinforced in bending with SRP and SRG. Three specimens were tested under four-point bending and the investigated parameters included the number of reinforcement plies and the type of bonding agents. The results of this work demonstrated that the use of these strengthening systems can lead to an increase in flexural capacity up to 100%.

Four-point bending tests on beams reinforced in flexure with SRP and SRG were also reported by [Huang et al., 2005]. In addition to an increase of 20% in ultimate flexural strength (Figures 2.10-2.11), the use of mortar in SRG ensured a good freeze-thaw durability, high resistance to de-icing salts, compatibility with thermal expansion coefficients of concrete, non-flammability, and non-toxicity.

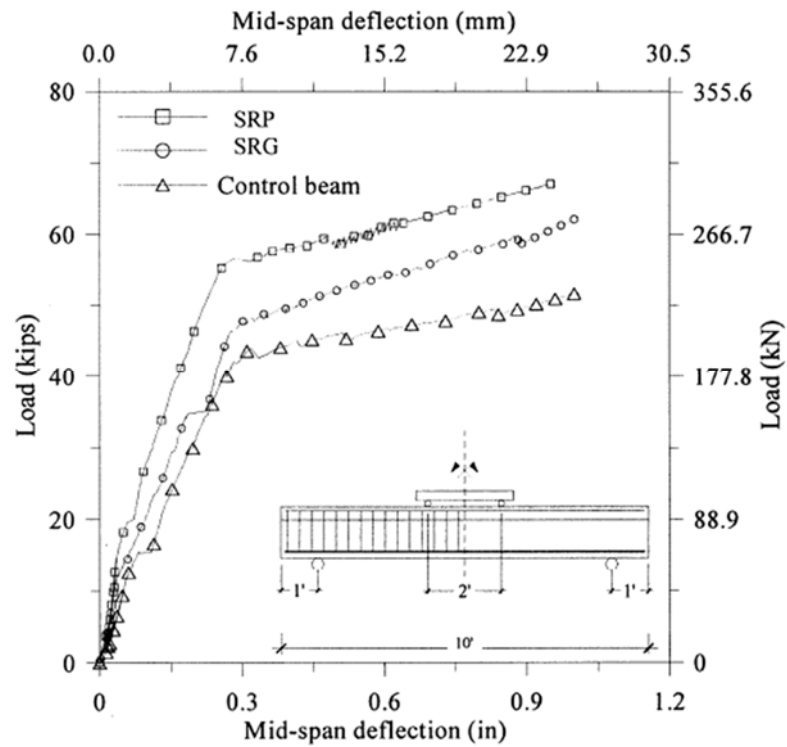


Figure 2.10. Load-midspan deflection of reinforced concrete beams with and without SRG strengthening elements [Huang et al., 2005]

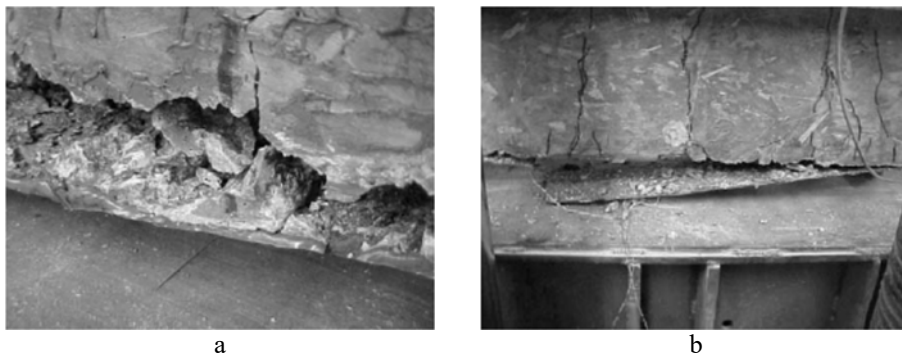


Figure 2.11. Failure of SRG strengthened reinforced concrete beams. SRP (a), SRG (b) [Huang et al., 2005]

The flexural performance of RC beams reinforced with SRG were also investigated by [Bencardino et al., 2010] through flexural and flexural/shear tests. The use of a different number of layers of SRG led to

an increase of about 40% in flexural capacity, and a reduction of about 30% in terms of maximum deflection.

[Da Porto et al., 2012] carried out a series of experimental tests on RC beams reinforced with SRG after the beams were repaired with polymer-modified mortars to simulate a real on-site application. The tested strengthening system were manufactured with two types of mortar: a thixotropic mortar matrix “FR”, which enabled a good impregnation of the fabric, and a “KF” type of mortar matrix, which resulted in a poor impregnation of the steel cords. Despite the lower level of impregnation obtained with the KF type mortar, high bond strength values were observed, suggesting that SRG represents a good alternative to epoxy resin strengthening systems, in particular in situations requiring enhanced fire resistance, in presence of high humidity or high temperature, in absence of skilled labour.

[Bencardino and Condello, 2015b] published a large database of experimental results for RC beams strengthened in bending with bonded SRG and SRP systems and suggested a theoretical model to estimate the enhancement in flexural capacity provided by the strengthening systems. The analytical models used for FRP reinforcement, was applied to SRG and SRP strengthening systems and proved to yield reliable results (see Table 2.9).

Table 2.9. Efficiency coefficients for SRG system

Beam	Teng et al. $\alpha = \epsilon_{f,theo} / \epsilon_{f,exp}$		$\beta = F_{u,theo} / F_{u,exp}$	
	Mean	Design	Mean	Design
G1	1.18	0.95	1.08	1.01
G1-U	0.80	0.64	1.08	1.01
SRG-1	e	e	0.98	0.94
SRG-2	0.54	0.43	0.93	0.88
B-2	0.86	0.69	0.93	0.88
B-3	0.86	0.69	0.94	0.89
B-4	0.73	0.59	0.84	0.78
G1	1.18	0.95	1.08	1.01

¹ [Bencardino and Condello, 2014]; ² [Barton et al., 2005]; ³ [Pecce et al., 2006]

[Bencardino and Condello, 2015a] proposed a Finite Element model to simulate experimental tests on beam externally reinforced with SRG systems and successfully captured the structural behaviour of the strengthened beams, including the development of cracking and failure mode.

[Napoli and Realfonzo, 2015] carried out experimental work on RC slabs reinforced in flexure with SRG systems and subjected to four-point bending. The effect of number of layers and density of the steel tape on maximum capacity, deformability and failure modes was investigated. This work confirms the good performance of the SRG systems, especially those using a low density textile mesh, both in single or double layer; slab strengthened with two SRG layers showed an increase of strength fully comparable to specimens strengthened with one layer of medium density textile mesh. The authors also developed an analytical model to predict the flexural enhancement and assess the performance of models currently used for FRP sheets and included in CNR-DT200 R1 and ACI 440.2R.

2.6.2 Confinement of RC prismatic specimens and RC cylinders

[Thermou et al., 2013] examined the performance of SRG in confining concrete prismatic specimens (Figure 2.12a). Three different types of SRG jackets with varying density and different rates of the applied axial compressive load were examined. In general, the test results showed a strength decrease with the application of a dynamic load but the results were non-conclusive.

[Thermou et al., 2015] conducted an investigation to evaluate the performance of SRG confined cylinders (Figure 2.12b) under monotonic concentric uniaxial compression load. The parameters investigated were concrete strength and type of steel mesh. Two group of cylinders were tested: group “A” with a relatively low compressive strength concrete; and group “B” with a moderate compressive strength concrete. Four specimens were tested in each group: unconfined control specimens, specimens wrapped with a high density steel fabric, specimens wrapped with a medium density steel fabric and specimens wrapped with a low density fabric (Figure 2.13). Two commercially available types of steel fabric were used for these tests and two overlap lengths were examined.

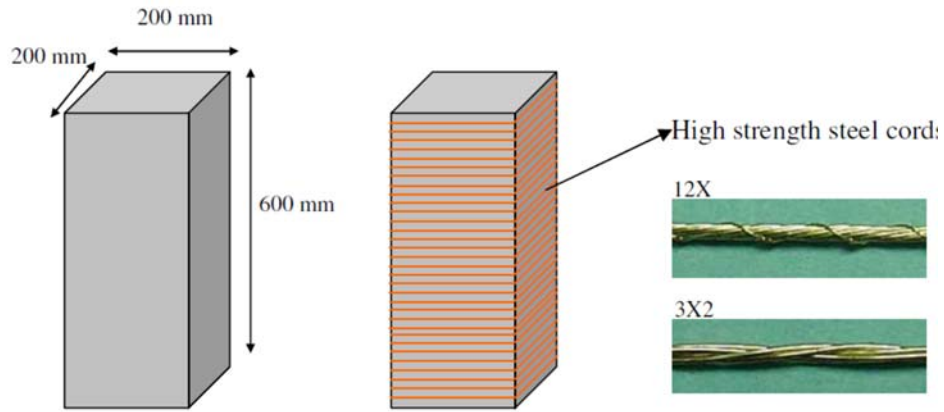


Figure 2.12a. Strengthening of prismatic specimens by steel cords [Thermou et al., 2013]

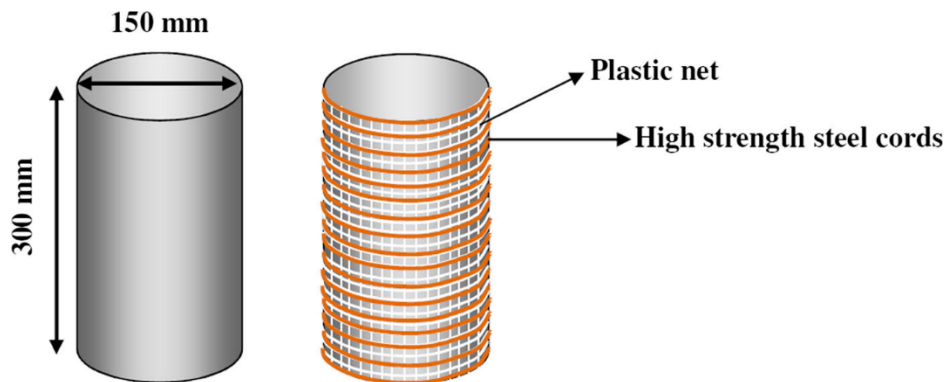


Figure 2.12b. Strengthening of cylinder by steel cords [Thermou et al., 2015]

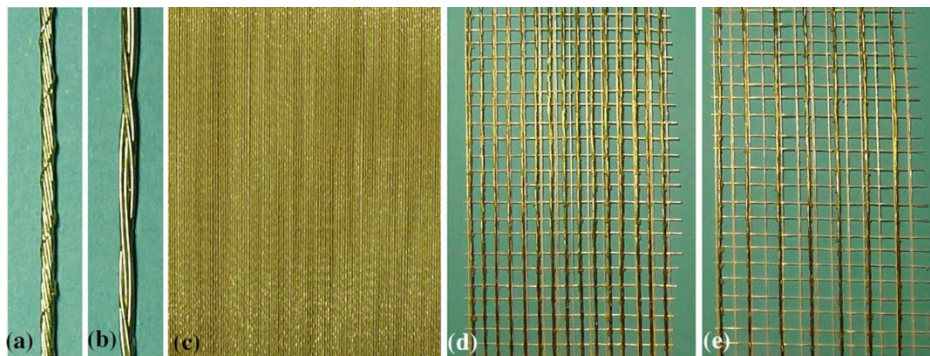


Figure 2.13. Cords (a-b) and textile steel mesh, high density (c), medium density (d) and low density (e) [Thermou et al., 2015]

The experimental tests results provided evidence that the confinement increased both compressive strength and deformation capacity. The low density SRG jackets resulted in relatively higher performance thanks to a good interlock between the fabric and the mortar, which was affected by grid spacing and axial stiffness/strength of the fabric.

The influence of the cross section shape on the behaviour of SRG for confinement of prismatic concrete under concentric uniaxial compression load was investigated experimentally by [Thermou et al., 2016]. Circular specimens were tested alongside square specimens and square specimens with rounded edges (Figures 2.14-2.15). As expected, it was observed that strength and deformation capacity increased when changing the shape of the cross section from square to circular. An analytical framework was also proposed to predict lateral confining pressure and normalized compressive strength of non-circular specimens and the performance of FRP confinement models available in the literature was also assessed.

[Thermou and Hajirasouliha, 2018] lately presented experimental tests regarding on compressive strength of concrete columns confined with SRG and as a result the efficiency of this strengthening system.

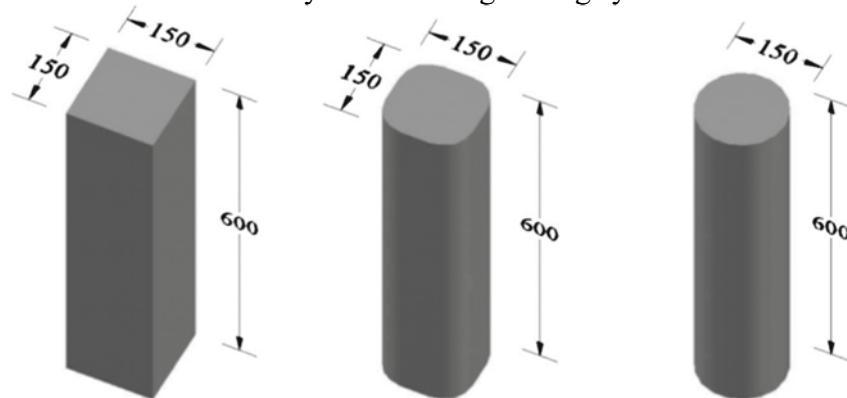


Figure 2.14. Specimen geometry and cross section shapes (dimensions in mm)
[Thermou et al., 2016]



Figure 2.15. Preparation of the steel-reinforced fabrics and fabrication of the SRG jackets to circular and square cross section specimens [Thermou et al., 2016]

2.6.3 SRG jacketing of columns

[Thermou et al., 2007] carried out an experimental study on the seismic performance of substandard reinforced concrete members strengthened with metallic (high-strength steel cord) fabric jackets. The tests showed that high strength steel cords metallic fabrics combined with conventional cementitious grouts can effectively increase the strength and the deformation capacity of sub-standard elements and can be a valid alternative to glass and carbon FRP confinement (Figures 2.16-2.17). Recently, [Thermou et al., 2018] published a paper on SRG jacketing of RC columns.

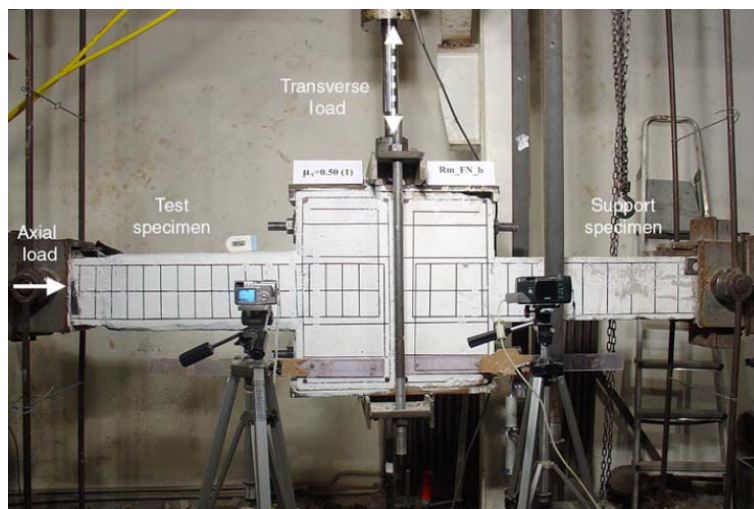


Figure 2.16. Test set up [Thermou et al., 2007]

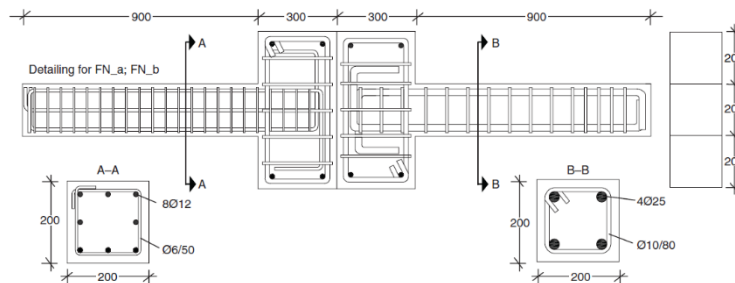


Figure 2.17. Test assembly: geometry and reinforcement details (dimensions in mm)
[Thermou et al., 2007]

2.6.4 Slab reinforced with SRG

[Alkhroaji and Thomas, 2005] carried out a comparative study on the use of SRP and SRG systems to increase the flexural capacity of concrete beams. SRP and SRG improve the capacity by 34% and 24%, respectively, when compared to the control beam. The authors also discussed an application using a combination of Dry carbon-fabric sheets and Hardwire® systems to upgrade the Hippodrome theatre in Baltimore, in which the composites were externally bonded to the bottom of the elevated upper balcony slab.

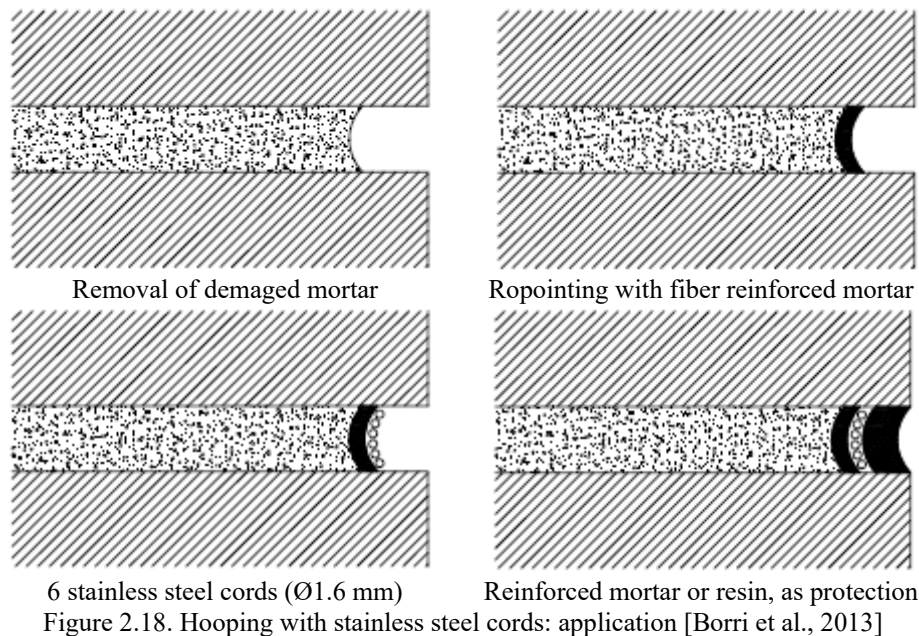
2.7 Strengthening of reinforced masonry structures

2.7.1 SRG strengthening system applied on arches and vaults of beams

A detailed discussion on this topic is presented in Chapter 6 along with the description of full-scale tests on timber masonry vaults strengthened with Steel Reinforced Grout.

2.7.2 SRG reinforcement for confinement

[Borri et al., 2013] carried out experimental tests on masonry columns confined with steel cord wrapping (Figure 2.18).



This confining method was applied on columns with different cross-section geometries (octagonal, square, and rectangular) and using different confining systems. The experimental tests examined the behaviour of columns with equivalent reinforcement ratio, and show that columns strengthened with pre-tensioned steel cords achieved an ultimate strength approximately 20% larger than that of the specimens strengthened with steel cords, with displacements approximately 40% smaller.

[Fossetti et al., 2016] examined the compressive behaviour of masonry columns made with clay brick and reinforced with steel wire collaring. Columns retrofitted with basalt fibers (BF) and high strength steel wires in

mortar joints (SW) were tested until failure along with control specimens. Two typologies of masonry were considered by varying the mortar composition. An average increase in the maximum strength value of 44% was found for specimens reinforced with BF, while a 25% increase was found for SW specimens. If ultimate strain capacity and energy absorption are considered, an increasing equal to 35% and 106% was found for BF specimens and 101% and 203% for SW specimens. Figure 2.19 summarises the failure modes observed for each confinement solution.

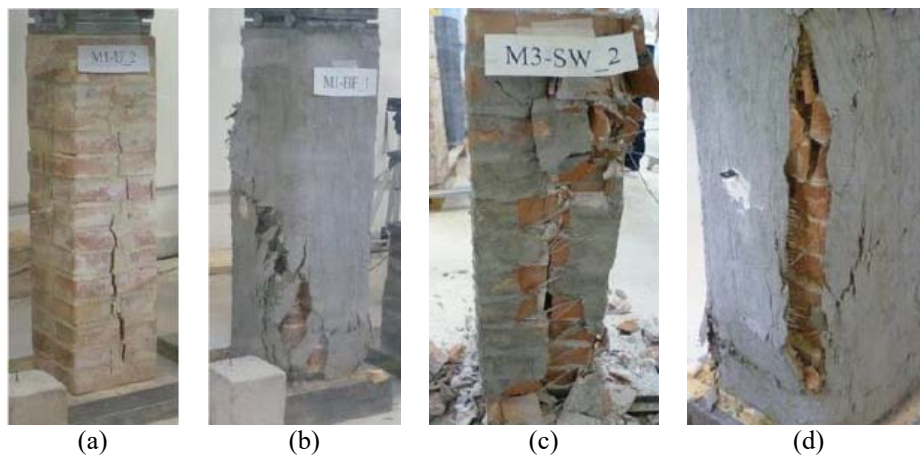


Figure 2.19. Failure mode for clay brick masonry columns: (a) unconfined; (b) confined with BFRCM wraps; (c) reinforced by steel wire collaring. (d) Tensile fracture of the basalt fiber mesh. [Fossetti et al., 2016]

2.7.3 Out-of-plane reinforcement for walls

[Valluzzi et al., 2014b] evaluated the effectiveness of SRG reinforcement in enhancing the out-of-plane performance of walls. Different types of matrices for the steel fabric reinforcements were examined, including cementitious mortar and magnesia-based mortar. SRG strengthening systems with magnesia-based mortar showed a good performance in terms of both maximum load and displacement capacity, achieving an increase of up to 75% in strength and more than twice the displacement capacity of cementitious mortars. The typical failure mode characterised by matrix splitting and fibres slippage was observed in all specimens.

[De Santis, Casadei, De Canio et al., 2016], carried out full-scale shake table tests to examine the out-of-plane behaviour of C-shaped tuff walls strengthened with SRG systems with hydraulic lime mortar. The strengthening solutions employed the use of both horizontal reinforcing

strips and connectors. The strengthened systems were able to resist a level of excitation up to 5 times higher, from 0.29g to 1.51g, and exhibited a deformation capacity up to 3 times higher. The observed failure modes were limited to cracking in the substrate, without any collapse of large portions of masonry and even without any damage in the reinforcement.

2.7.4 In-plane reinforcement wall

[Borri et al., 2011], investigated the shear contribution offered by steel cord like reinforcement in brick panels (Figure 2.20). Tests were carried out using different types of mortars and different characteristics of steel reinforcement (density of cords, size of the reinforcing). An increase in the shear strength of panels reinforced with steel cords was observed (Table 2.10), with this being higher in the case of masonry with initial low shear strength.

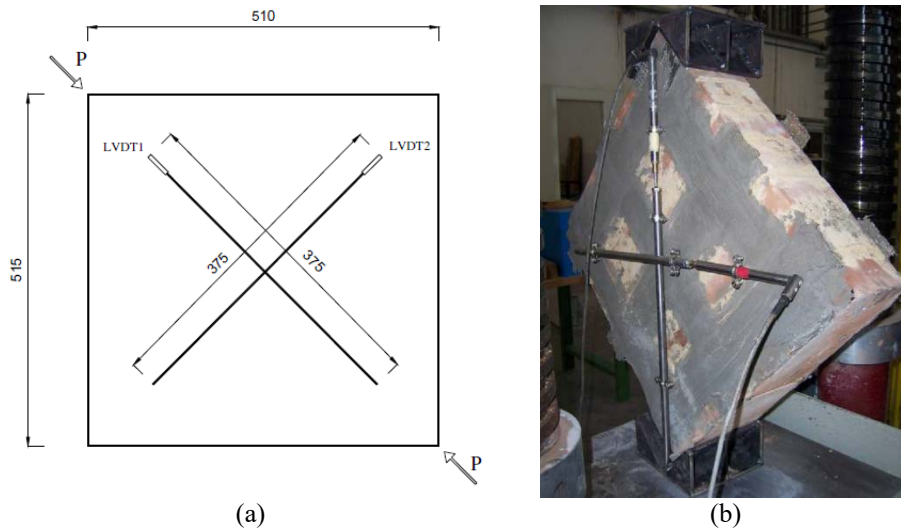


Figure 2.20. Geometrical configuration and boundary conditions for masonry panels tested in diagonal compression [Borri et al., 2011]

Table 2.10. Experimental results about panels manufactured hydraulic lime mortar (PRN) with cement mortar(PRC)

Series	Specimen	Steel cords type	Reinforced sides	Reinforcement width (mm)	τ_{\max} (N/mm ²)	$\tau_{\max, \text{reinf}}/\tau_{\max, \text{unrein}}$
1	PRN 1-2-3-4-5-6	-	-	-	0.094	—
2	PRN 7,8	2	2	50	0.39	4.15
3	PRN 9,10	2	2	25	0.34	3.62
4	PRN 11,12	2	1	50	0.209	2.22
5	PRN 13,14	1	2	25	0.225	2.4
6	PRN 15	2	50	0.278	2.96	397
7	PRN 16	1	1	50	0.25	2.66
8	PRC 1,2	—	—	—	0.54	—
9	PRC 3,4,5	1	2	50	0.865	1.6
10	PRC 6,7	1	2	25	0.738	1.37
11	PRC 8	1	1	50	1.093	2.03
12	PRC 9,10,11	2	2	50	0.804	1.49
13	PRC 12,13	2	2	25	0.917	1.7
14	PRC 14	2	1	50	0.74	1.37

[Capozucca, 2016] investigated the in-plane performance of walls reinforced with SRG. In particular, the authors tested wallettes specimens made with two leaves of brickwork masonry and intermediate grout. The bare specimens were initially tested under compression and shear loading and subsequently strengthened with two types of externally bonded composite reinforcement: diagonal Glass-FRP strips and steel fibre reinforced cement grout. In both cases, higher ductility and better energy dissipation capacity were observed. Failure of the specimens strengthened with SRG occurred due to local instability of steel in the mortar matrix.

2.7.5 Reinforcement of masonry ring-beams

[Borri et al., 2010] conducted tests on masonry ring-beams reinforced with SRG (Figure 2.21) and the results are summarised in Table 2.11. Two beams were tested under horizontal load (Figure 2.22), while a third beam was subjected to vertical load (Figure 2.23). Different collapse mechanisms were observed as a function of the type of loading. The beams subjected to horizontal loading experienced a classic flexural type of failure due to

crushing in the compression zone and flexural cracking concentrated in the mid-span region. The beam tested under vertical loading failed due to sliding of the steel reinforcement and cementitious matrix along the bottom bed joint. The results are summarised in Table 2.12.



Figure 2.21. Ring – beams built by perforated bricks and SRG laminates [Borri et al., 2010]



Figure 2.22. Test setup scheme: horizontal action [Borri et al., 2010]



Figure 2.23. Test setup scheme: vertical action [Borri et al., 2010]

Table 2.11. Test results

Specimens	Experimental failure Load (kN)	Load point deflections (mm)	Exper. Moment capacity (kNm)	Theor. Moment capacity (kNm)	Mexp/ Mtheor	Failure mode
SG.01	42.27	36.45	27.47	24.59	1.12	Crushing
SG.02	36.43	26.31	23.68	24.59	0.96	Crushing
SG.03	35.99	64.9	23.39	24.16	0.97	Shear sliding

2.7.6 Reinforcement of curved structural elements

The State-of-the-Art on curved structural elements is reported in Chapter 5.

2.7 CONCLUDING REMARKS

The “State of the Art” examined in this chapter highlights the merits of using mortar-based innovative strengthening systems and their potential application in a variety of scenarios, including seismic upgrading and strengthening of historical monuments.

Although several studies examining the use of SRG to enhance the structural behaviour of both concrete and masonry structural elements have already been carried out, several issues still remain open and require further investigation. Open issues include for example:

- bond behaviour of SRG to concrete/masonry
- bond anchorage length
- lap-splice strength of multi-layer systems
- long term tensile properties and bond behaviour of SRG

The following chapters will explore in more depth some of the issues highlighted above and will focus on the mechanical characterization of SRG systems and their bond performance in strengthening different types of masonry structural elements, including both linear and curved elements. The experimental work presented in the following will assist in gaining an invaluable insight into the behaviour of SRG and provide a large database of results that can be used to validate existing predictive models and develop more reliable design guidelines.

3. Methodology chapter

3.1 Research Methodology

The experimental work discussed herein focuses on the use of a steel textile embedded in lime mortar (Steel Reinforced Grout - SRG) [De Santis et al., 2017a] to be used as strengthening system for masonry structures. As current guidelines and recommendations on Fabric Reinforced Cementitious Mortar (FRCM) (ACI 549) do not yet include provisions for SRG, a complete characterization of the material and its structural performance as strengthening system is needed.

This chapter describes the overall methodology implemented to investigate performance of SRG application in masonry substrate; multi-scale experimental test for detecting bond behaviour and full-scale experimental program carried on vaults reinforced with Steel Reinforced Grout in order to achieve the objectives set out in Chapter 1. The extensive experimental program is discussed in detail, including basic material characterization and small and medium-scale structural testing. The ways in which the experimental data are collected and analyzed is also presented.

3.2 Experimental Program

The experimental program is designed to address both scientific and technological challenges, as well as to develop knowledge and establish testing protocols that can be easily transferred to and complement current guidelines.

Figure 3.1 presents a flowchart summarizing the integrated experimental program carried out in this research. The different phases of testing are shown, including type of test method, examined parameters and

strengthening systems, and expected contribution to certification and accreditation procedures and design rules.

Novel measuring techniques, such as the contactless Digital Image Correlation (D.I.C.), are adopted to acquire full-field displacement and strain measurements, alongside more conventional techniques (such as potentiometers, LVDTs, extensometer, wire transducers).

It should be noted that, although durability tests on SRG systems are not included in this experimental program, a parallel series of tests has been undertaken by De Santis and co-authors [[De Santis, de Felice, Napoli, Realfonzo, 2016](#)]. The results of these accelerated tests have confirmed the superior durability performance of the SRG system under investigation and confirmed their suitability for masonry applications.

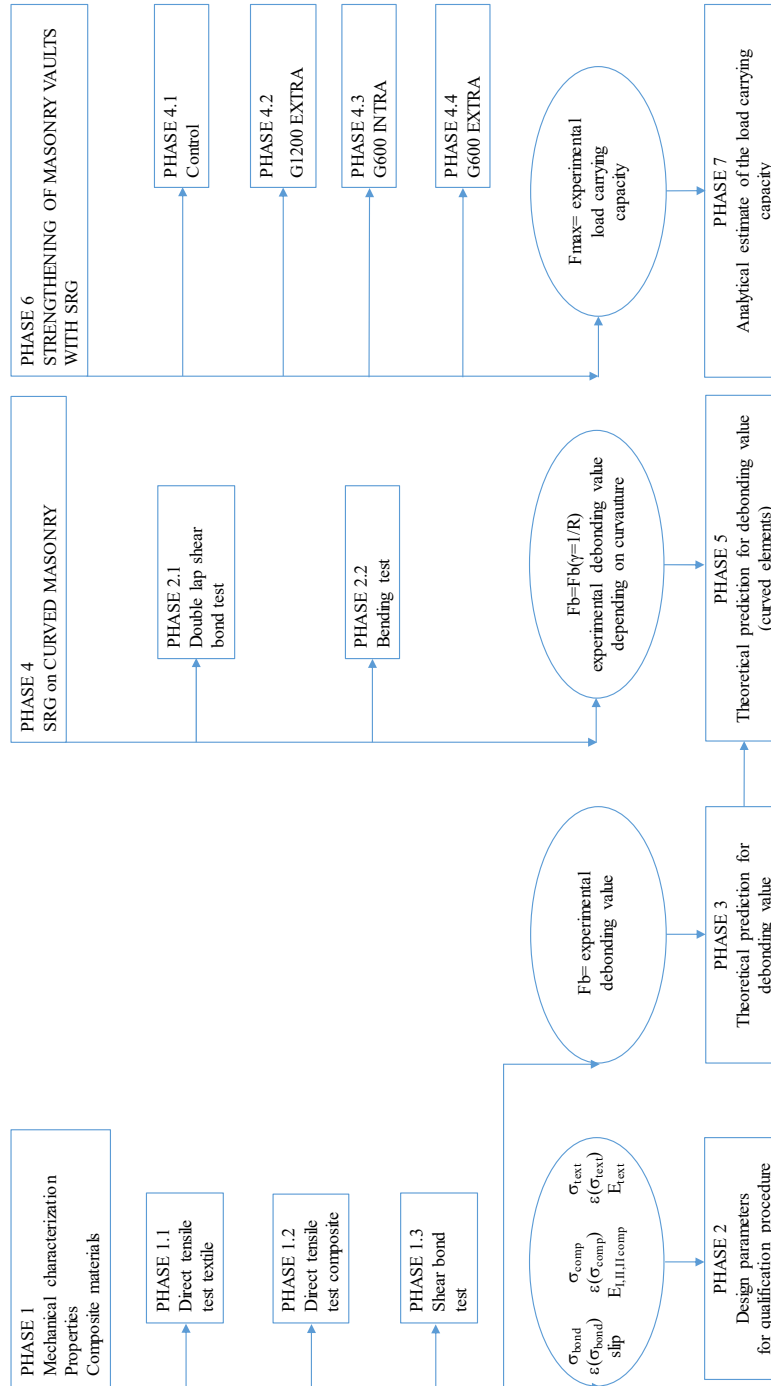


Figure 3.1. Experimental program flowchart

3.3 Materials

The SRG strengthening system comprises steel textile and lime mortar. Two types of steel fabrics are used in this study:

- Ultra High Tensile Strength Steel (UHTSS), galvanized (zinc coated) carbon steel textile made of cords, spaced 0.157 cords/mm (Figure 3.2a), each of which is obtained by twisting 2 wires around 3 rectilinear ones (Figure 3.2c) having 0.108mm^2 cross section area
- Ultra High Tensile Strength Steel (UHTSS), galvanized (zinc coated) carbon steel textile made of cords, spaced 0.314 cords/mm (Figure 3.2b), each of which is obtained by twisting 2 wires around 3 rectilinear ones (Figure 3.2c) having 0.216mm^2 cross section area; the properties of the steel is collected in Table 1.b (only for arch reinforcement)

The physical properties of the steel fabrics are shown in Figure 3.2 and Table 3.1, whilst the mechanical properties will be discussed in detail in Chapter 4.

The average mechanical properties of the lime based mortar, which included geo-polymeric binders (natural kaolin and bauxite), are summarized in Table 3.2.

Given the primary use of the examined SRG, clay bricks and mortar joints with a relatively low strength are used as masonry substrate (see Tables 3.3 and 3.4). Table 3.1 lists the label used in this paper, the cord density (c) and spacing (i), the surface mass density (γ), and the equivalent (design) thickness (t).

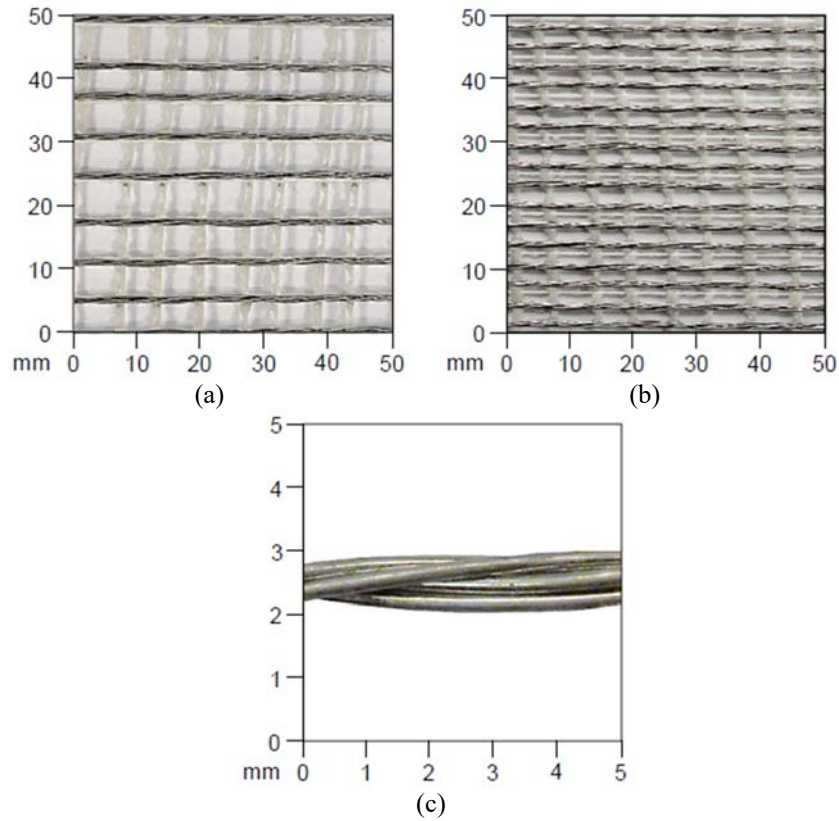


Figure 3.2. Steel mesh having 0.108mm² cross section area (a), steel mesh having 0.2016 mm² cross section area (b) and architecture of an individual strand(c)

Table 3.1. Physical properties of steel textile (Datasheet)

Textile	c [cords/in]	c [cords/mm]	i [mm]	γ [kg/m ²]	t_f [mm]
Galvanized carbon steel cords – $\gamma=670$ [kg/m ²]	4	0.157	6.35	670	0.084
Galvanized carbon steel cords – $\gamma=1340$ [kg/m ²]	8	0.314	3.18	1340	0.168

c = cord density; i = spacing; γ = surface mass density; t = equivalent (design) thickness

Table 3.2. Properties of mortar (Tests conducted in the laboratory)

[De Santis et al., 2017a]

Mortar	f_{cm} [N/mm ²]	E_{cm} [kN/mm ²]	f_{tm} [N/mm ²]
Lime based mortar with geo-polymeric binders	20.6	11.42	5.42

Table 3.3. Properties of substrate (Datasheet)

Substrate	Thick clay brick [mm]	Compressive strength [N/mm ²]	Tensile strength [N/mm ²]	Young's modulus [kN/mm ²]
Masonry prisms	55	14.8	2.5	5.76

Table 3.4 Mortar joints (Datasheet)

Mortar joint	f_{cm} [N/mm ²]
Mortar matrix	5

3.4 Material properties, qualification procedures of SRG (Phases 1 and 2)

Basic material tests are carried out to fully characterize the SRG system in terms of both tensile behavior as well as bond performance to masonry. The following tests are conducted:

1. direct tensile test on the bare steel textile [Napoli et al., 2016 - De Santis et al., 2016 - De Santis et al., 2017a] to obtain peak stress and strain, and Young's modulus.
2. direct tensile test on SRG composite coupons [de Felice et al., 2014 – De Santis and de Felice, 2015b – Carozzi and Poggi, 2015 – Napoli, de Felice, De Santis, Realfonzo, 2016 - De Santis, de Felice, Napoli, Realfonzo, 2016 - De Santis et al., 2017a] to determine the overall stress-strain response and the main mechanical parameters at all stages of loading (uncracked, cracking stage, fully cracked)
3. single lap shear bond tests [de Felice et al., 2014 - De Santis and de Felice, 2015b - De Santis et al., 2017a] to detect the maximum load that can be transferred from the strengthening system to the substrate, as well as the corresponding slip and failure mode.

Finally, the procedures that was proposed by Ascione [2015] is implemented in an attempt to provide a unified framework for the certification and accreditation of the strengthening systems and determine their design mechanical values. This procedure uses data obtained from both direct tension and bond pull-out tests and correlates them to the structural performance of the SRG system. Recently, in current year 2017,

this procedure has been also modified and parameters obtained through it are compared to the original one (see Chapter 4).

Finally, the performance of SRG systems is compared to that of more established FRCM systems [Olivito et al. 2016 - Roscini et al., 2016 - Lignola et al., 2017 – Carozzi et al. 2017 – Leone et al., 2017 - Caggegi et al, 2017 - De Santis et al., 2017a].

3.5 Evaluation of bond behavior of SRG applied to curved masonry substrate via double-lap shear bond and bending tests (Phase 3)

One of the primary applications of strengthening systems for masonry structures is the rehabilitation or upgrade of vaults and arches. Phase 3 of the experimental program aims at assessing the performance of the investigated SRG systems on curved elements. Series of small-scale structural tests are performed on SRG bonded to both straight and curved portions of masonry elements as detailed below:

- a) double lap shear bond test: to obtain tensile load as a function of curvature value;
- b) four-point bending test: to calculate failure (tensile strength) load as a function of curvature value.

Concave and convex masonry assemblies are used to simulate the application of the strengthening system to the intrados or the extrados of a masonry arch/vault (see Chapter 5). The results from this phase of testing will assist in the development of design recommendations.

3.6 Experimental tests on masonry arches strengthened with SRG (Phase 6)

The structural performance of SRG is examined in more depth through a series of tests on full-scale masonry vaults (see Chapter 6). In this phase of testing, the following strengthening configurations are assessed:

- i. control test without any reinforcements;
- ii. extradosal reinforcement comprising fabric density = 1200g/m^3 - 8cords/inch);

-
- iii. intradoxal reinforcements comprising fabric density = 600g/m^3 - 4cords/inch) and anchors;
 - iv. extradoxal reinforcement comprising fabric density = 600g/m^3 - 4cords/inch).

The experimental results from this phase are compared in terms of load, displacements and strains. These tests are designed to assess the effect of geometrical properties of the vaults, strengthening configuration (geometry of the steel fabric, use at intradox or extradox), and anchorage solutions on overall structural performance and can be used to assess current design rules or developed new models.

3.7 Simplified design equations (Phases 3, 5 and 7)

The results from the various phases of testing are examined in detail with the aim of developing simple, yet reliable design recommendations. The recommendations provide range from the initial certification and accreditation of the strengthening system to the development of a fundamental bond model and detailing rules.

In particular:

- 3.1.1 theoretical prediction for debonding value (Phase 3, see Chapter 4);
- 3.1.2 proposal of analytical procedure for the reinforcement of masonry curved members (Phase 5, see Chapter 5);
- 3.1.3 analytical estimate of the load carrying capacity (Phase 7, see Chapter 6).

4. SRG system properties and experimental tests for accreditation

ABSTRACT

Fabric Reinforced Cementitious Matrix (FRCM) composites are currently receiving great attention for strengthening reinforced concrete and masonry structures, as they improve the capacity with minimum mass increase. Although there is a large number of FRCM systems available in the market that have been applied in strengthening applications on site, a deeper understanding of their mechanical behaviour and of the associated parameters needed for design recommendations is still required. For this purpose, an experimental investigation is carried out in Roma Tre University, on Steel Reinforced Grout systems. This research presents the certification proceeding for these systems, made by steel textiles strengthening, by means of tests to characterize their composite materials properties and to study reinforcement-to-substrate bond behaviour. According to CNR-DT 200 R1/2013 an analytical approach is proposed to obtain a prediction on failure bond value, modifying necessarily the existing formula.

This work is performed within a Round Robin Test program organized by the Rilem TC 250-CSM (Composites for Sustainable strengthening of Masonry) and involving a total of twenty European laboratories and eleven industrial partners [De Santis et al. 2017, Caggegi et al. 2017, Carozzi et al. 2017, De Santis et al. 2017, Leone et al. 2017, Lignola et al 2017]. Therefore, SRG systems are also compared to other FRCM, comprising aramid, basalt, carbon, glass and polyparaphenylene benzobisoxazole (PBO) textiles systems and studied in Roma Tre University, in the just mentioned context of Round Robin Test. It is very important underline that,

for all of systems, each textile is matched into mortar matrix, provided by the same supplier.

As a result, thanks to this document, SRG properties are highlighted aiming at justifying and supporting, in a scientific method, their application for retrofitting of existing buildings.

4.1 INTRODUCTION

The need for increasing the safety and the resilience of existing structures to natural hazards such as earthquakes, subsidence, and floods, often requires retrofitting. Among the different possible solutions, externally bonded reinforcements (EBRs) with composite materials are receiving greater attention [Valluzzi et al., 2014a], as they provide a significant strength increase without altering the original geometry and mass of the structural element. EBRs consist of a high strength textile applied to the substrate either with a polymeric or with an inorganic matrix. Mortar-based systems, named either “Textile Reinforced Mortar” (TRM) or “Fabric Reinforced Cementitious Matrix” (FRCM), offer a better vapour permeability, fire resistance and compatibility with the substrate than Fabric Reinforced Polymers. However, these advantages are counter balanced by lower bond properties. A more complex stress transfer needs to activate, in which the tensile stress in the reinforcement should first be transferred to the matrix and then from the matrix to the substrate. Different failure modes may occur, including slippage of the textile within the matrix, cracking of the matrix, loss of adhesion between matrix and substrate, and cohesive fracture within the substrate [Carozzi et al. 2014, Carozzi and Poggi, 2015; de Felice et al., 2014, Ascione et al., 2015]. At present time, despite of the extensive use of FRCMs in rehabilitation works, only the US ACI [ACI 549.4R-13] code is available as a guide to design repair and strengthening works on masonry and reinforced concrete structures. Moreover, experimental testing of FRCMs presents several difficulties due to the intrinsic brittle nature of the inorganic matrix.

This chapter presents, at the first instance, the results of an experimental study on Steel Reinforced Grout, consisting in two typology of steel, galvanized and stainless, combined with lime or mineral-cementitious mortars, to compare with performances of other strengthening systems made by composites comprising aramid, basalt, carbon, glass, and PBO embedded into matrices, lime and cementitious based. All tests were

performed in Roma Tre University, and as part of a Round Robin Test organised by RILEM Committee TC 250-CSM, RILEM procedures and recommendations were followed [[RILEM Instructions - De Santis et al., 2017a](#)].

This research contributes to the knowledge of the behaviour of these systems, including tensile strength and stiffness, and bond performance (in terms of load transfer capacity and failure mode) on brickwork substrate [[Caggegi et al., 2017](#), [Lignola et al., 2017](#), [Carozzi et al., 2017](#), [Leone et al., 2017](#), [De Santis et al., 2017a](#)]. For this reason, in particular, direct tensile tests are carried out on dry textile and composite materials specimens to derive strength, peak strain and tensile modulus of elasticity. Single-lap shear bond tests are performed on brickwork substrate to determine the bond performance in terms of strength and failure mode. Test results are combined to derive engineering design parameters and to provide a theoretical prediction in terms of debonding value.

Different displacement measurement methods are used, to improve the reliability of recorded data. The reliability of setups (specimen manufacturing, gripping methods, displacement/strain measurements) is assessed for contributing to the development of standardized testing methodologies for product qualification and material acceptance purposes.

4.2 EXPERIMENTAL INVESTIGATIONS

4.2.1 Experimental plan

The following tests are carried out [[Roscini et al., 2016](#)]:

- i) tensile tests (Figure 4.1a) on steel textiles, to obtain peak stress and strain, and Young's modulus.
- ii) tensile tests (Figure 4.1b) on SRG specimens, which provides the whole stress-strain response and the main mechanical parameters of the three response stages, consisting in: (i) un-cracked stage (in which the mortar matrix contributes to both load bearing capacity and stiffness), (ii) crack development stage (during which crack pattern develops progressively), and (iii) cracked stage (in which crack pattern is completely developed). Direct tensile tests on SRG composites provides the constitutive behaviour of the reinforcement and allows evaluating the increase in strength provided by the matrix [[de Felice et al. 2014](#); [De Santis and de Felice, 2015a](#)].

iii) single-lap shear bond tests (Figure 4.1c), to detect the maximum load that can be transferred from the strengthening system to the substrate, and the corresponding slip and failure mode. The SRG-to-substrate bond behaviour plays a crucial role in most applications, in which the load is transferred by shear, providing the effective stress limit in the reinforcement after which debonding occurs [De Santis and de Felice, 2015b].

All test results are provided by exploitation ratio, which is a measure of the efficiency of the reinforcement, and is defined as the stress in the textile at debonding (σ_b) divided by its tensile strength. This latter is derived from direct tensile tests on either dry textile (σ_t) or composite material (σ_c) specimens.

As just above mentioned, tensile tests on SRG specimens and single-lap shear bond tests are performed according to RILEM TC-250 CSM procedures. Regarding tensile tests, the instructions in “Round-robin test on the tensile behaviour of mortar-based strengthening systems” document are reported, meanwhile for shear bond ones, the “Round-robin test on the bond performance of mortar-based strengthening systems on masonry substrate” report is applied.

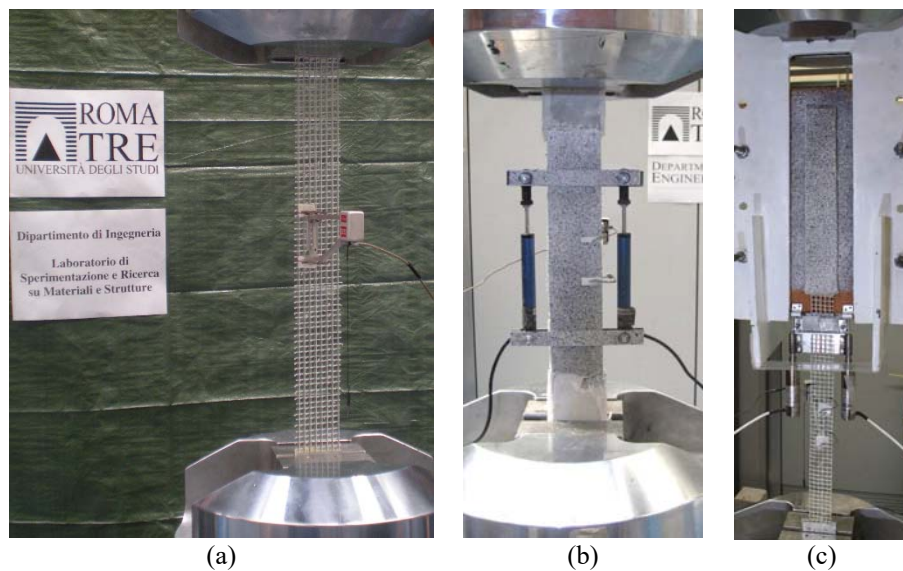


Figure 4.1. Experimental setups for tensile tests on dry textile steel (a), SRG coupons (b), and for shear bond tests (c).

4.2.2 Materials

The studied strengthening systems consist of two main elements, a mortar and a fabric grid. Each combination, depending on materials and morphological characteristics of elements, is made by same supplier.

Regarding textile specimens, they are labelled according to the notation TT-NN, TT indicating the material of textile (as collected in the Table 4.1) and, NN being the progressive number of the specimens.

For all coupons samples made with composite materials, it used TT-MM-NN notation, where TT indicating the material of textile, MM being mortar typology (as reported in the Table 4.2) and, finally, NN being the progressive number of the specimens.

About shear bond test, brickworks specimens are named with the notation TT-MM-BMAS-NN, TT indicating the material of textile, MM being mortar typology, -BMAS suffix as “Brick MASonry” (Table 4.3) for the substrate, finally, NN being the progressive number of the specimens.

4.2.2.1 Steel textiles

In this experimental study, two types of fabric grids are investigated. The properties of textiles, are collected in Table 4.4.

4.2.2.2 Mortar matrices

Textiles are combined with three different mortar matrices, as described in the Table 4.5.

4.2.2.3 Strengthening systems

Three typologies of steel reinforced grout strengthening systems are manufactured by means two typologies of textiles matched with three mortars.

The bond performance of these SRG strengthening systems is tested on brickwork substrate. Aiming at reproducing the characteristics of the masonry of historical buildings, relatively weak clay bricks (compressive strength of 15N/mm^2) and lime mortar (5N/mm^2) are used to manufacture the prisms used as substrates.

Table 4.1. Textiles description

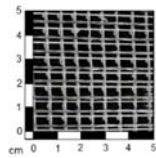
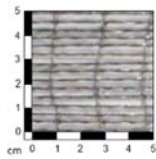
Textile	Label	Image	Description
Steel	GS		The Galvanized Steel textile comprised Ultra High Tensile Strength Steel (UHTSS) cords with 6.35mm spacing, 0.084mm design thickness and 670g/m ² surface mass density. Each cord is obtained by twisting 2 wires around 3 rectilinear ones, having 0.108mm ² cross section area.
Steel	SS		The SS textile is characterized by AISI 304 Stainless Steel (SS) made of cords, with 3.18 mm spacing. Each cord is obtained by twisting 5 wires having 0.119 mm ² cross section area; 0.188mm design thickness and 1500g/m ² surface mass density.

Table 4.2. Mortar matrices description

Mortar	Label	Description
Lime (Geopolymer binders)	G	The “G” lime-based mortar, including geopolymer binders (natural kaolin and bauxite), is included in M15 strength class. The physical properties of this mortar matrices, namely vapour permeability m , compressive strength f_{cm} and Young's modulus E_{cm} , are respectively ≥ 16 , 20.6 N/mm ² and 11.42kN/mm ² .
Mineral-Cementitious	M	The matrix named “M” is a fabric reinforced cement mortar with natural kaolin and bauxite binders and also organic additives, included in M25 strength class. It has 16.4N/mm ² compressive strength and 15kN/mm ² Young's modulus.
Lime	L	This lime-based mortar matrix, identified by label “L”, includes natural pozzolan and silica aggregates. It is characterized by 6.40N/mm ² compressive strength, 6.31kN/mm ² Young's modulus, and 1.24N/mm ² tensile strength.

Table 4.3. Strengthening systems description

Supplier and Composite (textile & mortar)	Name
1_ Galvanized Steel textile and lime -Geopolymer binders- mortar	GS and G
2_ Galvanized Steel textile and Mineral-cementitious mortar	GS and M
3_ Stainless Steel textile and Lime mortar	SS and L
Substrate: Brick MASonry	add -BMAS

Table 4.4. Textiles properties (Data sheet)

Textile	Label	c	i	γ (Surface mass density)	t (Design thickness)	Notes
		[cords/mm]	[mm]	[g/m ²]	[mm]	
Galvanized Steel	GS	0.157	6.350	670.00	0.0840	Galvanized cords, Unidirectional Stainless steel cords, Unidirectional
Stainless Steel	SS	0.315	3.180	1500.00	0.1880	

Table 4.5. Mortars properties (Data sheet)

Mortar type	Label	μ [-]	f_{cm} [N/mm ²]	E_{cm} [kN/mm ²]	f_{tm} [N/mm ²]
Lime and geopolymer	G	≥ 16 (15-35)	> 15	9.00	5.00
Cement (Mineral)	M	20.00	25.00	15.00	n.a.*
Lime	L	< 30	> 15	n.a.*	n.a.*

n.a.* = not available

4.2.3 Manufacturing of specimens

Composite materials coupons subjected to direct tensile tests are manufactured, according to RILEM TC-250 CSM procedures (Figure 4.2), with Perspex moulds, kept wet for 2 days, cured at 95% R.H. for 24h. After demoulding, cured in water for 27 days (under small weights), stored on a plane surface «lying sideways on» and on supports for uniform drying and, finally, left for 15 days in laboratory conditions (18–20°C temperature and 50–60% RH) before testing. At the end of this casting process, coupons are made (Figure 4.4). In order to prevent early failures, it is very important that, at its last sides, the coupon is wrapped by two GFRP layers.

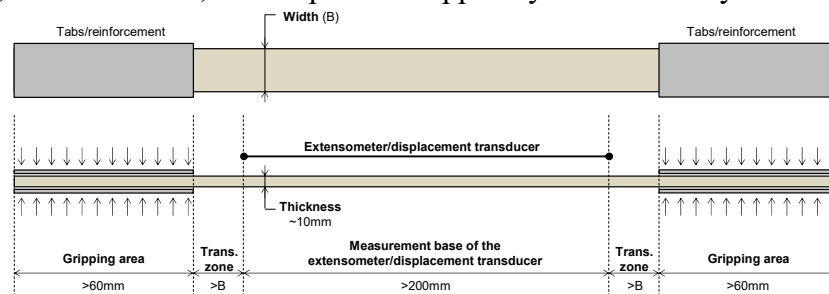


Figure 4.2. FRCM specimen geometry (the measures are only advised)

For shear bond tests, following RILEM TC-250 CSM procedures (Figure 4.3), masonry prisms are built having 12cm×12cm base, kept wet for 15 days and stored in laboratory conditions (18–20°C temperature and 50–60% RH) for 15 days. Reinforcements are applied with aluminium moulds and kept wet for 2 days. After demoulding, specimens are wetted for 26 days and stored in laboratory for 15 days before testing (Figure 4.5). Aiming at ensure a good clamping, two aluminium tabs are applied at the last side of the textile, in accordance to UNI EN 2561 recommendations [UNI EN 2561]. It is necessary to underline the importance of ensuring adequate curing conditions on FRCM systems after manufacturing of specimens for both tensile and shear bond tests. In particular, curing under wet conditions prevents the mortar matrix from drying out and the development of any cracking phenomena. Wet conditions have also to be ensured, given the high porosity of clay masonry which will absorb the moisture from the mortar matrix. Therefore, curing of specimens under wet conditions is strictly recommended upon the completion of both brickwork manufacturing and FRCM strengthening application, in order to ensure an effective stress-transfer mechanism at the reinforcement/substrate interface and to avoid premature failure.

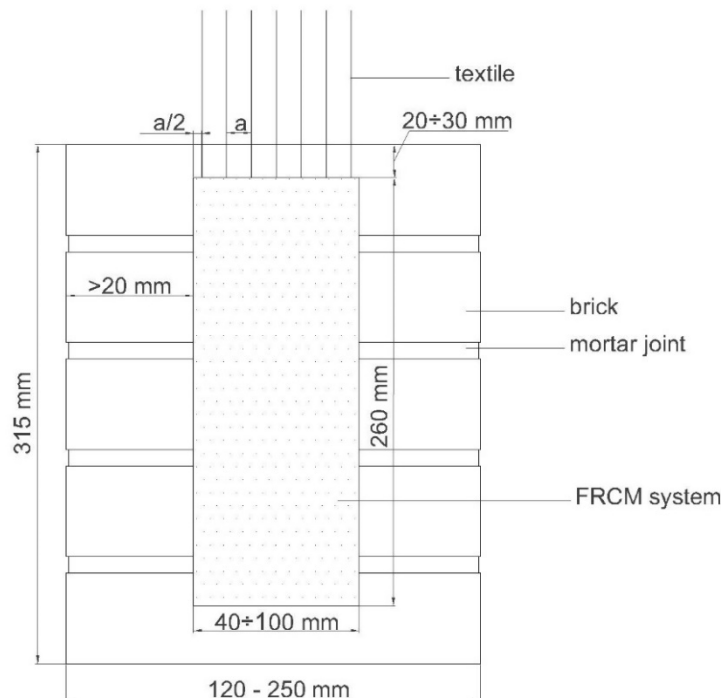


Figure 4.3. FRCM reinforcement applied on brickwork masonry geometry



Fig. 4.4.1. Plexiglass moulds



Fig. 4.4.2. FRCM coupons casting



Fig. 4.4.3. Keeping in water



Fig. 4.4.4. Storing on a plane surface
«lying sideways on»



Fig. 4.4.5. Drying for 15 days
on supports for uniform drying



Fig. 4.4.6. Specimen before testing

Figure 4.4. Composite material specimens manufacturing procedure



Fig. 4.5.1. Masonry prisms manufacturing



Fig. 4.5.2. Prisms curing in laboratory conditions



Fig. 4.5.3. Prisms before reinforcement applying



Fig. 4.5.4. Aluminium moulds



Fig. 4.5.5. FRCM first layer



Fig. 4.5.6. Textile inside mortar



Fig. 4.5.7. FRCM second layer



Fig. 4.5.8. Reinforcement applied



Fig. 4.5.9. Keeping wet for 26 days



Fig. 4.5.10. Prisms FRCM reinforced

Figure 4.5. Shear bond test specimens manufacturing procedure

4.2.4 Experimental setups

All tests are carried out using a Material Testing Systems (MTS) 500kN hydraulic actuator under displacement control with a value of machine compliance $<0.05\%$ (Figures 4.6.1, 4.6.2, 4.6.3). The applied load is recorded by an integrated load cell (accuracy 0.2% and resolution 0.01kN). Due to the possible occurrence of brittle phenomena, different displacement rates are selected for each test type, such as 0.02mm/s for tensile tests on are specimens, 0.01mm/s for tensile tests on composite specimens, and 0.003mm/s for shear bond tests. Data are acquired at 10Hz sampling.

In tests on dry textile specimens, the displacement is recorded by the LVDT integrated in the testing machine, with 0.05% accuracy and $1\mu\text{m}$ resolution. A MTS extensometer having 50mm gage length, $+25/-5\text{mm}$ range, 0.18% accuracy and $10\mu\epsilon$ resolution, is also used to record locally the strain.

In direct tensile tests on composite materials coupons, two additional potentiometers ($\pm 5\text{ mm}$ range, 0.05% accuracy, $<10^{-4}\text{mm}$ resolution) are used to measure the global displacement excluding gripping areas.

In shear bond tests, an extensometer is applied to the unbonded textile to calculate its strain value and a couple of LVDT transducers, with a value of linearity deviation $< \pm 0.5$ (± 0.25) [% F.S.] and $43[\text{mV/V/mm}]$ accuracy, are used to measure the relative displacement (slip) between reinforcement and substrate at the loaded end of the bonded area [De Santis and de Felice, 2015a - De Santis and de Felice, 2015b – Roscini et al. 2016]. Digital Image Correlation (D.I.C.) is used with an acquisition frequency of 1 photo every 4s for tensile tests or every 10s for shear bond tests, to detect displacement and strain fields, as well as the slip between textile and substrate. The use of more methods for the measurement of displacements improves the reliability of recorded data and allows for a validation of both test results and measurement methods. DIC algorithm associates each pixel with a shade of grey, in order to identify its position, on each photo taken during the test (Figure 4.7). Therefore, it provides the temporal evolution of the positions of the matrix points, on the specimen surface.

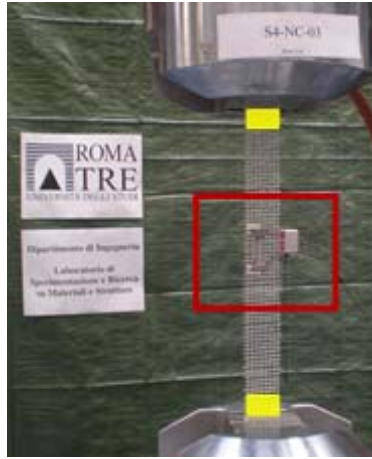


Fig. 4.6.1. Extensometer on textile

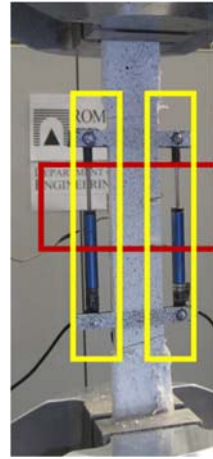


Fig. 4.6.2. Extensometer (red), potentiometers (yellow) and DIC speckle pattern on coupon surface



Fig. 4.6.3. Extensometer (red), LVDTs (yellow), DIC on markers and DIC speckle pattern on reinforcement surface and on marker (light blue)

Figure 4.6. Traditional instrumentation setup

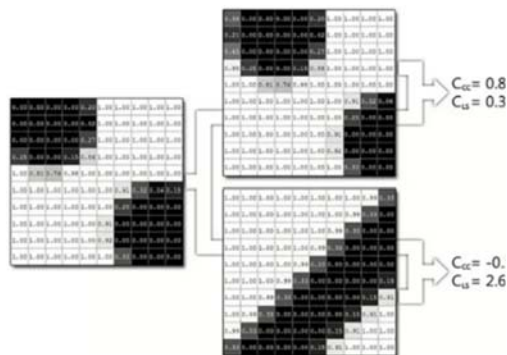


Fig. 4.7.1. Grey-scale matrix



Fig. 4.7.2. Speckle pattern on reinforcement

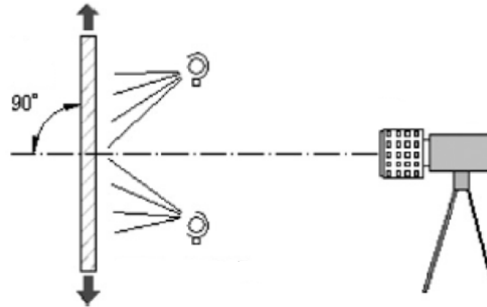


Fig. 4.7.3. Theory of high resolution camera position for DIC

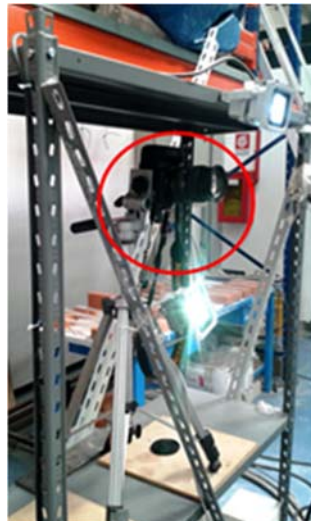


Fig. 4.7.4. High resolution camera for DIC detection

Figure 4.7. Contact-less method DIC setup

4.3 STEEL REINFORCED GROUT EXPERIMENTAL RESULTS

In this section, the results about Steel Reinforced Grout strengthening systems, are presented according to the format of the qualification procedure proposed in [Ascione et al., 2015] (Figure 4.8.1).

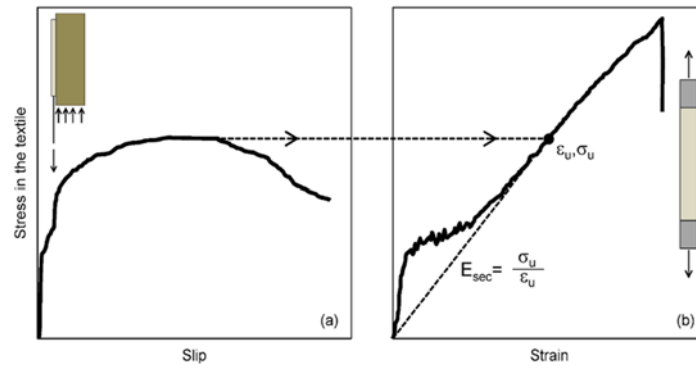


Figure 4.8.1. Ascione et al. [2015] proposed procedure for accreditation of strengthening system

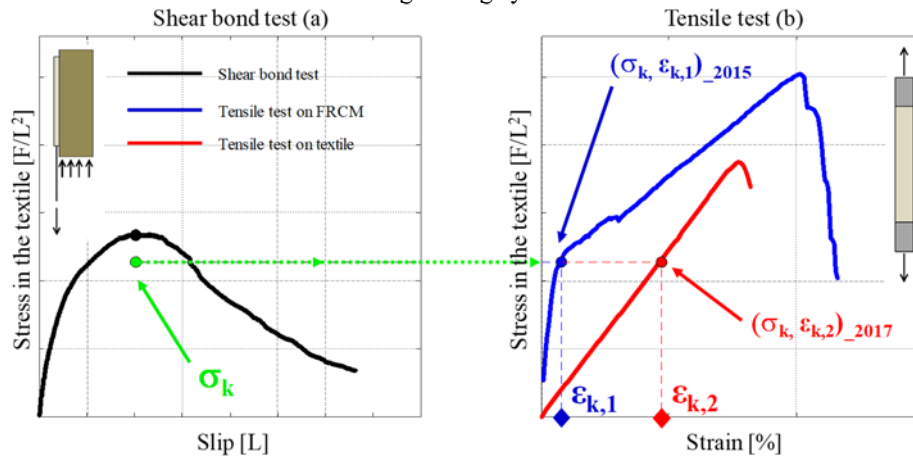


Figure 4.8.2. Comparison between procedure proposed by Ascione et al. [2015] and procedure developed in 2017

where:

σ_k = characteristic stress

$\epsilon_{k,1}$ = strain value detected in tensile test on FRCM (Figure 4.8.2b blue curve)

$\epsilon_{k,2}$ = strain value detected in tensile test on textile (Figure 4.8.2.b red curve)

$(\sigma_k, \epsilon_{k,1})_{2015}$ = qualification point in procedure proposed by Ascione et al. [2015]

$(\sigma_k, \epsilon_{k,2})_{2017}$ = qualification point in procedure developed in 2017

$E_k = \sigma_k / \epsilon_{k,1}$ = secant elastic modulus

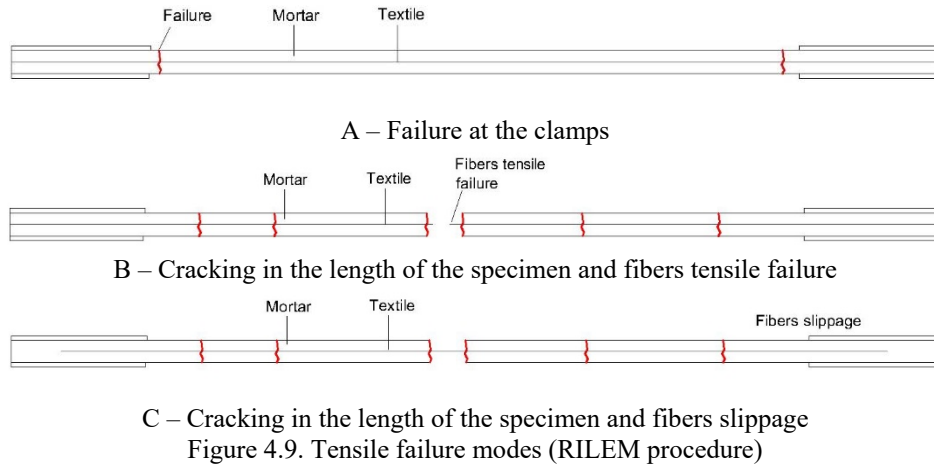
E_{text} = Young's modulus of textile

At the same time, even a second procedure is developed in 2017 to qualify these strengthening system (Figure 4.8.2), in order to simplify post-processing and to obtain parameters for accreditation.

In procedure proposed in Ascione and co-authors [2015], displacements controlled monotonic shear bond tests are performed. Force values are divided by the cross section area of the textile, and stress-slip curves are built (Figure 4.8.2a). Monotonic direct tensile tests are carried out under displacement control up to failure, and stress-strain response curves are derived (Figure 4.8.2b, blue curve). The characteristic stress (σ_k) from shear bond tests is identified on the stress-strain response curve of FRCM coupon under tension (blue curve), together with the corresponding strain ($\varepsilon_{k,1}$). This point ($\sigma_k, \varepsilon_{k,1}$) conventionally qualifies the system on the considered substrate. The secant elastic modulus is derived as E_k ($\sigma_k/\varepsilon_{k,1}$ ratio).

Meanwhile, in the second procedure proposed in 2017, the characteristic stress (σ_k) from shear bond tests (Figure 4.8.2a) is identified on the stress-strain response curve of textile under tension (Figure 4.8.2b, red curve), together with the corresponding strain ($\varepsilon_{k,2}$). This point ($\sigma_k, \varepsilon_{k,2}$) conventionally qualifies the system on the considered substrate. Strain characteristic value could be also calculate from characteristic stress value divided by Young's modulus of textile (E_{text}), as previously calculated in textile tensile test.

Therefore, response curves are plotted in terms of stress-slip curves (shear bond tests) and stress-strain (tensile tests). The graphs collected in the following paragraphs, show the envelope of the curves filled in yellow for shear bond tests, and in grey and in blue for direct tensile tests on dry textile specimens and FRCM composites, respectively. Individual tests are also represented by thin curves. Finally, thick curves represent the average of each set of tests. In each system, qualification parameters about "2015" and "2017" procedures are reported on the graphs. The outcomes for SRG tensile tests and shear bond test are completed by failure modes for each test. Finally, all of experimental results carried out for SRG strengthening system, according to procedure available in CNR [CNR DT-200 R1/2013], with appropriate modifications considering SRG-to-substrate behaviour, are processed to provide an analytical approach to calculate the theoretical failure load.



Regarding tensile tests, according to RILEM TC-250 CSM recommendations, three failure modes can be observed and are reported in Figure 4.9: A) failure near the clamping area, B) fibre tensile rupture combined with cracking of the specimen and C) fibre slippage within the matrix combined with cracking of the specimen. In Figure 4.10, all the possible failure modes for shear bond tests are collected, depending on wherein debonding occurs [de Felice et al., 2014, Ascione et al. 2015]. In failure mode “A”, debonding occurs in the substrate. The debonding of “B” failure mode happens, at the other hand, at the interface between mortar and substrate. If debonding occurs at the interface textile-mortar, failure mode is “C”. In “D”, the sliding of the textile happens inside the mortar. Finally, in both “E” and “F” failure modes, the rupture of textile occurs.

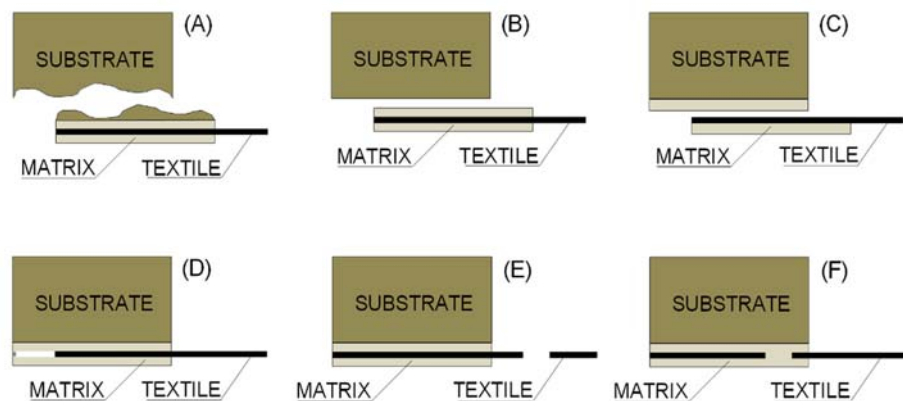


Figure 4.10. Shear bond test failure modes [de Felice et al., 2014 -Ascione et al. 2015]

4.3.1 GS-G system (galvanized steel and lime with geopolymer binders mortar)

4.3.1.1 GS Steel textile

The response of steel textile displays a first linear elastic behaviour, with a Young's modulus average value of 181.10kN/mm^2 (Table 4.7). After this, a steel hardening phase starts up to maximum value of strength. Maximum peak stress value (maximum of the average curve) is 3200.18N/mm^2 and the corresponding strain is 2.23% (Figure 4.12b). Cords almost fail at the same time. This is the meaning of a correct load distribution among the cords.

4.3.1.1.1 Durability of GS steel textile

In order to verify possible decreases about mechanical characteristics of these composite materials through the time, durability test against salt attack is carried out. Before this document, some researchers [Borri and Castori, 2011, Borri et al., 2015, De Santis and de Felice, 2015b, Franzoni et al., 2017] studied durability influence on mechanical characteristics steel textiles. In particular, this document produces results regarding this galvanized steel textile tensile tests, after aged in Solution Ocean Water for 2000h and 3000h prepared according to the US standard [ASTM D1141-98](#). By observation of Scan Electron Microscope (S.E.M.) images about cords aged in Solution Ocean Water for 2000h (Figure 4.11b) and 3000h (Figure 4.11c), it can be seen that at 2000h an oxide makes protecting galvanized single cord (area of the image coloured as rainbow effect) and after this, at 3000h, it cracks by flakes. It can be assumed that, thanks to this protecting oxide, not any serious corrosion phenomenon by pitting on the steel wire, which probably arises after 3000h ageing treatment in Solution Ocean Water, are observed.

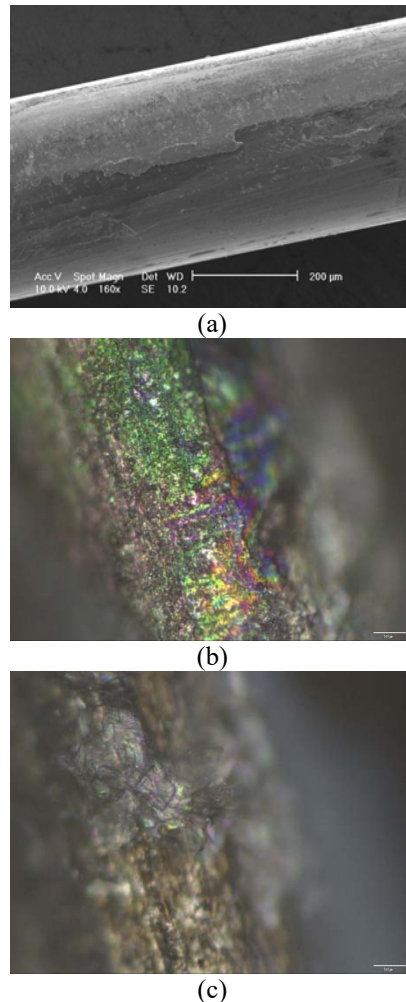


Figure 4.11. Microscope analysis. (a) none ageing (optical microscope), (b) 2000h(SEM), (c) 3000h(SEM)

Tensile mechanical results, in terms of tensile strength (f_t) and modulus of elasticity (E_f), are collected in Table 4.6, comparing with other data already available in literature. These outcomes respect the requirements of a maximum reduction of strength and Young's modulus of 15%, for the qualification of composite reinforcements in the US standard [ASTM D 1141 – 98 (Reapproved 2003)] and in the Italian Guidelines [Linea Guida per la identificazione, la qualificazione ed il controllo di accettazione di

compositi fibrorinforzati a matrice polimerica (FRP) da utilizzarsi per il consolidamento strutturale di costruzioni esistenti].

Table 4.6. Results of tensile tests on textile specimens (CV in round brackets)

Specimen	Ageing	Number of tests	f_f (N/mm ²)	F_f (kN/m)	ε_f (%)	E_f (kN/mm ²)
S4	None	6	3186.1 (0.8%)	267.6	2.26 (3.6%)	183.7 (1.9%)
S4	S.O.W. 15 days	3	3112.9 (0.9%)	261.5	2.11 (2.0%)	178.3 (0.8%)
S4	S.O.W. 30 days	3	3061.2 (0.4%)	257.1	2.27 (4.9%)	176.8 (0.9%)
S4	S.O.W. (1000h = 41 days)	3	3044.1 (1.0%)	255.7	2.20 (1.8%)	176.2 (0.6%)
S4	90° flexure	3	2687.4 (3.1%)	225.7	1.80 (3.1%)	165.7 (1.0%)
S4	90° flexure + S.O.W. 41 days	3	2574.5 (1.0%)	216.3	1.82 (2.7%)	161.0 (0.2%)
S4	S.O.W. (2000h = 83 days)	5	2969.3 (1.9%)	221.4	2.04 (1.9%)	189.0 (1.03%)
S4	S.O.W. (3000h = 125 days)	5	2988.8 (2%)	191.2	2.01 (4.3%)	190.8 (1.04%)

4.3.1.2 GS-G composite under tensile loading

GS-G stress-strain is characterized by a first linear elastic branch, with an average value of Young's modulus at 1st stage of 914.00kN/mm² (Table 4.8). Large variation of E_I data between specimens 3rd and 4th could be depend on differences in manufacturing phase and in clamping methods. In this first phase, tensile mortar contribution results very small. Once the mortar reaches its peak strength, cracking development initiates: this is the second stage. After, in the third and last stage, the Young's modulus is very similar to the steel textile one, because mortar is completely cracked and just steel cords have tensile resistance, up to their rupture (4.12b). Then test is finished.

4.3.1.3 GS-G-BMAS shear bond performance

These specimens are made with 40mm of reinforcement width applied on the substrate and 5 steel cords.

Stress-slip curves display a first linear behaviour; the maximum peak value of the average curve is 3032.14N/mm² (Table 4.10), corresponding a slip value of 2.91mm and a strain of 3.23% (Figure 4.12a). It is mostly detected

a “F-C” failure mode (Table 4.11), with the tensile rupture of the textile out of the bonded area combined with debonding at the interface textile-mortar. From data collected in the tables, debonding strength can be compared to composite specimens under tensile tests. This is the reason why the strengthening system works very well but without achieving the reinforcement-to-substrate shear bond strength.

Table 4.7. GS series

GS series	Peak stress	Peak strain	Young's modulus
	σ_t	$\varepsilon(\sigma_t)$	E
	N/mm ²	%	kN/mm ²
01	3213.60	2.34	176.00
02	3190.70	2.20	183.10
03	3188.90	2.19	181.10
04	3209.90	2.26	182.20
05	3197.80	2.17	183.10
Average	3200.18	2.23	181.10
St. dev.	11.15	0.07	2.97
CoV [%]	0.35	3.09	1.64

Table 4.8. GS-G series

GS-G series	Peak stress	Peak strain	Young's modulus		
	σ_c	$\varepsilon(\sigma_c)$	E _I	E _{II}	E _{III}
	N/mm ²	%	kN/mm ²		
01	3545.54	1.92	795.00	178.50	191.72
02	3466.58	2.10	1026.30	71.40	191.99
03	3383.45	2.02	667.80	93.30	184.38
04	3359.91	2.13	1220.30	137.40	169.28
05	3551.22	2.00	860.60	170.70	185.59
Average	3461.34	2.03	914.00	130.26	184.59
St. dev.	88.81	0.08	214.51	47.02	9.23
CoV [%]	2.57	4.11	23.47	36.10	5.00

Table 4.9. GS-G failure modes




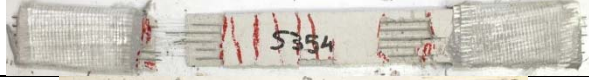






Specimen	Failure mode image	Failure mode typology
GS-G-01		A
GS-G-02		A
GS-G-03		A-B
GS-G-04		A-B
GS-G-05		A-B

Table 4.10. GS-G-BMAS series

GS-G-BMAS series	Peak stress	Peak strain	Exploitation ratio		Peak slip
	σ_b	$\varepsilon(\sigma_b)$	σ_b/σ_c	σ_b/σ_t	$s(\sigma_b)$
	N/mm ²	%	-	-	mm
01	3062.33	5.62	0.88	0.96	3.35
02	3029.63	3.38	0.88	0.95	2.58
03	3032.84	4.19	0.88	0.95	3.19
04	2999.51	1.63	0.87	0.94	3.00
05	3036.37	1.33	0.88	0.95	2.42
Average	3032.14	3.23	0.88	0.95	2.91
St. dev.	22.37	1.79	0.01	0.01	0.40
CoV [%]	0.74	55.40	0.74	0.74	13.64

Table 4.11. GS-G-BMAS failure modes

Specimen	Failure mode image	Failure mode typology
GS-G-BMAS-01		F
GS-G-BMAS-02		F
GS-G-BMAS-03		F
GS-G-BMAS-04		F-C
GS-G-BMAS-05		C

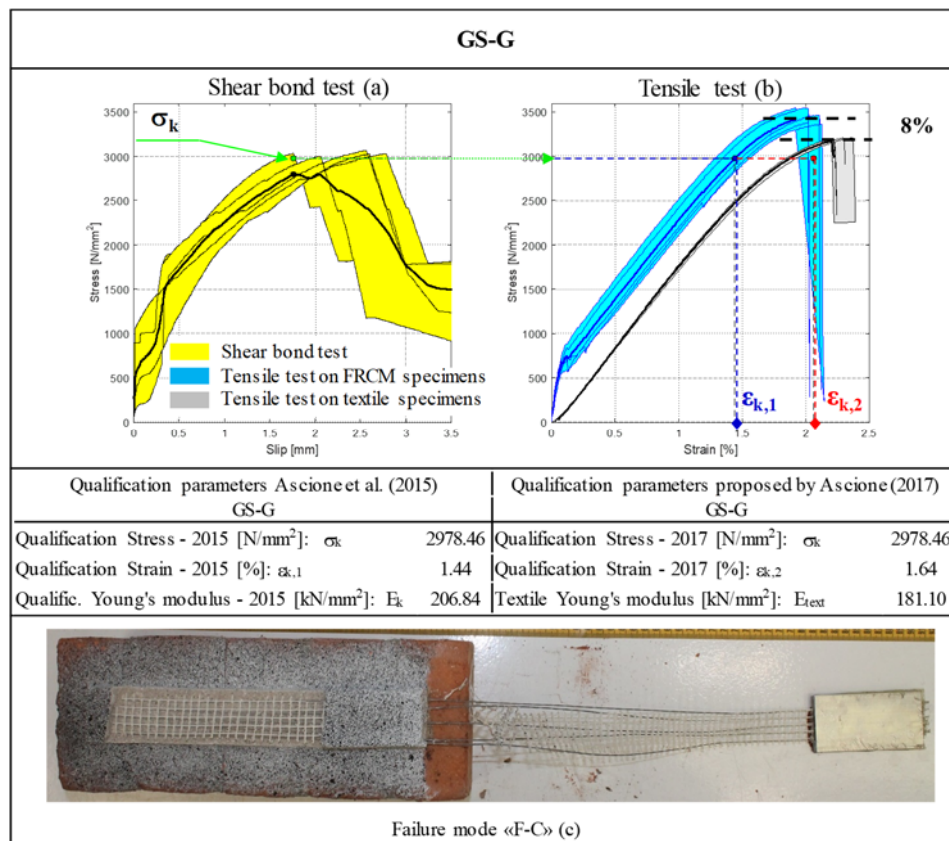


Figure 4.12. Qualification procedures GS-G

Values calculated for post-processing of strengthening system are:

σ_t = peak stress in tensile test on textile

$\epsilon(\sigma_t)$ = strain corresponding to peak stress in tensile test on textile

E = Young's modulus in tensile test on textile

σ_c = peak stress in tensile test on composite materials

$\epsilon(\sigma_c)$ = strain corresponding to peak stress in tensile test on composite materials

E_I = Young's modulus at un-cracked stage, the 1st one, (in which the mortar matrix contributes to both load bearing capacity and stiffness) in tensile test on composite materials

E_{II} = Young's modulus at crack development stage, the 2nd one, (during which crack pattern develops progressively), in tensile test on composite materials

E_{III} = Young's modulus at cracked and the 3rd stage (in which crack pattern is completely developed), in tensile test on composite materials

σ_b = peak stress in bond tests

$s(\sigma_b)$ = value of slip corresponding to peak stress in bond tests. Slip defines the relative displacement between reinforcement and substrate at the loaded end of the bonded area

σ_b/σ_c = exploitation ratio is a measure of the efficiency of the reinforcement, and is defined as the stress in the textile at debonding (σ_b) divided by tensile strength derived from direct tensile tests on composite (σ_c) specimens

σ_b/σ_t = exploitation ratio is a measure of the efficiency of the reinforcement, and is defined as the stress in the textile at debonding (σ_b) divided by tensile strength derived from direct tensile tests on dry textile (σ_t).

4.3.2 GS-M system (*galvanized steel and mineral mortar*)

4.3.2.1 GS Steel textile

Just above explained in 4.3.1.1 paragraph.

4.3.2.2 GS-M composite under tensile loading

These coupons are made by galvanized steel textile and mineral-cementitious mortar. The stress-strain curves derived from the tensile tests of these GS-M specimens, are characterised by an initial linear-elastic response (Figure 4.13b), with an average value of Young's modulus of 1718.02 kN/mm^2 (Table 4.13), and a little contribution of mortar to tensile strength. After this first phase, mortar cracking starts in the second stage of the test: cracks are distributed to their full length. It can be underlined that for this typology of mineral-cementitious mortar, second stage is shorter than other reinforcements, because of its mechanical properties decreasing during curing, due to high adsorption rate of water in masonry. This is the reason why the strengthening system with mineral-cementitious mortar is preferable to be applied on concrete substrate, given that the concrete has a low absorption rate, which does not result in any loss of mechanical properties [De Santis et al. 2017]. The third stage has a Young's modulus almost similar to steel one, under tensile test. Just reached maximum strength in the cords, they break and then test finishes.

4.3.2.3 GS-M-BMAS shear bond performance

The stress-slip curves, resulting from the shear bond tests of GS-M strengthening system on masonry substrate, are characterised by a first linear branch up to a strength value corresponding to a failure in the mortar. Then, the load increases until detachment of the strengthening system occurs at the interface between reinforcement and substrate (failure mode A), combined with debonding within the substrate (failure mode B). The exploitation ratio related to the tensile strength of the textile (of the composite) is about 77% (73%) (Table 4.15). After comparing GS-G-BMAS and GS-M-BMAS behaviour, it is very clear the dependence of the results on the mechanical properties of the mortar. Both types of specimens were made in the same construction technique, stored under the same curing conditions and carried out using the same test setup. The mortar is the only difference: in GS-G a lime based mortar is used and in GS-M a mineral-cementitious one. In brickwork reinforced with mineral-cementitious mortar the failure mode is characterized by a combination of

“A” and “B” modes (Table 4.16). The corresponding exploitation ratios with composite materials coupons performance under tensile test are 88% (GS-G) (Table 4.10) and 73% (GS-M) (Table 4.15). In the other hand, in lime base mortar reinforcement, wherein the failure occurs with the rupture of the textile, the exploitation ratio value with respect to textile σ_b/σ_t is 95% compared to 77% about mineral-cementitious base one.

Therefore, from these results, it is highlighted that when the mortar is stiffer, a cohesive debonding process involving the substrate occurs, due to stress concentrations. Contrary, the more ductile mortar ensures a uniform transfer of stress from the reinforcement to the substrate, more or less according with the research data published about FRP.

Table 4.12. GS series

GS series	Peak stress	Peak strain	Young's modulus
	σ_t	$\varepsilon(\sigma_t)$	E
	N/mm ²	%	kN/mm ²
01	3213.60	2.34	176.00
02	3190.70	2.20	183.10
03	3188.90	2.19	181.10
04	3209.90	2.26	182.20
05	3197.80	2.17	183.10
Average	3200.18	2.23	181.10
St. dev.	11.15	0.07	2.97
CoV [%]	0.35	3.09	1.64

Table 4.13. GS-M series

GS-M series	Peak stress	Peak strain	Young's modulus		
	σ_c	$\varepsilon(\sigma_c)$	E _I	E _{II}	E _{III}
	N/mm ²	%	kN/mm ²		
01	3528.28	1.88	1561.60	168.10	194.25
02	3121.94	1.92	1943.20	93.00	195.44
03	3375.17	1.86	1670.40	129.40	178.84
04	3298.41	1.74	1290.20	107.90	186.52
05	3501.23	2.10	2124.70	97.50	175.46
Average	3365.01	1.90	1718.02	119.18	186.10
St. dev.	164.95	0.13	326.29	30.74	8.94
CoV [%]	4.90	6.86	18.99	25.79	4.80

Table 4.14. GS-M failure modes






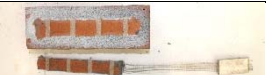




Specimen	Failure mode image	Failure mode typology
GS-M-01		A
GS-M-02		A-B
GS-M-03		A-B
GS-M-04		A-B
GS-M-05		A

Table 4.15. GS-M-BMAS series

	Peak stress	Peak strain	Exploitation ratio		Peak slip
GS-M-BMAS series	σ_b	$\varepsilon(\sigma_b)$	σ_b/σ_c	σ_b/σ_t	$s(\sigma_b)$
	N/mm ²	%	-	-	mm
01	2049.40	1.52	0.61	0.64	1.69
02	2327.11	1.63	0.69	0.73	2.69
03	2366.79	4.15	0.70	0.74	2.73
04	2809.94	3.48	0.84	0.88	1.73
05	2790.33	2.64	0.83	0.87	2.31
Average	2468.71	2.68	0.73	0.77	2.23
St. dev.	326.40	1.14	0.10	0.10	0.50
CoV [%]	13.22	42.60	13.22	13.22	22.53

Table 4.16. GS-M-BMAS failure modes

Specimen	Failure mode image	Failure mode typology
GS-M-BMAS-01		B-A
GS-M-BMAS-02		B-A
GS-M-BMAS-03		A-C
GS-M-BMAS-04		F
GS-M-BMAS-05		B-A

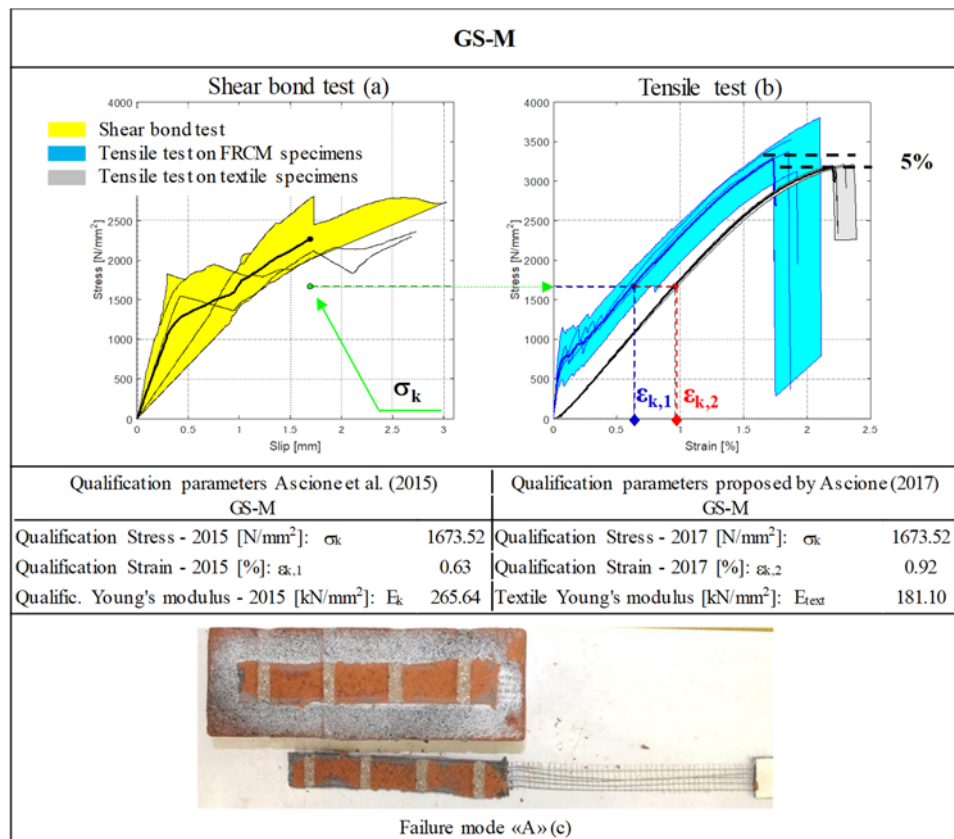


Figure 4.13. Qualification procedures GS-M

4.3.3 SS-L system (*stainless steel and lime mortar*)

4.3.3.1 SS Steel textile

Stress-strain curves are characterized by a first linear-elastic branch (Figure 4.14b), with a Young's modulus average value of 131.32 kN/mm^2 ; after this, the curve gets plateau in the hardening steel phase. Main stress value is 2083.89 N/mm^2 , corresponding to a strain value of 2.29% (Table 4.17). Just reached the maximum value of stress, one by one wires, making 13 ropes of the specimen, start to fail up to stress getting to zero.

4.3.3.2 SS-L composite under tensile loading

The SS-L specimens show, under tensile test, an initial elastic behaviour (Figure 4.14b) with Young's modulus of 547.54 kN/mm^2 (Table 4.18), which is the slope at I stage of this composite material. In this first phase, there is a small contribute of mortar to tensile behaviour. Just achieved maximum value of mortar tensile strength, cracking develops corresponding the second stage. Then, in the last and third stage, all cracks occur and in this case the stiffness is similar to steel textile one.

Just after peak value of strength, 13 ropes fail and the test finishes. In this case, in all the specimens, failure pattern evolves along to their full length, than other strengthening systems. As result, just steel tensile basically contributes to tensile strength. Indeed peak values of strength are very similar to textile tensile test ones.

In conclusion and as reported in Table 4.18, all tests were characterised by a first stage that ends in a very high value, a second stage during which seven to eleven cracks occurred and finally by a third stage, in which only the steel textile is working and provides the tensile strength results. The Young's modulus at the third stage (177.78 kN/mm^2) is very close to that of steel textile (131.32 kN/mm^2), as shown in Table 4.17.

4.3.3.3 SS-L-BMAS shear bond performance

Stress-slip curves in SS-L-BMAS shear bond tests show a first linear phase (Figure 4.14a); the maximum value of mean curve is 1169.19 N/mm^2 , corresponding a slip value of 3.40mm and a strain value of 0.97% (Table 4.20). Failure mode is "D" type in all the specimens, wherein textile sliding occurs inside the mortar (Table 4.21).

Just achievement maximum strength value, residual friction behaviour between steel and mortar is recorded.

Table 4.17. SS series

SS series	Peak stress	Peak strain	Young's modulus
	σ_t	$\varepsilon(\sigma_t)$	E
	N/mm ²	%	kN/mm ²
01	2110.50	2.65	138.20
02	2036.60	2.16	94.10
03	1833.06	2.02	108.40
04	2366.41	2.43	163.80
05	2072.90	2.18	152.10
Average	2083.89	2.29	131.32
St. dev.	190.92	0.25	29.35
CoV [%]	9.16	10.95	22.35

Table 4.18. SS-L series

SS-L series	Peak stress	Peak strain	Young's modulus		
	σ_c	$\varepsilon(\sigma_c)$	E _I	E _{II}	E _{III}
	N/mm ²	%	kN/mm ²		
01	2474.96	1.95	556.10	15.80	174.40
02	2416.66	1.75	692.60	-	181.70
03	2369.88	1.57	504.90	-	184.20
04	2581.96	1.90	492.00	-	170.80
05	2398.41	1.70	492.10	29.50	177.81
Average	2448.37	1.77	547.54	22.65	177.78
St. dev.	83.99	0.15	85.28	9.69	5.40
CoV [%]	3.43	8.67	15.58	42.77	3.04

Table 4.19. SS-L failure modes

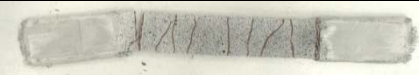









Specimen	Failure mode image	Failure mode typology
SS-L-01		A-B
SS-L-02		A-B
SS-L-03		A
SS-L-04		A
SS-L-05		A

Table 4.20. SS-L-BMAS series

SS-L-BMAS series	Peak stress	Peak strain	Exploitation ratio		Peak slip
	σ_b	$\varepsilon(\sigma_b)$	σ_b/σ_c	σ_b/σ_t	$s(\sigma_b)$
	N/mm ²	%	-	-	mm
01	1113.73	0.62	0.45	0.53	3.15
02	1312.64	-	0.54	0.63	3.70
03	1206.19	1.24	0.49	0.58	3.38
04	1031.81	1.04	0.42	0.50	3.66
05	1181.58	-	0.48	0.57	3.11
Average	1169.19	0.97	0.48	0.56	3.40
St. dev.	104.94	0.32	0.04	0.05	0.28
CoV [%]	8.98	32.96	8.98	8.98	8.12

Table 4.21. SS-L-BMAS failure modes

Specimen	Failure mode image	Failure mode typology
SS-L-BMAS-01		D
SS-L-BMAS-02		D
SS-L-BMAS-03		D
SS-L-BMAS-04		D
SS-L-BMAS-05		D

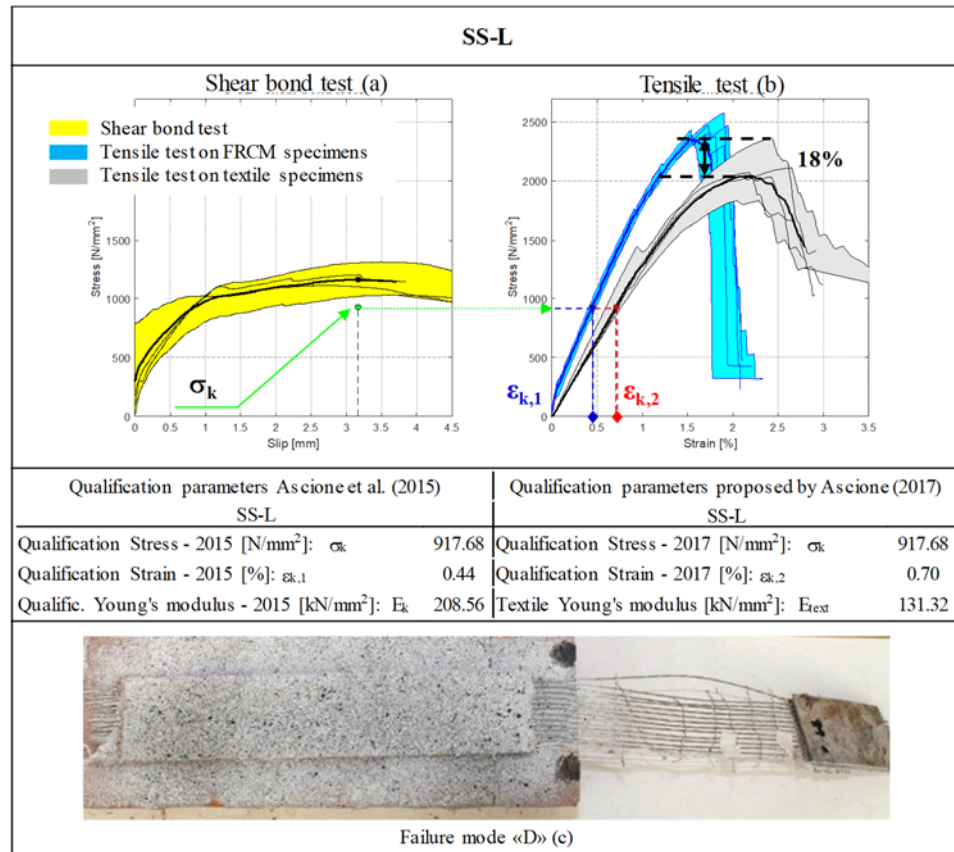


Figure 4.14. Qualification procedures SS-L

4.4 FAILURE BOND ANALYTICAL PROCEDURE FOR SRG STRENGTHENING SYSTEM-TO-MASONRY SUBSTRATE

According to Italian Guidelines CNR DT-200, theoretical debonding load (F_b) is calculated for Steel Reinforced Grout, thanks to experimental results from our department activities and available in literature as well [De Santis et al. 2017a]. The procedure followed in the literature [Napoli et al., 2016] was adopted in this study, considering conditions which depend on where the failure takes place. According to the “Design by testing” approach recommended by the Annex D of Eurocode 0, k_g coefficient provided for SRG is calibrated. Therefore, for this reason, formula published in CNR DT-200 R1/2013 (4.1), regarding FRP, is modified in order to respect SRG debonding characteristics. Nevertheless, for SRG tests which present a failure mode “A”, FRP formula is used, because failure happens in substrate. On the other hand, for textile rupture (“E”, “F” failure modes), “ α ” percentage of voids index is 100, because failure occurs out of the reinforcement, not depending on influence of adhesion corresponding to the interface mortar-textile, as usual in failure mode “C”.

FRP (CNR DT-200 R1/2013)

$$F_b = b_f \cdot \sqrt{2 \cdot E_f \cdot t_f \cdot k_b \cdot k_g \cdot \sqrt{f_{cs} \cdot f_{ts}}} \quad (4.1)$$

$$k_b = \sqrt{\frac{2 - \frac{b_f}{b}}{1 + \frac{b_f}{b}}} \geq 1 \quad (4.2)$$

$$F_b = \sqrt{\overset{\text{FRCM}}{E_f \cdot t_f \cdot \Gamma_f}} \quad (4.3)$$

$$\Gamma_f = \alpha \cdot k_g \cdot \sqrt{f_{cm} \cdot f_{tm}} \quad (4.4)$$

where:

F_b = failure bond strength

b_f = width of reinforcement (1, where failure doesn't happen in the substrate)

b = width of substrate

E_f = modulus of elasticity of reinforcement

t_f = equivalent thickness

k_b = geometrical coefficient (dimensionless value)

k_g = coefficient to be calibrated (with the dimensions of a length)

Γ_f = specific fracture energy

α = voids area, where matrix crosses textile

f_{cm} =compression strength of mortar

f_{tm} = tensile strength of mortar

$f_{c,s}$ =compression strength of substrate (18.5 N/mm² [Napoli et al., 2016])

$f_{t,s}$ = tensile strength of substrate (1.88 N/mm² [Napoli et al., 2016]).

In this calibration procedure, substrate mechanical characteristics are used when failure mode occurred in substrate (“A”, “A-B” and “A-C”).

Finally, considering SRG-to-masonry bond behaviour, thanks to experimental results from tests just above collected in this work, and others available from scientific literature, as reported in Table 4.22 [De Santis et al., 2017a], the average value of k_g coefficient, for each laboratory is calibrated for determination of bond strength (Table 4.23, Table 4.24, Table 4.25).

F_{th} is theoretical values of debonding load, evaluated for $k_g = 1$.

Though different laboratories, k_g values result very similar for each system (Table 4.26).

Table 4.22. Experimental data for mortar properties characterization
[De Santis et al., 2017a]

Mortar type	Label	f_{cm} [N/mm ²]	E_{cm} [kN/mm ²]	f_{tm} [N/mm ²]
Lime and geopolymer	G	20.60	11.42	5.42
Cement (mineral)	M	56.3	22.01	10.31
Lime	L	6.40	6.31	1.24
Fiber reinforced cement mortar	F	22.7	10.0 ^a	11.2

^a = Data Sheet

where:

f_{cm} = compressive strength

E_{cm} = Young’s modulus

f_{tm} = tensile strength

[illegible]

Table 4.24. GS-M – SS-L series

Specimen	F _b [N/mm]	FM	%voids	Ef [N/mm ²]	t _f [mm]	k _b [-]	k _g [mm]	f _{cm} [N/mm ²]	f _{tm} [N/mm ²]	F _{th} [N/mm]	k _g [mm]
GS-M-BOL-1	140.3	B-A ^s	100	186500	0.084	1.35	1	18.5	1.88	4994.515182	
GS-M-BOL-2	183.5	B-A ^s	100	186500	0.084	1.35	1	18.5	1.88	4994.515182	
GS-M-BOL-3	200.9	C	90	186500	0.084	1	1	56.3	10.31	8242.464374	
GS-M-BOL-4	197.9	B-C ^s	100	186500	0.084	1	1	18.5	1.88	4298.594249	
GS-M-BOL-5	175.9	B-A ^s	100	186500	0.084	1.35	1	18.5	1.88	4994.515182	
Average	179.7										0.000962369
CV	13.50%										
GS-M-RM3-1	170.1	B-A ^s	100	186500	0.084	1.35	1	18.5	1.88	4994.515182	
GS-M-RM3-2	193.1	B-A ^s	100	186500	0.084	1.35	1	18.5	1.88	4994.515182	
GS-M-RM3-3	198.4	A-C ^s	90	186500	0.084	1.35	1	18.5	1.88	4738.213135	
GS-M-RM3-4	235.9	F	100	186500	0.084	1.35	1	56.3	10.31	10094.91597	
GS-M-RM3-5	234.3	B-A ^s	100	186500	0.084	1.35	1	18.5	1.88	4994.515182	
Average	206.36										0.001002104
CV	13.70%										
SS-L-RM3-1	209.4	D	77	129700	0.188	1	1	6.4	1.24	3252.442953	
SS-L-RM3-2	246.8	D	77	129700	0.188	1	1	6.4	1.24	3252.442953	
SS-L-RM3-3	226.8	D	77	129700	0.188	1	1	6.4	1.24	3252.442953	
SS-L-RM3-4	194	D	77	129700	0.188	1	1	6.4	1.24	3252.442953	
SS-L-RM3-5	222.1	D	77	129700	0.188	1	1	6.4	1.24	3252.442953	
Average	219.82										0.004567884
CV	9.00%										

^s = substrate mechanical characteristics

Table 4.25. R-F series

[illegible]

Table 4.26. k_g coefficient calibrated for SRG strengthening system

SRG Strengthening system	k_g
GS-G BOL	0.00186
GS-G RM3 1/5*	0.00199
GS-G RM3 6/10**	0.00174
GS-M BOL	0.00096
GS-M RM3	0.0010
SS-L RM3	0.00456
R-F CH	0.00023
R-F NA	0.00029
R-F SAN	0.00029

*=specimens made by supplier with a 40mm of mortar width and five cords

**=specimens made in Roma Tre University Laboratories with a 50mm of mortar width and seven cords.

Where:

GS-G BOL = composite materials made by galvanized steel and lime with geopolymer binders mortar and tested in Bologna (BOL) University Laboratories

GS-G RM3 = composite materials made by galvanized steel and lime with geopolymer binders mortar and tested in Roma Tre (RM3) University Laboratories

GS-M BOL = composite materials made by galvanized steel and mineral mortar and tested in Bologna (BOL) University Laboratories

GS-M RM3 = composite materials made by galvanized steel and mineral mortar and tested in Roma Tre (RM3) University Laboratories

SS-L RM3 = composite materials made by stainless steel and lime mortar and tested in Roma Tre (RM3) University Laboratories

R-F CH = composite materials made by stainless steel ropes and fibre-reinforced cement mortar with polymeric additives and tested in Chieti (CH) University Laboratories

R-F NA = composite materials made by stainless steel ropes and fibre-reinforced cement mortar with polymeric additives and tested in Napoli-Federico II (NA) University Laboratories

R-F SAN = composite materials made by stainless steel ropes and fibre-reinforced cement mortar with polymeric additives and tested in Sannio (SA) University Laboratories

4.5 COMPARISON BETWEEN SRG AND FRCM SYSTEMS

According to the same procedure, as well as just reported above in this Chapter for SRG strengthening systems, experimental results on FRCM systems are collected. These FRCM consist of six textiles, as reinforcements and three mortar matrices, matched one to each other according to supplier recommendations. Morphological and geometrical properties for textiles are collected, in Table 4.29 (pictures) and Table 4.27 (Data sheets). At the same time, ones for mortars are described in Table 4.30 and Table 4.28 (Data sheets).

Regarding FRCM (Table 4.31), performances are analysed in the following paragraph, in terms of mechanical characteristics and by means of qualification procedures.

These systems are nominated in accordance with labels applied on SRG.

Table 4.27. Textiles properties (Data sheets)

Textile	Label	γ (Surface mass density)	t (Design tickness)	Grid spacing	Notes
		[g/m ²]	[mm]	[mm]	
Basalt	B	250.00	0.0580	25x25	Coated
Carbon	C20	170.00	0.0470	20x20	Coated
Carbon	C10	168.00	0.0470	10x10	Dry
Glass	G	250.00	0.0470	25x25	Coated
Aramid Glass	AG	250.00	0.0300	15x18	Coated
PBO	P	44.00	0.0140	15x15	Dry

Table 4.28. Mortars properties (Data sheets)

Mortar type	Label	μ	f_{cm}	E_{cm}	f_{tm}
		[-]	[N/mm ²]	[kN/mm ²]	[N/mm ²]
Geopolymer	C	Classe I SD<5m	>55	25.00	10.00
Fabric reinforced cement with polymeric additives	CC	n.a.*	>20	7.00	3.50
Fabric reinforced cement with polymeric additives	CM	n.a.*	20.00	7.50	3.50

* = not available

Table 4.29. Textiles description

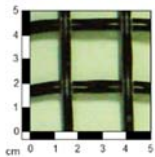
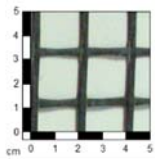
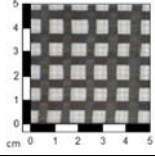
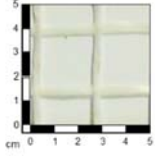
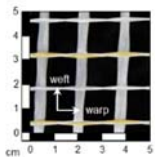
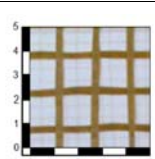
Textile	Label	Image	Description
Basalt	B		This textile B comprises basalt fabrics produced by melting and spinning volcanic rocks, with a coating for improving the adhesion to the matrix, arranged in a bidirectional and balanced grid 25mm spaced.
Carbon	C20		C20 is a bidirectional and balanced carbon fabrics made of coated bundles, with 20mm spacing. The design thickness is 0.047mm.
Carbon	C10		C10 comprises bundles of dry carbon fabrics with a mesh grid of 10 mmX10 mm and a design thickness of 0.047mm.
Glass	W		The W textile is made of Alkali-Resistant glass fabrics arranged in a bidirectional grid 25mm spaced in both directions.
Aramid-Glass	AG		The AG textile is characterized by Alkali-Resistant glass fabrics in weft direction (spacing 18mm), and glass and aramid fabrics in warp direction (spacing 15mm). AG textile is tested in the main (warp) direction.
PBO	P		The PBO textile comprises a bidirectional balanced polyparaphenylene benzobisoxazole (PBO) fabrics with 15mm spacing(in weft and warp directions), 0.014 mm design thickness and a density of 44 g/m ² .

Table 4.30. Mortar matrices description

Mortar	Label	Description
Cementitious	C	This is a geopolymer mortar with natural kaolin and bauxite binders; it is characterized by 56.3N/mm ² compressive strength, 22.01kN/mm ² Young's modulus and 10.30N/mm ² tensile strength.
Cementitious	CC	The "CC" cementitious mortar is reinforced by short fabrics. It is used for concrete(c) substrate. Its compressive strength f_c and flexural tensile strength f_t are equal to 20kN/mm ² , Young's modulus is 7.0kN/mm ² and 3.5N/mm ² , respectively.
Cementitious	CM	The "CM" cementitious mortar is reinforced by short fabrics. It is used for masonry(m) substrate. Its compressive strength f_c and flexural tensile strength f_t are equal to 20N/mm ² , Young's modulus is 7.5kN/mm ² and 3.5N/mm ² , respectively.

Table 4.31. Strengthening systems description

Supplier and Composite (textile & mortar)	Name
4_ BASALT mesh and LIME mortar	B and L
5_ CARBON mesh and CEMENT mortar	C20 and C
6_ CARBON mesh and CEMENT mortar	C10 and CC
7_ GLASS mesh and LIME mortar	W and L
8_ GLASS-ARAMID mesh and LIME mortar	AG and G
9_ PBO mesh and CEMENT mortar	P and CM
Substrate: Brick MASonry	add –BMAS

4.5.1 B-L system (basalt and lime mortar)

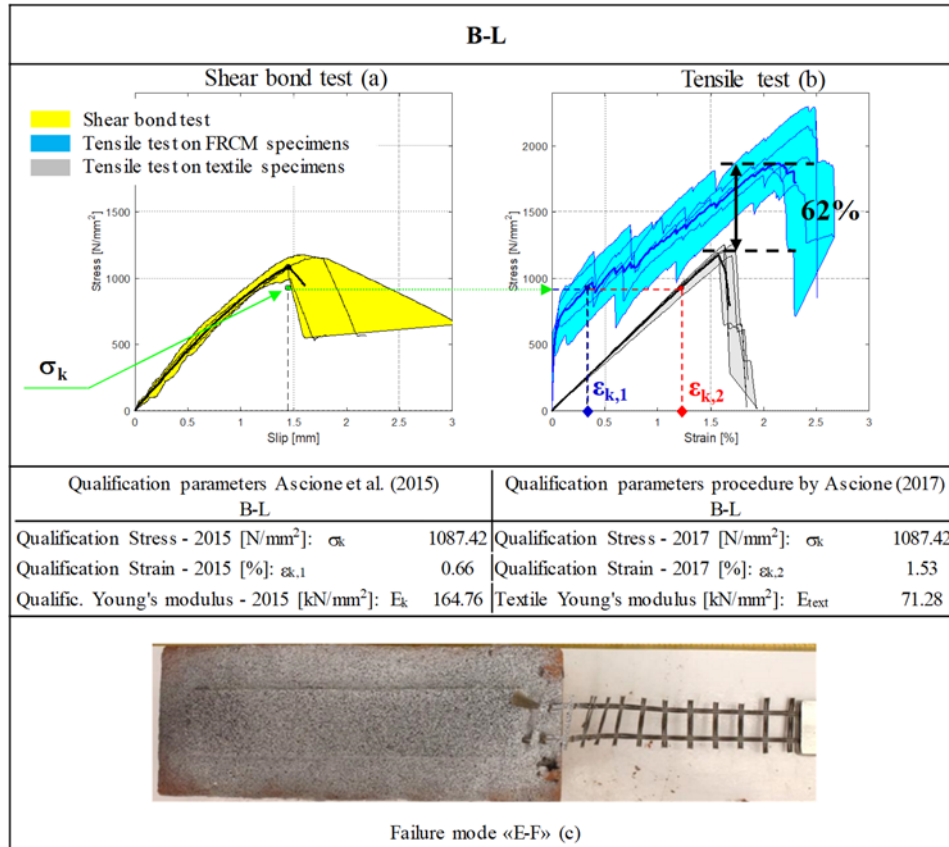


Figure 4.15. Qualification procedures B-L

The response of the basalt textile displays a linear elastic behaviour until failure (Figure 4.15b), which occurs near the gripping areas, due to the stress concentration. The stress-strain curve of B-L composite (Figure 4.15b) shows a first linear elastic branch, with uncracked mortar and a Young's modulus of 1598.52kN/mm². The second branch displays several jumps associated to cracking. In the third stage, just finished cracking develop, it shows an overall tangential stiffness similar to that dry textile one (74kN/mm²). However, matrix provides a significant contribution to the maximum stress, which entails a mortar to textile load transfer across the cracks and a redistribution of the stress among the fabrics. Regarding shear-bond tests (Figure 4.15a), all the specimens present a similar failure mode, consisting in the tensile rupture of one yarn in the unbonded portion of the textile, followed by the rupture of the second yarn within the matrix.

4.5.2 C20-C system (carbon and cementitious mortar)

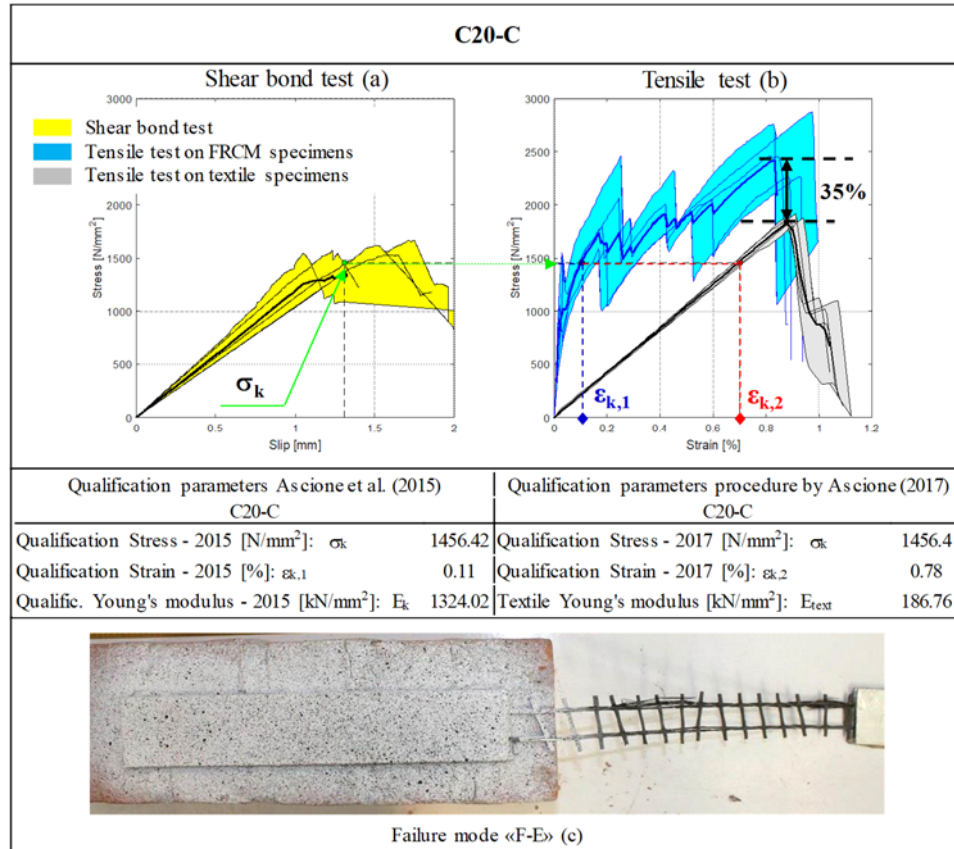


Figure 4.16. Qualification procedures C20-C

C20 textile displays a linear-brittle behaviour (Figure 4.16b) and the presence of the coating partially prevents the rupture of the wires in several different points. The mean value of the peak stress is 1876.4 N/mm^2 and that of the Young's modulus is 186.8 kN/mm^2 . The mortar matrix has a strong incidence on the tensile behaviour of the C20-C system (Figure 4.16b). The peak stress is 2525.6 N/mm^2 and the Young's modulus is 199.4 kN/mm^2 . In shear bond tests (Figure 4.16a), failure occurred by the tensile rupture of the textile out of the bonded area, or within the matrix close to loaded end, with a maximum mean stress of 1587.6 N/mm^2 . This indicates that the tensile strength of the textile is lower than the reinforcement-to-substrate shear bond strength, even if the values of the exploitation ratios (σ_b/σ_c and σ_b/σ_t) (Table 4.34), lower than one, suggest that this rupture is associated to a non-uniform load distribution among the fabric bundles.

4.5.3 C10-CC system (carbon and cementitious mortar)

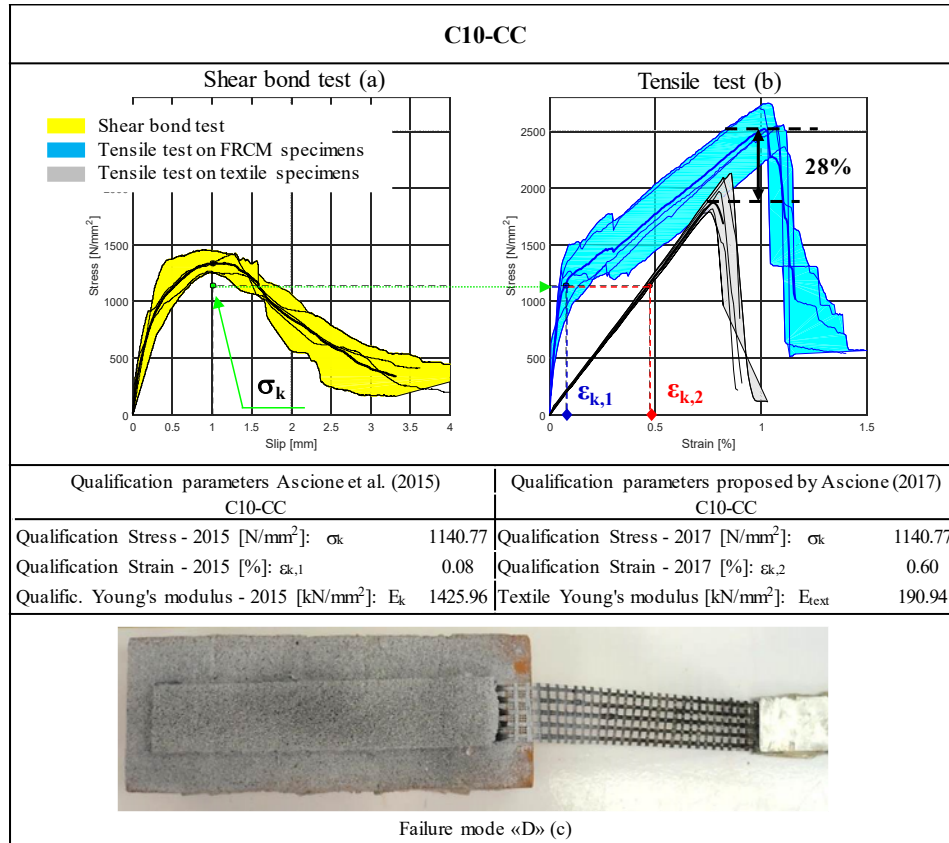


Figure 4.17. Qualification procedures C10-CC

The tensile behaviour of C10 textile is characterized by a linear response up to the brittle failure (Figure 4.17b), which occurs by the rupture of the individual carbon wires in different points, such that it is not possible to identify a unique rupture section of the specimen. The mean value of the peak stress is 1964.6 N/mm^2 . The response of the composite clearly shows the important contribution of the mortar matrix in the initial (uncracked) stage (which may be easily expected), but also after the crack pattern has completely stabilized (Figure 4.17b). The peak stress is 2509.26 N/mm^2 . In shear bond tests, failure occurs by the slippage of the textile out of bonded area, with a maximum mean stress of 1360.12 N/mm^2 , followed by a progressive reduction of the load during progressive slippage (Figure 4.17a).

4.5.4 W-L system (glass and lime mortar)

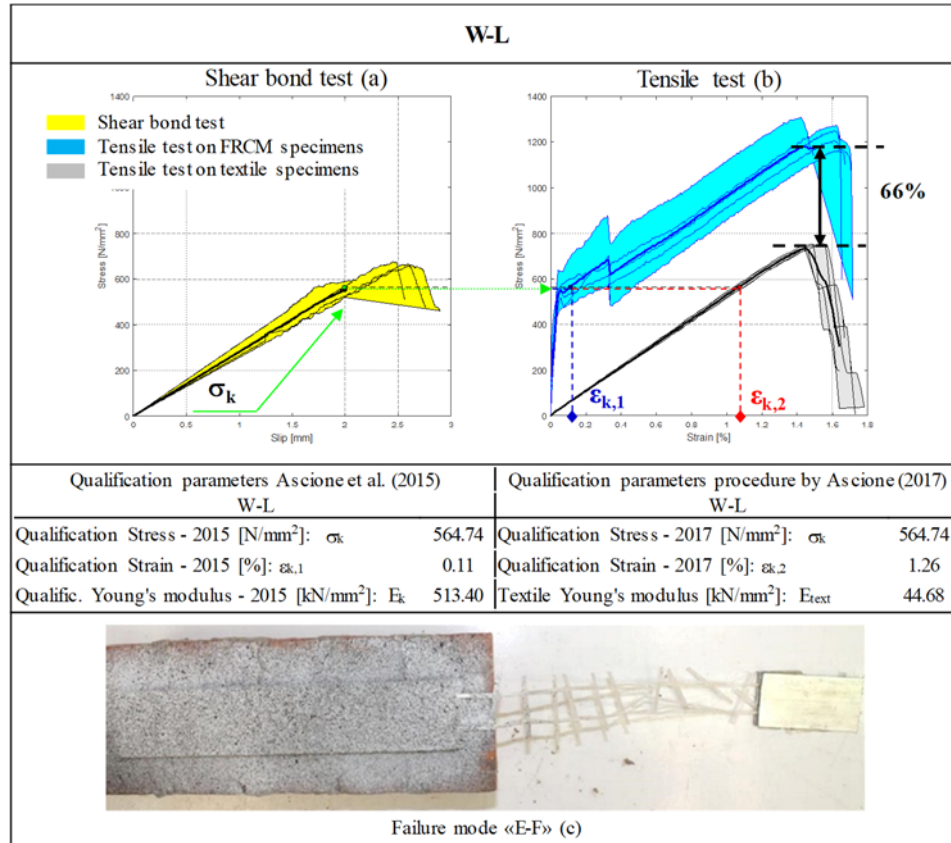


Figure 4.18. Qualification procedures W-L

A linear elastic branch up to failure (Figure 4.18b) characterizes the stress-strain behaviour of the glass textile. The average Young's modulus is 44.7 kN/mm^2 and the average strength 747 N/mm^2 . The W-L specimens display an initial elastic behaviour (Figure 4.18b) with Young's modulus of 1592 kN/mm^2 , until the appearance of the first crack in the matrix. By comparing the results of direct tensile tests, it clearly appears that the mortar, although cracked, provided a significant contribution (67%) to the tensile strength of the composite. Shear bond tests (Figure 4.18a) on W-L composites show the rupture of a yarn out of the bonded area (Figure 4.18c), followed by that of the other yarn within the mortar matrix. The exploitation ratio σ_b/σ_t is almost 90%, indicating that the bond strength is higher than the tensile strength of the textile. However, the exploitation ratio σ_c/σ_t is about 50% (Table 4.34). This difference is because the unbounded textile is not embedded into the matrix.

4.5.5 AG-G system (aramid glass and lime with geopolymer binders mortar)

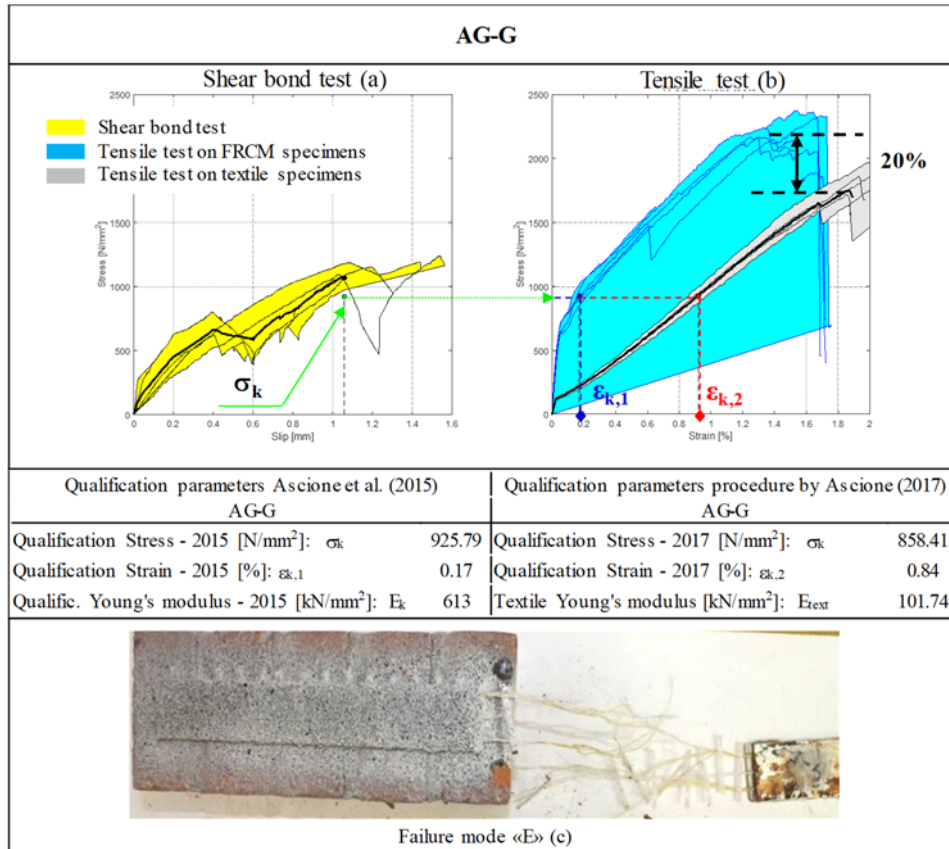


Figure 4.19. Qualification procedures AG-G

The behaviour of Aramid-Glass textile is linear elastic up to failure (Figure 4.19b). In this case, a telescopic failure occurred at the same time in all the yarns. In glass-aramid composites, the stress-strain curve shows a first linear elastic stage (Figure 4.19b), with Young's modulus of 1420.7kN/mm², before the opening of cracks in the matrix. The failure mode is the same in all the specimens, with a single main crack near the gripping area. The failure modes, in shear bond tests, are similar in all specimens: after an initial nonlinear branch (Figure 4.19a), all of the three yarns of the glass fabrics fails in the unbonded region (Figure 4.19c). At that stage, however, aramid fabrics are still capable of sustaining the load, therefore, after a slight decrease in the stress-slip curve, the load increased up to the failure of aramid yarns. The exploitation ratio related to the tensile strength of the textile (of the composite) is about 60% (50%) (Table 4.34).

4.5.6 P-CM system (PBO and cementitious mortar)

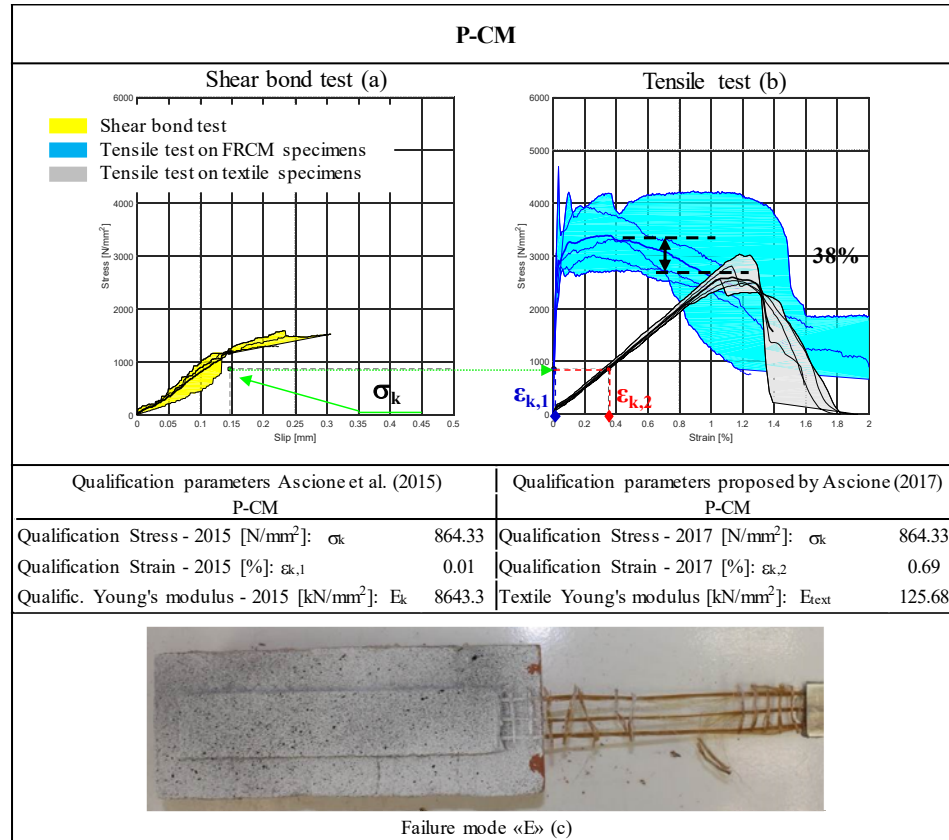


Figure 4.20. Qualification procedures P-CM

Stress-strain curves of PBO textile under tensile test show a first linear-elastic (Figure 4.20b) behaviour with a Young's modulus of 125.68 kN/mm^2 . Just achieved maximum value of strength, telescopic failure occurs in PBO yarns, in grips area, because of stress concentration, due to Araldite stiffness. Regarding the coupon tests, cementitious mortar matrix has a strong influence on the tensile behaviour of the P-CM: stress-strain curves are characterized by an initial linear-elastic (uncracked) stage up to mortar failure development (Figure 4.20b), with a very high value of the slope, about 8940 kN/mm^2 . Therefore, PBO system has an average value of tensile Young's modulus greater than other strengthening systems, due to short fabrics, inside mortar, increasing tensile stiffness and strength. The second stage, in this case, is undetectable as shown by only one crack in the specimens. Third stage has a Young's modulus value smaller than

the first one: just arrived maximum value of strength, textile cracks and starts sliding phenomena, corresponding to stress-strain curves decreasing. Telescopic failure [D'Antino et al., 2014] happens in the mortar: it can underline an attritive residual behaviour in the curves, due to this sliding. In shear bond tests (Figure 4.20a), failure occurs by the tensile rupture of the textile out of the bonded area with a peak value of mean stress of 1596.54N/mm^2 , corresponding a slip value of 0.25mm . Failure mode always results “E” typology (Figure 4.20c), with the rupture in unbonded textile and consequently textile sliding in the mortar: it can observe this phenomenon also in shear bond test curves, wherein attritive residual behaviour is observed, due to this sliding.

4.5.7 Round Robin Test results

In this paragraph, the results comparison how the SRG and FRCM are reported for each test:

1. Textile tensile test (data in Table 4.32, stress-strain in Figure 4.21)
2. Composite material specimen tensile test (data in Table 4.33, stress-strain in Figure 4.22)
3. Shear bond test (data in Table 4.34, stress-strain in Figure 4.23)

4.5.7.1 Textile tensile test

Table 4.32. Textile tensile tests results (average values)

System	Peak stress	Peak strain	Young's modulus
	σ_t	$\varepsilon(\sigma_t)$	E
	N/mm^2	%	kN/mm^2
GS	3200.18	2.23	181.1
SS	2083.89	2.29	131.32
B	1224.83	1.65	71.28
C20	1876.4	0.9	186.76
C10	1964.62	0.81	190.94
W	747.03	1.51	44.68
AG	1867.9	2.02	101.74
P	2684.66	1.14	125.68

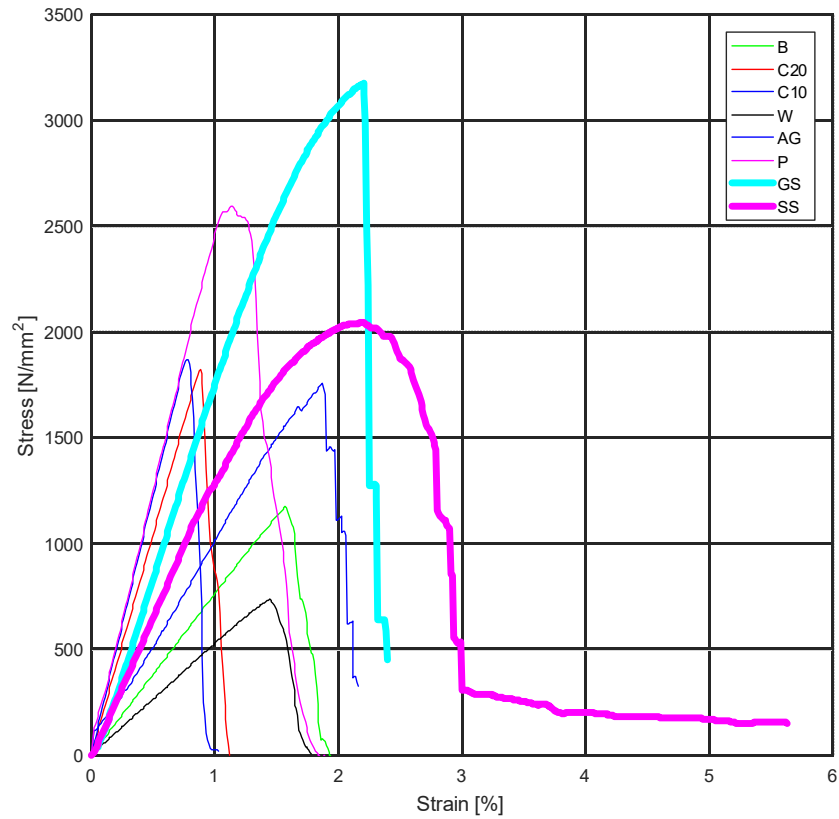


Figure 4.21. Stress-Strain graphs for textile tensile tests (average values)

It can underline from the graphs of Figure 4.21 that all textiles are characterized by a first linear behaviour up to the failure, except to SS textile (stainless steel), which presents a ductile behaviour. The highest tensile value is about galvanized steel textile (GS), achieving a value of 3200 N/mm^2 .

For the sake of completeness, in post peak branch, it can observe loss of load steps, corresponding to failure of each cord (in steel textile) or yarn (in fabric textile).

4.5.7.2 Composite material specimen tensile test

Table 4.33. FRCM tensile tests results (average values)

System	Peak stress	Peak strain	Young's modulus		
	σ_c	$\varepsilon(\sigma_c)$	E_I	E_{II}	E_{III}
	N/mm ²	%	kN/mm ²		
GS-G	3461.34	2.03	914	130.26	184.59
GS-M	3365.01	1.9	1718.02	119.18	186.1
SS-L	2448.37	1.77	547.54	22.65	177.78
B-L	1985.3	2.32	1598.52	47.76	74.31
C20-C	2525.58	0.89	5946.48	-	199.44
C10-CC	2509.26	1	1782.24	65.7	154.63
W-L	1241.7	1.58	1591.78	42.06	51.57
AG-L	2239.63	1.42	1420.7	72.3	134.29
P-CM	3694.29	0.27	8939.72	1008.94	-22.75

Comparison between all direct tensile tests on composite materials, indicates that (Figure 4.22):

-tensile behaviour of SRG assumes a three stages response [De Santis and de Felice 2015a, De Santis et al., 2017b]. Stress values of SRG, made by galvanized steel reinforcement, are higher than stainless one. Regarding other FRCM systems, except to the one realized with PBO reinforcement, all of them are also characterized with three stage behaviour: in these, cracks development (stage II) is clearly identified in stress-strain curves, but also in strain plots resulting from DIC “time laps”. For this reason, D.I.C. results are also useful because, in post processing phase, base length points can be selected on ROI (Region of Interest), comprising failures pattern. Young’s modulus at 3rd stage in composite materials is similar to textile;

-mortar contribute in SRG is lower than other FRCM system. Indeed, in SRG, mortar contribute assumes values of 5-8-18% (GS-G, GS-M, SS-L), than to, for example, 62% in B-L system (Figure 4.15b), 35% for C20-C one (Figure 4.16b) and 38% in W-L composite materials (Figure 4.18b). Last three systems are characterized by coated textile and spaced wire of 20mm. Then, mortar-interface adhesion and, accordingly, better interlocking are favoured;

-however, in SRG, mortar provides stress redistribution, allowing, even if small, final strength contribution;

-highest peak stress values are detected in GS-G system and in GS-M system because of tensile strength of galvanized steel. SS-L composite material made by stainless steel and embedded in lime mortar is characterized by a little bit lower value of strength than ones made with galvanized steel;

-results depend on manufacturing and curing phases: for this reason, adequate instruments help to make specimens. At the same time, in order to process data, it is very important increasing number of tests;

-aiming at avoiding stress concentration and premature failures, clamping method should be improved. It is necessary that mortar is gripped with enough lateral pressure, because of preventing of sliding textile.

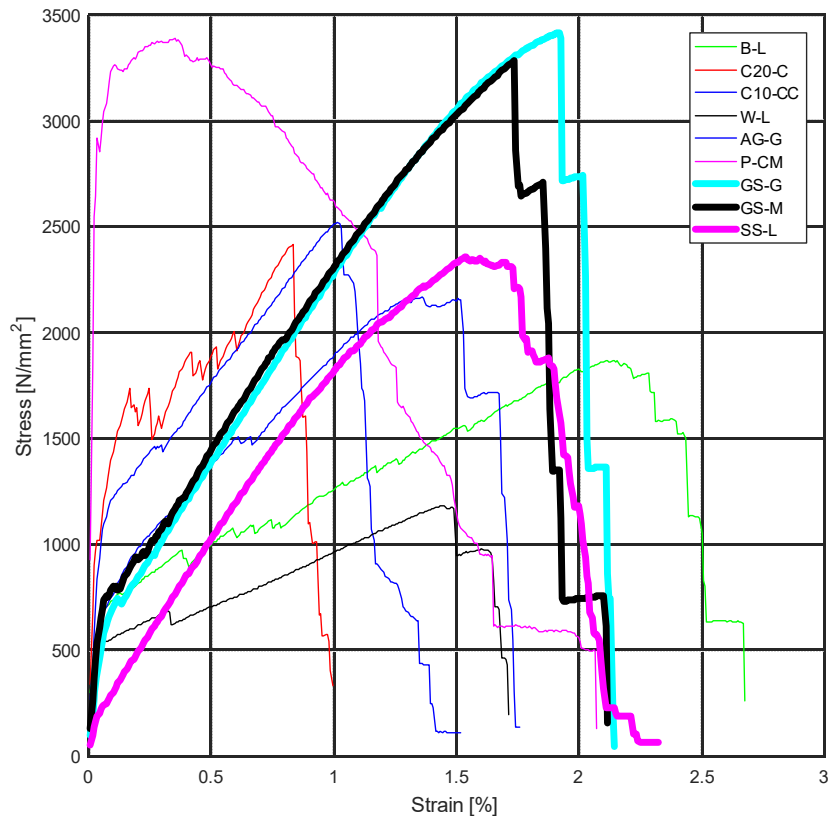


Figure 4.22. Stress-Strain graph for direct tensile test on composite material specimens (average values)

4.5.7.3 Shear bond test

Table 4.34. Shear bond tests results (average values)

System	Peak stress	Peak strain	Exploitation ratio		Peak slip
	σ_b	$\varepsilon(\sigma_b)$	σ_b/σ_c	σ_b/σ_t	$s(\sigma_b)$
	N/mm ²	%	-	-	mm
GS-G-BMAS	3032.14	3.23	0.88	0.95	2.91
GS-M-BMAS	2468.71	2.68	0.73	0.77	2.23
SS-L-BMAS	1169.19	0.97	0.48	0.56	3.4
B-L-BMAS	1117.45	2.5	0.56	0.91	1.52
C20-C-BMAS	1587.57	1.02	0.63	0.85	1.41
C10-CC-BMAS	1360.12	0.83	0.53	0.69	1.08
W-L-BMAS	644.42	2.15	0.52	0.86	2.34
AG-L-BMAS	1138.01	2.78	0.51	0.61	1.27
P-CM-BMAS	1596.54	1.53	0.43	0.59	0.25

Regarding single lap shear bond tests, outcomes indicate that (Table 4.34):
 -best bond behaviour (Figure 4.23) performances in SRG-to-masonry are detected, especially in GS-G-BMAS specimens with values in terms of tensile failure (3032.14N/mm²) and slip (2.91mm), which are higher than either steel reinforcements and FRCM;

-thanks to exploitation ratio, efficiency of the systems is expressed. In SRG systems made by galvanized steel, σ_b/σ_c and σ_b/σ_t , referring to the tensile strength of the textile and of the composite, the average values are around 80%. In particular, for GS-G efficiency is characterized by exploitation ratio values of 0.88 for σ_b/σ_c and 0.95 for σ_b/σ_t . In this case, it means that bond behaviour depends on composite and textile strength contribution and, as a results, it shows an efficient interlocking, because of spaced grid and adhesion at the interface steel-mortar (Figure 4.24);

Conversely, lower efficiency is observed in SS-L system ($\sigma_b/\sigma_c=0.48$ and $\sigma_b/\sigma_t=0.56$), associated to textile sliding (Figure 4.25);

In the other hand, in systems wherein failure happens in unbonded textile (B-L-BMAS, C-20-C-BMAS and W-L-BMAS), σ_b/σ_t value is close to 1 and, at the same time, σ_b/σ_c is half the other, because of good interlocking due to coated textile and spaced grid (just observed in direct tensile tests on FRCM coupons). For example, in Figure 4.26 the picture regarding B-L system (opening of mortar by a chisel after testing) is reported, in order to

show what happened inside the reinforcement. Bidirectional grid allows mechanical phenomenon of interlocking. Therefore, thanks to opposition of transversal fabrics against to shear direction, longitudinal fabrics are “locked” owing to cross nodes;

-it is underlined that results on bond behaviour depend on manufacturing and curing conditions. Especially in the case of specimens cast for shear bond tests, difficulties are higher because of the reinforcement application on masonry substrate.

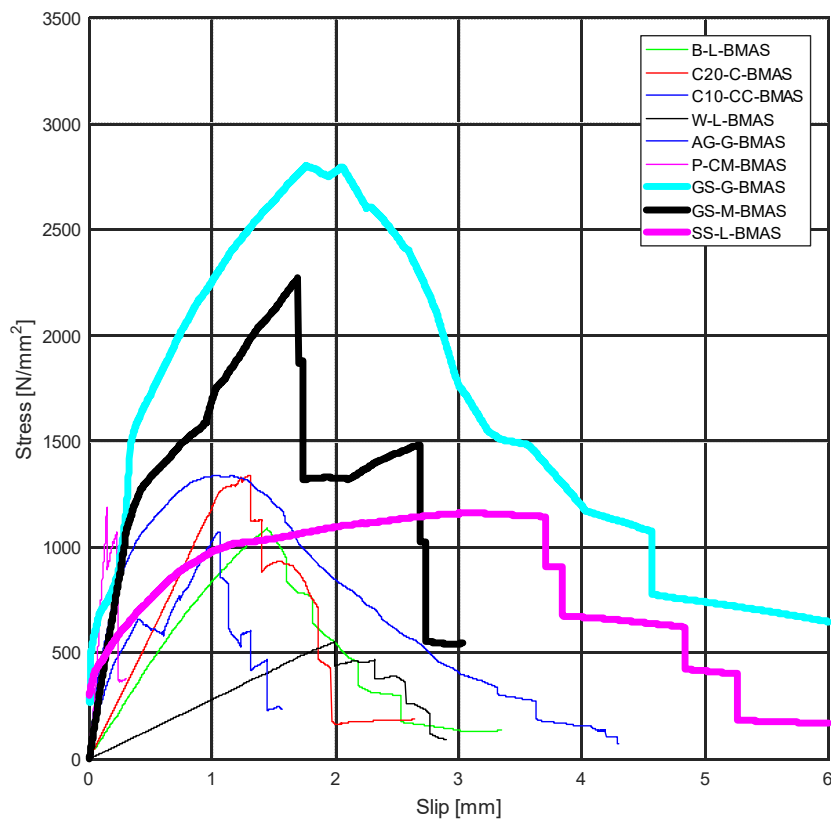


Figure 4.23. Stress-Slip graph for shear bond tests results (average values)



Figure 4.24. Focus on interlocking in GS-G system



Figure 4.25. Textile sliding in SS-L system



Figure 4.26. Focus on cross nodes in B-L system

4.5.8 Qualification procedures

Finally, in Table 4.35, qualification parameters are reported, following procedures proposed in [Ascione et al. 2015] and in “2017” one, as just above both described. In this way, in order to find out design properties and performances about these strengthening systems, it is possible obtain an overview on their behaviour, thanks to comparing results.

Table 4.35: qualification procedure comparing

System	Qualification #1 - 2015			Qualification #2 - 2017		
	σ_k	ε_{k1}	E_k	σ_k	ε_{k2}	E_{text}
	N/mm ²	%	kN/mm ²	N/mm ²	%	kN/mm ²
GS-G	2978.46	1.44	206.84	2978.46	1.64	181.10
GS-M	1673.52	0.63	265.64	1673.52	0.92	181.10
SS-L	917.68	0.44	208.56	917.68	0.70	131.32
B-L	1087.42	0.66	164.76	1087.42	1.53	71.28
C20-C	1456.42	0.11	1324.02	1456.42	0.78	186.76
C10-CC	1140.77	0.08	1425.96	1140.77	0.60	190.94
W-L	564.74	0.11	513.40	564.74	1.26	44.68
AG-G	925.79	0.17	544.58	925.79	0.91	101.74
P-CM	864.33	0.01	8643.3	864.33	0.69	125.68

In design field of civil engineer, strain is the main parameter to use. In seismic area, ductility structure behaviour is pursued than high resistance one. The reasons are due to aimed at ensuring high periods of oscillation for the building and, as a result, high displacements of themselves, enough to guarantee energy dissipation capacity.

Best parameters are detected in galvanized steel and lime mortar strengthening system (GS-G), in both qualification procedures, thanks to higher value of strain and even one of stress.

Comparing to galvanized steel systems, reinforcement made by basalt and lime presents good performances, above all in “2017” procedure, with a strain value of 1.53%, very close to GS-G one.

4.5.9 Digital Image Correlation method in FRCM mechanical characterization

Digital Image Correlation is used like contact-less measurement method to validate traditional instruments, as extensometers, potentiometers and LVDTs (linear variable differential transformer). Thanks to DIC, it can detect displacement field identification and, as a result, strain field one (such as reported in Chapter 5 and in Chapter 6 for middle-scale and full-scale test).

Basically, this innovative method results helpful to study strengthening system behaviour during test time and for post processing procedure, to analyse recorded data.

Aiming at understanding DIC advantageous, in the following Figures are collected displacements and strains development plot, obtained by means of DIC method, thanks to Ncorr software in Matlab code [Blaber et al., 2015], for tensile test on FRCM coupons (Figure 4.28) and shear bond test on the same reinforcement applied on masonry substrate (Figure 4.29).

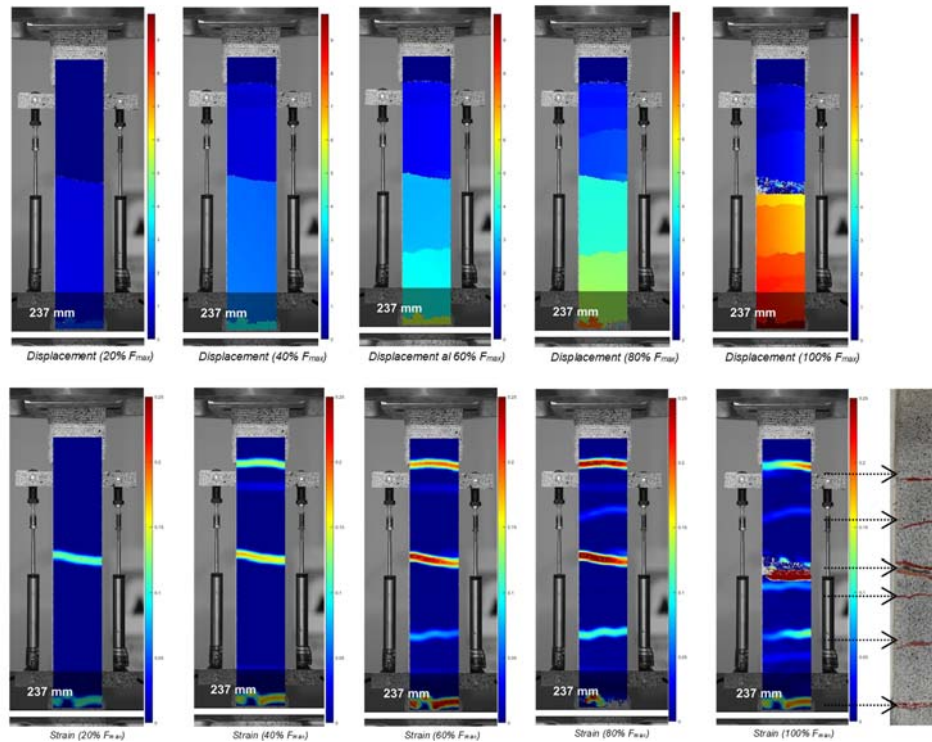


Figure 4.27. Displacements and strains development plot for coupons tensile test

It can completely match the failure pattern in the last strain plot, calculated at 100% of load, with the cracks detected in the real image of the same specimen. In this way, thanks D.I.C. contact-less method, opening failures can be studied, even the smallest ones, although(unless) using high resolution camera. Regarding shear bond test, by analysis displacement plot, it results debonding behaviour of the reinforcement applied on masonry substrate, strictly depending on load increasing: it is clear how displacement development follows the stress-transfer mechanism stages (Figure 4.30b), corresponding to different points of the idealized P - g global slip response for FRP (Figure 4.30a) [T. D'Antino et al., 2014 - Malena et al., 2014 - Carloni et al., 2015].

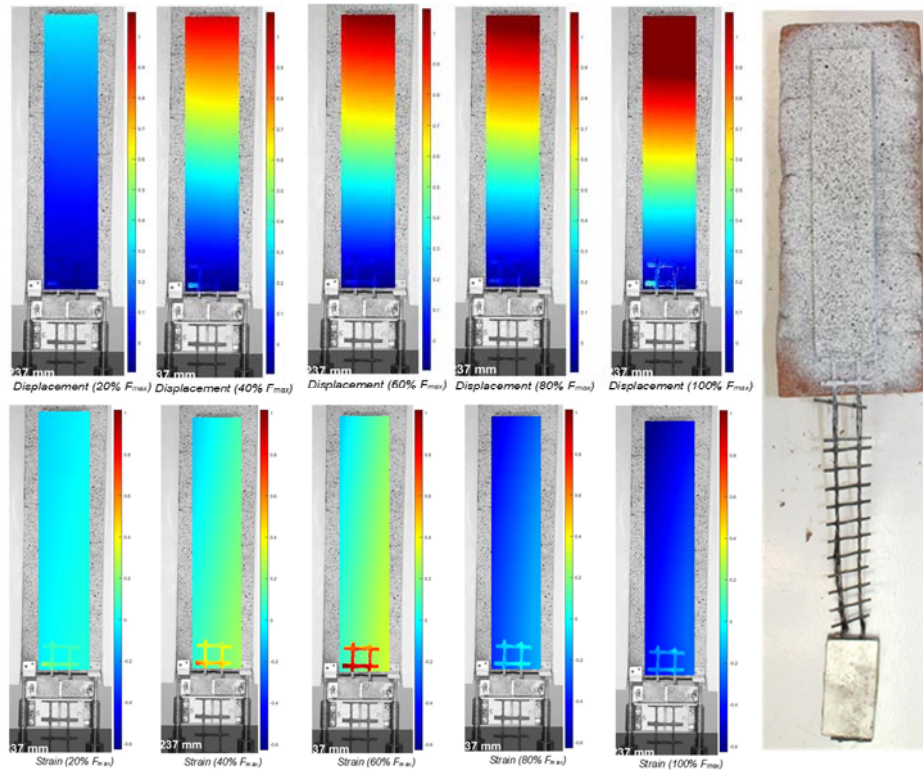


Figure 4.28. Displacements and strains development plot for shear bond test

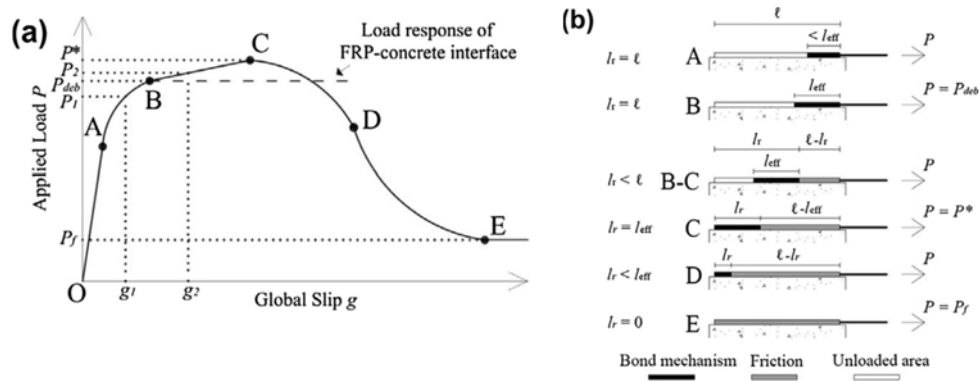


Figure 4.29. Stress-transfer mechanism stages (b), idealized $P - g$ global slip response for FRP(a)

4.6 CONCLUDING REMARKS

The mechanical characterization of Steel Reinforced Grout composites are carried out through tensile and shear bond tests.

Three SRG systems are tested and results are compared to FRCM systems ones.

The tests provided information on:

- i) textile behaviour
- ii) mortar contribution in strength and stiffness
- iii) maximum stress, corresponding slip and failure mode in shear bond test
- iv) qualification parameters
- v) Advantages and drawbacks of SRG

i) Regarding tensile test on textiles, the higher strength is recorded in galvanized steel (GS), with an average value of 3200N/mm^2 , corresponding to a peak strain of 2.23%.

Nevertheless, all curves (Figure 4.21) about direct tensile tests on textiles are characterized by a first linear behaviour up to the failure.

ii) In SRG, mortar provides stress redistribution, allowing, even if small, final strength contribution. The increase in tensile strength provided by the matrix is 5% in GS-S, 8% in GS-G and 18% in SS-L.

iii) Through exploitation ratio coefficients, it is calculated efficiency of performances in SRG-to-masonry substrate: in particular, exploitation ratio values in GS-G systems are 0.88 for σ_b/σ_c and 0.95 for σ_b/σ_t . Therefore, it means that bond behaviour depends on composite and textile strength contribution. In the other hand, values of $\sigma_b/\sigma_c=0.48$ and $\sigma_b/\sigma_t=0.56$ in SS-L system demonstrate a low effectiveness observed, associated to textile sliding (“D” failure mode).

iv) Considering qualification procedures, best parameters are detected in GS-G strengthening system with high values either of stress and strain. At the same time, because mineral-cementitious mortar are stronger than masonry, GS-M could not achieve the same parameters. Comparing with other FRCM systems, with the purpose of structural design in seismic area, B-L qualification value of strain, calculated by means of “2017” proposed accreditation procedure, is very close to GS-G system in the same procedure.

- v) Thanks to this document, it is clear how strengthening systems realized with steel reinforcements are better in terms of mechanical behaviour and design parameters. The following advantages justify SRG systems:
- ductility improving is a requirement in seismic area construction and these SRG, as above described, provide a better solution in retrofitting of existing building;
 - at the same time, steel properties also ensure shear strength;
 - the uncoated, galvanised steel offers a good interlocking with the mortar, which is also ensured by the spaced grid that makes the adhesion easier. At the other hand in strengthening system with stainless steel and lime mortar, failure bond happens by sliding textile (“D”);
 - in cultural heritage retrofitting, because of compatibility at the interface reinforcement-historical surface, increasing bond behaviour as well, application of SRG made by steel textile and lime mortar is preferred than other solutions. This is the reason why, steel and cementitious mortar systems are not employed to reinforce masonry substrates, but for concrete surface are. Therefore, these systems, like GS-M (steel textile and mineral-cementitious mortar reinforcement) one, may be suitable for modern structures and infill panels, in which vapour

permeability is not a requirement and significant values of load are expected to be transferred. Failure mode “A” in GS-M bond behaviour clearly shows it (Figure 4.27).

On the other hand, there are challenges associated with manufacturing/handling of the FRCM coupons and of masonry prisms as well as with the application of the reinforcement on the masonry support. Special care shall be taken during the preparation of the specimens, by using skilled labour, to reduce the error percentage and to minimise scatter in the experimental test results.



Figure 4.30. Detachment at the interface mortar-masonry substrate

5. SRG bond on curved masonry substrate

ABSTRACT

Steel Reinforced Grout (SRG), consisting in Ultra High Tensile Strength Steel unidirectional textile embedded into lime mortar, is an effective and cost efficient solution for the reinforcement of existing structures. Nevertheless, the existing knowledge is still insufficient for its confident in the field, especially for some applications, as those on masonry arches and vaults, despite they often need retrofitting due to their high vulnerability towards earthquakes, support displacement and asymmetric loads. One of the critical issues is the reinforcement-to-substrate bond behaviour since, if no mechanical anchors are included in the design, it rules the effectiveness of the reinforcement. This research deals with the bond behaviour of Steel Reinforced Grout applied to curved masonry substrates. Double-lap double-prism push-pull and four-point bending tests were carried out on small-scale curved masonry prisms reinforced with SRG. Aiming at investigating both intrados and extrados reinforcement solutions, the surfaces of application were either convex or concave, with different values of the curvature radius. Both the side of the masonry prism and its lower surface, provided with the SRG reinforcement, were monitored with Digital Image Correlation to detect displacements, strains, and damage development. Test results contribute to the knowledge on the SRG-to-masonry bond behaviour and could help developing design relationships for the reinforcement of masonry curved members. The work aims at contributing to the existing knowledge on the bond behaviour of mortar-based composites and to the development of standardized guidelines for shear bond tests, which are needed to improve the reliability of the mechanical parameters of the TRM systems and the safety level of reinforced structures.

5.1 INTRODUCTION

The load-bearing capacity of masonry vaults, especially that of the most slender ones, strongly depends on shape and slenderness, making them particularly vulnerable against unsymmetrical service loads, support displacements and seismic actions. Nowadays, the vaults of numerous existing structures need retrofitting works to ensure an adequate safety level according to current standard codes. To this purpose, externally bonded reinforcements with composite materials are particularly advantageous, since they provide high mechanical performances with minimum thickness and mass increase, they can be applied to curved substrates and can adapt to various shapes, and are relatively cost-efficient [Garmendia et al., 2011 - Borri and Castori, 2008 - Castori, Borri, Corradi, 2016 - Faraboschi, 2004 - Valluzzi, Valdemarca, Modena, 2016]. Mortar-based composites, named Textile Reinforced Mortars (TRM), Fabric Reinforced Cementitious Matrix (FRCM) or, when comprising steel textiles, Steel Reinforced Grout (SRG), offer better behaviour at high temperatures, relatively lower costs and easier application to wet or irregular surfaces with respect to Fibre Reinforced Polymers (FRPs), thanks to the use of an inorganic matrix in place of the epoxy resins. When the matrix is a lime-based mortar, these systems also ensure the vapour permeability, physical-chemical compatibility with the substrate, and reversibility (i.e., possibility of being removed without damage in the original substrate) that make them suitable for applications to historic masonry structures and compliant with the principles of preservation of architectural heritage [Garmendia et al., 2011 – Valluzzi et al., 2014a].

Among TRM composites, Steel Reinforced Grout, comprising Ultra High Tensile Strength Steel (UHTSS) textiles and mortar matrices, is one of the most promising solutions. A number of studies have been carried out to investigate it tensile [De Santis and De Felice, 2015a] and bond [De Santis and De Felice, 2015b - Ascione, de Felice, De Santis, 2015 - de Felice et al., 2014 - Razavizadeh, Ghiassi, Oliveira, 2014] behaviour. Nevertheless, the bond behaviour of SRG when applied to curved masonry substrates has not been properly investigated yet, despite it is crucial for the effectiveness of the strengthening work. Bond tests were carried out on concave [Malena and de Felice, 2014] or convex [De Santis and de Felice, 2016 - De Santis, 2017] masonry substrates, providing information on the influence on strength and failure mode of the normal stresses arising at the reinforcement to substrate interface (which, in their turn, are due to the

curvature of the surface). The existing knowledge is however still limited, causing non-negligible uncertainties in the design of the reinforcement of masonry arched members.

This chapter presents an experimental investigation carried out in the laboratory on the bond behaviour of SRG on curved masonry substrates via double-lap double-prism push-pull and four-point bending tests.

In the last years, several authors have shown the load-bearing improving of curved structural elements, such as arches, vaults and domes, thanks application of composite materials strengthening systems for retrofitting of existing buildings (e.g. [Borri et al., 2009 – Garmendia et al., 2014 – Castori et al., 2016]).

Aiming at analyzing how the strengthening system works in curved substrates, either at the intrados or at the extrados, this study will examine the reasons why collapse mechanisms happen and will offer solutions on a) how to avoid them by using composite materials, b) how to increase their effectiveness in providing structural capacity, and c) how the geometry of these structural elements affects their response after being strengthened. Taking into consideration curved structure like the arch, the collapse is generated by plastic hinges, in the number and position such as to create mechanisms, specifically in asymmetric load condition, 4 hinges kinematic collapse happens in the Figure 5.1.

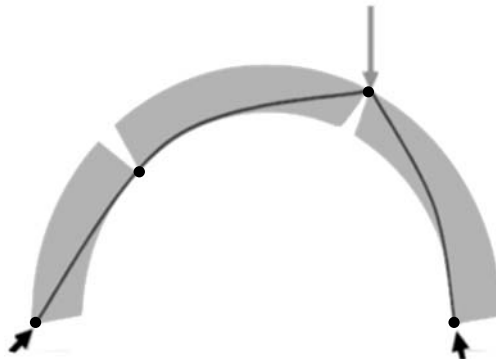


Figure 5.1. Hinges kinematic collapse, in asymmetric load condition

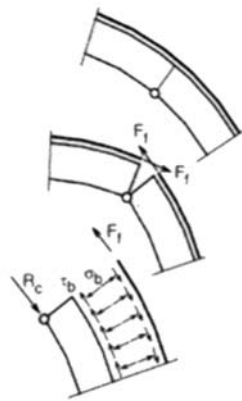


Figure 5.2. Intradosal hinge

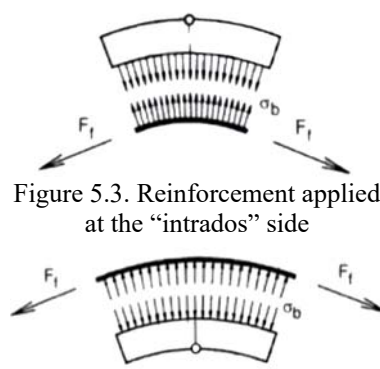


Figure 5.3. Reinforcement applied at the "intrados" side

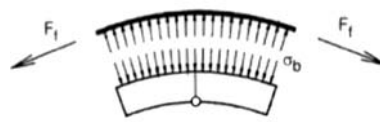


Figure 5.4. Reinforcement applied at the "extrados" side

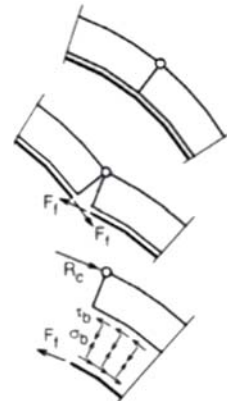


Figure 5.5. Extradosal hinge

In particular, about the reinforcements of the intrados surface (Figure 5.2, Figure 5.3), a radial stress is transferred from strengthening system to the masonry substrate, depending on its curvature. Due to this stress, the reinforcement debonds along the normal direction to the surface of itself. To avoid this debond SRG-to-substrate behaviour, it could be use a connectors system [Focacci, 2008].

At the other hand, in the reinforcements of extrados surface (Figure 5.4, Figure 5.5), a radial compression stress is transferred from strengthening system to masonry substrate, depending on its curvature [Focacci, 2008]. Then, the radial compression stress causes a frictional shear stress along the textile wherein starts the slippage of itself. Thanks to adhesion, frictional strength could add to reinforcement tensile strength, increasing debonding maximum load.

Therefore, in order to detect strengthening system application for both convex and concave masonry surface, portions of arches, characterized by full-scale geometry properties, are reinforced with SRG, both in intrados and extrados sides and in all the three different values of the curvature radius. Plane specimens (with no curvature) were also tested and taken as reference for comparisons. Digital Image Correlation was used in all the tests to integrate traditional measurement methods, validate displacement data, and derive additional information on crack pattern (occurrence, spacing, width and evolution of cracks). These results are also compared with the same ones with no curvature (control specimens).

5.2 EXPERIMENTAL PROGRAM

Tests are carried out on brickwork specimens made of ten 55mm thick clay bricks (14.8N/mm^2 compressive strength, 2.5N/mm^2 tensile strength and 5.76kN/mm^2 Young's modulus) and nine 10mm thick lime mortar joints (having compressive strength of about 5N/mm^2). Before manufacturing, the bricks are shaped to obtain prisms with either concave (Figure 5.6a) or convex (Figure 5.6b) curved surfaces and different curvature radius (R), namely 1800mm (Figure 5.7), 2650mm (Figure 5.8) and 5000mm (Figure 5.9), because of the most common used both in curved elements, like arches and vaults in new structures and in existing buildings.

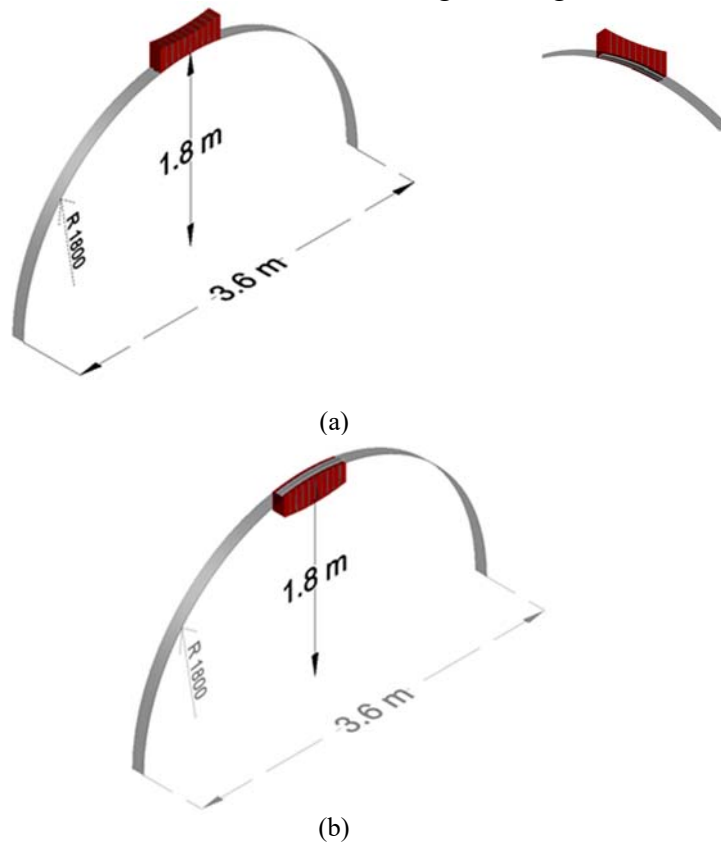


Figure 5.6. Curved specimens obtained as portion of most common curved structural elements

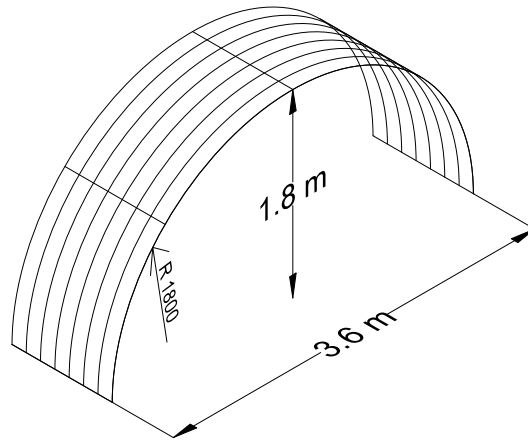


Figure 5.7. Arch or vault with curvature radius similar to specimens with 1800mm of radius

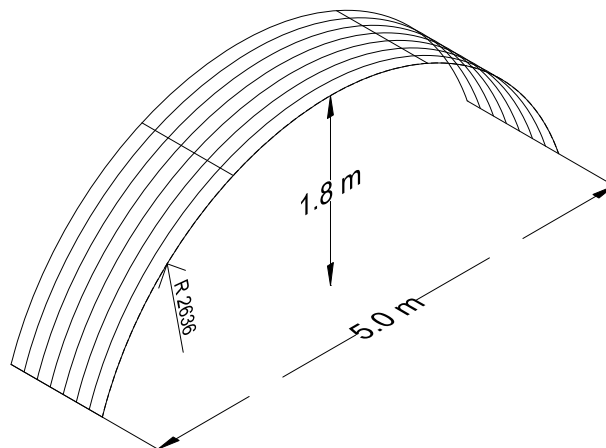


Figure 5.8. Arch or vault with curvature radius similar to specimens with 2650mm of radius

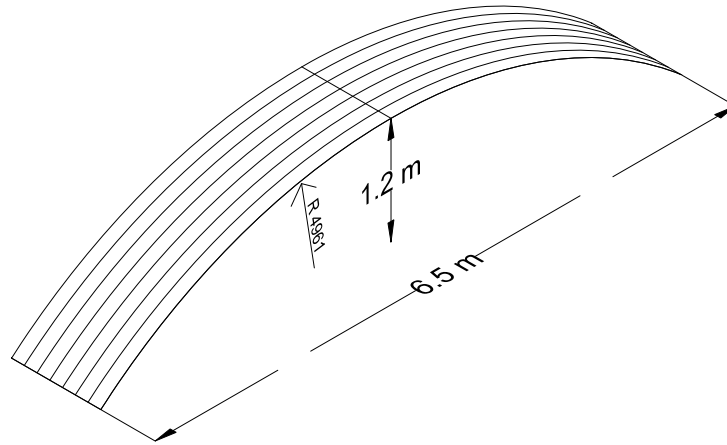


Figure 5.9. Arch or vault with curvature radius similar to specimens with 5000mm of radius

Specimens with plane surfaces are also tested. Three specimens for each type are manufactured and reinforced on one side (on the curved surface) with SRG. The steel textile comprised Ultra High Tensile Strength Steel (UHTSS) cords with 0.157 cords/mm spacing, 0.084mm design thickness and 670g/m² surface mass density. It has 3200N/mm² tensile strength and 190kN/mm² Young's modulus [De Santis et al., 2017a]. The matrix is a lime-based mortar with 20.6N/mm² compressive strength, 11.4kN/mm² Young's modulus, and 5.4N/mm² tensile strength. The reinforcement is bonded for a width of 50mm and an overall length of about 640mm, slightly changing with the curvature of the surface of application.

5.2.1 Manufacturing

For both specimens performed in double-lap double-prism push-pull and in four-point bending tests, just before realizing curve shaped brickwork, it is necessary to make drilling in bricks aiming at inserting steel bars in masonry (Figure 5.10). After, bricks are cut by a milling machine (Figure 5.12), following contours marked with papers shaped of curved elements design (Figure 5.11).



Figure 5.10. Drilling of bricks



Figure 5.11. Papers shaped of curved elements design



Figure 5.12. Milling machine

5.2.1.1 Double-lap double-prism push-pull manufacturing

Regarding double-lap double-prism push-pull specimens, steel bars are inserted inside the sample, welded to metal plates (Figure 5.13).

First at all, drilled bricks are saturated in the water (Figure 5.13a) in order to avoid that clay bricks will dry mortar, just applied, subtracting water due to their porosity. For brickwork realizing, drilled bricks are placed one on top of the another, alternately with 1cm of mortar thickness (Figure 5.13b - Figure 5.13c), inserting a plastic barrel into the hole of the brick to guarantee holes alignment in vertical direction. A wood support simplifies (Figure 5.13d) the bricks overlapping. At the end of 5th brick, the first metal bar is inserted in the holes and welded to a metal plate. At the same time, the second half of the brickwork is made, starting from second metal plate (Figure 5.13e - Figure 5.13f), also welded in the upper metal bar and overlapping other five bricks up to the whole height (Figure 5.13g - Figure 5.13h).

In this way, the bond behaviour between the reinforcement and the substrate can be studied, avoiding joints opening that may occur during push-pull setup configuration. Three specimens for each type of test and for each corresponding strengthening systems were made (Figure 5.15).



(a)



(b)



(c)



(d)

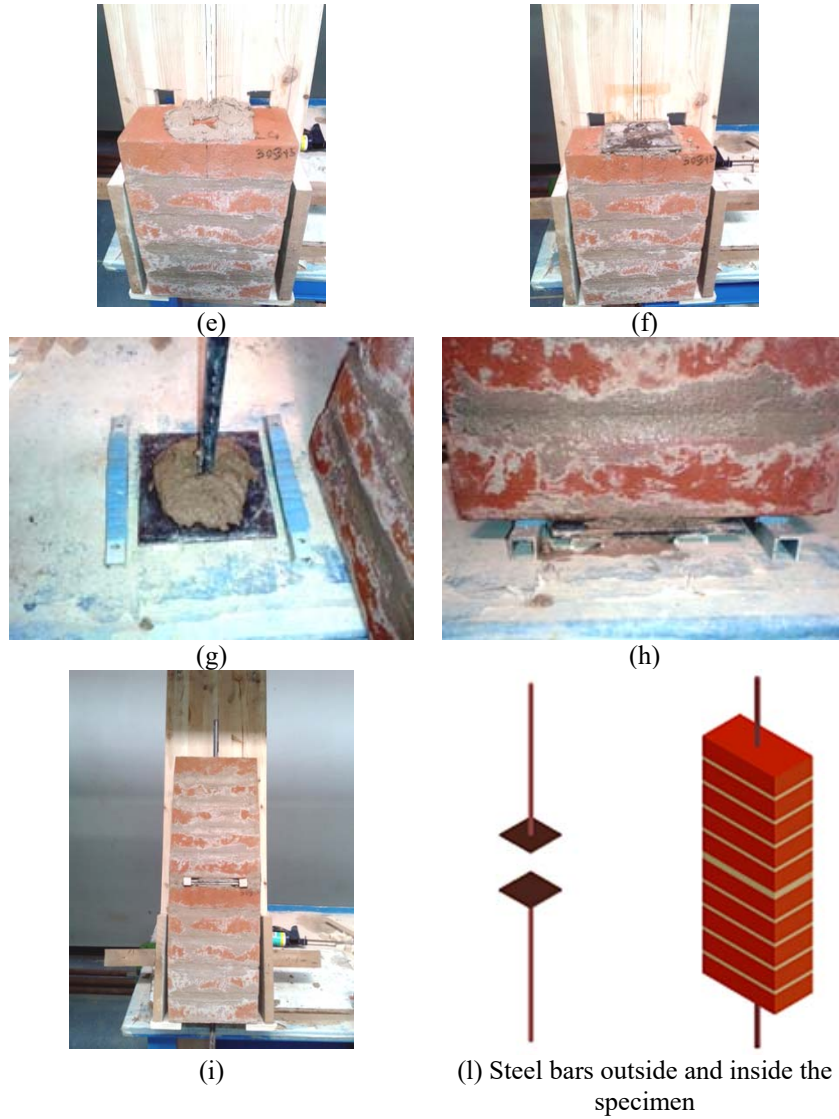


Figure 5.13. Procedure to insert steel bars

In order to detect strains during test execution, one resistive strain gauge is placed on one cord of the steel textile, before application (Figure 5.14). In particular, strain gauge is glued on a resin surface applied on a steel cord (Figure 5.14a). Accuracy value of strain gauge is $2.12 \pm 1\%$.



(a)



(b)



(c)

Figure 5.14. Strain gauge on the UHTSS cords (a), steel textile placed on the first layer of mortar (b), second layer of mortar applied between tracks(c).

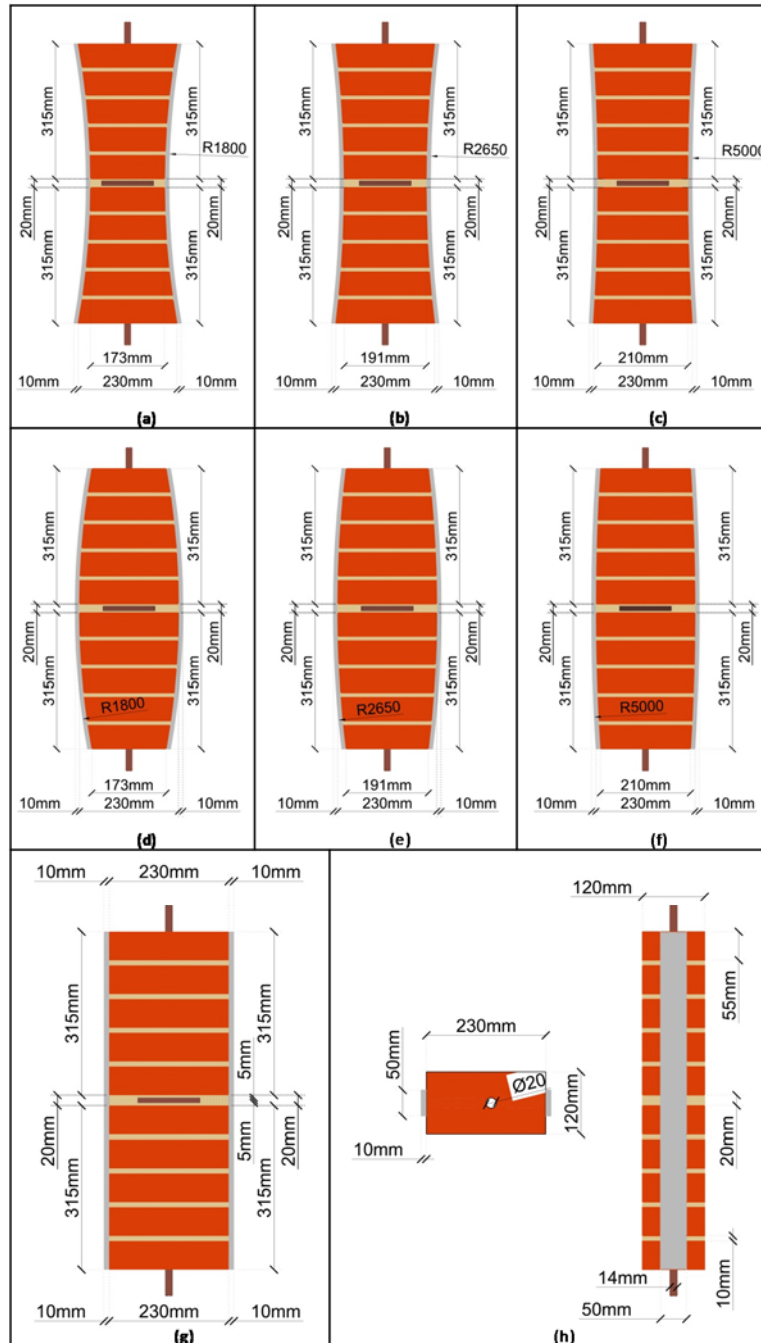


Figure 5.15. Lateral view (a-g) and bottom and side view (h) of the specimens under investigation with concave (a-c), convex (d-f) and plane (g) surface for double-lap double-prism push-pull.

5.2.1.2 Four-point bending test manufacturing

In order to avoid shear failure during the test, two $\varnothing 16$ steel rebars (Figure 5.16a – Figure 5.16b) are inserted (one per side of the prism) for a depth of about 200mm and injected with fluid grout. The same procedure followed for the double-lap double-prism push-pull specimens, was used in this time, without welding of the metal plates (Figure 5.17 – Figure 5.18). SRG is installed with a wet lay-up procedure after having cleaned and wet with water the surface of the substrate. Polyethylene moulds are used for laying the mortar, and removed 48 hours after installation. Specimens are cured in high relative humidity for 28 days and then stored in the laboratory for at least seven days before testing (Figure 5.19).

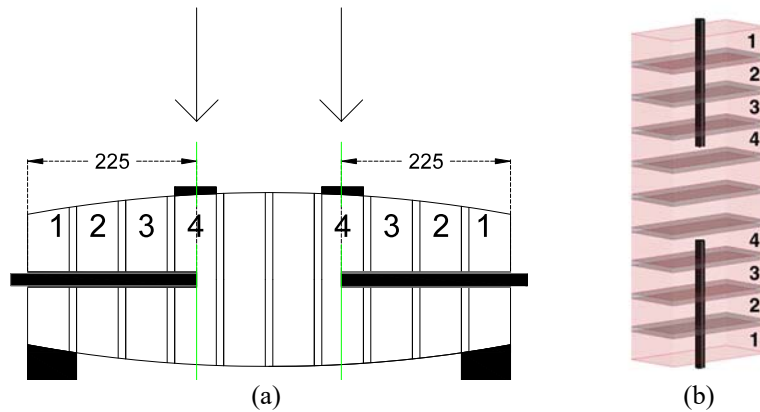


Figure 5.16. Steel bars inside the specimen, the scheme (a) and the “virtual” 3D render



Figure 5.17. Drilled brickwork from the top



Figure 5.18. Bar inserted



Figure 5.19. Brickwork realizing

About specimens for four-point bending test, before reinforcement installation (Figure 5.20), two resistive strain gauges are glued to the textile to measure strains during test execution (Figure 5.21). Also in these tests, each strain gauge is glued on a resin surface applied on a steel cord (Figure 5.21). Accuracy value of strain gauge is $2.12 \pm 1\%$. In Figure 5.22 and in Figure 5.23, specimens just before testing are shown.

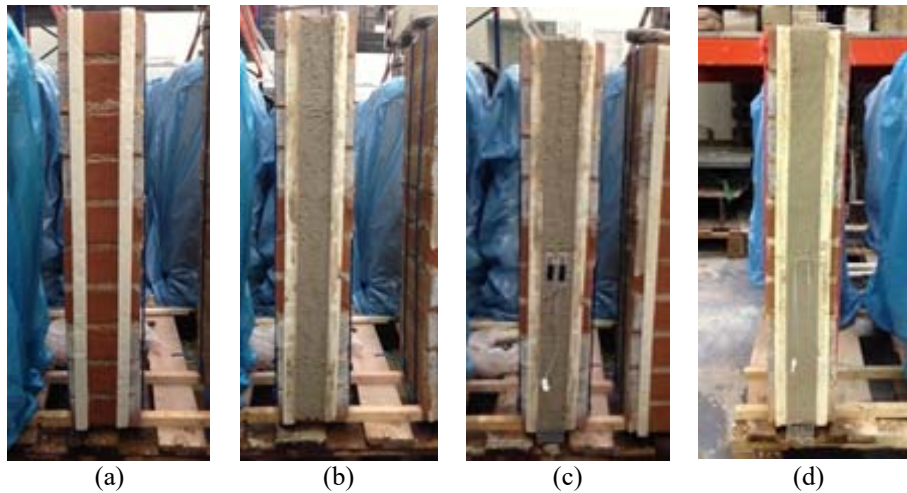


Figure 5.20. Masonry surface before reinforcing (a), first layer of mortar application (b), steel textile placed on the first layer of mortar (c), second layer of mortar applied between tracks (d).



Figure 5.21. Strain gauges on the UHTSS cords



Figure 5.22. Specimens before testing

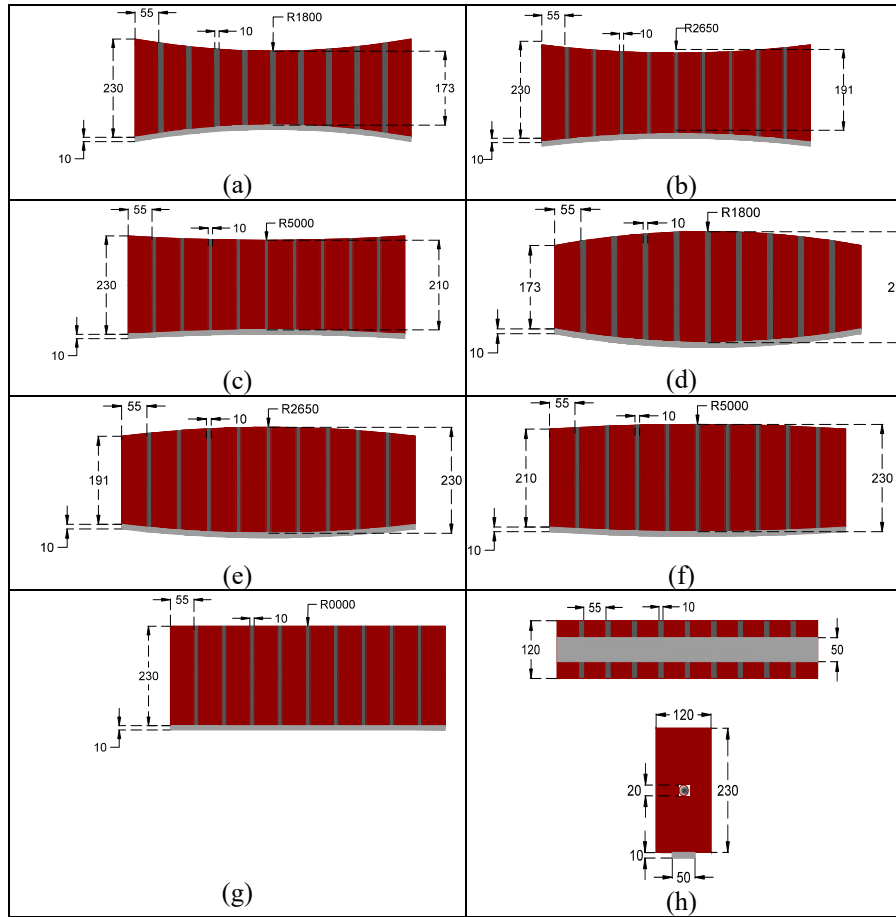


Figure 5.23. Lateral view (a-g) and bottom and side view (h) of the specimens under investigation with concave (a-c), convex (d-f) and plane (g) surface for four-point bending test.

5.3 TESTING SETUP

5.3.1 Double-lap double-prism push-pull tests setup

All these tests are carried out by MTS Universal Testing Machine load frame, with a 500kN hydraulic actuator and rate of 0.003 mm/sec (Figure 5.24 - Figure 5.25 - Figure 5.26), under displacement control.

Load is monitored by integrated LVDT in MTS and it is proportionally calculated in both sides with strain gauges applied (Figure 5.27) on steel cord (as described above).

In this test, the relative displacement between upper and lower prisms of the specimen is detected in each side by traditional instruments, such as LVDTs (Figure 5.28) and potentiometers (Figure 5.29) and a contact-less method as D.I.C. (Figure 5.30).

Regarding traditional instruments, in each face of the of the masonry prism, are placed one LVDT and one potentiometer. Other two potentiometers are added on the front and on the back sides in order to measure the length among the points where the device is installed on the specimen. Sampling frequency for data acquisition is 10Hz in LabView environment.

Displacement are determined as the sum of three values: the first one is the slip between the SRG strengthening system and the upper part of the specimen, the second is the slip between SRG and the lower part (Figure 5.31) and then the breadth of the failure in the middle joint. Thanks to contact-less method as D.I.C. (Digital Image Correlation), slip measurement could be detected between the SRG reinforcement on the external surface to the substrate in both prisms. In particular, “double 2D DIC” (double two-dimensional Digital Image Correlation) was used with two high-resolution cameras having been place in front of each reinforcement side. DIC frequency acquisition was one photo every 10 seconds.

By means of DIC method, not only the slip value during the double-lap shear bond test can be investigated but also the development of displacements and strains plots. In particular, the strain field, it can highlight how the crack pattern progresses and their opening throughout the test.

Finally DIC is a useful method to detect slip measurement, unless supposing completely adhesion between mortar and textile. Indeed, in each test, Digital Image Correlation monitoring allows to validate the accuracy and the reliability of data acquired by traditional instruments [De Santis, 2017 - Tekieli et al., 2017 - Roscini et al., 2017].



Figure 5.24. Concave specimen set up



Figure 5.25. Convex specimen set up

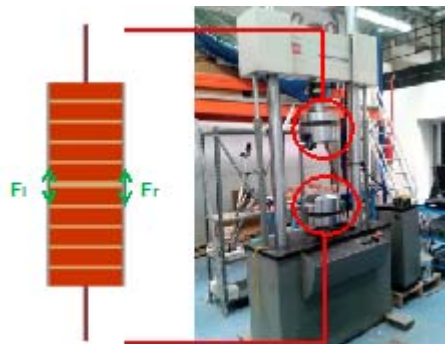


Figure 5.26. Set up design

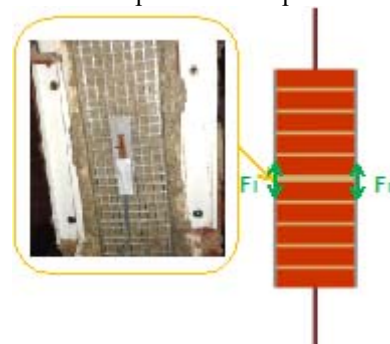


Figure 5.27. Strain gauge position with respect to the specimen

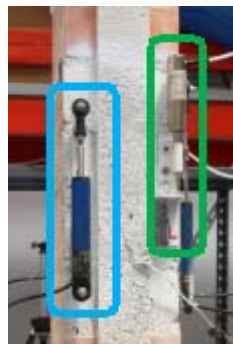


Figure 5.28. Potentiometers and LVDT

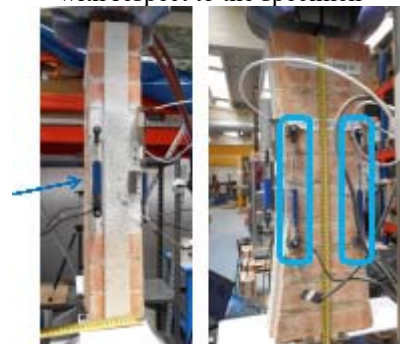


Figure 5.29. Potentiometers

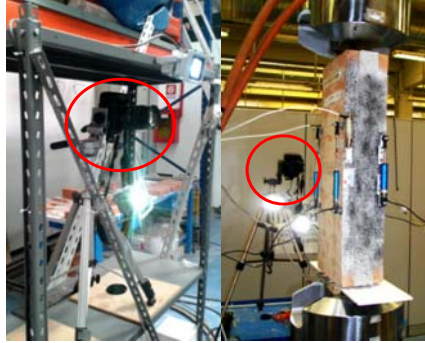


Figure 5.30. Double DIC camera

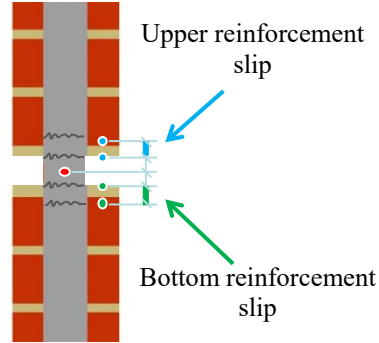


Figure 5.31. Upper and bottom reinforcement slip measurement

5.3.2 Four-point bending test setup

Specimens are placed on steel frames spanning 585mm, making use of shaped wood supports. Two Teflon sheets are used to minimize friction at the supports. Load is applied using a 250kN hydraulic actuator under displacement control at a rate of 0.01mm/s (Figure 5.32). A stiffened steel girder is used to apply the load to the brickwork prism in two points 70mm apart from the middle of the specimen. The load is measured by a load cell integrated in the actuator, while the strain in the steel cords are measured by the strain gauges. 2-D Digital Image Correlation method (DIC) [Tekieli et al., 2017] is used to monitor both the lateral and the lower surface of the specimen. To apply DIC the surfaces of the specimens are provided with a speckle pattern. Digital Images are taken during test execution every 5s (acquisition frequency is 1 photo every 5 seconds) and then post-processed to derive displacement and strain fields. In these tests, two high-resolution cameras are used: the first one is the “front camera” (Figure 5.33a) of the specimen (Figure 5.33c) to acquire displacements and strains plot on the front of the sample. At the same time is placed a second “camera on the below” (Figure 5.33b) of the specimen (Figure 5.33d) to detect displacements and strains plot under the sample, strengthening system comprised.

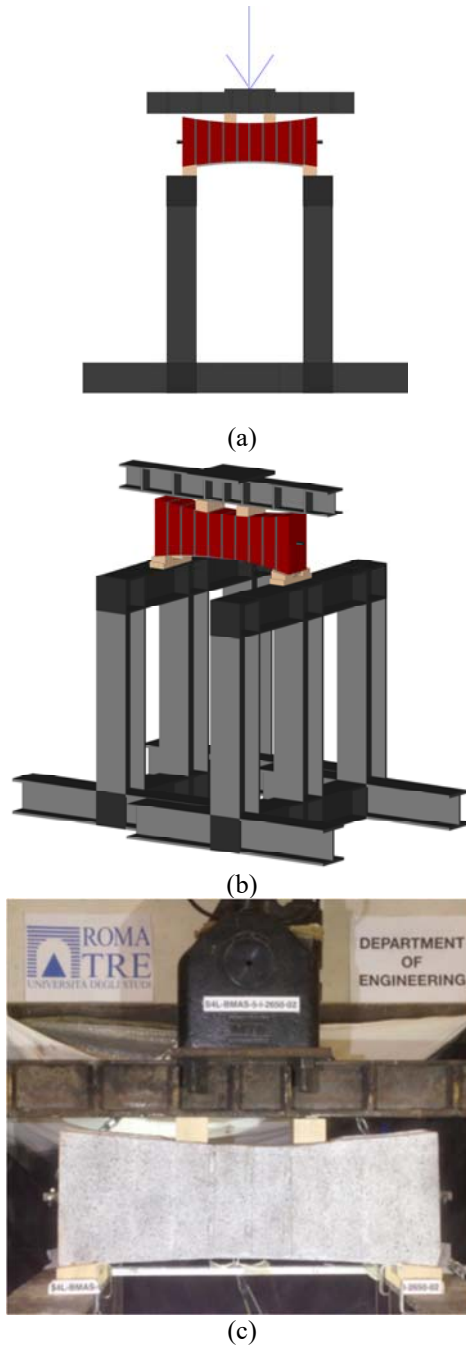


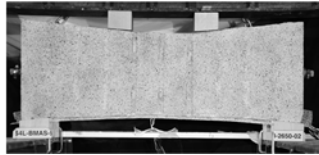
Figure 5.32. Experimental setup, front design(a), axonometric design(b), real image(c)



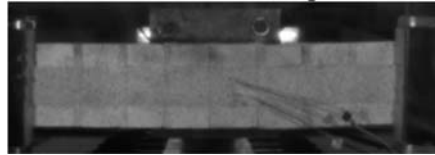
(a). Front camera



(b). Camera below the specimen



(c). DIC image (front camera)



(d). DIC image (camera on the bottom of the specimen)

Figure 5.33. DIC setup in four-point bending test

5.4 EXPERIMENTAL RESULTS

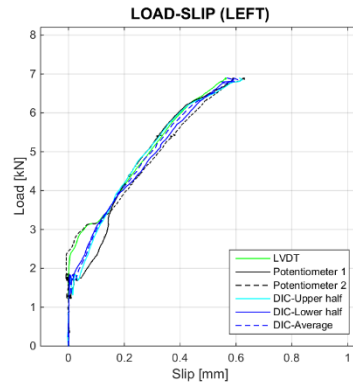
All experimental test results on curved masonry substrate, namely double-lap double-prism push-pull and bending tests, are shown in Figures 5.39 and 5.49, and reported in Tables 5.1 and 5.2, respectively. All specimens, the same for both typologies, are labelled according to the notation N-XXXX-NN, N indicating the shape of the surface (I for intrados, P for plane and E for extrados), XXXX being the curvature radius in mm (assumed negative for intrados surfaces and positive for extrados surfaces, and equal to 0000 for plane specimens) and, finally, NN being the progressive number of the specimens.

5.4.1 Double-lap double-prism push-pull tests results

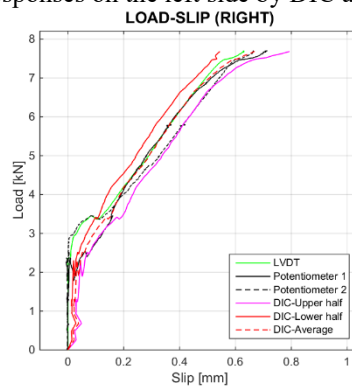
Table 5.1 collects the name of the specimen and its curvature radius (R), the failure mode, the failure area wherein the debonding is detected and the failure load (Fbmax) occurred in the debonding side. With the aim to provide further information, outcomes from double-lap shear tests on strengthened concave and convex substrates are given in Figure 5.39.

5.4.1.1 Reinforcement application on intradosal side

For the strengthening system at the intrados surface, the Figure 5.34 collects load-slip curves for each side (the left (a) and the right one (b)), comparing results coming from D.I.C. (upper half, lower half, average value), LVDTs (average value) and potentiometers (average value): perfect overlapping is shown in these graphs. Just debonding load achieved, failure mode is studied: in all tests, the failure mode occurred within the mortar, in the interface between steel textile and the first layer of the mortar (Figure 5.34c – Figure 5.36). In this particular test, as it's clear by DIC strains plot (Figure 5.35c – Figure 5.35d) crack opening happens at middle joint of the prism.



(a). Load-slip curve responses on the left side by DIC and traditional instruments



(b). Load-slip curve responses on the right side by DIC and traditional instruments



(c). Debonding failure mode

Figure 5.34. Concave test results

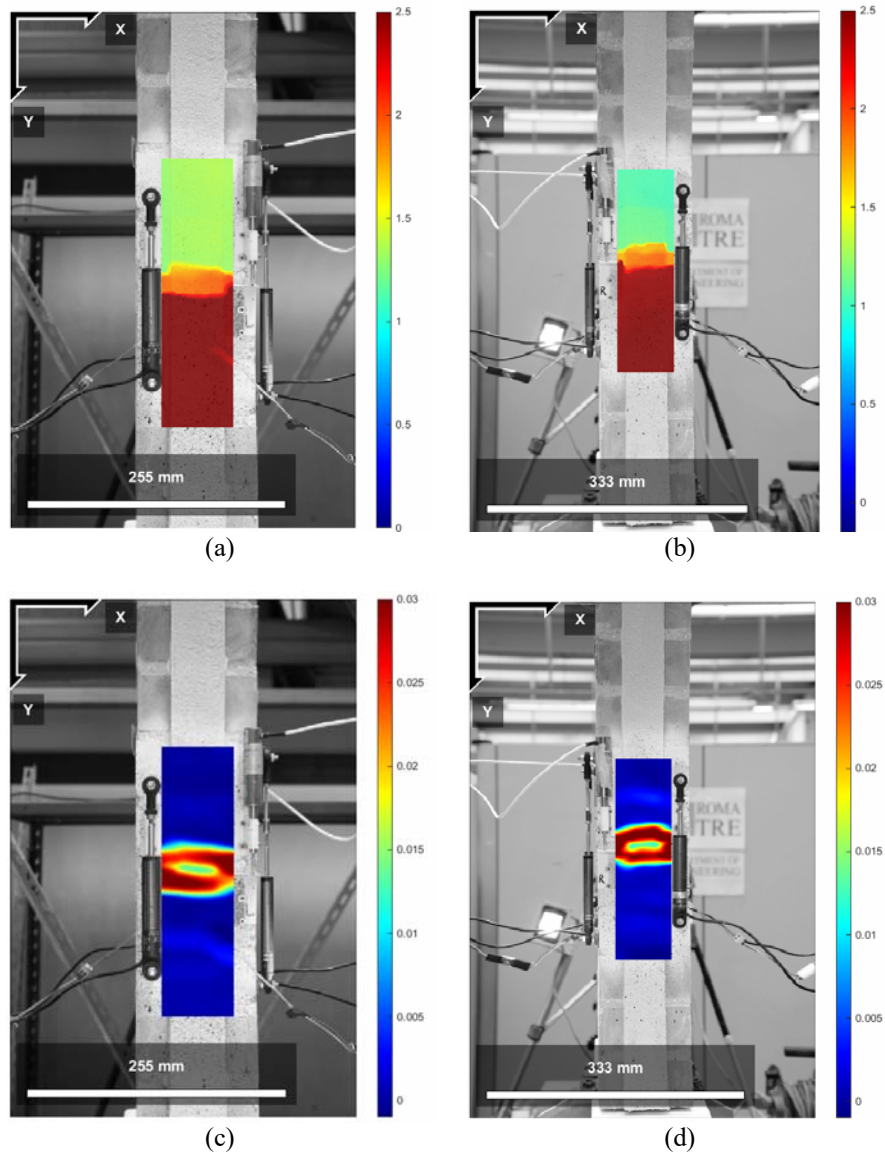


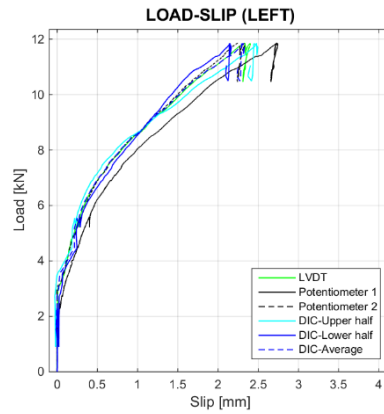
Figure 5.35. Concave test: vertical displacement just before failure, left side(a) and right side(b) and vertical strains just before failure, left side(a) and right side(b).

5.4.1.2 Reinforcement application on extradossal side

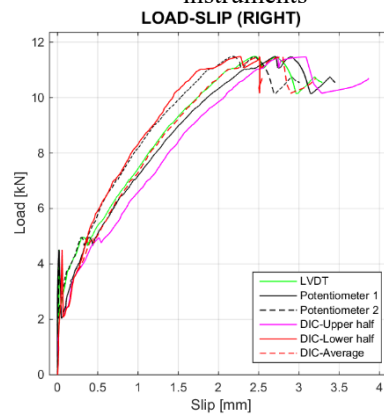
At the same time in the Figure 5.37 are reported results about reinforcement applied in extradossal side. Specifically, also in this test, the graphs show load-slip curves for either surface, the left one (Figure 5.37a) and the right one (Figure 5.37b), comparing data from D.I.C. post processing (upper half, lower half, average value), LVDTs (average value) and potentiometers (average value): as previous test, it's obvious the whole match between the measurement methods. As far as failure mode, debonding happens by “C” type (Figure 5.36 - Figure 5.37c) at the interface between steel textile and the first layer of the mortar, like in all the other specimens carried out in this double lap double prism push-pull tests. In this particular test, crack opening happens at middle joint of the prism (Figure 5.38c – Figure 5.38d).



Figure 5.36. Failure mode image and C failure mode [Ascione et al. 2015]



(a). Load-slip curve responses on the left side by DIC and traditional instruments



(b). Load-slip curve responses on the right side by DIC and traditional instruments



(c). Debonding failure mode

Figure 5.37. Convex test results

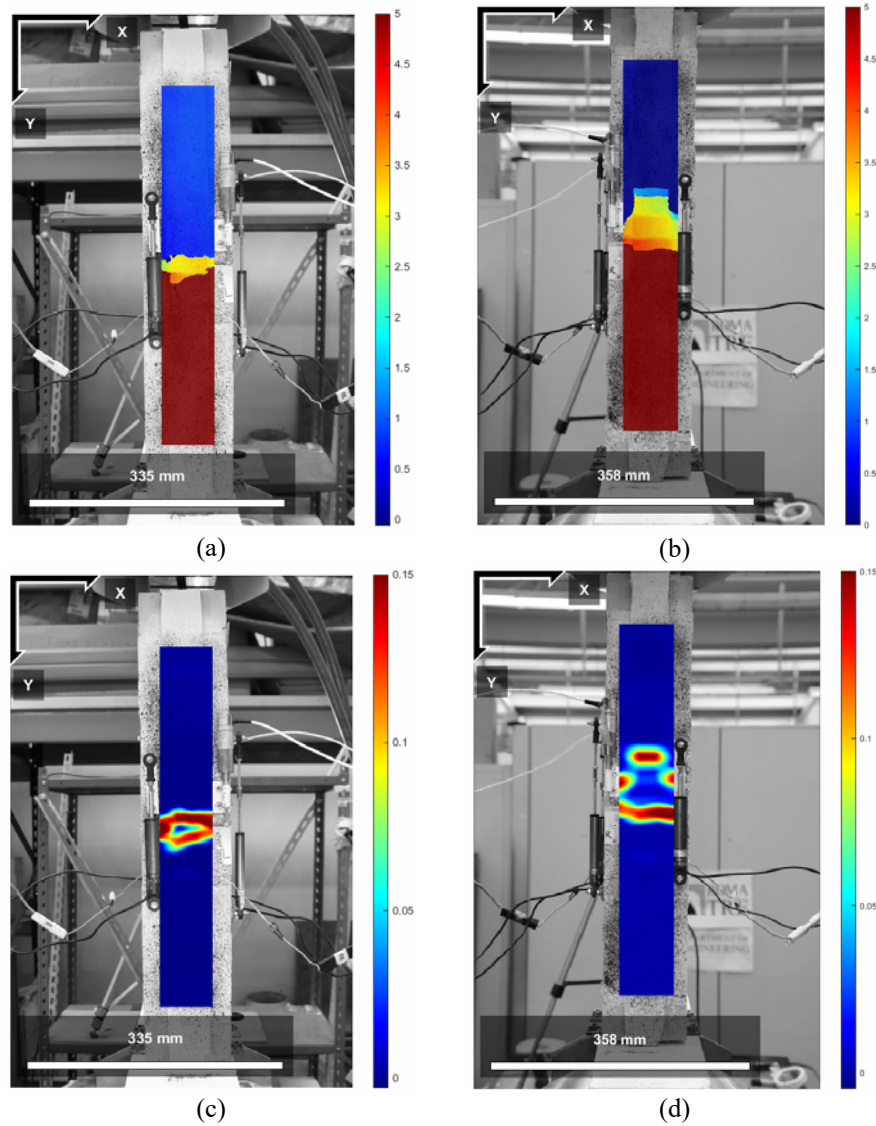


Figure 5.38. Concave test: vertical displacement just before failure, left side (a) and right side(b)and vertical strains just before failure, left side(a) and right side(b).

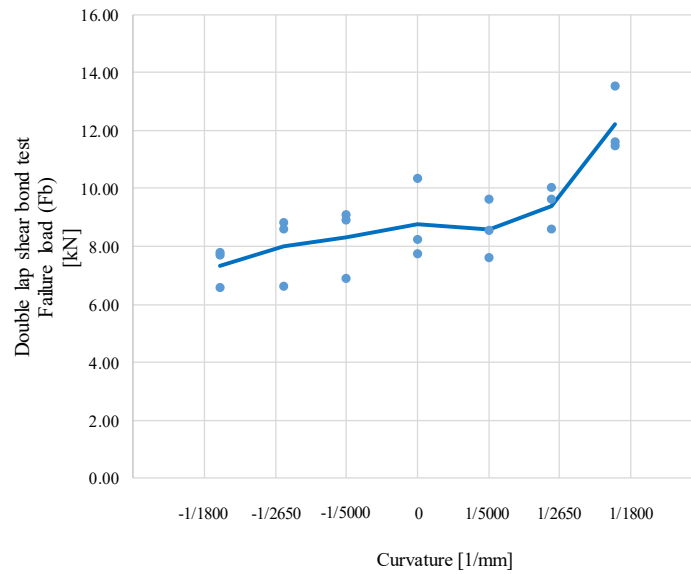


Figure 5.39. Double lap shear bond test failure load vs. curvature

Table 5.1: Tests results "Double-lap double-prism push-pull"

Specimen	R [mm]	Failure mode	Failure area	Fb max debonding side [kN]
I-1800-01	-1800	Debonding "C"	R-U	7.71
I-1800-02	-1800	Debonding "C"	L-D	7.77
I-1800-03	-1800	Debonding "C"	R-U	6.57
I-2650-01	-2650	Debonding "C"	L-U	6.59
I-2650-02	-2650	Debonding "C"	L-U	8.82
I-2650-03	-2650	Debonding "C"	L-U	8.59
I-5000-01	-5000	Debonding "C"	R-D	9.1
I-5000-02	-5000	Debonding "C"	R-U	6.89
I-5000-03	-5000	Debonding "C"	R-U	8.92
P-0000-01	∞	Debonding "C"	R-D	10.33
P-0000-02	∞	Debonding "C"	R-D	7.74
P-0000-03	∞	Debonding "C"	L-U	8.23
E-5000-01	5000	Debonding "C"	L-D	9.62
E-5000-02	5000	Debonding "C"	L-D	7.58
E-5000-03	5000	Debonding "C"	L-U	8.56
E-2650-01	2650	Debonding "C"	L-U	10.03
E-2650-02	2650	Debonding "C"	L-U	9.62
E-2650-03	2650	Debonding "C"	R-U	8.59
E-1800-01	1800	Debonding "C"	R-U	13.53
E-1800-02	1800	Debonding "C"	L-D	11.59
E-1800-03	1800	Debonding "C"	R-U	11.48

Fb= tensile load in the reinforcement

5.4.2 Four-point bending test results

Table 5.2 presents the name of the specimen and its curvature radius (R), the failure mode, the ultimate load (F_{\max}), the height of the section in the middle of the specimen (H), the distance depending on the neutral axis, detected by the use of DIC ($Z=H-y_{\text{dic}}$) and the corresponding tensile load in the reinforcement (F_b). This latter was calculated considering all the force applied in the specimen, following (Equation 5.1) for intradosal support, (Equation 5.2) rectilinear one and (Equation 5.3) extradosal one. When either damage developed before testing during manufacturing or handling or shear failure occurred at the mortar bed joint before the detachment of the SRG reinforcement, test results were excluded from statistics and not included in the plots.

Using DIC and in particular, considering the horizontal displacement values (Figure 5.40), the neutral axis position is detected, based on the speckle pattern behaviour, that is: in four-point bending scheme, above neutral axis, they move close, below the neutral axis, they move away. Two vertical lines through 4th and 8th bricks are identified, corresponding the same direction of the loads. Each line is characterized with a number of points (Figure 5.41). The left line (red colored) is identified with “XL abscissa” and the right line (black one) with “XR abscissa”. To subtract the rigid motion displacement of the sample, a 3rd vertical straight line is considered through the middle of itself, and it is named “XM abscissa”. In post processing phase of the tests, Matlab software, with “Ncorr” code, allows to calculate the final position points, just before the collapse by x,y coordinates of the different points (already identified), from input data referred image without any deformation (Figure 5.42) to the final displacements of the same points detected in deformed image (Figure 5.43), wherein, indeed, lines are modified.

Once the neutral axis is measured (Figure 5.44), it could be used in flexural moment calculation (Figure 5.45).

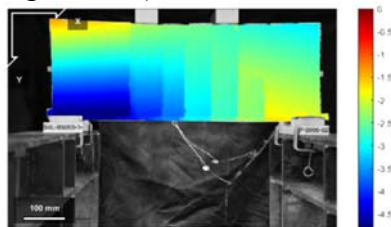


Figure 5.40. Horizontal displacement plot for front D.I.C.

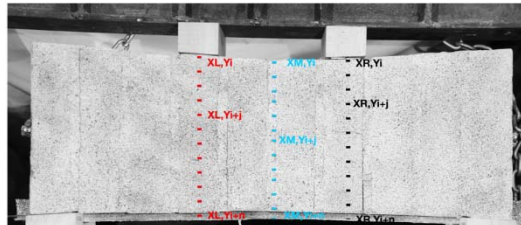


Figure 5.41. Points of vertical lines

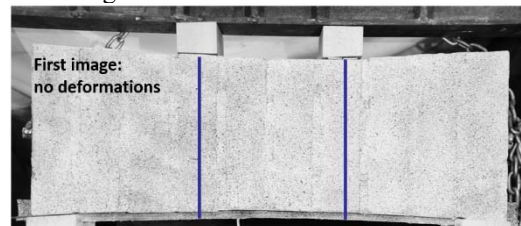


Figure 5.42. Indeformed vertical lines before bending test

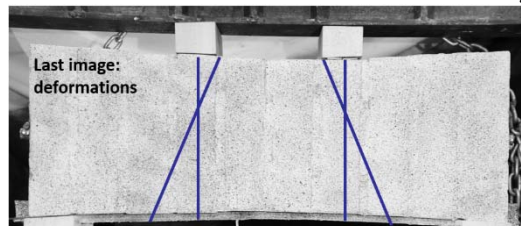


Figure 5.43. Image with deformations

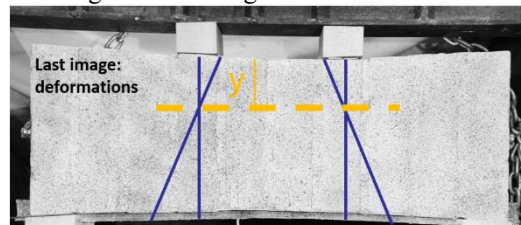
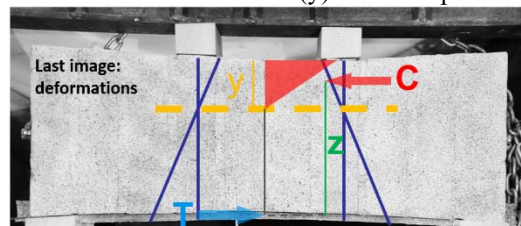
Figure 5.44. Neutral axis distance (y) from compressed surface

Figure 5.45. Neutral axis using for flexural moment calculation

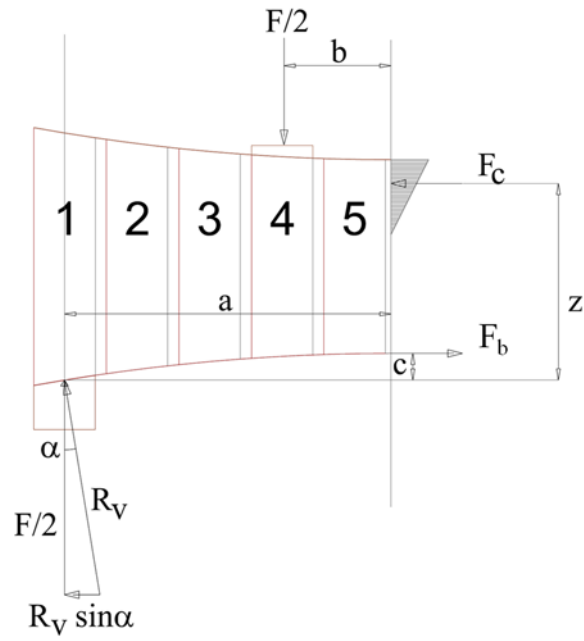


Figure 5.46. Intradosal surface procedure

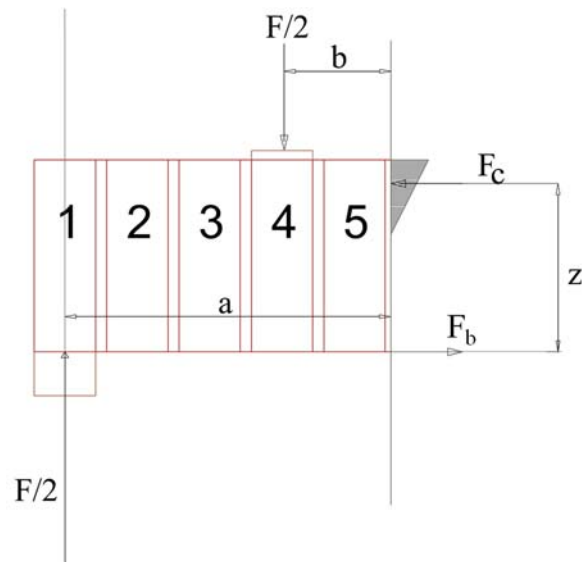


Figure 5.47. Rectilinear surface procedure

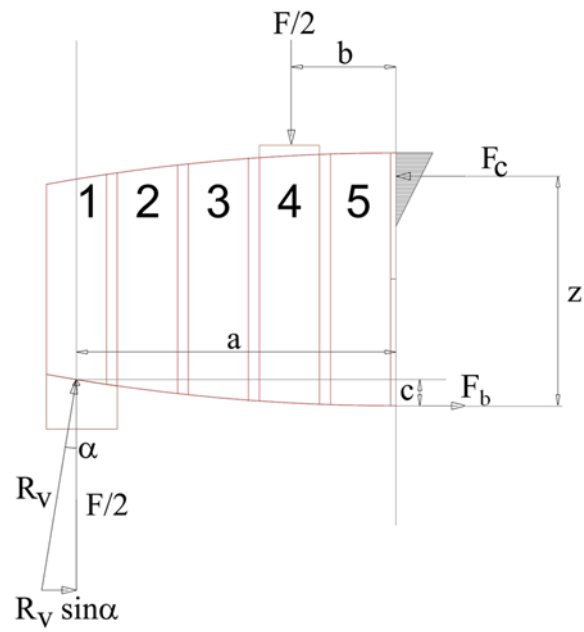


Figure 5.48. Extradossal surface procedure

Intradossal surface

$$\frac{F}{2} \cdot a - \frac{F}{2} \cdot b + R_v \cdot \sin \alpha \cdot (z + c) = F_b \cdot z$$

$$\frac{F}{2} \cdot a - \frac{F}{2} \cdot b + \frac{F}{2 \cdot \cos \alpha} \cdot \sin \alpha \cdot (z + c) = F_b \cdot z$$

$$\frac{F}{2} \cdot a - \frac{F}{2} \cdot b + \frac{F}{2} \cdot \tan \alpha \cdot (z + c) = F_b \cdot z$$

$$F_b = \left(\frac{F}{2} \cdot \frac{a}{z} - \frac{F}{2} \cdot \frac{b}{z} + \frac{F}{2} \cdot \tan \alpha \cdot \frac{(z + c)}{z} \right)$$

$$F_b = \frac{F}{2} \left(\frac{a}{z} - \frac{b}{z} + \tan \alpha \cdot \left(1 + \frac{c}{z} \right) \right)$$

$$F_b = \frac{F}{2} \left(\frac{a}{z} - \frac{b}{z} + \tan \alpha + \tan \alpha \left(\frac{c}{z} \right) \right) \quad (5.1)$$

Rectilinear surface

$$F_b \cdot z = \left(\frac{F}{2} \cdot a - \frac{F}{2} \cdot b \right)$$

$$F_b = \frac{\left(\frac{F}{2} \cdot a - \frac{F}{2} \cdot b \right)}{z} \quad (5.2)$$

Extradossal surface

$$\frac{F}{2} \cdot a - \frac{F}{2} \cdot b - R_v \cdot \sin \alpha \cdot (z - c) = F_b \cdot z$$

$$\frac{F}{2} \cdot a - \frac{F}{2} \cdot b - \frac{F}{2 \cdot \cos \alpha} \cdot \sin \alpha \cdot (z - c) = F_b \cdot z$$

$$\frac{F}{2} \cdot a - \frac{F}{2} \cdot b - \frac{F}{2} \cdot \tan \alpha \cdot (z - c) = F_b \cdot z$$

$$F_b = \left(\frac{F}{2} \cdot \frac{a}{z} - \frac{F}{2} \cdot \frac{b}{z} - \frac{F}{2} \cdot \tan \alpha \cdot \frac{(z - c)}{z} \right)$$

$$F_b = \frac{F}{2} \left(\frac{a}{z} - \frac{b}{z} - \tan \alpha \cdot \left(1 - \frac{c}{z} \right) \right)$$

$$F_b = \frac{F}{2} \left(\frac{a}{z} - \frac{b}{z} - \tan \alpha + \tan \alpha \left(\frac{c}{z} \right) \right) \quad (5.3)$$

Where:

$$c = c(\alpha)$$

$$z = H - \frac{y}{3}$$

$$\alpha = \arctg \left(\frac{a}{R} \right)$$

$$R_v \cdot \cos \alpha = \frac{F}{2}$$

$$R_v = \frac{F}{2 \cdot \cos \alpha}$$

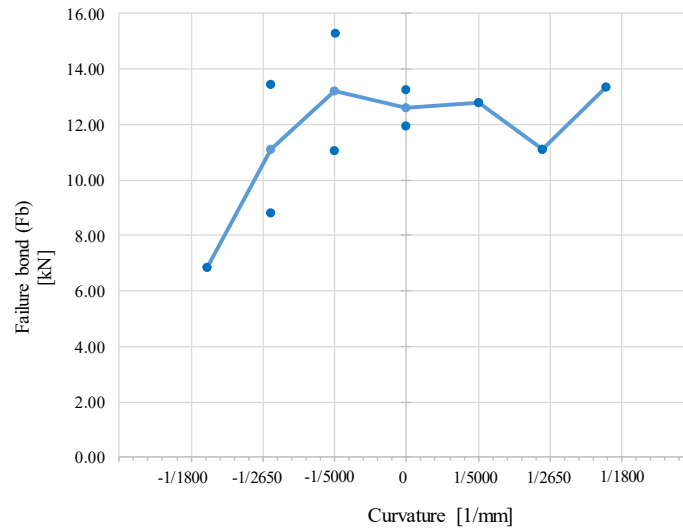


Figure 5.49. Failure load vs. curvature

Test results are shown in Figure 5.49 in terms of failure load versus curvature radius. F_b increases with the increase of the curvature of the substrate, due to the normal stresses arising at the SRG-to-masonry interface. In case of concave surfaces (intrados reinforcements) tensile stresses appear that cause a premature detachment of the composite due to peeling phenomenon. Detachment always activated in the central portion of the specimen, in which the bending moment is maximum and constant. Displacement and strain fields plot, detected by means of Digital Image Correlation on the lateral and lower surfaces of “I-5000-01” and “E-1800-01” specimens are respectively shown in Figure 5.50 and Figure 5.51. DIC method provided information on damage development during test execution, helping identifying the debonding side where SRG detachment activated.

Table 5.2. Tests results “Four-point bending test”

Specimen	R [mm]	Failure mode	Fmax [kN]	H [mm]	Z(DIC) [mm]	Fb [kN]
I-1800-01	-1800	Shear	18.1	173	-	-
I-1800-02	-1800	SRG detachment	9.54	173	152.167	6.83
I-1800-03	-1800	Shear	15	173	173-	-
I-2650-01	-2650	SRG detachment	14.5	191	173.633	8.82
I-2650-02	-2650	Shear	21.10	191	-	-
I-2650-03	-2650	SRG detachment	21	191	163.767	13.43
I-5000-01	-5000	SRG detachment	26.79	209	175.533	15.31
I-5000-02	-5000	SRG detachment	20.04	209	181.77	11.08
I-5000-03	-5000	Shear	17.9	209	-	-
P-0000-01	∞	SRG detachment	26.72	230	212.167	11.96
P-0000-02	∞	SRG detachment	28.12	230	201.9	13.23
P-0000-03	∞	Manufacturing	-	230	-	-
E-5000-01	5000	SRG detachment	27.41	230	192.133	12.80
E-5000-02	5000	Manufacturing	-	230	-	-
E-5000-03	5000	Shear	-	230	-	-
E-2650-01	2650	SRG detachment	26.06	230	199.867	11.08
E-2650-02	2650	Shear	-	230	-	-
E-2650-03	2650	Shear	23.6	230	-	-
E-1800-01	1800	SRG detachment	34.7	230	208.433	13.34
E-1800-02	1800	Manufacturing	-	230	-	-
E-1800-03	1800	Shear	20.4	230	-	-

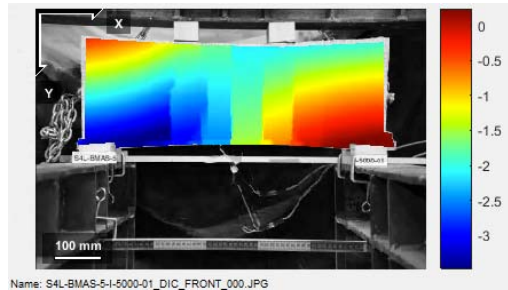
Where:

Fmax= ultimate load

H= height of the section in the middle of the specimen

Z=H-y_{dic}= the distance depending on the neutral axis, detected by the use of D.I.C.

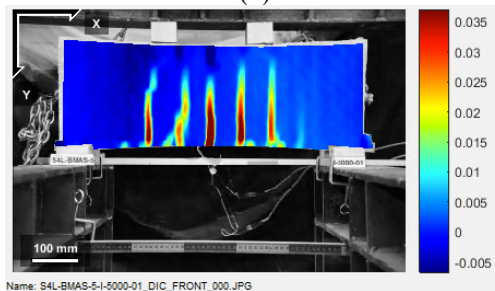
Fb= tensile load in the reinforcement



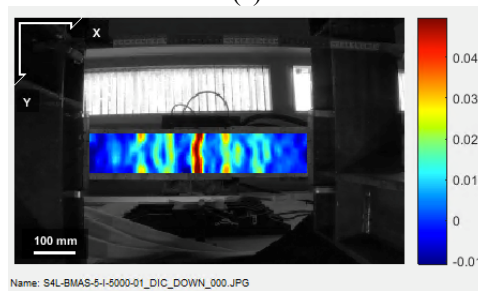
(a)



(b)



(c)



(d)

Figure 5.50. Test results provided by DIC: displacement (a,b) and strain (c,d) fields on lateral (a,c) and lower (b,d) surfaces at failure for intradosal specimen I-5000-01

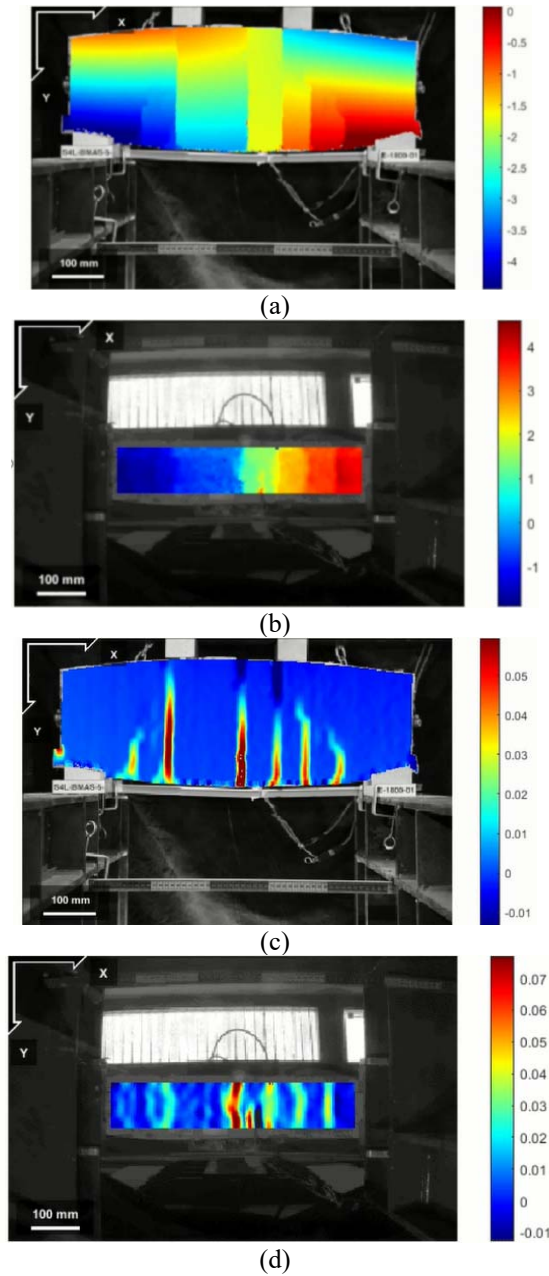


Figure 5.51. Test results provided by DIC: displacement (a,b) and strain (c,d) fields on lateral (a,c) and lower (b,d) surfaces at failure for extradossal specimen E-1800-01

5.5 BOND FAILURE FORCE TO CURVATURE RELATIONSHIP

From experimental results, bond failure force to curvature relationship is derived thanks to linear interpolation method. Therefore, data are post processed by means of statistical approach in order to provide a trend line for each test.

The trend line in double-lap double-prism push-pull test (Equation 5.4), collected in Figure 5.52, is:

$$y = 3344.4 \cdot \frac{1}{R} + 8.9457 \quad (5.4)$$

with a value of $R^2 = 0.741$.

For four-point bending test, the trend line (Equation 5.5), reported in Figure 5.53, is expressed in the formula below. The R^2 value in this case is 0.405.

$$y = 3588 \cdot \frac{1}{R} + 11.567 \quad (5.5)$$

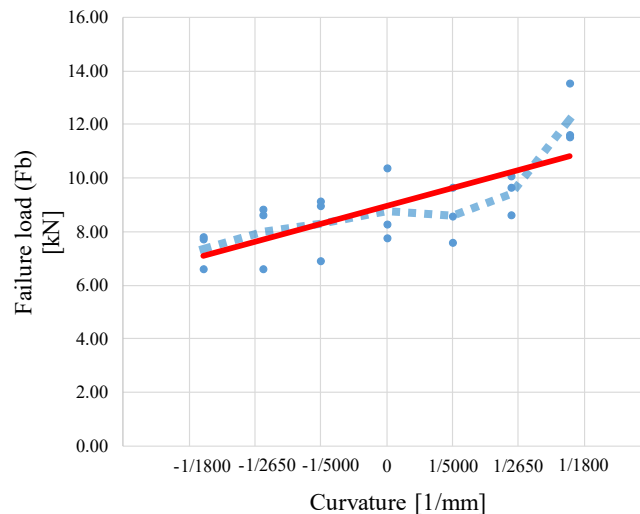


Figure 5.52. Trend line of double-lap double-prism push-pull tests

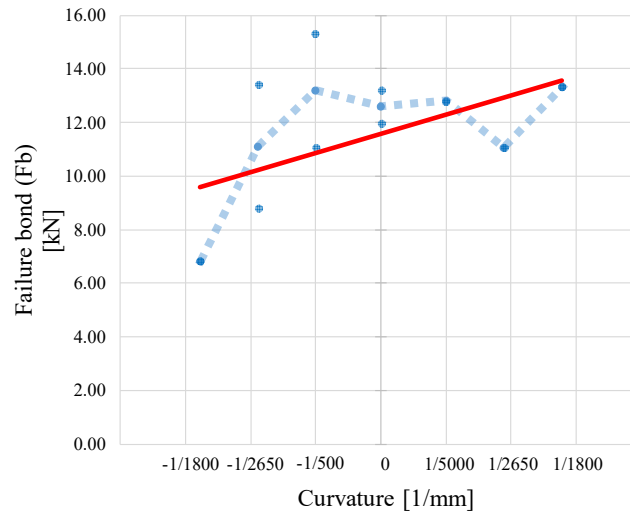


Figure 5.53. Trend line of four-point bending tests

Table 5.3. Failure bond prediction formula depending on curvature

Test	Trend line equation (linear) $y = mx + q$	Failure bond prediction formula	R^2
double-lap double-prism push-pull test	$y = 3344.4 \cdot \frac{1}{R} + 8.9457$	$F_{b_curv} = 3344.4 \cdot \frac{1}{R} + F_b$	0.741
four-point bending test	$y = 3588 \cdot \frac{1}{R} + 11.567$	$F_{b_curv} = 3588 \cdot \frac{1}{R} + F_b$	0.405

Where:

$m = \text{slope coefficient}$

$x = \frac{1}{R} = \text{curvature}$

$y = F_{b_curv} = \text{Failure bond, curved substrate}$

$y = F_b = \text{Failure bond (no curvature)}$

Despite of data give the scatter, because of experimental reasons especially in bending test, comparing both tests (Figure 5.52 – Figure 5.53), trend line equations are right well-fit each other (Table 5.3).

It is evident that slop coefficients (m) are very similar but the value corresponding to failure bond are different.

In order to avoid shear failure mode, steel bars are inserted in the masonry specimens, which were externally reinforced by means of SRP. Therefore, in four-point bending test failure load gets close to maximum value of bond capacity of SRG reinforcement.

On the other hand, failure bond value regarding double-lap test, results slightly lower than one recorded for bending test.

It may seem that, because of different set up test, inside mechanisms (such as clay brick crushing, punching), could prevent bond behaviour in the reinforcement, which, consequently, provides a lower value than expected one.

5.6 CONCLUDING REMARKS

i. The average values of load-slip curves resulting from the double lap-double prism push-pull tests are collected and given for each type of specimen in Figure 5.54. In agreement with previous published papers, in case of intradosal reinforcements, the maximum debonding load and the corresponding slip decrease as the curvature increases. On the contrary, when the reinforcement is applied on the extrados, the maximum debonding load and the associated slip values increase with the increase in the curvature. In other words it was shown that, in case of intradosal reinforcement, the debonding load depends on the radial stress transferred from the strengthening system to the masonry substrate and debonding occurs prematurely along the normal direction of the reinforcement. To avoid this “peeling” phenomenon, connectors anchored in the intradosal side are suggested.

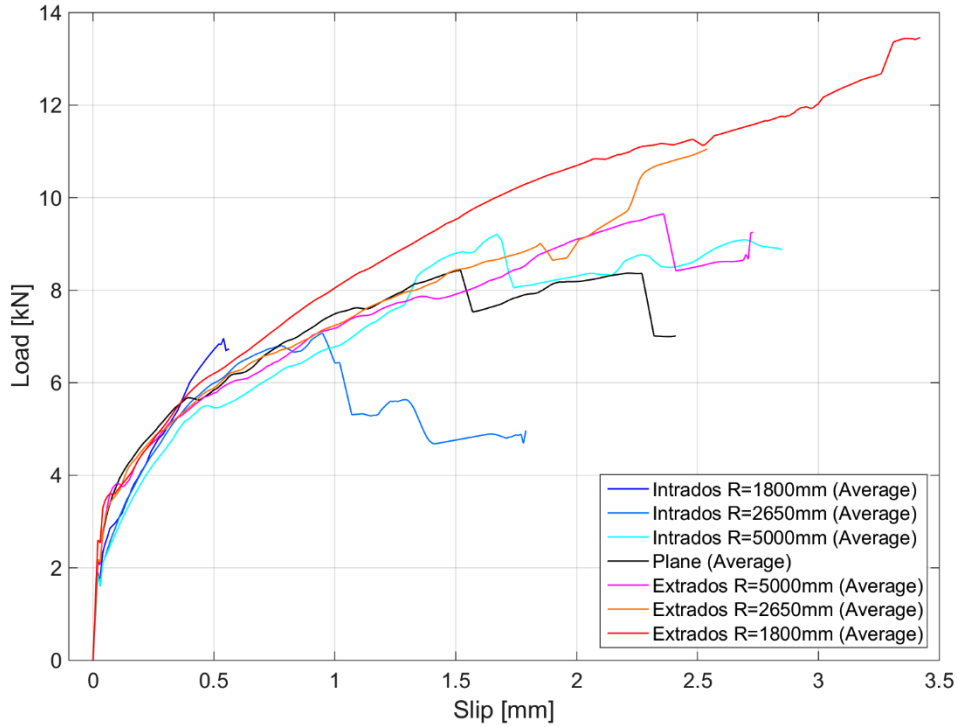


Figure 5.54. Average Load-Slip curve about SRG reinforcement comparing, characterized by different curvature radii.

Finally, reinforcement application results more effective in extradossal surface than in intradosal one, increasing curvature as well, because its bond strength is directly proportional to radial compression stress transferred from strengthening system to masonry substrate, and inversely to curvature radius (5.4).

$$\sigma_b = \frac{F_b}{b_f \cdot R} \quad (5.4)$$

Furthermore, strengthening system for arch retrofitting on the extradossal side works better than in intradosal one, unless not piers moving away to each other.

Comparing to each other extreme cases of two reinforcement typologies, maximum value of failure load recorded for extradossal reinforcement with 1800mm curvature radius is 39% greater than rectilinear reinforcement and, the minimum one intradosal reinforcement with 1800mm curvature radius is 16% less than rectilinear one.

In conclusion, this experimental campaign has given the opportunity to investigate the debonding mechanism on curved substrates, which consisted of full-scale specimens with geometrical properties as those found in arches. In this way, the construction of a great number of specimens was feasible, a fact that also proves the validity of the results. In terms of final outcomes, it was possible to mechanically characterise the strengthening reinforcement system on different curvature radii, not only through experiments but also through calibration of analytical models, aiming at simulating the real bond behaviour of the strengthening system.

ii. On the other hand, the four-point bending tests that were carried out to examine the bond behaviour of SRG on curved masonry substrate showed that the load transfer capacity is significantly influenced by the curvature of the masonry substrate. As just demonstrated by means of double lap results, also in this case, the normal stresses arising at the SRG to masonry interface, as an effect of the curvature, may activate a premature detachment (in case of concave surface) or delay it (in case of convex surface).

Such effect needs to be carefully taken into account in the design of an externally bonded reinforcement of a curved masonry member, with the aim of both estimating the effectiveness of the strengthening system and, if needed, include a suitable number of mechanical connectors to improve its adhesion to the substrate, confirming again using of this procedure, as above justified for reinforcement application on intradosal side. Nevertheless, because of limited number of available test results, it is difficult to develop and calibrate analytical design expressions and numerical models.

Manufacturing, curing, local imperfections and interaction between bending and shear effects may affect experimental results, complicating in some cases the reliable identification of the SRG-to-substrate bond strength with a four-point bending test setup.

iii. Regarding analytical procedure to predict failure bond value for curved substrate, two trend lines are provided from experimental data: the first one about double lap double prism push-pull test behavior, the second one for four-point bending test.

Comparing both trend line equations, they appear right best-fit linear curves each other, despite scattered data in bending test, due to experimental reasons.

6. Full-scale tests on timber masonry vaults strengthened with Steel Reinforced Grout

ABSTRACT

Masonry vaults can be particularly vulnerable against unsymmetrical service loads, support displacements and seismic actions, such that, in some cases, retrofitting is needed to ensure an adequate safety level according to current standard codes. Externally bonded composites are emerging as a possible retrofitting technique, but no experimental evidence is still available on the response of the vaults reinforced with composites taking into account the contribution of buttresses and backfill. This chapter describes an experimental investigation on four full-scale vault specimens. One of them was tested unreinforced, while the other ones were strengthened with Steel Reinforced Grout (SRG), comprising ultra high tensile strength steel cords, bonded with lime-based mortar either to the extrados or to the intrados. The vaults were subjected to cyclic loading at $1/3$ span. The backfill was visible through a panel of Plexiglas, allowing the use of Digital Image Correlation to measure the displacement field and derive information on damage pattern and arch-fill interaction. Tests showed that SRG prevented the development of the four-hinge mechanism and avoided damage concentrations, increasing the deflection capacity and the strength of the arch by 2-3 times. Finally, it is shown that a simplified analytical approach based on limit analysis provides a reliable estimate of experimental results..

6.1 INTRODUCTION

In many existing buildings all over the world, there are brick masonry vaults that either carry a floor or are simply a ceiling below the roof. They typically span some meters and their thickness ranges between 25cm (two brick heads) and 12cm (one brick head) or even 4-8cm. This latter typology of vaults, in which bricks are laid lengthwise in one single leaf, or multiple leaves, are named timbrel vaults, Catalan vaults (they are widely used in Catalonia, but also other Spanish regions, in Italy, etc.), or Guastavino vaults (from the name of the Spanish architect Guastavino who patented this arch style in the United States in 1885) [Ochsendorf, 2010]. Since their load carrying capacity mainly relies on the shape, the more slender vaults are particularly vulnerable against concentrated forces, unsymmetrical service loads, support displacements and seismic actions. Therefore, retrofitting works are sometimes needed to ensure an adequate safety level according to current standard codes. To this purpose, externally bonded reinforcements with composite materials are particularly advantageous, since they provide high mechanical performances with minimum thickness and mass increase [Valluzzi et al., 2014a].

In masonry arched members, due to the lack of tensile strength, a failure mechanism activates by the formation of four hinges, alternated at the intrados and at the extrados. Composite reinforcements prevent the opening of cracks and, therefore, the development of such collapse mechanism, avoid local falls of bricks, constrain the deflections of the vault and reduce the lateral thrust at the abutments [De Lorenzis et al., 2007]. In principle, the application of the strengthening system to one side only (either to the intrados or to the extrados) is sufficient to prevent the development of the hinges on this side and, therefore, the activation of the collapse mechanism, while bonding the composite material to both surfaces is unnecessary. The intrados reinforcement is faster and cheaper than the extrados one, since the intrados surface is easily accessible from below. Its concave curvature may however reduce the adhesion of the composite and mechanical pins could therefore be needed to improve the reinforcement-to-substrate bond strength. Many times, however, covering the lower surface of the vault is unfeasible since the paintings, the plaster or the fair face of the masonry have to be preserved, and the strengthening system needs to be applied to the extrados. The extrados reinforcement requires that the flooring and the backfill are removed, which entails longer and more expensive work, but this can be easily combined with building side buttress walls or backings

in solid brickwork over the abutments to constrain the deflection of the vault and inserting tie-bars to prevent the relative movement of the side walls.

In the last decades, research activities and field applications have mainly used composites with polymeric matrix (Fibre Reinforced Polymers, FRPs) [Valluzzi et al., 2001-Faraboschi, 2004 – Borri et al., 2009 – Borri et al., 2011 - Cescatti et al., to appear] and, more recently, with inorganic matrix, named Textile Reinforced Mortar (TRM) [Valluzzi et al., 2014a - Borri et al., 2009]. TRMs consist of high strength fabrics (unidirectional textiles or bidirectional meshes) applied to the external surface of the structural members by means of cement or lime mortars. The use of inorganic matrices in place of resins provides better resistance at high temperatures, a higher cost-efficiency, and the possibility of application to wet or irregular surfaces. TRMs with lime-based matrices also fulfil the preservation criteria required for applications to cultural heritage, as, with respect to cement mortars, they ensure a better physical/chemical compatibility with masonry substrates, vapour permeability, and reversibility/removability (possibility of being removed with minimum damage to the substrate). On the other hand, the TRM-to-substrate bond strength may be lower than that of FRPs. The bond resisting mechanism of TRM systems is itself more complex, as failure may occur not only by cohesive debonding within the substrate (as with FRPs) but also by detachment within the thickness of the system or by textile sliding within the matrix [De Santis et al., 2017b].

TRMs have already been proposed to retrofit masonry arches making use of basalt [Cescatti et al., to appear - Garmendia et al., 2014 – Ramaglia et al., 2017], polyparaphenylene benzobisoxazole (PBO) [Alecci et al., 2016], glass [Castori et al., 2016], and steel [Borri et al., 2009 - Cescatti et al., to appear – Girardello et al., 2013 – Garmendia et al., 2015]. They have been applied either to the intrados of the arch [Borri et al., 2009 - Garmendia et al., 2015], to its extrados [Borri et al., 2009 - Cescatti et al., to appear – Garmendia et al., 2014 – Alecci et al., 2016 – Castori et al., 2016, Garmendia et al., 2015], or to both surfaces [Borri et al., 2009 - Garmendia et al., 2014]. In some cases, mechanical connectors were used at the abutments to prevent end debonding [Borri et al., 2009], while in other studies the application of TRM systems was combined with the construction of additional vault rings to increase the arch thickness (the *tabicada* technique) [Castori et al., 2016]. With respect to the unreinforced specimens, the ultimate load of strengthened arches increased by 3 to 20

times, and even more in case of application to both surfaces. The presence of the reinforcement modified the failure mode, since the activation of the four-hinge mechanism that typically occurred on unreinforced arches was replaced by a combination of reinforcement debonding, shear sliding and crushing of masonry, or tensile rupture of the textile. The deflection capacity also increased, in terms of both peak displacement and ductility, which resulted up to 10-15 times larger than those of unreinforced specimens, especially when steel or PBO textiles were used. Relatively lower enhancements were instead generally found on vaults reinforced with weaker textiles (e.g., glass or basalt) due to the brittle failure occurring by rupture of the fibres.

Despite the variability of the results, which is due to the different specimen geometry, material properties, experimental setups and TRM systems under investigation, these studies demonstrated the effectiveness of mortar-based composites for retrofitting masonry arches. The strength improvement achieved with TRMs also resulted comparable, or even higher, to that obtained with FRPs [Borri et al., 2009 - Cescatti et al., to appear - Girardello et al., 2013]. Nevertheless, the specimens tested so far were generally free-standing arches, i.e., backfill was not included. Only few works [Ramaglia et al., 2017 – Girardello et al., 2013] took into account the influence of the buttresses. In [Girardello et al., 2013], however, the buttresses were not built in contrast with a reaction structure, while in [Ramaglia et al., 2017] only the vaults reinforced with TRM were provided with buttresses (that is, the retrofitting work included both the installation of the TRM and the construction of the buttresses). Finally, none of the specimens that have been tested so far were timbrel vaults, the most vulnerable vaulted structures. Therefore no experimental results are available on the gain in load carrying and deflection capacity that can be achieved with mortar-based composites applied to timbrel vaults that are filled to carry a floor on top and provided with buttresses, even if this situation is often faced in retrofitting works.

This paper describes an experimental investigation performed in the laboratory on four vault specimens with 2.9m span, 65cm rise and 55mm thickness, provided with buttresses and backfill. One specimen was unreinforced and three were reinforced with Steel Reinforced Grout (SRG), comprising unidirectional steel cords applied with a lime-based mortar [De Santis et al., 2017a], with the aim of enhancing the load carrying capacity. With respect to the other fabrics used in TRM reinforcements, steel fabrics are stiffer and stronger than glass and basalt, and thicker than carbon,

aramid and PBO, are more durable in alkaline environment, and their shape provides a better interlocking within the mortar matrix [Ascione et al., 2015]. To ensure durability, steel wires are coated with zinc to provide protection against salt attack and prevent rusting [De Santis et al., 2016]. SRG was applied either to the extrados or to the intrados of the vault to investigate the different strengthening layouts can could be faced in field applications. Digital Image Correlation was used to measure displacements. A vertical load was applied over the backfill at 1/3 span and increased cyclically up to failure to investigate the increase in load carrying and deflection capacity provided by SRG and the modification of the associated damage pattern, failure mode, and arch-fill interaction. Finally, the load carrying capacity of the strengthened arches is estimated by limit analysis, using both a static and a kinematic approach.

6.2 EXPERIMENTAL SETUP

6.2.1 Construction of the vault specimens

Four full-scale specimens of timbrel vaults were built in the laboratory, using clay bricks (with 250mm×120mm×55mm size, 15.8kN/m³ unit weight, 14.8N/mm² compressive strength, 2.5N/mm² tensile strength and 5.76kN/mm² Young's modulus [de Felice et al., 2015]) and 10mm joints of lime mortar (5.2N/mm² compressive strength, 0.8N/mm² tensile strength and 1.5kN/mm² Young's modulus). The vaults had 2790mm span, 500mm width, 650mm rise. The bricks were laid lengthwise, i.e., on the shortest side, which resulted in a thickness of 55mm (Figure 6.1).

The experimental setup was designed to apply the most severe static loading condition that a vault can experience, that is, a concentrated load at 1/3 span [de Felice, 2009]. On the other hand, the abutments were fixed, meaning that the relative support movements were assumed to be prevented (e.g., by means of tie-bars [De Santis, 2017]).

To realize the vaults, 205mm high abutments (Figure 6.2a) were first built in contrast with a reaction wall on one side and a stiff steel frame on the other side. Then, the arch barrel, made of 25 voussoirs, two entire bricks alternated with one brick and two half bricks, was built on wood forms (Figure 6.2b). Two buttresses, having 120mm thickness (one brick head), and 445mm height (seven layers), were built at each side (Figure 6.2c). The wood form was removed five days after the construction of the arch (Figure 6.2d). Two 20mm thick lateral panels, one of wood and one of Plexiglas,

were placed on wood supports, and connected by 12 $\varnothing 8\text{mm}$ threaded bars to minimize out-of-plane deflections (Figure 6.2e). The backfill, consisting of 4÷8mm grain size gravel with 12.5kN/m^3 weight and $\phi=39^\circ$ angle of internal friction, was set down manually (it was not densified mechanically), with a depth of 100mm in crown. Finally, a 20mm rubber mat was placed on top (Figure 6.2f).

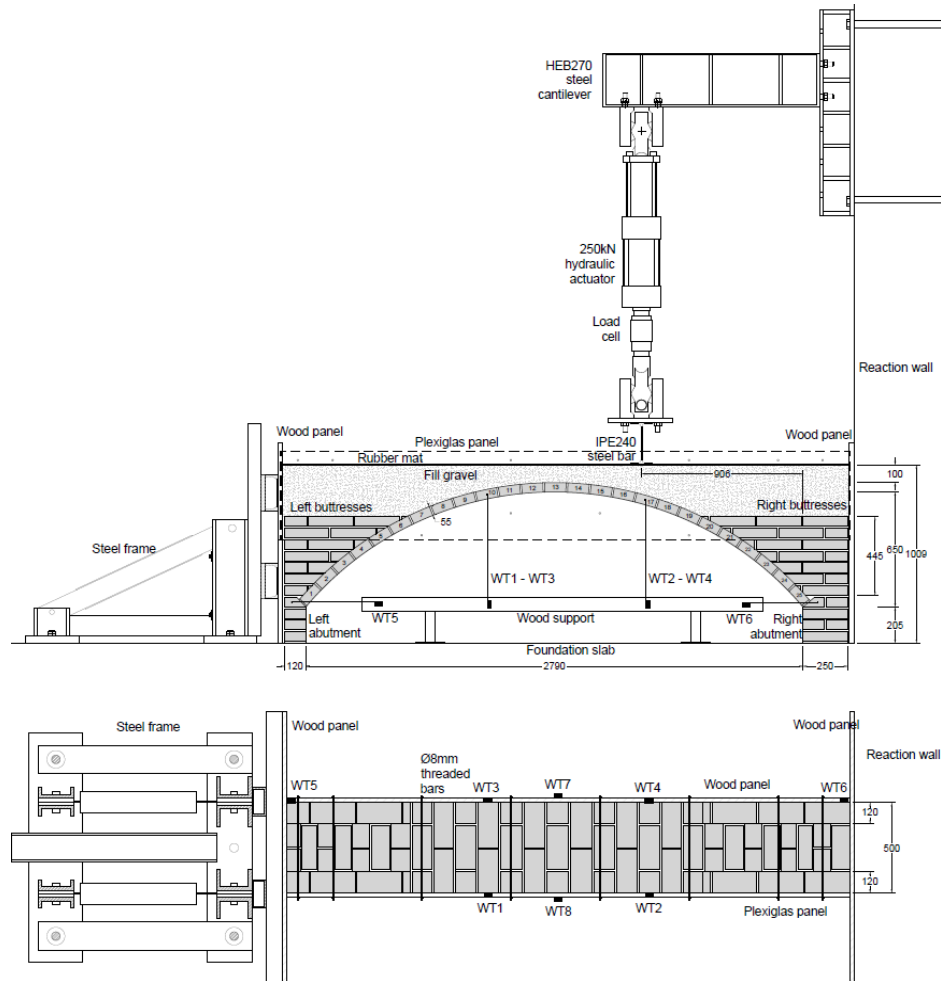


Figure 6.1. Side and top view of the experimental setup.

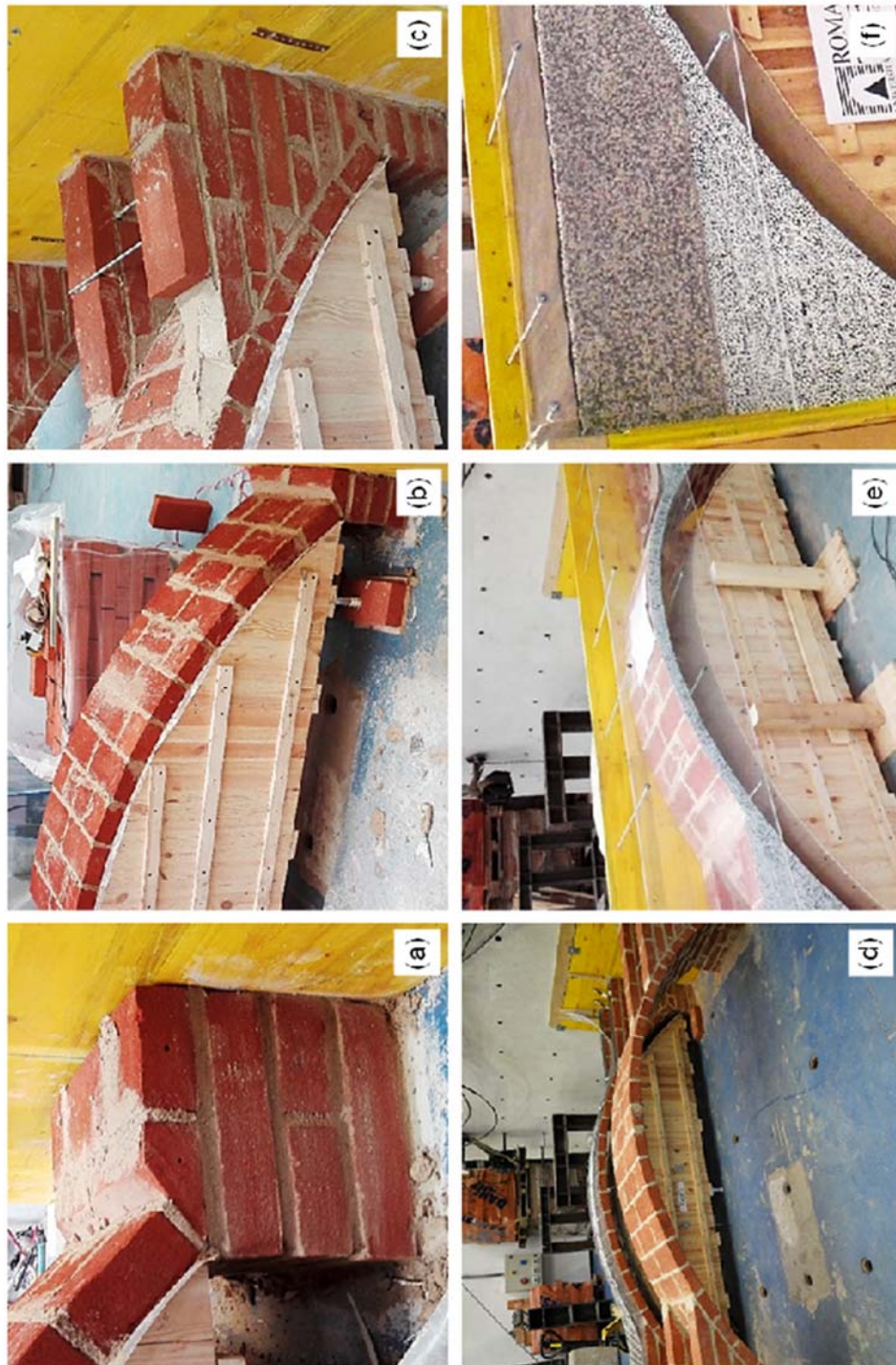


Figure 6.2. Construction of masonry vault specimens.

6.3 STRENGTHENING SYSTEM AND INSTALLATION

6.3.1 Materials

The SRG systems used in this study comprise unidirectional textiles of Ultra High Tensile Strength Steel (UHTSS) cords (Figure 6.3a). Cords are made of five wires with 0.11mm^2 cross section area each, three rectilinear and two twisted around them, galvanized (coated with zinc) to provide protection against rusting. Two textiles were used, having either 8 cords/inch or 4 cords/inch density. The former has 3.18mm cord spacing, 0.168mm design thickness and 1200g/m^2 surface mass density (Figure 6.3b), while the latter has 6.35mm cord spacing, 0.084mm design thickness and 670g/m^2 surface mass density (Figure 6.3c). The steel textiles have 3186N/mm^2 tensile strength (f_t), 184kN/mm^2 Young's modulus (E_f) and 2.26% ultimate strain (from direct tensile tests [De Santis and De Felice, 2015b]). To bond the steel textiles to the vault surface, a lime-based mortar was used, having grain size range of $0\div 1.4\text{mm}$, 20.6N/mm^2 compressive strength (from compression tests on cubic specimens), 11.4kN/mm^2 Young's modulus (from tests on cylinders), and 5.4N/mm^2 tensile strength (from three point bending tests).

For the 4 cord/inch textile, the SRG-to-brickwork bond strength is 2630N/mm^2 on plane substrate [De Santis et al., 2017a], 2880N/mm^2 on convex surface with curvature radius of $R=1800\text{mm}$ [De Santis, 2017], and 1720N/mm^2 for convex surface with $R=1800\text{mm}$ [Malena et al., 2017]; the effective transfer length was estimated in the order of 200-250 mm [De Santis et al., 2017b, De Santis et al., 2017a]. The SRG-to-brickwork bond strength of systems comprising 8 cord/inch textile is 647N/mm^2 on plane substrate, while no information is available on curved substrates.

The following specimens were tested:

- UNR: unreinforced;
- EX8: reinforced at the extrados with a 150mm wide strip of the 8 cord/in textile, with end connectors;
- EX4: reinforced at the extrados with a 150mm wide strip of the 4 cord/in textile, with end connectors;
- IN4: reinforced at the intrados with a 150mm wide strip of the 4 cord/in textile, with intermediate connectors;

The strengthening layouts were designed based on the different bond behaviour that SRG exhibits on curved surfaces. The textile with 8 cord/in, whose smaller spacing may reduce the textile-to-matrix bond strength, was used only for the extrados reinforcement, in which the curvature produces

compressive normal stresses that improve the bond performance [De Santis, 2017]. The 4 cord/in textile, instead, was used for both intrados and extrados reinforcements, because its larger cord spacing provides a better load transfer capacity, so it is suitable also for applications to concave surfaces in which tensile normal stresses take place at the reinforcement-to-substrate interface [Malena et al., 2017].

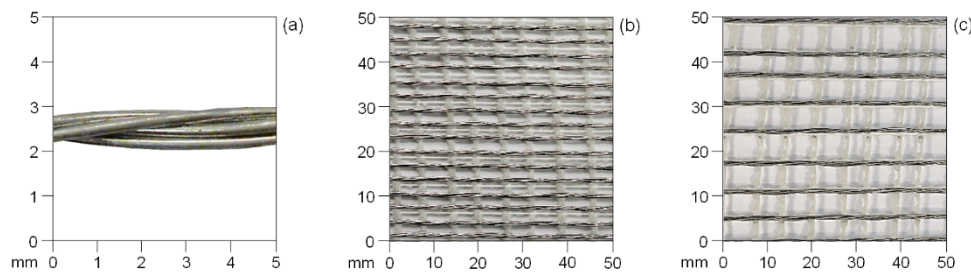


Figure 6.3. Ultra High Tensile Strength Steel (UHTSS) cord (a) and textiles with 8 cord/in density (b) and 4 cord/in density (c).

6.3.2 Extrados strengthening

Two specimens were reinforced at the extrados, one with the textile with 8 cords/in (EX8) and one with the textile with 4 cord/in (EX4). In both cases, a 150mm wide strip, corresponding to 48 or 24 cords, was bonded in the middle of the vault, and connected to the abutments by steel connectors to prevent end debonding. The cross section area of textile was $A_f=25.6\text{mm}^2$ for EX8 and $A_f=12.8\text{mm}^2$ for EX4. The strip was first cut to size and the connectors were prepared by rolling a 280mm long portion of textile. Resistive strain gauges were glued to record strains (Figure 6.4a). Then, the surface of the vault was cleaned with compressed air and wet with water. A first 5mm layer of mortar was laid down (Figure 6.4b). Then, the textile was placed by hand and pressed slightly, to make the fresh mortar protrude through the voids between the cords (Figure 6.4c). A 5mm layer of mortar was applied on top (Figure 6.4d). The overall SRG thickness was about 10mm (Figure 6.4e). Clearly, the thickness of the SRG strip may vary depending on the irregularities of the substrate, especially in field applications. Nevertheless, the variability of the TRM thickness is not expected to significantly affect the response of the reinforced structure provided that it does not exceed 15-20mm [Valluzzi et al., 2014a - De Santis et al., 2017b]. Finally, the connectors were inserted in $\varnothing 40\text{mm}$ holes drilled into the abutments (Figure 6.4f) and injected with a fluid lime-based grout. SRG was kept wet during the first seven days of curing and then left

in standard laboratory conditions (20-22°C temperature and 50-60% relative humidity) for about one month before testing.

6.3.3 Intrados strengthening

One specimen, named IN4, was reinforced at the intrados with the 4 cord/in textile. As in EX4, the steel strip was 150mm wide and included 24 cords ($A_f=12.8\text{mm}^2$). Due to the concave curvature of the substrate, which induces tensile stresses at the SRG-to-masonry interface, seven connectors were realized at 500mm (4 voussoirs) spacing to improve adhesion. To this aim, Ø30mm holes were drilled in the vault before installation (Figure 6.5a). Then, the intrados surface was cleaned and wet with water and the first 5mm layer of mortar matrix was laid down (Figure 6.5b). The textile, equipped with 20 strain gauges, was installed (Figure 6.5c). After the laying of the 5mm top layer of mortar, the steel connectors were inserted in the holes from below. Connectors consisted of a 100mm wide strip of steel textile, with a total length of 200mm, rolled in the initial 100mm upper portion and unfolded for the remaining 100mm lower portion (Figure 6.5d). They were fixed with a resin wedge that kept their shape (Figure 6.5e). A fluid grout was injected from below (Figure 6.5f); it filled the voids between the connector and the masonry within the hole and protruded in the backfill over the extrados, in order to consolidate a small amount of gravel and prevent pull-out.

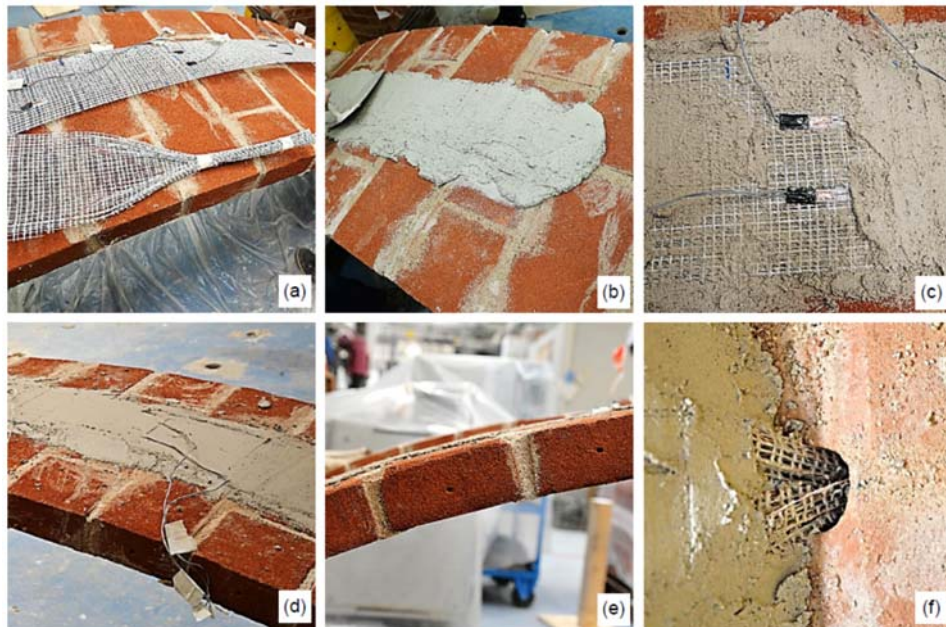


Figure 6.4. Installation of the SRG reinforcement at the extrados of the vault.



Figure 6.5. Installation of the SRG reinforcement at the intrados of the vault.

6.4 INSTRUMENTATION

The load was applied at 1/3 span by means of an MTS 250kN hydraulic actuator, fixed to a reaction wall by a HEB270 steel cantilever (Figure 6.1), and recorded by an integrated load cell. Displacement controlled loading-unloading cycles were performed at 0.05mm/s (loading) and 0.20mm/s (unloading) rate, with increasing amplitude up to failure. A 500mm long IPE240 steel bar was bolted to the head of the actuator to distribute the load over the entire width of the arch specimen and a 120mm large portion of the rubber mat. The load then spread through the gravel down to the vault extrados.

Four wire displacement transducers (WT) were installed on wood supports to measure the vertical displacement of two voussoirs, namely brick 17 (under the load, WT2 and WT4) and brick 10 (WT1 and WT3). Both the front (WT1 and WT2) and the back (WT3 and WT4) sides were monitored to detect possible undesired transversal mismatch. Two wire transducers (WT5 on the left and WT6 on the right) were installed to detect the movements of the abutments. Finally, two transducers were placed on the back wood panel (WT7) and on the front Plexiglas panel (WT8) to measure their out-of-plane deflection. For each of the three reinforced arches, 20 strain gauges were glued to the steel cords before SRG installation to measure the strain in the textile. Given the roughness of the cord surface, small plates of epoxy resin were realized to ensure the correct bond of the strain gauges. For each test, the positions of the strain gauges were selected based on the portions of reinforcement that were expected to undergo tensile stresses. In each of the selected positions, two strain gauges were installed and their average was taken as the strain in the textile in that point. Load, displacement and strain data were acquired at 10Hz sampling frequency.

In addition to these instruments, two-dimensional Digital Image Correlation (2D-DIC) was used to measure the displacements of the front side of the specimen. DIC is a full-field contactless optical method based on the correlation of the digital images taken during test execution, which provides the displacement field of the specimen surface [Blaber et al., 2015]. To apply DIC, a speckle pattern, made of randomly distributed black dots on a white background, was realized on the masonry of the arch barrel and of the buttresses, and the backfill was made of white and black grains. The Plexiglas panel allowed the front side of the specimen (both the brickwork and the gravel) to be visible. Artificial markers (metal plates

provided with the speckle pattern) were also placed on the IPE240 beam to record its displacement. DIC provided both the vertical and the horizontal displacements of the entire surface of the arch and of the buttresses, which would have been unfeasible with traditional devices, since an extremely large number of transducers would have been needed, with unsustainable efforts in terms of cost of equipment and test preparation [De Canio et al., 2016]. DIC also detected crack occurrence (even before it was visible to the naked eye) [Tekieli et al., 2017] and provided information on displacements and strains in the backfill, similarly to what has been recently done on filled arch bridge models with Particle Image Velocimetry (PIV) [Callaway et al., 2012]. During test execution, photographs were taken at 10s time interval with a Nikon D610 digital camera equipped with a lens with a focal length of 85mm. The camera was positioned on a stiff frame at 3.00m from the specimen. Pictures had 6016×4016 pixels, and one pixel had a size of 0.51mm. After the test, image processing made use of a biquintic B-splines sub-pixel interpolation scheme on the displacement field, which led to a resolution of less than 0.1mm and accuracy in the order of 0.1mm [Blaber et al., 2015 – Pan et al., 2009]. Errors related to radial lens distortion (caused by the optical distortion of the image in the zones at a larger distance from its centre) were corrected by the software [Blaber et al., 2015] to improve accuracy. This latter was evaluated as the correlation error between two consecutive pictures taken before the beginning of the test with no load applied, and ranged between 0.11mm and 0.28mm, in the central and in the lateral zones of the specimen, respectively.

6.5 TEST RESULTS

Aiming at showing the typical behaviour of a vault specimen (IN4 was selected as sake of example) and the actual constrain conditions provided by the experimental setup, the displacements measured by WT and DIC are represented against time in Figure 6.6. Downward displacements are assumed as positive, while upward displacements are assumed as negative. First, no mismatch was detected between the displacements on the front and on the back sides of the arch barrel (WT1 vs. WT3 and WT2 vs. WT4, Figure 6.6a), indicating that no transversal uneven redistribution of the load or non-uniform response of the specimen took place. Secondly, the abutments (monitored by WT5 and WT6) resulted basically fixed, especially the right one, which was in contrast with the reaction wall. The

maximum horizontal displacements were in the order of 1mm, and were mainly related to the compaction of the mortar joints and to small cracks developing during load cycles (Figure 6.6b). Finally, the agreement between the displacements recorded by wire transducers and DIC (Figures 6.6a,b) provides a validation of both measurement methods, despite the higher noise of DIC data for small displacements (of less than 1mm). The wood and Plexiglas panels (monitored by WT7 and WT8, respectively) provided a stiff constrain to the fill soil even if their out-of-plane displacements were not completely negligible (up to 1.4mm), especially in the final part of the test (Figure 6.6c).

The first unloading-reloading cycles were performed at 1kN interval (i.e., load was reduced when 1kN, 2kN, etc. were attained). These cycles mainly compacted the backfill without producing significant deflections of the arch barrel. Additionally, the residual displacements at the end of the unloading cycles were mainly related to such compaction of the gravel rather than to irreversible deflections of the vault, with the only exception of the last cycles (Figure 6.6d).

Test results are described and commented hereafter. The load-displacement response curves are shown in Figure 6.7, having the load on the y-axis and the vertical displacements of bricks 17 and 10 on the x-axis. As before, downwards displacements, as well as the load, are assumed as positive, while upwards displacement are assumed as negative. Figures 6.8-11 show the crack pattern and the failure modes of the tested specimens; Figures 6.9-11 also show the strain profiles in the steel textile, plotted for selected steps of the test identified by letters A-H and associated to progressive values of displacement of brick 17 (s) and of applied load (F). The strain profiles are not represented in the region where the SRG is compressed and does not provide any contributions. The damage patterns of the reinforced vaults are collected in Figure 6.12. The deformed configurations measured by DIC at peak and at collapse of the axis of the vault and of the top surface of the backfill are shown in Figure 6.13. Finally, the fields of vertical displacements (on which the self-weight and the external load spend work) recorded by DIC on the entire lateral specimen surface are shown in Figures 6.14 (at peak load) and 6.15 (at collapse) together with the arrows of total displacements.

Main test results are collected in Table 6.1, in which F_{\max} is the maximum load and ΔF_{\max} is its ratio with respect to that of the unreinforced vault, $s(F_{\max})^+$ and $s(F_{\max})^-$ are the displacements corresponding to F_{\max} of bricks 17 and 10, respectively, and s_u^+ and s_u^- are their ultimate displacements (at

failure). Finally, ε_{\max} is the maximum strain measured on the textile, σ_{\max} is the stress estimated as $\sigma_{\max} = \varepsilon_{\max} \cdot E_f$ (considering that the stiffening effect of the lime mortar matrix is negligible after cracking and that the steel cords exhibit a non-linear response only when the stress is close to the tensile strength [De Santis et al., 2017a - De Santis, de Felice, 2015b]), and η is the exploitation ratio of the tensile strength of the textile calculated as $\eta = \sigma_{\max} / f_t$.

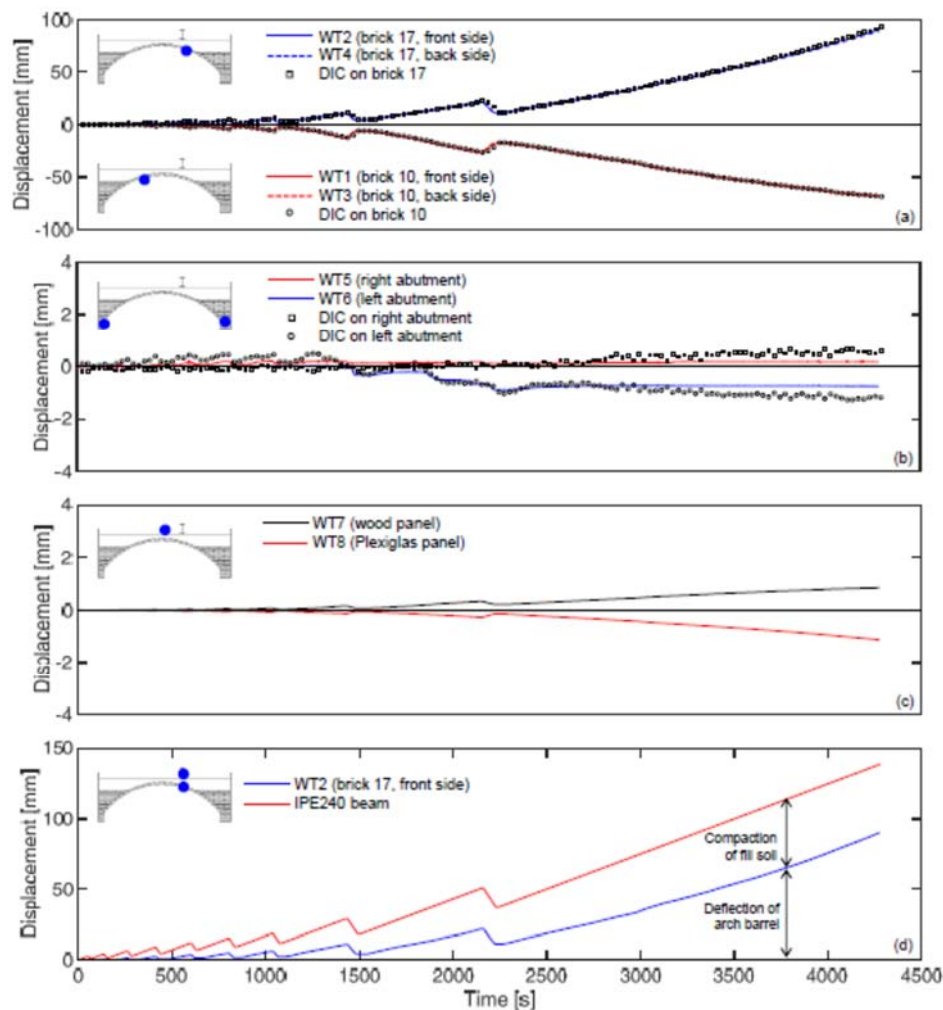


Figure 6.6. Vertical displacements of bricks 10 and 17 (a), horizontal displacements of the abutments (b), out-of-plane displacements of the wood and Plexiglas panels (c), and vertical displacements of brick 17 and of the IPE240 beam (d) vs. time.

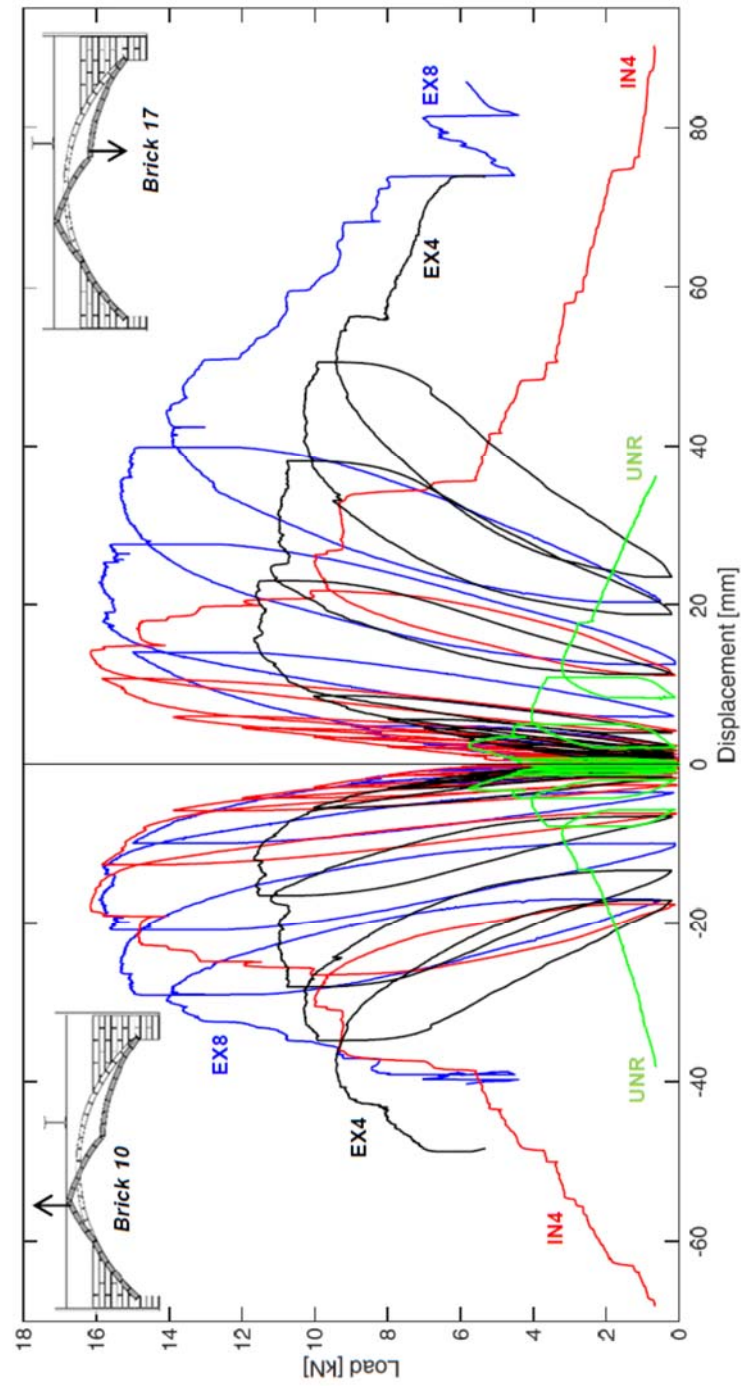


Figure 6.7. Load-displacement response curves.

Table 6.1. Test results

Specimen	F_{\max} [kN]	ΔF_{\max} [-]	$s(F_{\max})^+$ [mm]	$s(F_{\max})^-$ [mm]	s_u^+ [mm]	s_u^- [mm]	ξ_{\max} [-]	σ_{\max} [N/mm ²]	Failure mode
UNR	5.8	-	2.2	-3.1	36.1	-38.1	-	-	Four hinge mechanism
EX8	15.9	2.74	22.8	-17.0	85.8	-40.3	6.7×10^{-3}	1233	Crushing, SRG detachment, sliding
EX4	11.7	2.02	15.8	-12.0	73.9	-48.8	2.5×10^{-3}	460	Sliding and crushing
IN4	16.2	2.79	13.9	-17.9	90.3	-68.1	3.7×10^{-3}	681	SRG detachment, unfolding of connectors

6.5.1 Unreinforced vault

In the unreinforced arch (UNR), after the initial cycles that compacted the backfill, cracks appeared on the arch barrel after a load of 4kN was overstepped. This produced a reduction of the stiffness with the development of the first non-negligible vault deflections. A four-hinge mechanism developed, with hinges between bricks 6-7 (crack at the intrados), 11-12 (extrados), 16-17 (intrados, below the load), and 20-21 (extrados), as shown in Figure 6.8. The hinges in the central region of the arch (11-12 and 16-17) appeared before the peak load, while the other ones developed in the post-peak phase. The maximum load was 5.9kN. Then, a post-peak phase took place during which the load carrying capacity decreased linearly. At the end of the test, the displacement of brick 17 was $s(F_{\max})^+ = 36.1\text{mm}$ (downwards), while that of brick 10 was $s(F_{\max})^- = -38.1\text{mm}$ (upwards). The buttress walls reduced the real span of the arch, especially on its left side, whose upward movement was constrained. On the other side, a crack developed between the extrados of the arch and the buttress, which, therefore, had a negligible influence on the response of the vault since its right portion moved downwards.

It is worth noting that the load carrying capacity of the vault without backfill, estimated using a limit analysis approach, is 0.6kN if buttresses are neglected, 1.8kN if buttresses (but no backfill) are included, or, finally, 3.4kN if the self-weight and the load spreading effect of the backfill are considered but the contribution of this latter to the resistance (related to the passive pressures associated to vault upward deflections) is neglected.

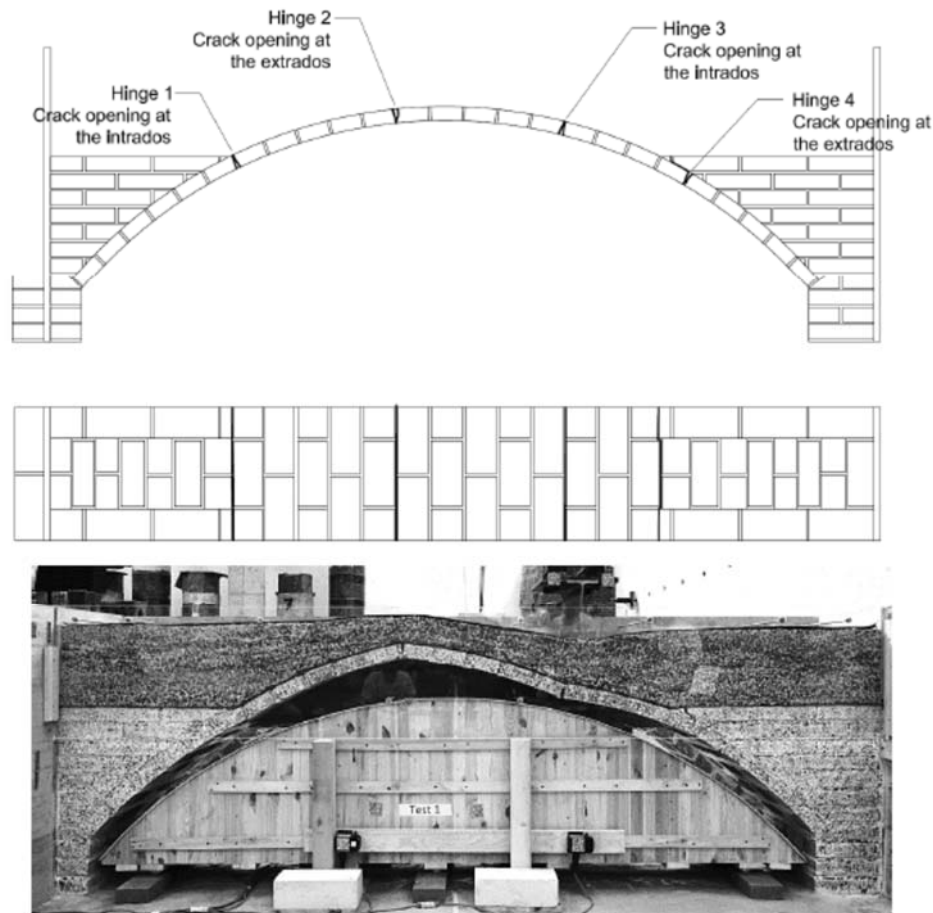


Figure 6.8. Failure mode of UNR specimen.

6.5.2 Vaults reinforced at the extrados

The vault reinforced with the 8 cord/in textile at the extrados (EX8) attained a maximum load of 15.9kN (+174% with respect to UNR). The SRG limited the opening of cracks at the extrados and the upward deflection of the arch, while a crack developed at the intrados between bricks 16-17 (below the load) and between bricks 5-6, also involving the left buttress wall (Figure 6.9). When approaching the maximum load, detachment activated at the textile-to-matrix interface, cracks appeared also at the extrados between bricks 12-13 (Figure 6.12b) and between brick 25 and the right abutment. With respect to UNR, the failure mechanism involved a larger portion of arch barrel, and the four hinges were associated to a shear

sliding between bricks 16-17 (Figure 6.12a) and to a significant crushing of the masonry. Apart from the compressed edges of the bricks at the hinges, a longitudinal crack also appeared in the middle of the arch barrel (Figure 6.12c), indicating that the reinforcement led to the attainment of a high bending moment, associated to high compressive stresses. At collapse, the vault detached from the right buttress, which was also involved in the failure mode, as it separated from the abutment and rotated around the springing section. Since the SRG was not visible during text execution, progressive damage development could not be detected. After the end of the test, the backfill was removed and the final damage pattern was surveyed. Detachment took place at the textile-to-matrix interface where the extrados was compressed, thus appearing mainly due to instability rather than to shear. On the other hand, the development of cracks at the extrados indicated that some sliding had occurred between the cords and the mortar, reducing the effectiveness of the reinforcement.

The stiffness of the reinforced arch in the very first phase of the test (load lower than 4kN) was basically the same of UNR, since the SRG was not involved in the response, as revealed by the negligible strain recorded on the cords (see the profile at stage A in Figure 6.9). Then, the load was transferred to the reinforcement between bricks 9 and 15 and between 21 and 25, where it was subjected to tensile stresses to constrain the opening of cracks at the extrados. This resulted in a stiffer behavior than UNR (Figure 6.7). Moreover, the SRG entailed a higher peak deflection, $s(F_{\max})^+$ being ten times larger. Accordingly, the displacement field recorded by DIC in the backfill indicated that, with respect to UNR, a larger volume of backfill was mobilized above the extrados surface of the vault that moved upwards (Figures 6.14a,b). Finally, at collapse, the extrados reinforcement allowed for a more distributed deflection of the left portion of the vault, moving upwards (note that the values of s_u^- are similar), while much larger displacements were recorded under the load (s_u^+) due to the concentration of rotation at the intrados hinge (between bricks 16 and 17).

The strain in the steel cords at the attainment of the peak load (stage E) was 2.8×10^{-3} (corresponding to a stress of about 515N/mm²) and was recorded by the strain gauges placed over brick 11 (Figure 6.9), while the maximum strain value was $\varepsilon_{\max} = 6.7 \times 10^{-3}$, corresponding to an estimated stress $\sigma_{\max} = 1230\text{N/mm}^2$ (38.7% of its tensile strength). Such strain level was reached at brick 11 in the first part of the post-peak phase (stages F and G). Then, it partially reduced to 5×10^{-3} (stage H) when the strain redistributed over a longer portion of SRG (between bricks 9 and 15). The most stressed portion

of SRG was far enough from the left abutment that the load was effectively transferred by SRG-to-substrate adhesion and the connector remained unused. It should also be considered that, in this region, the extrados of the vault was compressed and its upward movement was constrained by the buttress. The connector on the right abutment, instead, was involved in the response of the vault, especially when approaching failure, after the SRG had already detached from the masonry substrate. No pull-out failure however occurred.

EX4 specimen (reinforced at the extrados with the 4 cord/in textile) attained a maximum load of $F_{\max}=11.7\text{kN}$ (+102%), with a displacement of brick 17 of $s(F_{\max})^+=15.8\text{mm}$ (Figure 6.7). Failure occurred by shear sliding between bricks 16-17 and 17-18 (Figure 6.12d), at $s_u^+=73.9\text{mm}$. Cracks also appeared at the intrados between bricks 5-6, at the extrados between bricks 11-12 and 13-14, and, finally, at the extrados between brick 25 and the right abutment, with a detachment from the buttress (Figure 6.10). The position of the hinges was analogous to EX8. In EX4, however, no detachments were detected in the SRG (thanks to the better textile-to-matrix interlocking of the 4 cord/in textile with respect to the denser 8 cord/in one), apart from where shear failure took place and over bricks 6-8, which was probably related to a local dip of the vault surface (Figure 6.12e). A longitudinal crack developed (Figure 6.12f), but if it was narrower than in EX8, due to the lower applied load. The lower load carrying capacity with respect to EX8 may be attributed to the larger deformability of the SRG (which did not constrain the arch deflections with the same effectiveness), but also to local imperfections or initial misalignments of the bricks in the arch barrel below the load, where shear sliding occurred.

The displacement capacity of EX4 was similar to that of EX8, with an even slightly larger ultimate upward displacement (s_u^-), associated to a less steep post-peak branch, due to the lower axial stiffness of the reinforcement (Figure 6.7). Indeed, the deformed configurations at peak and at collapse show only slightly larger displacements of the entire left portion of the vault (moving upwards, Figures 6.13c,d, 6.14c,d and 6.15c,d). The displacements measured by DIC indicate that these larger displacements were associated to a higher concentration in the backfill over the extrados on the left side (Figures 6.14c and 6.15c).

Similarly to EX8, the portion of SRG that was significantly involved in the response was comprised between bricks 9 and 15, even if, in this case, strains mainly concentrated at brick 13, and near the left abutment (Figure

6.10). Since the load was lower than in EX8, however, the strain at peak load (stage C) was 1.8×10^{-3} (corresponding to a stress of 330 N/mm^2) at brick 13, while the maximum strain was $\varepsilon_{\max} = 2.5 \times 10^{-3}$ ($\sigma_{\max} = 460 \text{ N/mm}^2$, $\eta = 14.4\%$). The connector on the right abutment reached a strain of 1.8×10^{-3} at stage H (end of the post-peak phase, close to collapse) indicating that it contributed to the behaviour of the reinforcement system, but it was not pulled out. Finally, on the left portion of SRG, the strains were basically null.

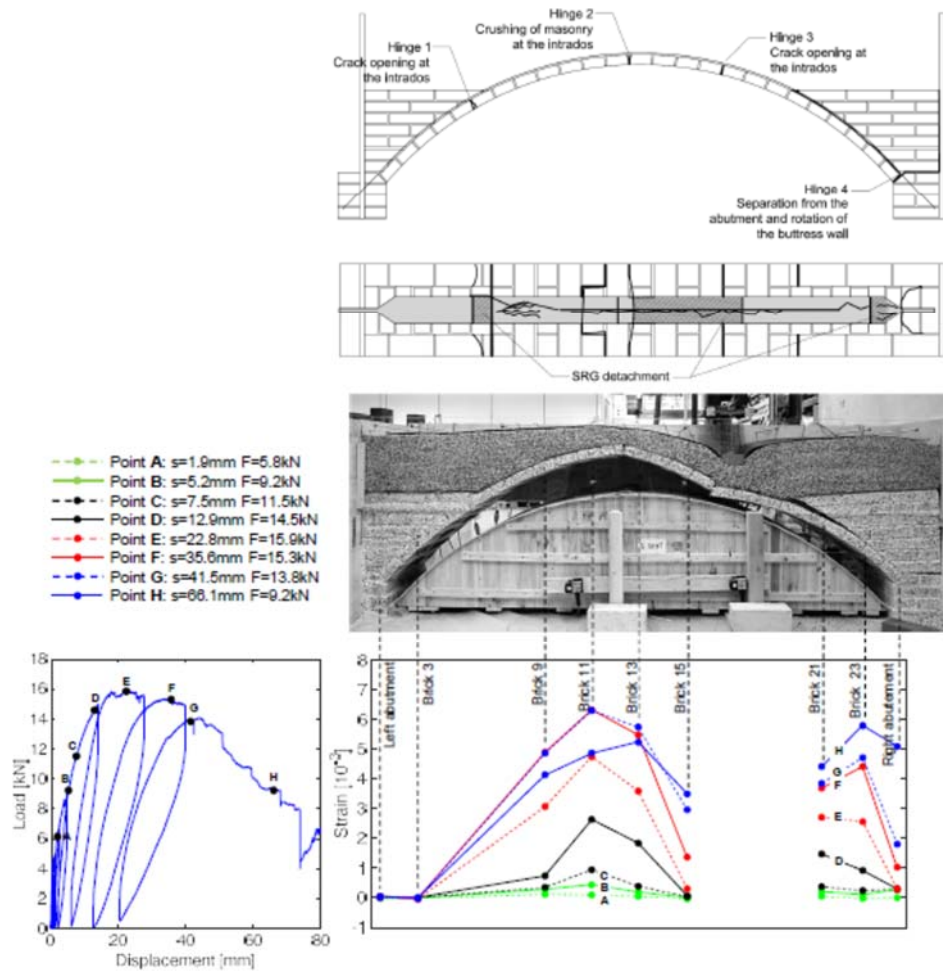


Figure 6.9. Crack pattern, failure mode and strains in the textile of EX8 specimen.

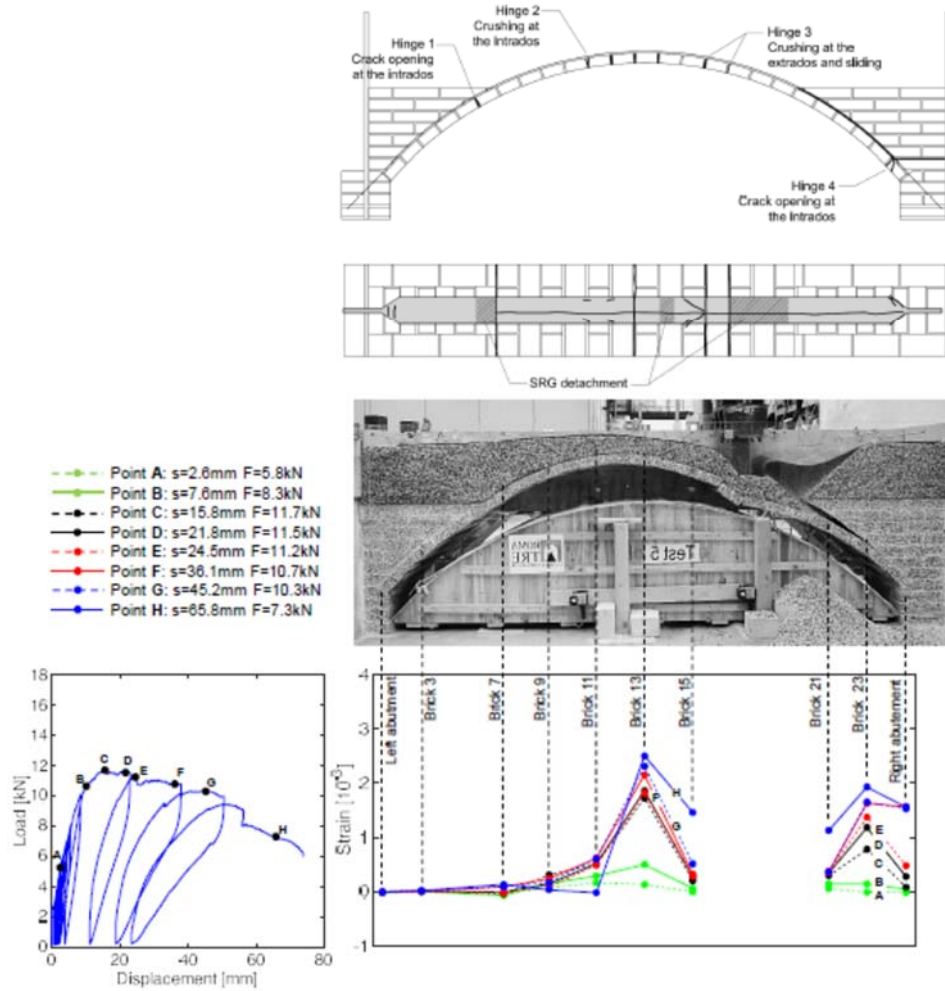


Figure 6.10. Crack pattern, failure mode and strains in the textile for EX4 specimen.

6.5.3 Vault reinforced at the intrados

The maximum load exhibited by the arch reinforced with the 4 cord/in textile at the intrados (IN4) was 16.2kN (+179%). The downward displacement of brick 17 at the peak $s(F_{\max})^+$ was lower than in EX8 and EX4 (Figure 6.7), due to the presence of the SRG at the intrados. This was not associated to an increase of the peak upward displacement of brick 10 $s(F_{\max})^-$, even if no reinforcements were bonded to the extrados. At the attainment of the peak load, SRG detached at the textile-to-matrix interface between the connectors in the whole central portion of the arch barrel, due to the tensile normal stresses caused by the concave curvature of the

substrate. Since the connectors did not pull out, the textile still worked as an unbonded tendon in this region and contributed to the load carrying capacity of the arch in the post-peak phase (Figure 6.12g). Between the left abutment and brick 8, instead, the SRG effectively prevented the opening of a crack at the intrados (Figure 6.12h). The steel cords experienced a strain of 1.1×10^{-3} (200N/mm²) at peak load (stage D) and of $\epsilon_{\max} = 3.7 \times 10^{-3}$ ($\sigma_{\max} = 681 \text{ N/mm}^2$, $\eta = 21.4\%$) at collapse (stage H), with a progressive increase between bricks 2-6, while a sudden strain growth was recorded at brick 8 in the very last part of the test (Figure 6.11). The SRG detachment from the substrate made the readings of the strain gauges unreliable between bricks 14-20 in the post-peak phase (stages from E to H).

None of the steel connectors was pulled out, indicating an effective anchorage in the arch section and in the backfill consolidated by the grout injection. Nevertheless, those in the middle of the arch (which experienced the highest stresses) were unfolded and their wedge was partially expelled, which compromised their effectiveness and led to a faster decrease of the post-peak strength with respect to the arches reinforced at the extrados. The ultimate displacements (s_u^+ and s_u^-) were slightly larger than in EX8 and EX4, but were associated to much lower load values.

After the detachment of SRG, hinges developed between bricks 6-7 (intrados), 10-11 (extrados), 16-17 (at the intrados, below the load), and 21-22 (extrados, with detachment from the buttress wall), as shown in Figures 6.11 and 6.12i. The masonry locally cracked where the hinges formed. The left buttress also cracked and detached from both the arch barrel and the abutment, but it was not directly involved in the collapse mechanism. Cracks in the buttress mainly developed during the unloading cycles due to its lower capacity of following the downwards deflection of the underlying vault that took place when the load decreased.

Both the deformed configurations and the displacement fields indicate that the intrados reinforcement entailed a more distributed downward deflection of the right portion of the vault (Figures 6.12e,f), while it did not prevent the localization of backfill mobilization on the other side, where a crack developed at the extrados and the arch barrel (Figure 6.14g). The comparison between EX4 and IN4 specimens, in which SRG had the same axial stiffness, indicates that the intrados reinforcement entailed a stiffer behaviour of the vault when subjected to vertical loads.

Thanks to the use of the Plexiglass panel, the backfill was visible and the displacement fields were measured by DIC. This provided information on the volume of gravel that was mobilized in the tests and on arch-fill

interaction. Some differences are clearly identifiable between the unreinforced vault and the reinforced ones. SRG entailed the involvement of a much larger volume of backfill, both on the left side (moving upwards) and on the right side (moving downwards). Furthermore, at peak load (Figure 6.14), when the displacement fields were mainly related to the load distribution, the inclination of the boundary lines that identify the volume of mobilized backfill was $36\text{--}37^\circ$ in UNR and $42\text{--}43^\circ$ in the other specimens. As a result, the portion of arch barrel involved in the response was larger in reinforced vaults (between bricks 15 and 18) than in the unreinforced ones (bricks 14-21).

At failure (Figure 6.15), the displacement fields, mainly related to the collapse mechanism (i.e., to the position of the hinges), indicate that in IN4 (Figure 6.15d) a larger volume of backfill was mobilized below the load with respect to the other specimens, thanks to the broader distribution of downwards displacement provided to the arch barrel by the intrados SRG. On the left side, instead, a localization of displacement was detected in IN4 (Figure 6.15d). Such concentration was found also in UNR (Figure 6.15a) but not in EX8 (Figure 6.15b) and EX4 (Figure 6.15c) in which the extrados SRG entailed a broader distribution the load transferred to the backfill by the arch barrel moving upwards.

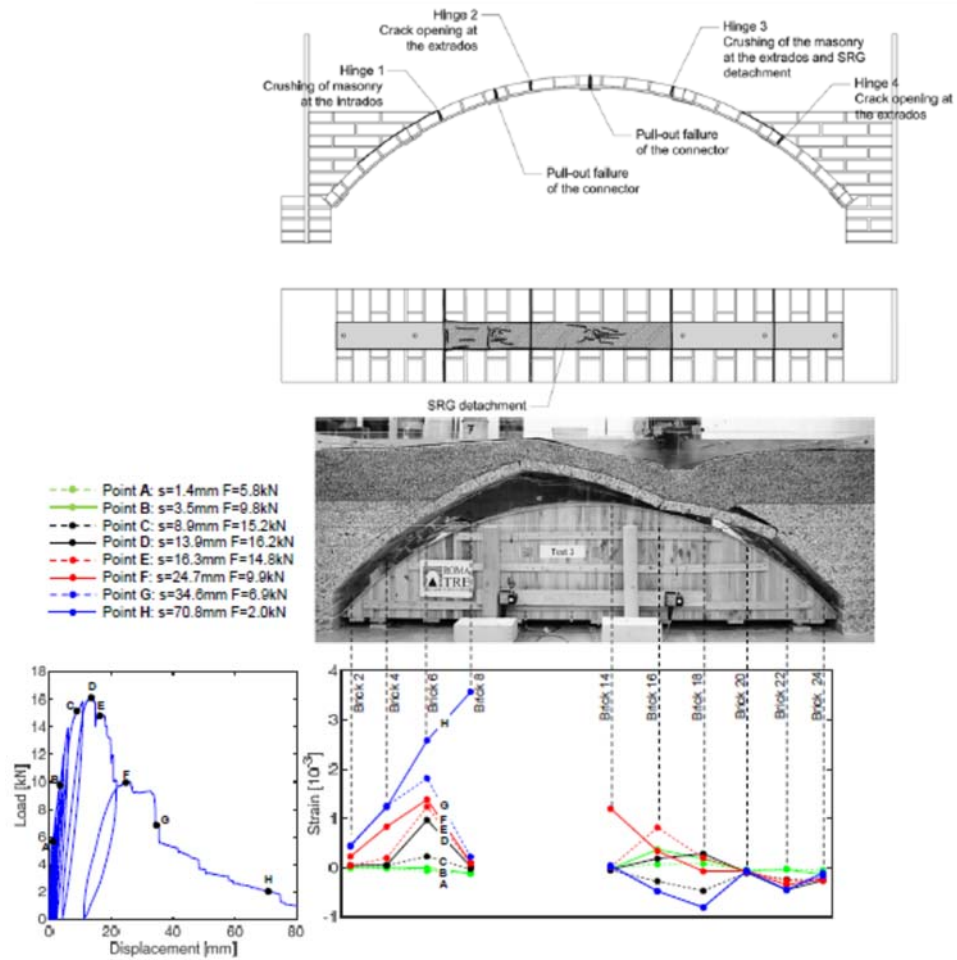


Figure 6.11. Crack pattern, failure mode and strains in the textile for IN4 specimen.



Figure 6.12. Damage pattern surveyed after the test on EX8 (a-c), EX4 (d-f) and IN4 (g-i) vault specimens.

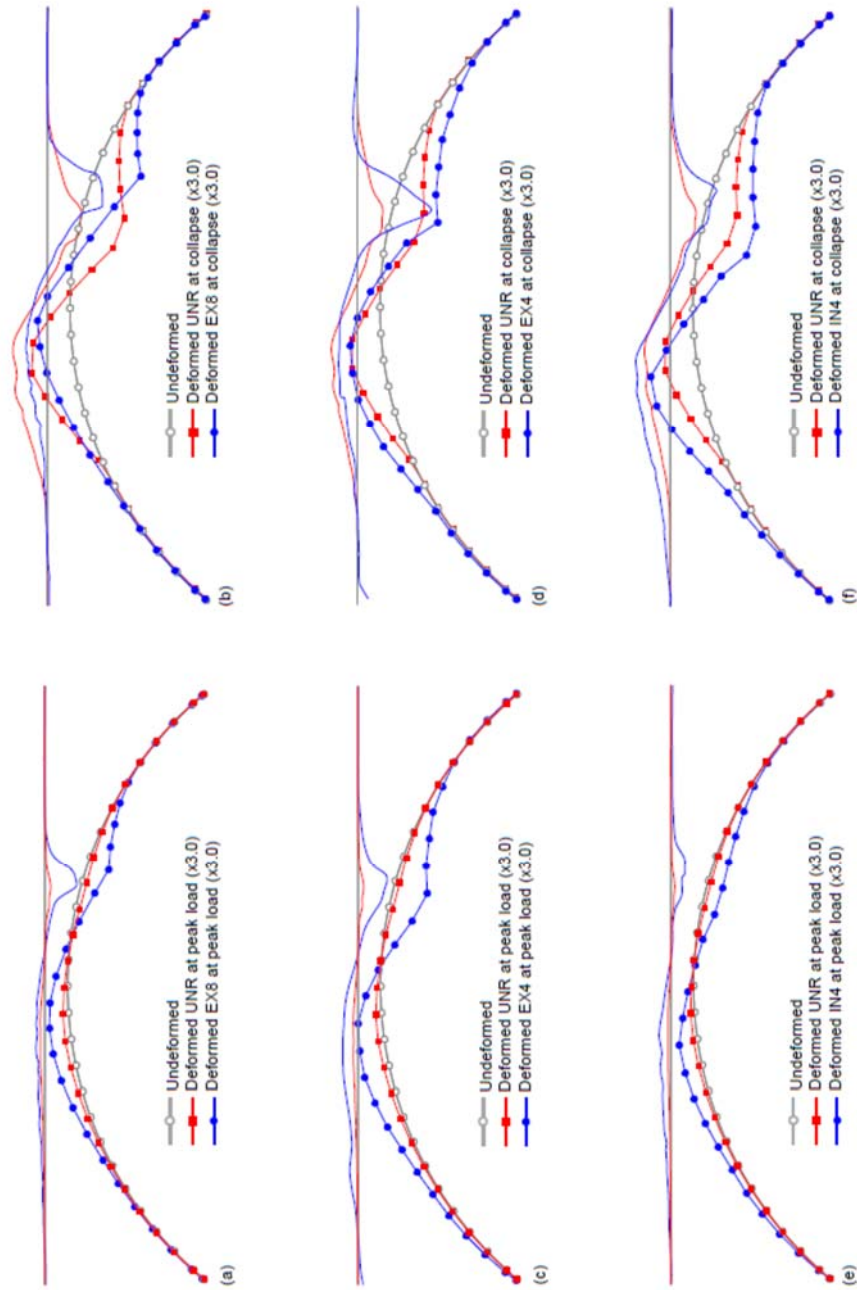


Figure 6.13. Deformed configurations of EX8 (a,b), EX4 (c,d) and IN4 (e,f) specimens compared to those of UNR at peak load (a,c,e) and at collapse (b,d,f).

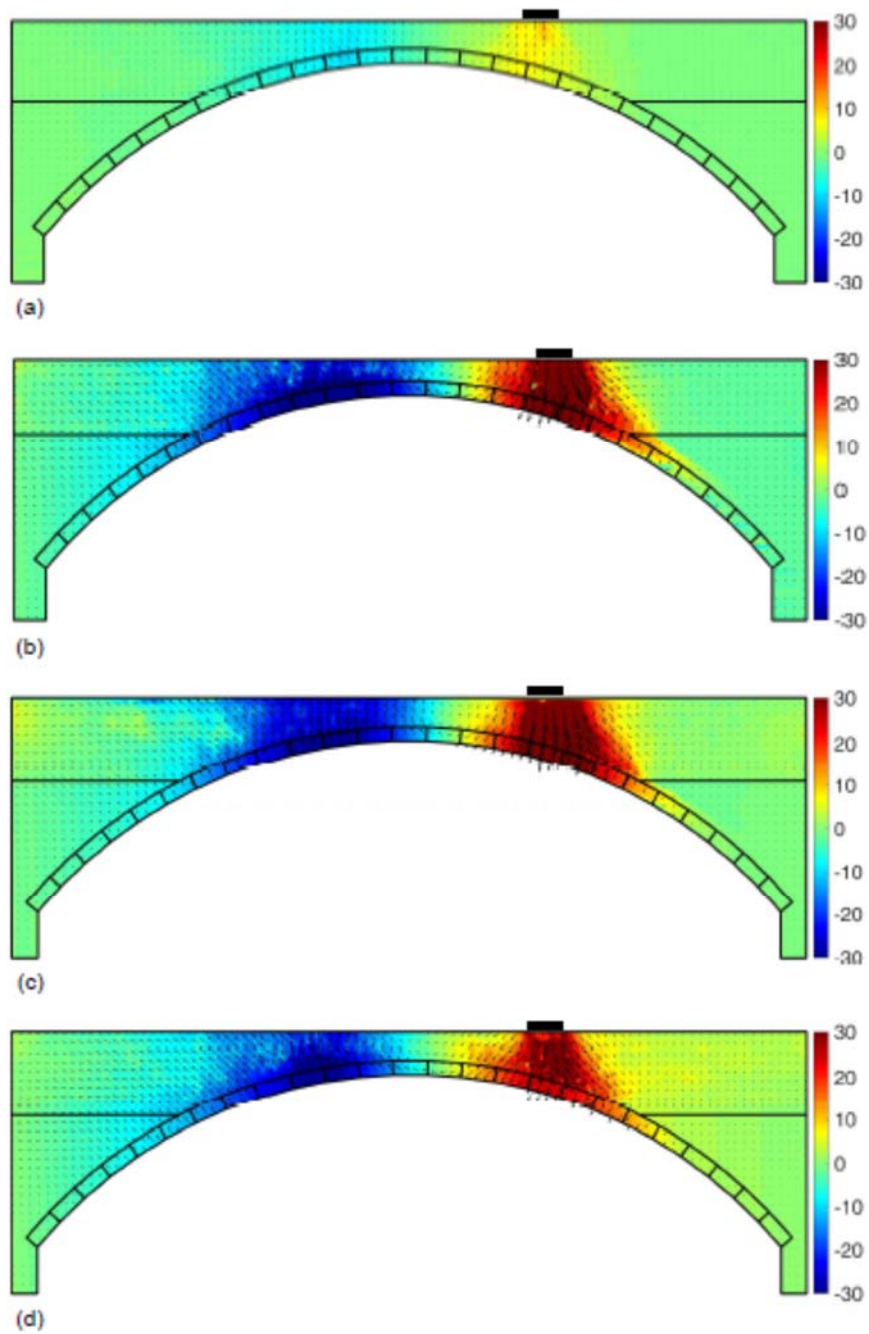


Figure 6.14. Field of vertical displacements and arrows of total displacements at peak load in UNR (a), EX8 (b), EX4 (c) and IN4 (d) specimens. Arrows scaled by 2.

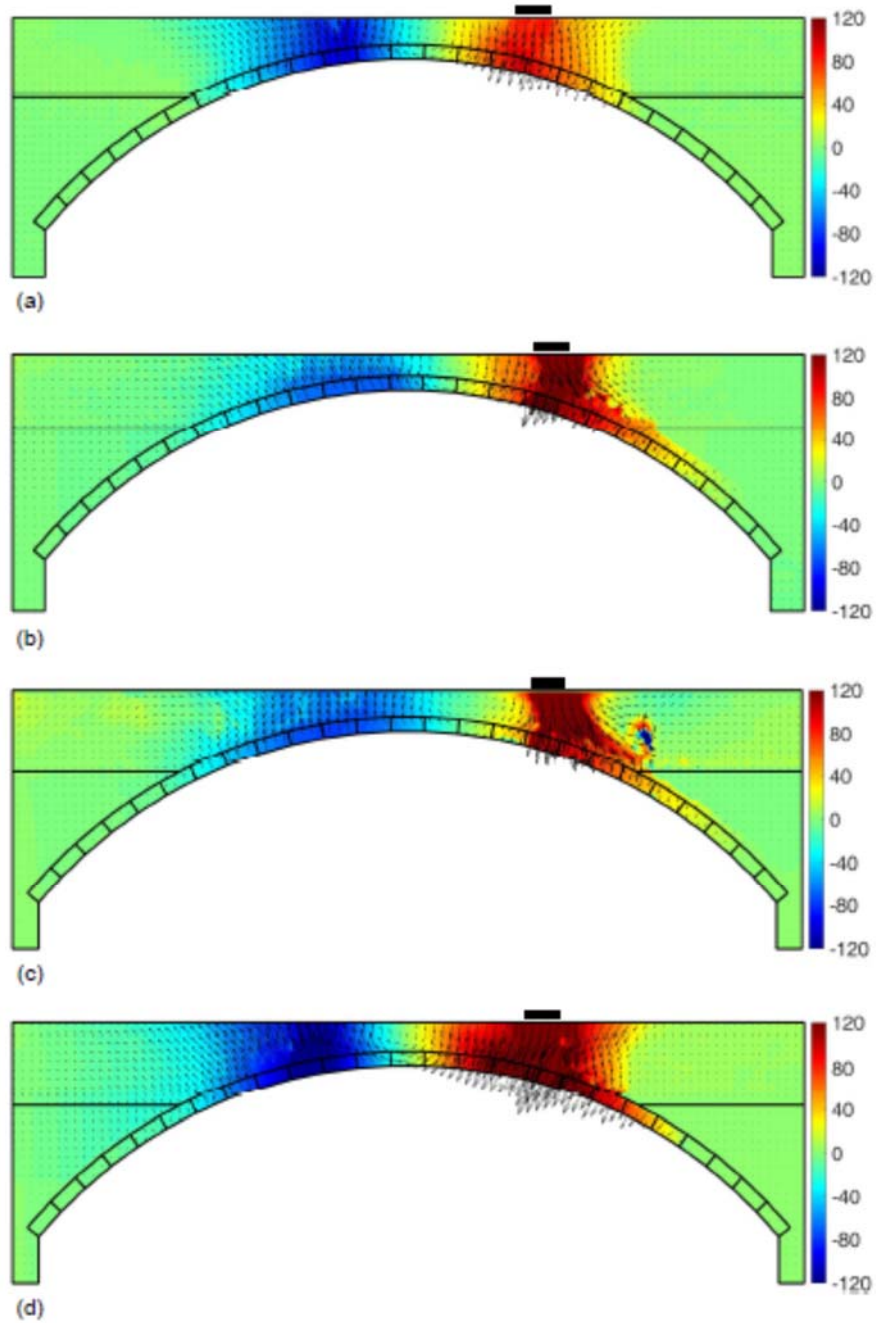


Figure 6.15. Field of vertical displacements and arrows of total displacements at collapse in UNR (a), EX8 (b), EX4 (c) and IN4 (d) specimens. Arrows scaled by 0.8.

6.6 ANALYTICAL ESTIMATE OF THE LOAD CARRYING CAPACITY

In this section, the load carrying capacity (F_{\max}) of the reinforced arch specimens EX8 and IN4 is estimated with a simplified analytical method based on limit analysis. EX4 is excluded because shear failure is not predicted by this approach. Both a static and a kinematic approaches are used, starting from the collapse mechanism observed in the experimental tests and identified by the position of the four hinges, as shown in Figure 6.16.

Masonry is assumed to have no tensile strength and infinite friction angle. For SRG, the maximum attainable load F_s assumed in the analysis is the product of the tensile strength $f_t=3186\text{kN/mm}^2$ and the cross section area of the textile, which results in $F_s=81.6\text{kN}$ for EX8 ($A_t=25.6\text{mm}^2$) and $F_s=40.8\text{kN}$ for IN4 ($A_t=12.8\text{mm}^2$). Finally, as for the backfill, the self-weight and the load spreading effect (depending on the angle of internal friction $\varphi=39^\circ$) are considered, but passive pressures are neglected.

In the static approach, the axial force (N) - bending moment (M) strength domain of the cross section is built for the vault reinforced at the extrados (Figure 6.17a) and at the intrados (Figure 6.17b). A compressive strength of the masonry of 8N/mm^2 is considered and it is assumed that failure is attained at the same time in the masonry and in the SRG. In the arch reinforced at the extrados, starting from the position of the hinges provided by experiments (Figure 6.16a), equilibrium is obtained requiring that the stress resultant in sections 1 and 3 (see Figure 6.17a) is applied at the hinges. The maximum statically and plastically admissible load F_{\max} is then obtained by imposing that in sections 2 and 4, the N,M stress state falls on the boundary of the domain. According to this approach, the balance and strength conditions are established only at the hinge sections. The static approach provides an estimated F_{\max} of 14.0kN (-12% with respect to the experimental value). In a similar manner, for the arch reinforced at the intrados (Figure 6.16b), the maximum load that is in equilibrium and satisfies the strength condition in Figure 6.17b is equal to 14.1kN , which is 13% lower than the experimental value.

In the kinematic approach, the collapse mechanism provided by the experiments is considered as shown in Figure 6.16, for either the reinforcement at the extrados or at the intrados, resulting in the vertical component (v) of the displacement field as depicted in the figure. It is assumed that the masonry is rigid and, for the sake of simplicity, that it has

infinite compressive strength, which yields that the hinges develop at the edge of the cross section. Collapse occurs when the work spent by the external loads (self-weight of vault and backfill, and external load F) in the displacement field (v) equals the maximum resisting work given by the tensile load F_s in SRG at hinges 2 and 4 in the arch reinforced at the extrados and at hinges 1 and 3 in that reinforced at the intrados. F_s spends work in the relative displacement associated with the hinge opening, which is given by $t \cdot \theta$, t being the thickness of the vault and θ the relative rotation of the two portions separated by the hinge. By using the kinematic approach, the estimated F_{\max} is 17.8kN for the arch reinforced at the extrados (+12% with respect to the experimental value) and 18.5kN for that reinforced at the intrados (+14%).

Both limit analysis approaches provide a reliable estimate of the load carrying capacity, thus appearing suitable for an expeditious assessment of the vault strengthened with externally bonded TRM/SRG and for a preliminary reinforcement design. However, the simplifying assumptions may result in a reduction of the accuracy, especially in the kinematic approach, for which the error is not on the safe side. Finally, differently from the present case, the position of the plastic hinges is generally unknown a priori and needs to be either assumed based on experience or determined as that associated to the lowest value of the external load.

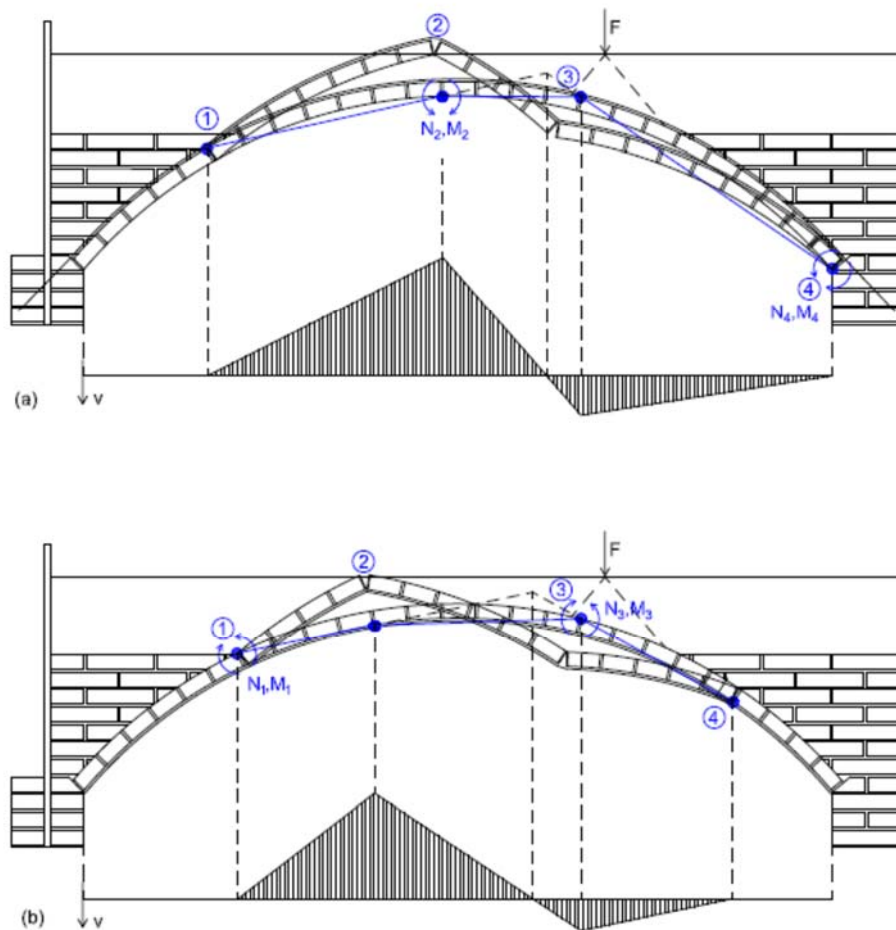


Figure 6.16. Collapse mechanisms of EX8 (a) and IN4 (b) specimens used for the analytical estimate of their load carrying capacity with limit analysis based approaches.

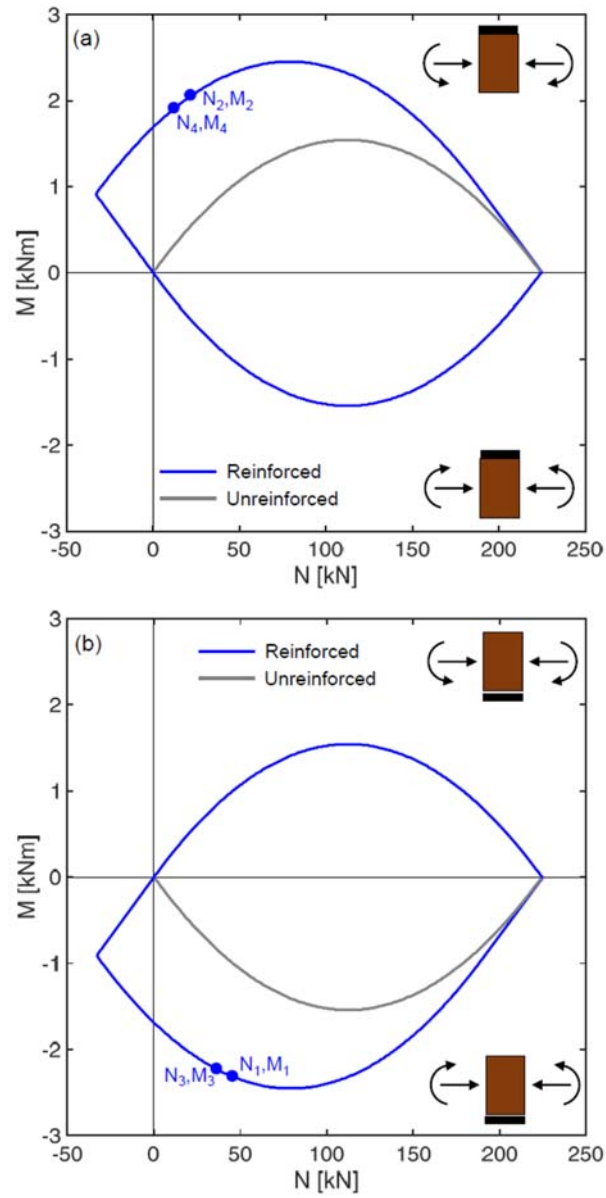


Figure 6.17. Axial load – bending moment strength domains of the cross section of the arch reinforced at the extrados (a) and at the intrados (b).

6.7 CONCLUDING REMARKS

An experimental investigation was carried out on full-scale masonry vaults, provided with buttresses and backfill, subjected to a cyclic load at 1/3 span. The specimens were strengthened with Steel Reinforced Grout, either to the extrados or to the intrados. Two textiles were used for extrados reinforcements, having density of either 8 cord/inch or 4 cord/inch. The former solution provided an increase of load carrying capacity of 174% with respect to the unreinforced specimen. Collapse occurred by a combination of crushing and shear sliding of brickwork and debonding of the reinforcement at the textile-to-matrix interface. SRG with the 4 cord/inch textile led to a relatively lower gain in strength (+102%), due to its higher deformability, which entailed larger deflections of the arch barrel up to the occurrence of a shear failure. The exploitation of the textile was lower than in the previous case, even if the lower cord density provided a better bond behaviour that prevented detachments. In extrados reinforcements, steel connectors effectively prevented end debonding at the abutments.

The intrados reinforcement was realized with the 4 cord/inch textile. In this case, the load carrying capacity of the vault was increased by 179%. The textile debonded from the substrate, due to the concavity of the intrados, between intermediate connectors (500mm spaced), which effectively prevented the complete SRG detachment.

With respect to the unreinforced specimen, all SRG systems limited the opening of cracks on their side (either extrados or intrados) and the activation of the four-hinge mechanism, avoided displacement concentrations and entailed a larger volume of mobilized backfill. Accordingly, the displacement capacity was improved in terms of both peak displacement (increased by 4-10 times) and ultimate displacement (up to two times).

Test outcomes clearly demonstrate the effectiveness of SRG for increasing the load carrying capacity of masonry vaults, and the important role played by the connectors, to be placed either at the abutments (extrados applications) or along the arch barrel (intrados applications). With respect to other studies on masonry arches retrofitted with TRMs [De Santis et al., 2017c], however, the gain in strength over unreinforced specimens was relatively lower. On the one hand, this is due to the presence of buttresses and backfill, which significantly contributed to the capacity of the vault, especially without reinforcement. On the other hand, the possible increase

of strength appears limited by the slenderness. Thin vaults retrofitted with stiff strengthening systems may fail by crushing due to the concentration of compressive stresses in the sections subjected to the highest bending moment. Vaults retrofitted with more deformable reinforcements, which allow for larger deflections, may instead fail by sliding due to the concentration of shear stresses. Clearly, the possible occurrence of shear failure may be caused also by reduced friction and cohesion or relatively low axial load at the joints, and was observed especially in flat arches [Garmendia et al., 2014 – Ramaglia et al., 2017 – Bernat-Maso et al., 2012]. The condition of fixed abutments assumed in this study cannot always be attained in practice, and therefore more investigations are needed to analyse the support displacement capacity of masonry vaults reinforced with externally bonded TRM/SRG composites. Furthermore, experimental tests under horizontal loads or on the shake table would be useful to investigate specifically their seismic behaviour. Finally, in order to improve both the effectiveness and the efficiency of the retrofitting works carried out on the built heritage within restoration and upgrade activities, numerical models and design criteria should be developed based on experimental results. As a first contribution, a simplified analytical approach based on limit analysis was used in this study that provides a reliable estimate of the load carrying capacity of the reinforced vault specimens, thus appearing suitable for expeditious assessment and preliminary design purposes.

7. Conclusions

A wide laboratory investigation was carried out devoted to (i) the mechanical characterization of steel reinforced grout (SRG) composites and (ii) to the load-carrying capacity of masonry vaults reinforced with SRG. The SRG systems tested in this study comprised ultra high tensile strength steel cords and lime-based mortar, and proved effective for the externally bonded reinforcement of masonry arched members. The experimental results presented in this work may be useful for the development and calibration of numerical models and design methods. The main conclusions are summarized hereafter.

As for the fundamental mechanical characterization:

- In direct tensile tests, SRG composites exhibited an average tensile strength of about 3400N/mm^2 , which corresponds to a maximum load per unit width of reinforcement of 290.7kN/m , a peak strain of 2.03% and, finally, a tensile modulus of elasticity in the cracked stage of 180kN/mm^2 .
- Single-lap shear bond tests revealed a substrate-to-SRG load transfer capacity of 253.5kN/m , corresponding to 87% of its tensile strength, proving the high efficiency of the system thanks to the good interlocking of the steel cords within the mortar matrix as well as to the bond strength of this latter when bonded to masonry substrates.
- An analytical relationship was proposed to estimate the SRG-to-substrate bond strength in case of detachment at the textile-to-matrix interface that accounts for the mechanical properties of the mortar and of the amount of matrix that passes through the voids of the fabric.
- An acceptance procedure was applied to derive design parameters that is based on the combination of the results of tensile and bond tests

As for the bond behaviour of SRG on curved substrates:

- double-lap double-prism push-pull tests and four-point bending tests showed a reduction of the bond strength, with respect to plane substrates, of up to 45% for concave substrates and an increase of 40% for convex surfaces (both with curvature radius of 1800mm).
- A simplified analytical relationship was proposed to represent the increasing trend of the bond strength with the curvature radius, which may be used for a preliminary estimate of the effectiveness of SRG reinforcements applied to vaulted members.

Full-scale tests on masonry vaults showed that:

- SRG increased the load-carrying capacity both when applied to the intrados and when applied to the extrados, with respect to the unreinforced specimen. More specifically, the intrados reinforcement, provided with intermediate connectors installed along the arch barrel at 50cm spacing, led to an increase of 179% of the load-carrying capacity. The extrados reinforcements, provided with end connectors in the abutments, entailed an increase of 100-174%
- The displacement capacity was also increased in terms of both peak displacement (by 4-10 times) and ultimate displacement (up to two times larger than that of the unreinforced specimen).
- A simplified analytical approach based on limit analysis provided a good estimate of the load-carrying capacity of the reinforced vault specimens

Digital Image Correlation was successfully applied in all experimental tests, in addition to traditional equipment. It provided information on SRG-to-substrate slip crack pattern, displacement/strain concentrations, arch-backfill interaction that would have been unavailable otherwise due either to the number of instruments that would have been needed or to the necessity of selecting the measurement points on the base of the crack pattern, which is unknown a priori.

FUTURE DEVELOPMENTS

For future researches, several topics might be studied, because require investigations in depth.

1) Durability has become an important issue: due to damages over the years, environmental conditions and weather agents, materials properties of strengthening systems and structural elements can modify through inherent chemical reactions development. For these reasons, stress transfer could change both between textile and matrix phases of the composite material and at the interface reinforcement-substrate, associated with a loss of failure bond load in long-term case. Establishing a good correlation between artificial ageing condition and real ageing in terms of effective time should be a solution for helping structural health monitoring and for performance preservation of retrofitting.

2) Aiming at improving performance prediction of the retrofitting applications, numerical models and design formulations should be developed thanks to post processing of experimental tests data.

3) In order to investigate the support displacement capacity of masonry arched members reinforced with externally bonded composites, experimental tests could be carried out with imposed relative displacement of the abutments. The seismic response should also be directly studied through quasi-static tests under horizontal loads or shake table tests. Finally, field tests could be performed to analyse the structural behaviour of strengthened vaults taking into account the actual site and boundary conditions. All these issues, which have poorly been investigated so far, definitely deserve much research to gain an improved understanding of the advantages and drawbacks of the use of externally bonded composites in the rehabilitation of masonry vaults.

REFERENCES

ACI 440.2R-08: “Guide for the Design and Construction of Externally Bonded FRP Systems for Strengthening Concrete Structures”

ACI 440.7R-10: “Guide for the Design and Construction of Externally Bonded Fiber-Reinforced Polymer Systems for Strengthening Unreinforced Masonry Structures”

ACI 549.4R-13: “Guide to Design and Construction of Externally Bonded Fabric-Reinforced Cementitious Matrix (FRCM) Systems for Repair and Strengthening Concrete and Masonry Structures”

AFGC: “Réparation et renforcement des structures en béton au moyen des matériaux composites”

ASTM D 1141 – 98 (Reapproved 2003): “Standard Practice for the Preparation of Substitute Ocean Water”

CNR-DT 200 R1/2013 – “Istruzioni per la Progettazione, l'Esecuzione ed il Controllo di Interventi di Consolidamento Statico mediante l'utilizzo di Compositi Fibrorinforzati - Materiali, strutture di c.a. e di c.a.p., strutture murarie”

EC 0: “Design by testing” approach recommended by the Annex D of Eurocode 0

FIB bulletin 40: “FRP reinforcement in RC structures”

FIB bulletin 40: “Externally applied FRP reinforcement for concrete structures: technical report prepared by a working party of the T5.1 FRP reinforcement for concrete structures”

FIB bulletin 40: “Model Code 2010”

RILEM TC-250 CSM Instructions

UNI EN 2561: “Aerospace Series - Carbon Fibre Reinforced Plastics – Unidirectional Laminates - Tensile Test Parallel To The Fibre Direction”

Alecci V, Focacci F, Rovero L, Stipo G, De Stefano M. Extrados strengthening of brick masonry arches with PBO–FRCM composites: Experimental and analytical investigations. *Compos Struct* (2016); **149**:184-196.

Alkhroaji T, Thomas J. Structural strengthening using advanced composites. *JEC – Composites* / n°15 February-March 2005.

Ascione L, de Felice G, De Santis S. A qualification method for externally bonded Fibre Reinforced Cementitious Matrix (FRCM) strengthening systems. *Composites Part B: Engineering* (2015); **78**: 497-506,.

Barton B, Wobbe E, Dharani LR, Silva P, Birman V, Nanni A, et al. Characterization of reinforced concrete beams strengthened by steel reinforced polymer and grout (SRP and SRG) composites. *Mater Sci Eng* (2005); **412**(1-2): 129-136.

Bencardino F, Ombres L. Structural Performance of RC Beams Strengthened by SRG and FRCM System. *34th International Symposium on bridge and structural engineering, Venice, 2010*.

Bencardino F, Condello A. Structural behaviour of RC beams externally strengthened in flexure with SRG and SRP systems. *International Journal of Structural Engineering* (2014); **5** (4): 346-368.

Bencardino F, Condello A. Reliability and adaptability of the analytical models proposed for the FRP systems to the Steel Reinforced Polymer and Steel Reinforced Grout strengthening systems. *Composites Part B* (2015); **76**: 249-259.

Bencardino F, Condello A. SRG/SRP–concrete bond–slip laws for externally strengthened RC beams. *Composite Structures* (2015); **132**: 804–815.

Bernat-Maso E, Gil L, Marcé-Nogué J. The structural performance of arches made of few voussoirs with dry-joints. *Struct Eng Mech* (2012); **44**(6):775-799.

Bilotta A, Ceroni F, Nigro E, Pecce M. Experimental tests on FRCM strengthening systems for tuff masonry elements. *Construction and Building Materials* (2017); **138**: 114–133.

Blaber J, Adair B, Antoniou A. Ncorr: Open-Source 2D Digital Image Correlation Matlab Software. *Exp Mech* (2015); **55**(6):1105-1122.

Borri A, Castori G. Research on composite strengthening of historical housebuilding: Retrofitting intervention for masonry arches and vaults. *Proceedings of the 6th International Conference on Structural Analysis of Historic Construction, SAHC08*, Bath; United Kingdom; 2 July 2008 through 4 July 2008; Volume 2, 2008, 921-929.

Borri A, Casadei P, Castori G, Hammond J. Strengthening of brick masonry arches with externally bonded steel reinforced composites. *J Compos Constr* (2009); **13**(6):468-475.

Borri A, Castori G, Corradi M, 2010. Seismic Upgrading Works carried out with Composite Materials on Historic Constructions. *Proceedings of the Tenth International Conference on Computational Structures Technology*, B.H.V. Topping, J.M. Adam, F.J. Pallarés, R. Bru and M.L. Romero, (Editors), Civil-Comp Press, Stirlingshire, Scotland.

Borri A, Castori G. Indagini sperimentali sulla durabilità di materiali compositi in fibra d'acciaio. *Proceedings of the 14th National Conference on L'Ingegneria Sismica in Italia (ANIDIS), September 18-22, 2011, Bari, Italy.*

Borri A, Castori G, M. Corradi M. Shear behavior of masonry panels strengthened by high strength steel cords. *Construction and Building Materials (2011); 25: 494–503.*

Borri A, Castori G, Corradi M. Intrados strengthening of brick masonry arches with composite materials. *Compos Part B-Eng (2011); 42(5):1164-1172.*

Borri A, Castori G, Corradi M. Masonry Confinement Using Steel Cords. *J. Mater. Civ. Eng. (2013); 25(12): 1910-1919.*

Borri A, Castori G, Corradi M, Speranzini E. Durability Analysis for FRP and SRG Composites in Civil Applications. *Key Engineering Materials (2015); 624: 421-428.*

Caggegi C, Carozzi FG, De Santis S, Fabbrocino F, Focacci F, Hojdys L, et al. Experimental analysis on tensile and bond properties of PBO and Aramid fabric reinforced cementitious matrix for strengthening masonry structures. *Composites Part B (2017); 127: 175-195.*

Callaway P, Gilbert M, Smith CC. Influence of backfill on the capacity of masonry arch bridges. *Proceedings of the Institution of Civil Engineers: Bridge Engineering (2012); 165(3):147-158.*

Cancelli AN, Aielli MA, Casadei P. Experimental investigation on bond properties of SRP/SRG – Masonry systems. *Proc. 8th Int. Symp. on FRPRCS-8 University of Patras, Patras, Greece, July 16-18, 2007*.

Capozucca R. Double-leaf masonry walls under in-plane loading strengthened with GFRP/SRG strips. *Engineering Structures* (2016); **128**: 453–473.

Carbone I, de Felice G. Bond performance of fiber reinforced grout on brickwork specimens. *Structural Analysis of Historic Construction – D’Ayala & Fodde (eds) © 2008 Taylor & Francis Group, London, ISBN 978-0-415-46872-5*.

Carloni C, D’Antino T, Sneed LH, Pellegrino C. Role of the Matrix Layers in the Stress-Transfer Mechanism of FRCM Composites Bonded to a Concrete Substrate. DOI: 10.1061/(ASCE)EM.1943-7889.0000883. © 2014 American Society of Civil Engineers. *J. Eng. Mech.*, 2015, 141(6): -1–1.

Carloni C, D’Antino T, Sneed LH, Pellegrino C. An Investigation of PBO FRCM-Concrete Joint Behavior using a Three-Dimensional Numerical Approach. ©Civil-Comp Press, 2015 *Proceedings of the Fifteenth International Conference on Civil, Structural and Environmental Engineering Computing*, J. Kruis, Y. Tsompanakis and B.H.V. Topping, (Editors Civil-Comp Press, Stirlingshire, Scotland).

Carozzi FG, Milani G, Poggi C. Mechanical properties and numerical modeling of Fabric Reinforced Cementitious Matrix (FRCM) systems for strengthening of masonry structures. *Composite Structures* (2014); **107**: 711–725.

Carozzi FG, Poggi C. Mechanical properties and debonding strength of Fabric Reinforced Cementitious Matrix (FRCM) systems for masonry strengthening. *Composites: Part B* (2015); **70**: 215–230.

Carozzi FG, Colombi P, Fava G, Poggi C. A cohesive interface crack model for the matrix–textile debonding in FRCM composites. *Composite Structures* (2016); **143**: 230–241.

Carozzi FG, Bellini A, D'Antino T, de Felice G, Focacci F, Hojdis L, et al. Experimental investigation of tensile and bond properties of Carbon-FRCM composites for strengthening masonry elements. *Composites Part B* (2017); **128**: 100–119.

Casadei P, Nanni A, Alkhrdaji T. Steel-reinforced polymer: An innovative and promising material for strengthening infrastructures. *Concr. Eng. Int.* (2005); **9** (1): 54–56.

Castori G, Borri A, Corradi M. Behavior of thin masonry arches repaired using composite materials. *Compos Part B-Eng* (2016); **87**:311–321.

Ceroni F, de Felice G, Grande E, Malena M, Mazzotti C, Murgo F, Sacco E, Valluzzi MR. Analytical and numerical modelling of composite-to-brick bond. *Materials and Structures* (2014); **47**:1987–2003.

Cescatti E, Da Porto F, Modena C. Analysis and comparison of EBR techniques applied on masonry vaults. ACI SP. *To appear*.

D'Antino T, Carloni C, Sneed LH, Pellegrino C. Matrix–fiber bond behavior in PBO FRCM composites: A fracture mechanics approach. *Engineering Fracture Mechanics* (2014); **117**: 94–111.

Da Porto F, Stievanin E, Gabin E, Valluzzi MR. SRG applications for structural strengthening of RC beams. *ACI Spec Pub* (2012); **286**: 119–132. <http://dx.doi.org/10.14359/5168390>.

De Canio G, de Felice G, De Santis S, Giocoli A, Mongelli M, Paolacci F, Roselli I. Passive 3D motion optical data in shaking table tests of a SRG-reinforced masonry wall. *Earthq Struct* (2016); **10**(1): 53–71.

de Felice G. Assessment of the load-carrying capacity of multi-span masonry arch bridges using fibre beam elements. *Eng Struct*, (2009); **31**(8):1634–1647.

de Felice G, De Santis S, Garmendia L, Ghiassi B, Larrinaga P, Lourenço PB, Oliveira DV, Paolacci F, Papanicolaou CG. Mortar-based systems for externally bonded strengthening of masonry. *Materials and Structures* (2014); **47**(12):2021–2037.

de Felice G, Aiello MA, Bellini A, Ceroni F, De Santis S, Garbin E, Leone M, Lignola GP, Malena M, Mazzotti C, Panizza M, Valluzzi MR. Experimental characterization of composite-to-brick masonry shear bond. *Mater Struct* (2015); **49**(7):2581–2596.

De Lorenzis L, Dimitri R, La Tegola A. Reduction of the lateral thrust of masonry arches and vaults with FRP composites. *Constr Build Mater*, (2007); **21**(7):1415–1430.

De Santis S and De Felice G, Tensile behaviour of mortar-based composites for externally bonded reinforcement systems. *Composites Part B: Engineering* (2015); **68**: 401-413.

De Santis S, de Felice G. Steel reinforced grout systems for the strengthening of masonry. *Compos Struct* (2015); **134**:533-548.

De Santis S, Casadei P, De Canio G, de Felice G, Malena M, Mongelli M, Roselli I. Seismic performance of masonry walls retrofitted with steel reinforced grout. *Earthquake Engineering and Structural Dynamics* (2016); **45**(2): 229-251

De Santis S, Roscini F, de Felice G. Experimental characterization of mortar-based reinforcements with carbon fabrics. *Brick and Block Masonry – Trends, Innovations and Challenges – Modena, da Porto & Valluzzi (Eds) © 2016 Taylor & Francis Group, London, ISBN 978-1-138-02999-6*

De Santis S, Napoli A, de Felice G, Realfonzo R. Strengthening of structures with Steel Reinforced Polymers: A state-of-the-art review. *Compos Part B-Eng* (2016); **104**: 87-110.

De Santis S and de Felice G. Bond behaviour of steel reinforced grout strengthening systems applied to the extrados of masonry vaults. *Proceedings of the 10th International Conference on Structural Analysis of Historical Constructions, SAHC 2016, Leuven; Belgium; 13 September 2016 through 15 September 2016; 2016, 344-350.*

De Santis S, Ceroni F, de Felice G, Fagone M, Ghiassi B, Kwiecień A, Lignola G, Morganti M, Santandrea M, Valluzzi MR, Viskovic A. Round Robin Test on tensile and bond behaviour of Steel Reinforced Grout systems. *Compos Part B-Eng* (2017); **127**:100-120.

De Santis S, Carozzi FG, de Felice G, Poggi C. Test methods for Textile Reinforced Mortar systems. *Compos Part B-Eng* (2017); **127**:121-132.

De Santis S. Bond behaviour of Steel Reinforced Grout for the extrados strengthening of masonry vaults. *Constr Build Mater* (2017); **150**:367-382.

De Santis S, Roscini F, de Felice G, Retrofitting Masonry Vaults with Basalt Textile Reinforced Mortar, *Key Engineering Materials* (2017), **747**: 250-257.

De Santis S, Roscini F, de Felice G, Full-scale tests on masonry vaults strengthened with Steel Reinforced Grout. *Composites Part B (2018): Engineering*, **141**: 20-36, ISSN 1359-8368, <https://doi.org/10.1016/j.compositesb.2017.12.023>.

Focacci Francesco, 2008. Rinforzo delle murature con materiali compositi. Progettazione - Calcolo – Esempi applicativi. Dario Flaccovio Editore, Palermo

Focacci F. D’Antino T. Carloni C, Sneed, LH, Pellegrino C. An indirect method to calibrate the interfacial cohesive material law for FRCM-concrete joints. *Mater. Des.* (2017); **128**: 206–217.

Foraboschi P. Strengthening of masonry arches with fiber-reinforced polymer strips. *J Compos Constr* (2004); **8**(3):191-202.

Fossetti M, Minafò G, Strengthening of Masonry Columns with BFRCM or with SteelWires: An Experimental Study. *Fibers* 4 (2) (2016) 15.

Franzoni E, Gentilini C, Santandrea M, Zanutto S, Carloni C, Durability of steel FRCM-masonry joints: effect of water and salt crystallization. *Materials and Structures/Materiaux et Constructions* (2017); **50** (4), Article number 201.

Garmendia L et al., Rehabilitation of masonry arches with compatible advanced composite material. *Construction and Building Materials* (2011); **25** (12): 4374–4385,.

Garmendia L, Larrinaga P, García D, Marcos I. Textile-Reinforced Mortar as strengthening material for masonry arches. *Int J Arch Her* (2014);**8** (5):627-648.

Garmendia L, Larrinaga P, San-Mateos R, San-José JT. Strengthening masonry vaults with organic and inorganic composites: an experimental approach. *Mater Des* (2015); **85**:102-114.

Ghiassi B, Verstrynge E, Lourenço PB., Oliveira DV. Characterization of debonding in FRP-strengthened masonry using the acoustic emission technique. *Engineering Structures* (2014); **66**: 24–34.

Girardello P, Pappas A, Da Porto F, Valluzzi MR. Experimental testing and numerical modelling of masonry vaults. In: *Proceedings of Int. Conf. on Rehabilitation and Restoration of Structures Chennai, India, 2013*.

Grande E, Imbimbo M, Sacco E. Modeling and numerical analysis of the bond behavior of masonry elements strengthened with SRP/SRG. *Composites: Part B* (2013); **55**: 128–138.

Grande E, Imbimbo M, Sacco E. Investigation on the bond behavior of clay bricks reinforced with SRP and SRG strengthening systems. *Materials and Structures* (2015); **48**: 3755–3770.

Huang X, Birman V, Nanni A, Tunis G. Properties and potential for application of steel reinforced polymer and steel reinforced grout composites. *Composites: Part B* (2005); **36**: 73–82.

Leone M, Aiello MA, Balsamo A, Carozzi FG, Ceroni F, Corradi M, et al. Glass fabric reinforced cementitious matrix: Tensile properties and bond performance on masonry substrate. *Composites Part B* (2017); **127**: 196-214.

Lignola GP, Caggegi C, Ceroni F, De Santis S, Krajewski P, Lourenço PB, et al. Performance assessment of basalt FRCM for retrofit applications on masonry. *Composites Part B* (2017); **128**: 1-18.

Malena M and de Felice G, Debonding of composites on a curved masonry substrate: Experimental results and analytical formulation. *Composite Structures* (2014), **112** (1): 194-206.

Malena M, De Santis S, Pantò B, de Felice G. A closed-form analytical solution to the debonding of SRG on curved masonry substrate. *Key Eng Mater* (2017); **747**:313-318.

Matana M, Galecki G, Maerz N, Nanni A. Concrete substrate preparation and characterization prior to adhesion of externally bonded reinforcement. *Proceedings of International Symposium on Bond Behaviour of FRP in Structures (BBFS 2005)* © 2005 International Institute for FRP in Construction.

Matana M, Nanni A, Dharani L, Silva P, Tunis G. Bond performance of steel reinforced polymer and steel reinforced grout. *Proceedings of International Symposium on Bond Behaviour of FRP in Structures (BBFS 2005)* © 2005 International Institute for FRP in Construction.

Napoli A, Realfonzo R. Reinforced concrete beams strengthened with SRP/SRG systems: Experimental investigation. *Construction and Building Materials* (2015); **93**: 654–677.

Napoli A, de Felice G, De Santis S, Realfonzo R. Bond behaviour of Steel Reinforced Polymer strengthening systems. *Composite Structures* (2016); **152**: 499–515.

Ochsendorf J. Guastavino Vaulting. The Art of Structural Tile. *Princeton: Princeton Architectural Press, 2010*.

Ombres L. Analysis of the bond between Fabric Reinforced Cementitious Mortar (FRCM) strengthening systems and concrete. *Composites: Part B* (2015); **69**: 418–426.

Olivito RS, Codispoti R, Cevallos AO. Bond behavior of Flax-FRCM and PBO-FRCM composites applied on clay bricks: Experimental and theoretical study. *Composite Structures* (2016); **146**: 221–231.

Pan B, Qian K, Xie H, Asundi A. Two-dimensional digital image correlation for in-plane displacement and strain measurement: a review. *Meas. Sci. Technol.* (2009); **20**(6):062001.

Papanicolaou CG, Triantafillou TC, Kyriakos K, Papathanasiou M, Textile-reinforced mortar (TRM) versus FRP as strengthening material of URM walls: in-plane cyclic loading. *Materials and Structures* (2007); **40**: 1081–1097.

Papanicolaou CG, Triantafillou TC, Papathanasiou M, Kyriakos K, Textile reinforced mortar (TRM) versus FRP as strengthening material of URM walls: out-of-plane cyclic loading. *Materials and Structures* (2008); **41**:143–157.

Pecce M, Ceroni F, Prota A, Manfredi G. Response prediction of RC beams externally bonded with steel-reinforced polymers. *J Compos Constr*2006; **10**(3):195-203.

Ramaglia G, Lignola GP, Balsamo A, Prota A, Manfredi G. Seismic strengthening of masonry vaults with abutments using Textile Reinforced Mortar. *J Compos Constr* 2017; **21**(2):04016079.

Razavizadeh A, Ghiassi B, Oliveira DV. Bond behavior of SRG-strengthened masonry units: Testing and numerical modeling. *Construction and Building Materials* (2014); **64**: 387–397.

Roscini F, De Santis S, de Felice G. Experimental investigation on the mechanical behaviour of mortar-based strengthening systems. *Proceedings of 10th International Conference on Structural Analysis of Historical Constructions (SAHC2016), 12-16 September 2016, Leuven, Be.*

Roscini F, De Santis S, de Felice G, 2016. Evaluation of the bond behaviour of Steel Reinforced grout applied to curved masonry substrate via bending test. *PROHITECH'17 3rd International Conference on Protection of Historical Constructions, At Lisbon, Portugal*.

Sneed LH, Verre S, Carloni C, Luciano Ombres L. Flexural behavior of RC beams strengthened with steel-FRCM composite. *Engineering Structures* (2016); **127**: 686–699.

Stievanin E, da Porto F, Panizza M, Garbin E, Modena C. Bond characterization between historical concrete substrate and SRG/SRP strengthening systems. *Research and Applications in Structural Engineering, Mechanics and Computation – Zingoni (Ed.)* © 2013 Taylor & Francis Group, London, ISBN 978-1-138-00061-2.

Tekieli M, De Santis S, de Felice G, Kwiecień A, Roscini F. Application of Digital Image Correlation to composite reinforcements testing. *Compos Struct* (2017); **160**:670-688.

Tetta ZC, Koutas LN, Bournas DA. Textile-reinforced mortar (TRM) versus fiber-reinforced polymers (FRP) in shear strengthening of concrete beams. *Composites Part B* (2015); **77**: 338-348.

Thermou GE, S. J. Pantazopoulou. SJ Metallic fabric jackets: an innovative method for seismic retrofitting of substandard RC prismatic members. 1464–4177 (Print) 1751–7648 (Online) © 2007 Thomas Telford and fib.

Thermou GE, Katakalos K, Manos G. Influence of the loading rate on the axial compressive behaviour of concrete specimens confined with SRG jackets. *COMPdyn 2013 4th ECCOMAS Thematic Conference on Computational Methods in Structural Dynamics and Earthquake Engineering* M. Papadrakakis, V. Papadopoulos, V. Plevris (eds.) Kos Island, Greece, 12–14 June 2013.

Thermou GE, Katakalos K, Manos G. Concrete confinement with steel-reinforced grout jackets. *Materials and Structures* (2015); **48**: 1355–1376.

Thermou GE, Katakalos K, Manos G. Influence of the cross section shape on the behaviour of SRG-confined prismatic concrete specimens. *Materials and Structures* (2016); **49**: 869–887.

Thermou, G.E., Katakalos, K., Manos, G. Experimental investigation of substandard RC columns confined with SRG jackets under compression. *Composite Structures* (2018); **184**: 56-65.

Thermou, G.E., Hajirasouliha, I. Compressive behaviour of concrete columns confined with steel-reinforced grout jackets. *Composites Part B: Engineering* (2018); **138**: 222-231.

Triantafillou TC, Plevris N, Strengthening of RC beams with epoxy-bonded fibre-composite materials. *Materials and Structures* (1992); **25** (4): 201-211.

Valluzzi MR, Valdemarca M, Modena C. Behaviour of brick masonry vaults strengthened with FRP laminates. *J Compos Constr* (2001); **5**(3): 163-169.

Valluzzi MR, Oliveira DV, Caratelli A, Castori G, Corradi M, Gianmarco de Felice G, Garbin E, Garcia D, Garmendia L, Grande E, Ianniruberto U, Kwiecien' A, Leone M, Lignola GP, Lourenço PB, Malena M, Micelli F, Panizza M, Papanicolaou CG, Prota A, Sacco E, Triantafillou TC, Viskovic A, Zaja B, Zuccarino G. Round Robin Test for composite-to-brick shear bond characterization. *Materials and Structures* (2012); **45**: 1761–1791.

Valluzzi MR, Modena C, de Felice G. Current practice and open issues in strengthening historical buildings with composites. *Mater Struct* (2014); **47**(12):1971-1985.

Valluzzi MR, Da Porto F, Garbin E, Panizza M. Out-of-plane behaviour of infill masonry panels strengthened with composite materials. *Materials and Structures* (2014); **47**: 2131–2145.

Wobbe E, Silva P, Barton BL, Dharani LR, Birman V, Nanni A, Alkhrdaji T, Thomas J and Tunis G, 2004. Flexural capacity of RC beams externally bonded with SRP and SRG. *In International SAMPE Technical Conference* (pp. 3009-3016).

RINGRAZIAMENTI

Il ringraziamento principale è per il Chiar.mo Professor Gianmarco de Felice per avermi dato la possibilità di vivere un'esperienza professionale e personale unica. Dal suo esempio e dai suoi preziosi insegnamenti ho avuto il grande onore di acquisire nuove competenze e di approfondire le mie conoscenze. Grazie alla sua guida, abbiamo affrontato insieme tantissime e importantissime sfide, che hanno arricchito il percorso di Dottorato di occasioni e di risultati di indiscutibile valore per la ricerca scientifica.

Ringrazio infinitamente il Dr. Stefano De Santis, perché lavorare insieme è stato un vero e proprio privilegio. Far parte della stessa squadra mi ha permesso di osservare direttamente la sua preparazione, il suo impegno e la sua dedizione per il lavoro di ricerca. I suoi consigli tecnici e umani sono stati sempre motivo di crescita e di miglioramento.

Grazie al Senior Lecturer Dr. Maurizio Guadagnini del “Department of Civil and Structural Engineering – The University of Sheffield”, per la sua vicinanza e il suo supporto fondamentali sia nel mio periodo di ricerca come Visiting a Sheffield, sia durante tutto il periodo di scrittura della tesi. Lo ringrazio altresì, insieme a tutto lo “Sheffield Team”, per avermi accolta nella loro Family: tutti grandi colleghi e amici.

Ringrazio il Prof. Fabrizio Paolacci, la Dr.ssa Marialaura Malena e il Dr. Daniele Corritore per la loro professionalità e disponibilità, che sempre mi hanno riservato. Grazie all'Arch. Lorena Sguerri e a tutto il personale tecnico del Laboratorio PRISMA, Sig. Mario Colantuono e Sig. Roberto Candelaresi per la collaborazione e l'aiuto durante tutte le prove sperimentali.

Grazie a tutto il personale amministrativo della Sezione di Civile, in particolar modo la Dr.ssa Marina Cibati e la Dott.ssa Carla Quattrocioche per la loro assistenza e la loro cortesia.

Ringrazio Niki Trochoutsou, Valeria Rizzo e Pietro Meriggi, con l'augurio che la loro esperienza di dottorato sia appagante ed entusiasmante come lo è stata per me.

A tutti gli studenti e soprattutto a tutti i tesisti triennali e magistrali che sono stati coinvolti nei nostri progetti di ricerca rivolgo un grandissimo “grazie” per l'impegno e la passione profusi nei loro lavori di tesi.

Ringrazio i miei Genitori, per credere sempre in me e più di me.

Grazie a tutta la mia Famiglia, alle mie nonne, ai miei zii e a mio cugino Francesco, sempre presenti nel sostenermi.

Ringrazio infine i miei Amici, vicini e lontani, per essermi accanto, in ogni momento.